THE GEOCHEMISTRY OF METHANE ISOTOPOLOGUES

David Texan Wang

B.S., California State University, Los Angeles, 2011

Submitted in partial fulfillment of the requirements
for the degree of Doctor of Philosophy

at the MASSACHUSETTS INSTITUTE OF TECHNOLOGY
and the WOODS HOLE OCEANOGRAPHIC INSTITUTION

June 2017

AUTHOR: David T. Wang
Department of Earth, Atmospheric and Planetary Sciences, MIT
Marine Chemistry and Geochemistry Department, WHOI
MIT/WHOI Joint Program in Oceanography/Applied Ocean Science and Engineering
5th May 2017

CERTIFIED BY: Shuhei Ono
Associate Professor of Geochemistry, MIT
Thesis Supervisor

ACCEPTED BY: Shuhei Ono
Chair, Joint Committee for Chemical Oceanography

THE GEOCHEMISTRY OF METHANE ISOTOPOLOGUES

David Texan Wang

Submitted to the Joint Program in Oceanography/Applied Ocean Science and Engineering,
Massachusetts Institute of Technology & Woods Hole Oceanographic Institution,
on 5th May 2017, in partial fulfillment of the requirements for the degree of
Doctor of Philosophy in the field of Geochemistry

Abstract

This thesis documents the origin, distribution, and fate of methane and several of its isotopic forms on Earth. Using observational, experimental, and theoretical approaches, I illustrate how the relative abundances of $^{12}CH_4$, $^{13}CH_4$, $^{12}CH_3D$, and $^{13}CH_3D$ record the formation, transport, and breakdown of methane in selected settings.

Chapter 2 reports precise determinations of $^{13}CH_3D$, a "clumped" isotopologue of methane, in samples collected from various settings representing many of the major sources and reservoirs of methane on Earth. The results show that the information encoded by the abundance of $^{13}CH_3D$ enables differentiation of methane generated by microbial, thermogenic, and abiogenic processes. A strong correlation between clumped- and hydrogen-isotope signatures in microbial methane is identified and quantitatively linked to the availability of H_2 and the reversibility of microbially-mediated methanogenesis in the environment. Determination of $^{13}CH_3D$ in combination with hydrogen-isotope ratios of methane and water provides a sensitive indicator of the extent of C–H bond equilibration, enables fingerprinting of methane-generating mechanisms, and in some cases, supplies direct constraints for locating the waters from which migrated gases were sourced. Chapter 3 applies this concept to constrain the origin of methane in hydrothermal fluids from sediment-poor vent fields hosted in mafic and ultramafic rocks on slow- and ultraslow-spreading mid-ocean ridges. The data support a hypogene model whereby methane forms abiotically within plutonic rocks of the oceanic crust at temperatures above ca. 300 °C during respeciation of magmatic volatiles, and is subsequently extracted during active, convective hydrothermal circulation. Chapter 4 presents the results of culture experiments in which methane is oxidized in the presence of O_2 by the bacterium *Methylococcus capsulatus* strain Bath. The results show that the clumped isotopologue abundances of partially-oxidized methane can be predicted from knowledge of $^{13}C/^{12}C$ and D/H isotope fractionation factors alone.

THESIS SUPERVISOR: Shuhei Ono, Ph.D.
TITLE: Associate Professor, MIT

Contents

List of Figures

List of Tables

Acknowledgments

I fear that this section will not do justice to the people I have not the space to thank individually. Alas, here goes. To those whose names are not specifically listed here, thank you too.

I wish first to thank Shuhei Ono. The work this thesis represents could not have happened without his bold vision and the license to explore and question that working in his lab afforded. His unbridled optimism, breadth of scientific curiosity, personal integrity, and accessibility to his personnel are traits I one day hope to emulate. I thank him for his nonjudgmental yet appropriately measured support of many of my ideas—even those that led nowhere—, for believing in me even when I found it difficult to do so myself, and for teaching me to change pump oil, build vacuum lines, and drink Icelandic vodka.

I also wish to thank my thesis committee members Jeff Seewald, Roger Summons, and John Pohlman, for their input and genuine interest in my projects, for their coauthorship on one or more manuscripts, and for serving as sounding boards for questions about life and career. Meg Tivey is thanked for chairing my defense and for her comments on this thesis.

Many members of the Ono lab have contributed time or ideas towards the work in this thesis. I particularly wish to acknowledge Danielle Gruen, who has been a wonderful friend, stand-in sibling, and multi-talented colleague. Without her efforts in the field and the lab, we would not have made the discovery of the "hot cow" that is now perhaps the MIT Hardcore Stable Isotope Laboratory's best-known result. Bill Olszewski has been a fount of technical wizardry and occasional oddball humor, both of which are appreciated. Eoghan Reeves, Genming Luo, Andrew Whitehill, Shikma Zaarur, Yenny Gonzales Ramos, and Jeemin Rhim are thanked for their company both at and away from the shop.

Other members of the E25-6th floor community have made it worth coming into work each day. These include my officemates Ana de Santiago Torio, Gilad Antler, Mirna Daye, and Kristin Woycheese, and reliable sources of conversation Simone, Sharon, Christine, Xiaolei, Ross, Shane, Emily, Robert, Haitao, Annie, Christopher, Ainara, and Melody. My fellow JP students—including Ning, Nick, Kate, Evan, Rene, and Craig—provided much needed inspiration (and commiseration and distraction) at times.

I have had the privilege of working in several other labs during the past six years. Tanja Bosak served as my co-advisor for my Generals project on sulfate reducing bacteria. I thank her for welcoming me into her lab, for helping me become a more succinct writer and shrewd reader, and for her encouragement at a particularly frustrating point in my research. I also thank Mak Saito, who took me under his wing my first year, offered the opportunity to join my first oceanographic cruise (and first equator-crossing!), and—after I splashed some acid on myself while hastily preparing reagents before departing for said cruise—kindly drove me to his house so that I could have a shower, a change of clothes, and a day-old scone. I thank Jeff Seewald for making me feel welcome in his group while I puttered about trying to deuterate his lab.

Many thanks are due to members of the Bosak, Saito, and Seewald labs. Min Sub Sim showed me how to work with sulfate-reducing bacteria, and Peter Hedman, Alex Evans, and Laura Meredith provided assistance at one time or another during my first two years at MIT. Help or advice from Sean Sylva, Jill McDermott, Dawn Moran, Matt McIlvin, Tyler Goepfert, and others in the Fye and Watson Buildings at WHOI are gratefully acknowledged.

Several other faculty members dispensed much needed advice at one point or another, including Ed Boyle, Scott Wankel, Dave Glover, Amanda Spivak, Scott Doney, Carl Lamborg, and Frieder Klein. Bernhard Peucker-Ehrenbrink, Liz Kujawinski, and Mark Kurz assisted in navigating the administrative waters of the JP. Rachel Stanley kindly served as chair for my thesis proposal defense. I thank those instructors in whose courses I did not actually enroll, but who still allowed me to participate in their study tours—David McGee, Taylor Perron, and Oli Jagoutz (MIT), Rob Sohn, Meg Tivey & Andrew Daly (Geodynamics 2015, WHOI), John Shaw (Harvard), and Grant Garven (Tufts).

The administrators in E25, particularly Melody Abedinejad, Mary Eliff, and (briefly) Annora Borden, are thanked for making life easier in too many ways to name. I also thank the staff of the MIT Joint Program Office (Ronni Schwartz and Kris Kipp), PAOC administration (Christine Maglio), ERL administration (Anna Shaughnessy and Josh Kastorf), EAPS HQ (esp. Roberta Allard, Angela Ellis, Brian Smith, and Mark Pendleton), the WHOI MC&G Department (esp. Mary Zawoysky), and the Academic Programs Office (Julia Westwater, Lea Fraser, Tricia Morin Gebbie, Christine Charette, Valerie Caron, Meg Tivey, and Jim Yoder). Also, I want to acknowledge the security staff at WHOI—they more than once let me into a locked building or gave me a lift back to Winding Lane—, as well as the custodial staff at MIT, particularly Sergio Medina, who I could always count on to share stories and snacks when working late into the night.

I have been lucky enough to be plugged into several wonderful scientific communities outside of MIT and WHOI, thanks in no small part to Shuhei and several collaborators. Thanks goes to the instructors and students of the International Geobiology Summer Course 2013 (it didn't suck!) for exposing me to the geobiological sciences, and the Agouron Institute and the Henry Houghton fund of PAOC for sponsoring my participation. The Deep Carbon Observatory (DCO) funded much of the work in this thesis, and also afforded me the opportunity to attend and present at several meetings; Craig Schiffries, Mitch Sogin, Barbara Sherwood Lollar, Kai-Uwe Hinrichs, and Fumio Inagaki, among others, are thanked for these opportunities. Two other much-needed breaks punctuated my graduate studies. I thank Jen Shosa, Michael Lawson, Mike Formolo, Glenn Hieshima, and everyone else who made being an intern at ExxonMobil interesting and fun. I also thank my entire IODP Expedition 370 "T-Limit" family, particularly Verena Heuer, Fumio Inagaki, Akira Ijiri, Flo Schubotz, Hayley Manners, Masanori Kaneko, Bernhard Viehweger, and Art Spivack for a great few months at sea and in Kochi.

Miscellaneous thanks goes to the folks at Aerodyne Research (Dave Nelson, Barry McManus, Joanne Shorter, Mark Zahniser, Christoph Dyroff, and Stanley Huang) for technical support, Issaku Kohl for organizing the return of a stranded sample, L. Taras Bryndzia for arranging funding from Shell through the Society of Energy Fellows at MIT to support my last year of studies, Chris Clayton for sharing unpublished data which helped frame my views on the origin of H in thermogenic hydrocarbons, Carolyn Ruppel for connecting me to the gas hydrates world, Jeff Dick for technical support related to CHNOSZ, Jordan Bird for sampling a rice paddy, my previous research mentors (Andre Ellis, Oliver Dorigo, and Chintda Santiskulvong) for introducing me to science, Penny Morrill for telling me something I needed to hear, and Lisa Morgan Morzel for gifting me her DCO hat.

My friends outside of EAPS and the JP have played no insignificant role in helping me maintain perspective on life. For this, I thank my roommates past and present (esp. Nate, Diego, and Benedikt), sailing partner (Pablo), friends from Harvard EPS (Yanpeng and Joe), fellow Boston-area EEP alumni (including David, Alex, Daniel, and Matt), and friends from the MIT Concert Band (Melissa, Tom C., Brynna, Faith, and many others). Tom Reynolds deserves a special mention; his work ethic and constant encouragement as conductor has made me a much improved trumpet player over my almost five years with the band.

Finally, I thank my parents. They have been voices of encouragement and reason during my happiest days and my darkest. This doctoral thesis completes what they came to the U.S. decades ago to begin, but ultimately chose not to finish so that their son might have a better shot at doing so himself.

FINANCIAL SUPPORT

The research activities documented in this thesis were made possible by grants to my advisor from the U.S. National Science Foundation (NSF award EAR-1250394), the National Aeronautics and Space Administration (NASA) Astrobiology Institute (NAI, University of Colorado, Boulder, CAN 7 under Cooperative Agreement NNA15BB02A), the Department of Energy (DOE, Small Business Innovation Research program, contract DE-SC0004575), the Alfred P. Sloan Foundation via the Deep Carbon Observatory, and a Shell Graduate Fellowship through the MIT Energy Initiative.

I completed the bulk of the work in this thesis while being supported by a National Defense Science and Engineering Graduate (NDSEG) Fellowship awarded through the Office of Naval Research of the U.S. Department of Defense. The Stanley W. Watson Fellowship Fund provided support during my first summer term at WHOI. The Charles M. Vest Presidential Fellowship at MIT supported me in the first year of my Ph.D. studies. I received additional support that year through NSF award EAR-1159318 (to S. Ono and T. Bosak) and the Walter & Adel Hohenstein Graduate Fellowship of Phi Kappa Phi. The MIT Earth Resources Laboratory and PAOC Houghton Fund funded my attendance at several conferences.

Chapter 1

Introduction

Methane is the simplest and most abundant hydrocarbon. Figure 1.1 shows some statistics on the portions of the methane cycle that this thesis touches upon.

1.1 ESSENTIAL DEFINITIONS

The *isotopologues* (or isotopic homologues) of a compound have the same elemental composition and chemical structure, but differ only in the identity of the isotopes of one or more atoms. The word *isotopologue* is also seen as *isotopolog*.

The goal of this thesis is to help map the distribution and behavior of the four most abundant methane isotopologues at the Earth surface and in the crustal subsurface. These isotopologues are shown in Figs. 1.2 and 1.3 (approximate ranges of abundance for the singly-substituted methane isotopologues are shown in Fig. 1.4) and written in the isotope exchange reaction below:

$$^{13}CH_4 + {}^{12}CH_3D \rightleftharpoons {}^{13}CH_3D + {}^{12}CH_4 \tag{1.1}$$

In this reaction, one deuterium (D) is exchanged for one hydrogen (H), while leaving in place the two different carbon (C) isotopes and the three other H's to which each C is connected. The equilibrium constant for this reaction is primarily a function of temperature (the effect of pressure is negligible at near-surface conditions), and is shown in Fig. 1.3. The equilibrium constant for this reaction asymptotically approaches unity as temperatures increase towards infinity. A sample of methane whose relative abundance of isotopologues obey the relation $(^{13}CH_4)(^{12}CH_3D) = (^{13}CH_3D)(^{12}CH_4)$ (i.e., has a reaction quotient equal to unity) is said to have a *stochastic distribution* of isotopes among isotopologues. At lower temperatures, the equilibrium constant is greater than one, albeit only slightly, by 0.6% or 6‰ (permil) at room temperature. The origin of this *clumpiness* at equilibrium at lower temperatures arises from a disproportionate lowering of zero-point energy upon clumping of two or more heavy isotopes (Fig. 1.5). For more on this topic, readers are referred to Eiler (2007).

Attainment of equilibrium in CH_4 clumped isotopologue abundances requires reordering of the C–H bonds within molecules. This may occur by homogeneous (direct) exchange of H between two CH_4 molecules, or by all CH_4 molecules independently exchanging H with a second species (heterogeneous). Understanding the mechanisms enabling exchange in various environments is vital for correct interpretation of classical and novel stable isotope geothermometers. Figure 1.6 shows the many pathways by which several single-carbon compounds can exchange isotopes with compounds in the C–O–H system.

1.2 PREVIEW OF THESIS CONTENT

Several labs are now able to make measurements of the reaction quotient of Reaction 1.1, to better than 0.05% (or 0.5‰). These include John Eiler's lab at Caltech (Stolper *et al.*, 2014b), Shuhei Ono's lab at MIT (Ono *et al.*, 2014), and Ed Young's lab at UCLA (Young *et al.*, 2016). For those interested in the race towards measuring intact methane isotopologues, readers are referred to Jones (2012).

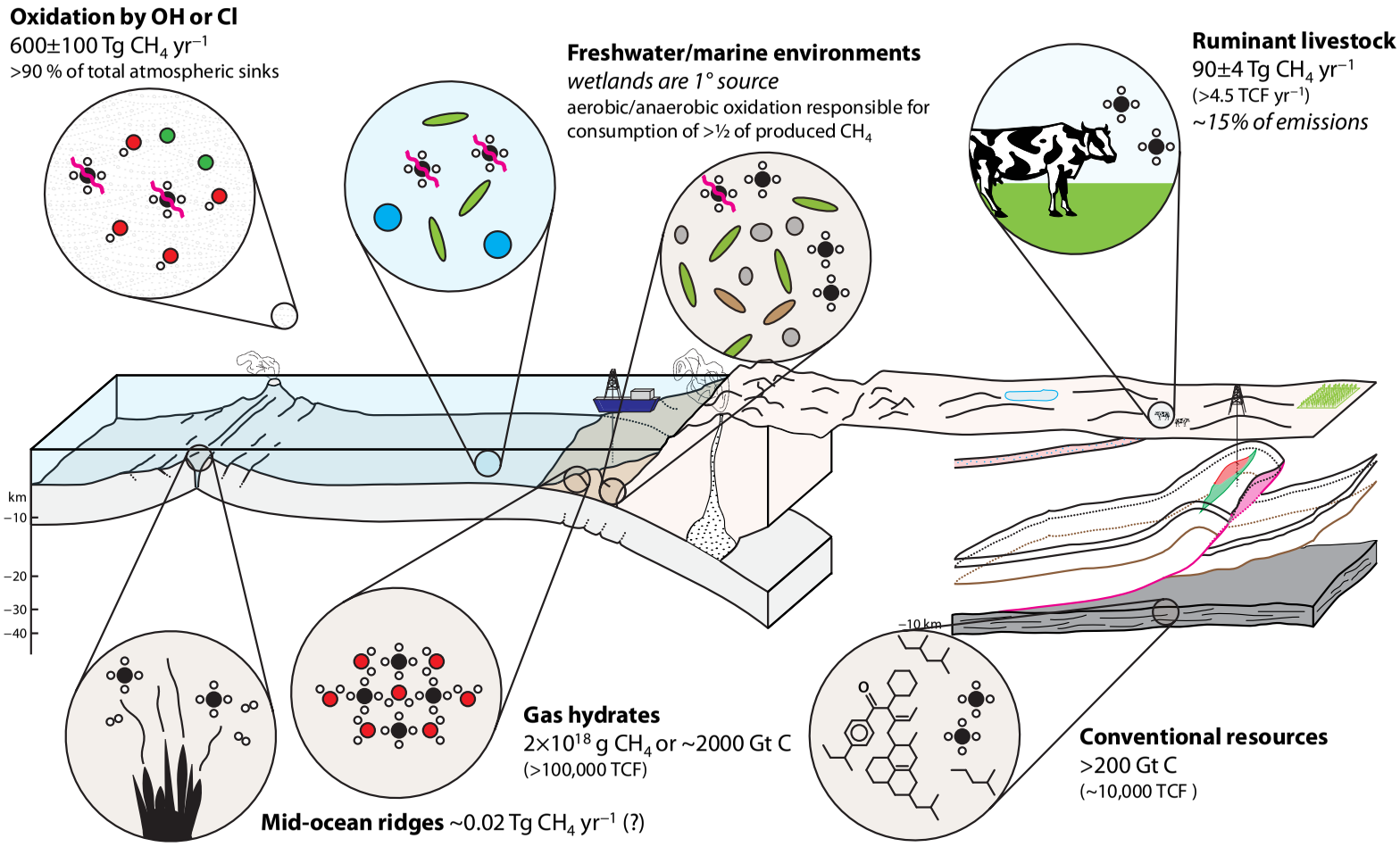

Figure 1.1 | Some of the many reservoirs and fluxes of methane on Earth, and their relative magnitudes (Kvenvolden, 1988; Keir, 2010; IPCC, 2013; Kirschke *et al.*, 2013).

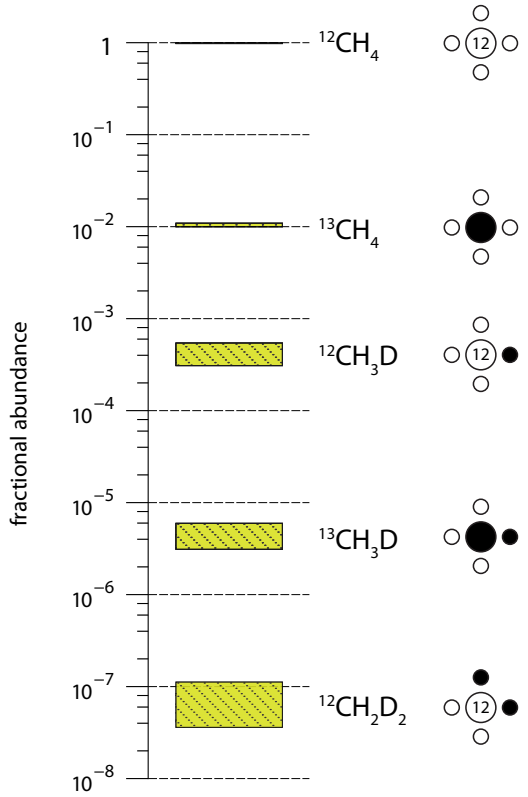

Figure 1.2 | Relative abundance of the five most abundant methane isotopologues in nature.

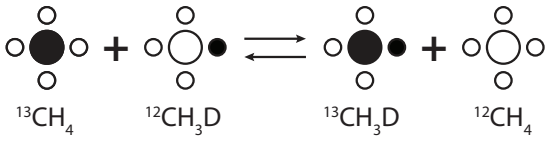

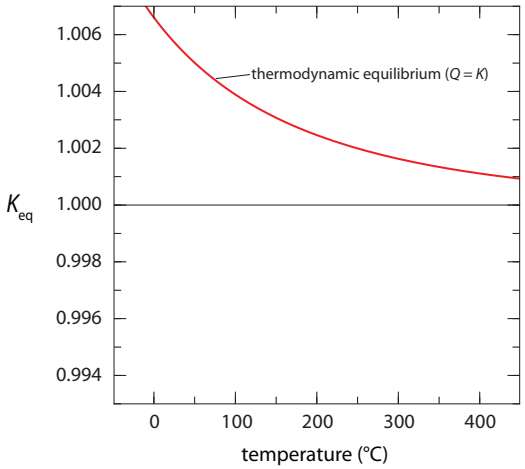

Figure 1.3 | Temperature-dependence of the equilibrium constant for the isotopologue exchange reaction in Reaction 1.1 (also shown graphically at top).

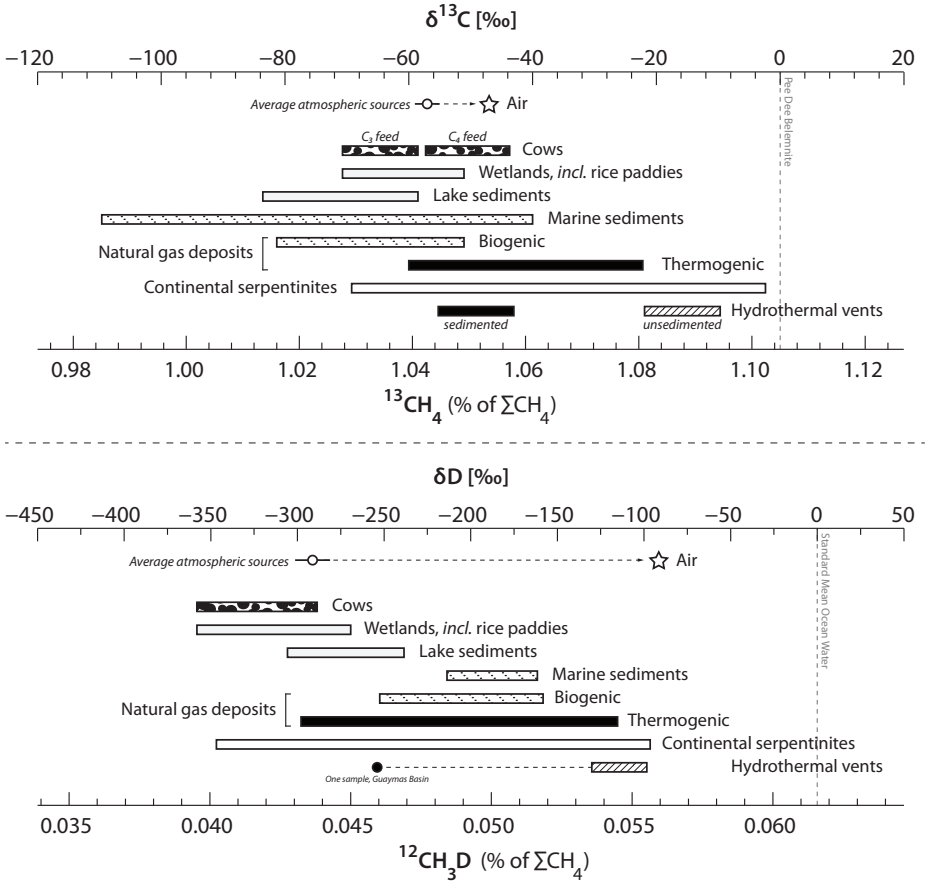

Figure 1.4 | Typical abundances of $^{13}CH_4$ (*top*) and $^{12}CH_3D$ (*bottom*) in nature.

Figure 1.5 | Zero-point energy lowering and the origin of non-stochastic clumped isotopologue composition at equilibrium. The zero-point energy (the energy of the ground state, the quantum state with the lowest possible energy) of a molecule of methane is lowered upon substitution of heavy isotopes. The amount by which the zero-point energy is lowered upon double-isotope substitution (e.g., $^{12}CH_4$ to $^{13}CH_3D$) is slightly greater than the sum of the effects of substituting only one heavy isotope (to make $^{13}CH_4$ and $^{12}CH_3D$). This deviation from the "rule of the geometric mean" (Bigeleisen, 1955) is particularly pronounced at lower temperatures, and is the origin of the preferential clumping at equilibrium shown in Fig. 1.3. For a detailed treatment, readers are referred to Eiler (2007).

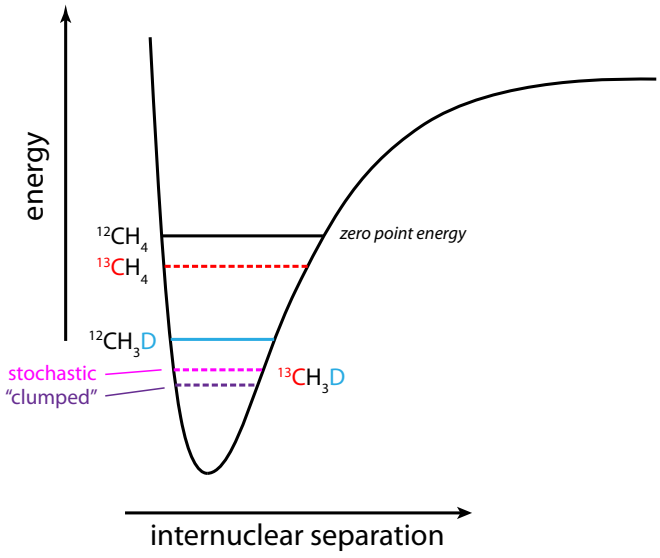

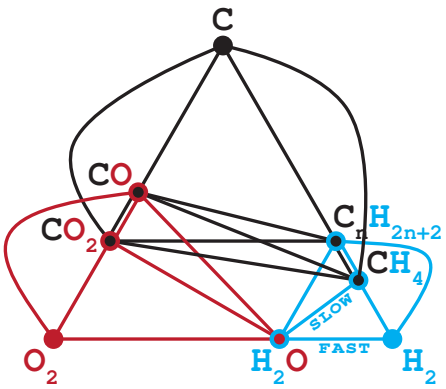

Figure 1.6 | Pathways for isotopic exchange between major species in the system C–O–H. The core & ring of nodes with two colors represent the central & outer atoms, respectively. Each line in this diagram represents a geothermometer comprising the isotope ratios of the corresponding element in the species at the nodes connected by the line. (Not shown: H_3COOH, H_2CO, CH_3OH)

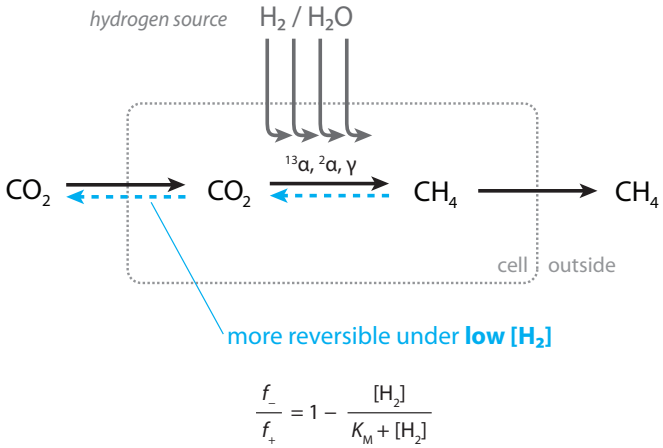

Figure 1.7 | Preview of one of the main conclusions of Chapter 2: The isotopic composition of methane produced by methanogenesis is determined by reversibility, which in turn is related to free energy (for which the primary variable in most environments is H_2 concentration).

Chapters 2, 3, and 4 and Appendix A describe insights we have gleaned while studying the origin of C, H, and carbon-hydrogen bonds in CH_4 using measurements and models of the abundance and behavior of methane isotopologues. Chapter 2 presents the first survey of the abundance of fully-resolved $^{13}CH_3D$ in various environments on Earth, and shows how and why microbial methanogenesis occurring under high H_2 and low CO_2 levels might leave a very distinct record in the isotopic composition of the CH_4 produced (Fig. 1.7). Chapter 2 also briefly touches on a potential for hydrogen exchange observed in high-maturity thermogenic gases.

Chapter 3 presents a study that attempts to address the oft-contentious question of where and how methane in seafloor hydrothermal systems forms. A diagram showing the several main proposed avenues for methane formation in such systems is in Fig. 1.8. There is interest in knowing the answer to this question because of potential implications for the origin of life at deep-sea hot springs.

Chapter 4 is an experimental and theoretical study that illustrates how one major sink of methane in the environment, aerobic methanotrophy, affects the isotopologue abundances of leftover methane (Fig. 1.9). The results and equations can be generalized to other major methane sinks (including oxidation by OH and Cl in the atmosphere; Whitehill *et al.*, 2017), and to other isotopologues (e.g., $^{12}CH_2D_2$).

Research on the behavior of methane isotopologues like $^{13}CH_3D$ have a natural alignment to many of the questions that are important and possibly unanswered in assessment of petroleum systems, particularly in poorly understood basins (Fig. 1.10). In particular, measurements of methane isotopologues can

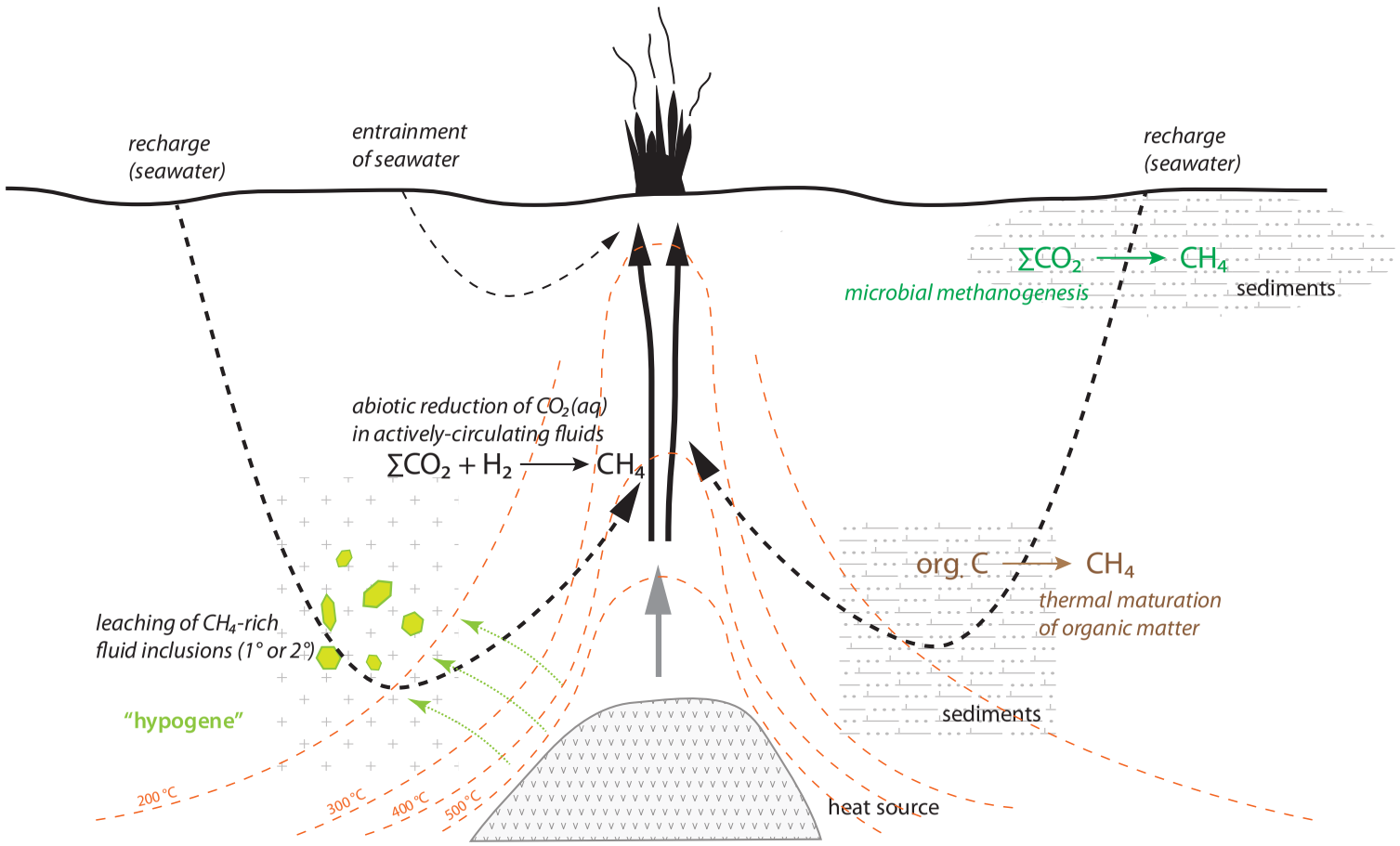

Figure 1.8 | Pathways for methane formation in mid-ocean ridge hydrothermal systems. Chapter 3 shows how data from sediment-poor systems are most compatible with what we term a *hypogene* origin for methane in vent fluids at oceanic spreading centers.

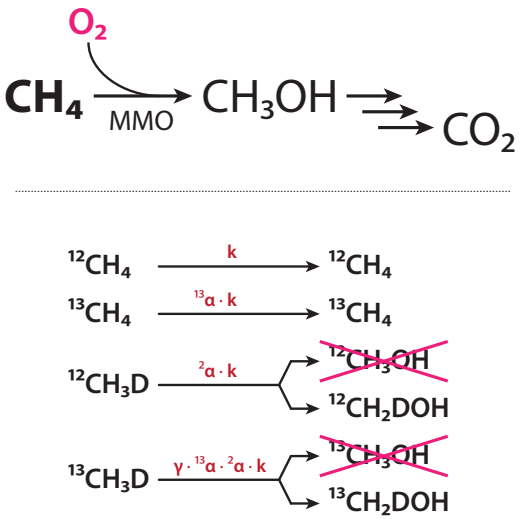

Figure 1.9 | Reaction scheme for four stable isotopologues of methane during methane oxidation. Abstraction of D is ~100× slower than H-abstraction. Substitution of D at an adjacent site has a small (~10%) effect (Nesheim and Lipscomb, 1996). This means that the D/H fractionation comes mostly from the ¾ probability associated with abstraction of H from monodeuterated methane.

Chapter 4 and Whitehill *et al.* (2017) show that fractionations are related by: $^{13}CH_3D/^{12}CH_4 = \gamma \times (^{13}C/^{12}C) \times (D/H)$, where γ is a number close to 1.000 (identical within error for OH and aerobic methanotrophy, and slightly less than 1 for Cl). Together, these fractionation factors constrain the effects on $^{13}CH_3D$ by the major methane sink reactions in the atmosphere and in oxic microbial habitats on Earth.

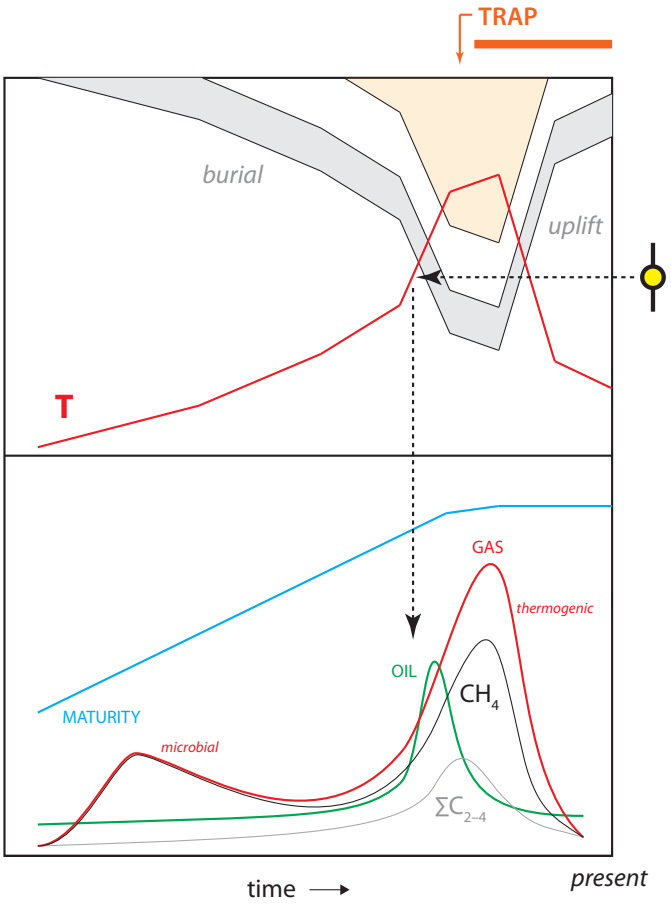

Figure 1.10 | Petroleum system applications of $^{13}CH_3D$. The potential application space of methane isotopologue geothermometry and geospeedometry include the ability to link key hydrocarbon system elements (particularly elements of source, charge, and trap) in time and space, to calibrate and/or validate basin model predictions and coupled source rock maturation simulations, and to define a new metric of maturity based solely on fluid chemistry.

- place quantitative constraints on the stability and origin of C–H bonds in hydrocarbons in the Earth's subsurface;
- test interpretive models of natural gas composition and gas isotope systematics; and
- be used to help anchor the chemistry of natural gases to time and temperature.

Appendices A and B represent some initial efforts to read the hydrogen-isotope and clumped isotopologue record of natural gases and define what those records mean.

Appendix C offers miscellaneous tricks, tips, and data that didn't fit anywhere else.

Chapter 2

Nonequilibrium clumped isotope signals in microbial methane

ABSTRACT

Methane is a key component in the global carbon cycle with a wide range of anthropogenic and natural sources. While isotopic compositions of methane have traditionally aided source identification, the abundance of its multiply-substituted "clumped" isotopologues (e.g., $^{13}CH_3D$) has recently emerged as a proxy for determining methane-formation temperatures. However, the impact of biological processes on methane's clumped isotopologue signature is poorly constrained. Here, we show that methanogenesis proceeding at relatively high rates in cattle, surface environments, and laboratory cultures exerts kinetic control on $^{13}CH_3D$ abundances and results in anomalously elevated formation temperature estimates. We demonstrate quantitatively that H_2 availability accounts for this effect. Clumped methane thermometry can therefore provide constraints on the generation of methane in diverse settings, including continental serpentinization sites and ancient, deep groundwaters.

A version of this chapter has been published as:

Wang, D. T.; Gruen, D. S.; Lollar, B. S.; Hinrichs, K.-U.; Stewart, L. C.; Holden, J. F.; Hristov, A. N.; Pohlman, J. W.; Morrill, P. L.; Könneke, M.; Delwiche, K. B.; Reeves, E. P.; Sutcliffe, C. N.; Ritter, D. J.; Seewald, J. S.; McIntosh, J. C.; Hemond, H. F.; Kubo, M. D.; Cardace, D.; Hoehler, T. M. & Ono, S. (2015) Nonequilibrium clumped isotope signals in microbial methane. *Science,* **348**, 428–431. doi:10.1126/science.aaa4326

2.1 MAIN TEXT

Carbon ($^{13}C/^{12}C$) and hydrogen (D/H) isotope ratios of methane are widely applied for distinguishing microbial from thermogenic methane in the environment (Welhan and Lupton, 1987; Whiticar, 1990; Sherwood Lollar *et al.*, 2002; Flores *et al.*, 2008; Sherwood Lollar *et al.*, 2008; Pohlman *et al.*, 2009; Baldassare *et al.*, 2014) as well as for apportioning pathways of microbial methane production (Whiticar *et al.*, 1986; Burke *et al.*, 1988; McCalley *et al.*, 2014). This bulk isotope approach, however, is largely based on empirical observations, and different origins of methane often yield overlapping characteristic isotope signals (Schoell, 1988; Whiticar, 1990; Whiticar, 1999; Pohlman *et al.*, 2009; Etiope and Sherwood Lollar, 2013). Beyond conventional bulk isotope ratios, it has become possible to precisely measure the abundance of multiply-substituted "clumped" isotopologues (e.g., $^{13}CH_3D$) (Ono *et al.*, 2014; Stolper *et al.*, 2014b). In particular, the abundances of clumped isotopes makes it possible to obtain information about the temperature at which C–H bonds were formed or last equilibrated (Ono *et al.*, 2014, and Fig. 2.5). Formation temperatures of both thermogenic and microbial methane in natural gas reservoirs can be estimated on the basis of clumped isotopologues (Stolper *et al.*, 2014a). The mechanisms by which isotopologues attain distributions consistent with thermodynamic equilibrium, however, remain unclear because bulk methane isotopes ($\delta^{13}C$ and δD) often reflect kinetic isotope fractionations (Whiticar, 1999; Valentine *et al.*, 2004), and H-isotope exchange between methane and water is sluggish (Reeves *et al.*, 2012).

To test if clumped methane thermometry can be widely applied for methane sources beyond natural gas reservoirs, we examined methane samples from diverse systems, including lakes, wetlands, cow rumen, laboratory cultures of methanogenic microbes, and geological settings that may support abiogenic methane production. We measured the relative abundances of four methane isotopologues ($^{12}CH_4$, $^{13}CH_4$, $^{12}CH_3D$ and $^{13}CH_3D$) using a recently-developed tunable laser spectroscopy technique (Ono *et al.*, 2014, and § 2.4).

Our measurements for dominantly-thermogenic gases from the Marcellus and Utica Shales (Burruss and Laughrey, 2010; Baldassare *et al.*, 2014) yielded $\Delta^{13}CH_3D$-based temperatures of 147^{+25}_{-22} °C and 160^{+29}_{-25} °C, respectively. The clumped-isotope temperature for the Marcellus Shale sample is comparable to, although slightly lower than, estimates by Stolper *et al.* (2014a) of 179–207 °C (Fig. 2.1). In addition, microbial methane in pore waters and gas hydrates from northern Cascadia margin sediments (Pohlman *et al.*, 2009), and from wells producing from coal seams in the Powder River Basin (Flores *et al.*, 2008; Bates *et al.*, 2011) yielded $\Delta^{13}CH_3D$ temperatures of 12–42 °C and 35–52 °C, respectively. These are consistent with their expected low formation temperatures. Furthermore, thermogenic methane sampled from a hydrothermal vent in the Guaymas Basin, Gulf of California (Welhan and Lupton, 1987), yielded a $\Delta^{13}CH_3D$ temperature of 326^{+170}_{-95} °C, within error of the measured vent temperature (299 °C; Reeves *et al.*, 2014). Therefore, our data provide independent support of the hypothesis that $^{13}CH_3D$ abundance reflects the temperature at which methane is generated in these sedimentary basins (Stolper *et al.*, 2014a).

In contrast, we found that methane sampled from lakes, a swamp, and the rumen of a cow carry $^{13}CH_3D$ signals that correspond to anomalously high $\Delta^{13}CH_3D$ temperatures (139–775 °C, Fig. 2.1A) that are well above the environmental temperatures (<40 °C). Such signals are clearly not controlled by equilibrium. Notably, a positive correlation between $\Delta^{13}CH_3D$ and the extent of D/H fractionation between methane and environmental water [$\varepsilon_{methane/water}$;[1] Fig. 2.2] suggests a strong link between isotopologue (i.e., $^{13}CH_3D$) and

[1] The abundance of $^{13}CH_3D$ is captured by a metric, $\Delta^{13}CH_3D$, which quantifies its deviation from a random distribution of isotopic substitutions amongst all isotopologues in a sample of methane: $\Delta^{13}CH_3D = \ln Q$, where Q is the reaction quotient of the isotope exchange reaction: $^{13}CH_4 + {}^{12}CH_3D \rightleftharpoons {}^{13}CH_3D + {}^{12}CH_4$, where the δ-values are conventional isotopic notation, e.g., $\delta D = (D/H)_{sample}/(D/H)_{reference} - 1$. Mass spectrometric measurements yield Δ_{18}, a parameter that quantifies the combined abundance of $^{13}CH_3D$ and $^{12}CH_2D_2$. For most natural samples of methane, Δ_{18} is expected to be directly-relatable to $\Delta^{13}CH_3D$ as measured by laser spectroscopy. The D/H fractionation between methane and environmental water is defined as $\varepsilon_{methane/water} = (D/H)_{methane}/(D/H)_{water} - 1$.

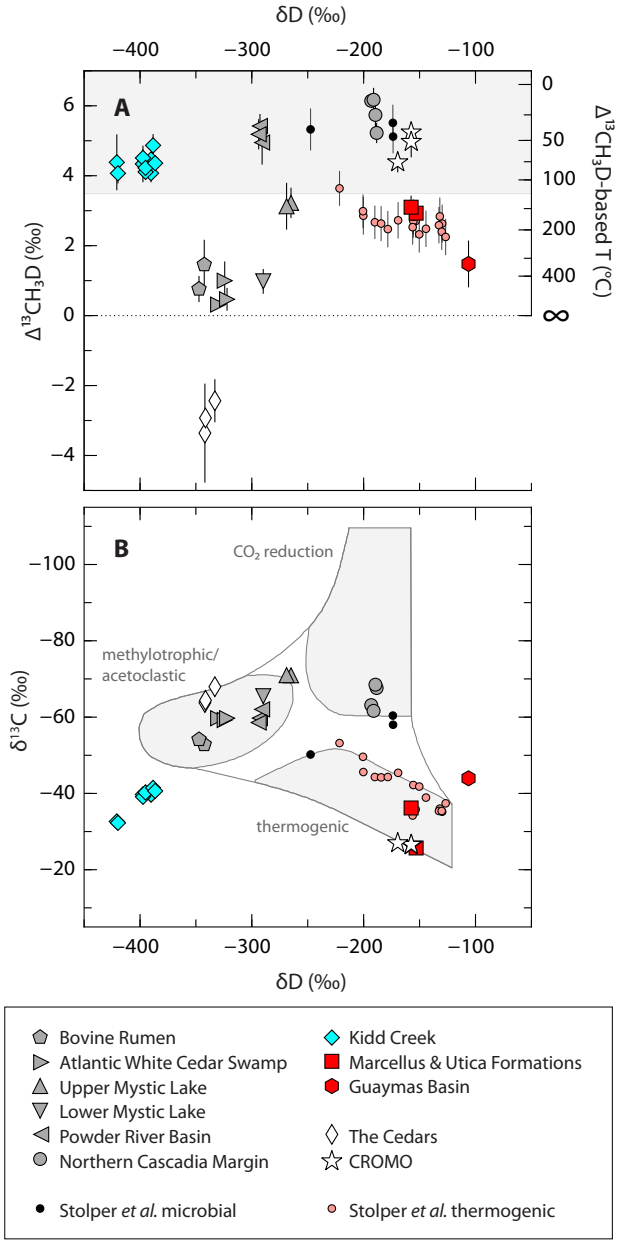

Figure 2.1 | Isotopologue compositions of methane samples. **(A)** $\Delta^{13}CH_3D$ plotted against δD. The $\Delta^{13}CH_3D$ temperature scale corresponds to calibration in Fig. 2.5. Error bars are 95% confidence intervals (Table 2.1). Data from Stolper *et al.* (2014a) were scaled to their corresponding $\Delta^{13}CH_3D$ values (Stolper *et al.*, 2014b). The shaded area represents the temperature range within which microbial life has been demonstrated to date (Takai *et al.*, 2008). The hatched line represents $\Delta^{13}CH_3D = 0‰$ ($T \rightarrow \infty$); data plotting below this line cannot yield corresponding apparent temperatures. **(B)** $\delta^{13}C$ plotted against δD, showing characteristic fields for different methane sources from Whiticar (1999).

isotope (D/H) disequilibria. In contrast, the above mentioned methane samples from sedimentary basins appear to have attained hydrogen-isotope equilibrium with associated waters at or near the temperatures indicated by the $\Delta^{13}CH_3D$ data (Fig. 2.2).

To confirm these observations from the natural environment, we demonstrated that strong disequilibrium $^{13}CH_3D$ signals are also produced by cultures of methanogenic archaea in the laboratory (Fig. 2.3). Thermophilic methanogens cultured at 40 to 85 °C produced methane with $\Delta^{13}CH_3D$ values from +0.5 to +2.3‰ (corresponding to $\Delta^{13}CH_3D$ temperatures of 216–620 °C), and mesophilic methanogens cultured at ambient temperature produced methane with conspicuously "anti-clumped" signatures (i.e., values of $\Delta^{13}CH_3D < 0$‰, for which no apparent temperature can be expressed) as low as −1.3‰ (Fig. 2.3). Methane from cultures is also characterized by large kinetic D/H fractionation with respect to water (Balabane *et al.*, 1987; Valentine *et al.*, 2004). Because laboratory cultures are grown under optimal conditions (high H_2 and high CO_2), these anti-clumped $\Delta^{13}CH_3D$ and low $\varepsilon_{methane/water}$ values are primarily expressions of kinetic isotope effects. Consequently, the distribution of samples with $\Delta^{13}CH_3D$ and $\varepsilon_{methane/water}$ values in Fig. 2.2 can be explained by microbial methanogenesis operating on a spectrum between fully kinetic (low $\Delta^{13}CH_3D$ and low $\varepsilon_{methane/water}$) and equilibrium (high $\Delta^{13}CH_3D$ and high $\varepsilon_{methane/water}$) end-members.

We constructed a mathematical framework to describe the controls on the correlation of $\Delta^{13}CH_3D$ and $\varepsilon_{methane/water}$ signals from hydrogenotrophic methanogenesis. The model largely follows those developed for microbial sulfate reduction (Rees, 1973; Wing and Halevy, 2014) and predicts the isotopologue compositions of product methane as a result of a series of enzymatic reactions (Fig. 2.8 and § 2.4.7). Using isotope fractionation factors estimated from theory, experiments, and observations as input parameters (Table 2.3), our model reproduces the observed correlation between $\Delta^{13}CH_3D$ and $\varepsilon_{methane/water}$ of natural samples (Fig. 2.2). The isotopologue compositions of product methane reflect the degree of metabolic reversibility. Fully reversible reactions yield equilibrium end-members (Holler *et al.*, 2011), while irreversible reactions result in kinetic (disequilibrium) end-member signals. In this model, the reversibility is linked to available free energy (Holler *et al.*, 2011; Wing and Halevy, 2014), in this case expressed as H_2 concentration ($[H_2]$). The model can explain the relationship among $[H_2]$, $\varepsilon_{methane/water}$ (Burke, 1993), and $\Delta^{13}CH_3D$ via Michaelis-Menten kinetics, and can predict the patterns observed in diverse settings ranging from marine sediments (low $[H_2]$, high $\Delta^{13}CH_3D$ and $\varepsilon_{methane/water}$) to bovine rumen (high $[H_2]$, low $\Delta^{13}CH_3D$ and $\varepsilon_{methane/water}$) (Fig. 2.4). We note that mixing of methane sources with different $\delta^{13}C$ and δD values or oxidation of methane could also alter the relationships over the primary signal of microbial methanogenesis (§ 2.5.1). Likewise, inheritance of clumping signals from precursor organic substrates (e.g., via acetoclastic or methylotrophic methanogenesis) cannot be entirely ruled out and awaits experimental validation.

We showed above that the combination of $\Delta^{13}CH_3D$ and $\varepsilon_{methane/water}$ values provides mechanistic constraints on whether methane was formed under kinetic vs. near-equilibrium conditions. Next, we used this framework to place constraints on the origins of methane at two sites of present-day serpentinization in Phanerozoic ophiolites [The Cedars (Morrill *et al.*, 2013) and Coast Range Ophiolite Microbial Observatory, CROMO (Cardace *et al.*, 2013)] in northern California, and in deep (> 2 km below surface) fracture fluids with billion year-residence times in the Kidd Creek mine, Canada (Sherwood Lollar *et al.*, 2002; Holland *et al.*, 2013).

Methane collected from groundwater springs associated with serpentinization at The Cedars yielded anti-clumped $\Delta^{13}CH_3D$ signals (−3‰) with low $\varepsilon_{methane/water}$ values (Figs. 2.1A and 2.2). The data plot along the microbial (kinetic) trend defined in Fig. 2.2, supporting a previous hypothesis that methane at The Cedars is being produced by active microbial methanogenesis (Morrill *et al.*, 2013). The exceptionally high H_2 concentration (up to 50% by volume in bubbles) at The Cedars indicates the massive excess of electron donor. This, along with severe inorganic carbon limitation [due to high pH (>11) and precipitation of carbonate minerals (Morrill *et al.*, 2013)], drives the formation of methane carrying strong kinetic imprints, consistent

with the observed anti-clumped $\Delta^{13}CH_3D$ signals (Fig. 2.4).

Despite the similarity in geologic setting, methane associated with serpentinization at CROMO (Cardace *et al.*, 2013) revealed very different $\Delta^{13}CH_3D$ values that correspond to low apparent temperatures (42–76 °C) and plot close to the equilibrium line (Fig. 2.2). While the conventional $\delta^{13}C$ and δD values of methane from CROMO are nearly identical to those of the Utica Shale sample (Fig. 2.1B), methane at CROMO carries much higher $\Delta^{13}CH_3D$ values (Fig. 2.1A). The origin of methane at the CROMO site remains unresolved (Cardace *et al.*, 2013), but the comparably high $\Delta^{13}CH_3D$ values at CROMO suggest that methane here could be sourced from a mixture of thermogenic and microbial methane. Alternatively, lower H_2 availability at CROMO compared to The Cedars (Table 2.4), may support microbial methanogenesis under near-equilibrium conditions (Fig. 2.4). Regardless, the different isotopologue signatures in methane from CROMO vs. The Cedars demonstrate that distinct processes contribute to methane formation in these two serpentinization systems.

Deep, ancient fracture fluids in the Kidd Creek mine in the Canadian Shield (Holland *et al.*, 2013) contain copious quantities of both dissolved methane and hydrogen (Sherwood Lollar *et al.*, 2002). The Kidd Creek methane occupies a distinct region in the $\Delta^{13}CH_3D$ vs. $\varepsilon_{methane/water}$ diagram (Fig. 2.2), due to strong D/H disequilibria between methane and water (Sherwood Lollar *et al.*, 2008) and low $\Delta^{13}CH_3D$ temperature signals of 56–90 °C that are consistent with other temperature estimates for these groundwaters (Sherwood Lollar *et al.*, 2008). Although the specific mechanisms by which the proposed abiotic hydrocarbons at Kidd Creek are generated remain under investigation (Sherwood Lollar *et al.*, 2002; Sherwood Lollar *et al.*, 2014), the distinct isotopologue signals provide further support for the hypothesis that methane here is neither microbial nor thermogenic.

Our results demonstrate that measurements of $^{13}CH_3D$ provide information beyond the simple formation temperature of methane. The combination of methane/water D/H fractionation and $^{13}CH_3D$ abundance enables the differentiation of methane that has been formed at extremely low rates in the subsurface (Pohlman *et al.*, 2009; Bates *et al.*, 2011; Holler *et al.*, 2011) from methane formed in cattle and surface environments in which methanogenesis proceeds at comparatively high rates (Johnson and Johnson, 1995; Varadharajan and Hemond, 2012).

NOTE ADDED DURING THESIS PREPARATION: I do not favor the use of the term *formation temperature*. This term has a distinct and widely-accepted meaning in industries associated with subsurface resources (particularly within the disciplines of formation evaluation, reservoir engineering, and petrophysics). Practitioners of isotope geochemistry can better communicate by using less-ambiguous wording such as *temperatures of methane generation* and *clumped isotopologue temperatures*. The distinction between these two concepts is important because—as this thesis demonstrates—apparent temperatures derived from equilibria between methane isotopologues are often different from the temperatures at which methane was generated. Methane may also be generated at one temperature, and later "scrambled" (its C–H bonds rearranged/equilibrated) at a different temperature; only the temperature of last equilibration would be recorded by $\Delta^{13}CH_3D$ values.

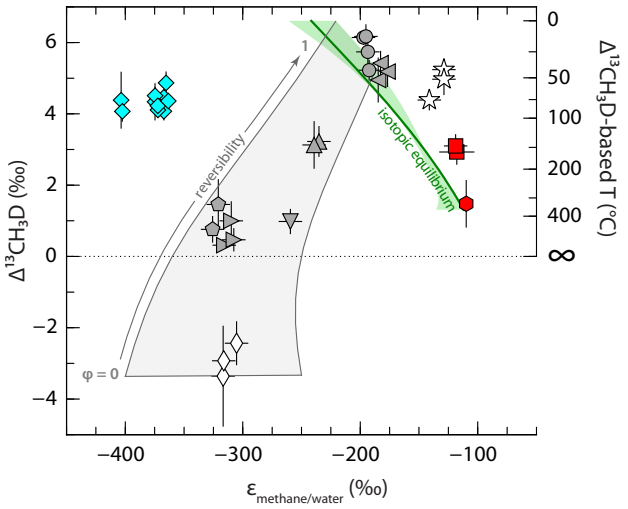

Figure 2.2 | Extent of clumped- and hydrogen-isotopic disequilibria in methane. Symbols and vertical error bars are the same as those in Fig. 2.1. Horizontal error bars represent uncertainties on estimates of $\varepsilon_{methane/water}$[1] (Table 2.4). The solid green curve represents isotopic equilibrium, with the $\varepsilon_{methane/water}$ calibration given by Horibe and Craig (1995). Green shading represents ranges of $\varepsilon_{methane/water}$ calibrations from published reports (Fig. 2.7). Gray shading represents model predictions from this study for microbial methane formed between 0 and 40 °C. Metabolic reversibility (φ) increases from bottom ($\varphi = 0$, fully-kinetic) to top ($\varphi \rightarrow 1$, equilibrium) within this field (see § 2.4.7).

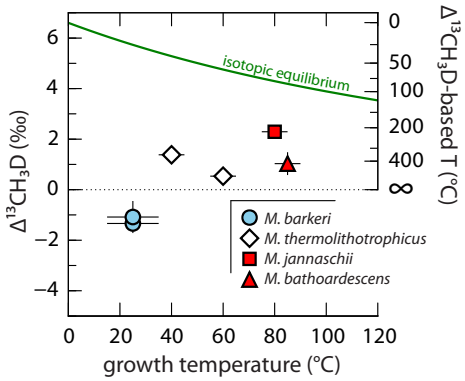

Figure 2.3 | $\Delta^{13}CH_3D$ values of methane produced by hydrogenotrophic methanogens in batch cultures reflect kinetic effects. Data and error bars are from Table 2.2. The green line represents clumped isotopologue equilibrium (i.e., samples for which $\Delta^{13}CH_3D$ temperature is equal to growth temperature; Fig. 2.5).

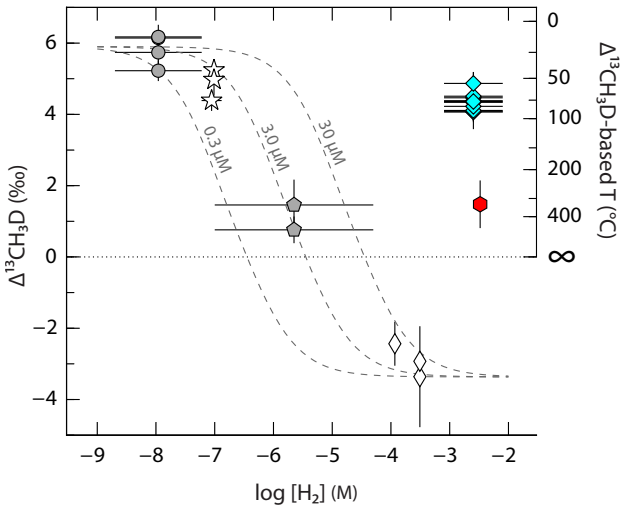

Figure 2.4 | Relationships between $\Delta^{13}CH_3D$ and H_2 concentration for microbial methane. Symbols and vertical error bars are the same as in Fig. 2.1. The H_2 data are from Table 2.4; when a range of $[H_2]$ values is given, points are plotted at the geometric mean of the maximum and minimum values. Dashed lines represent model predictions for microbial methane produced at 20 °C, calculated using K_M's of 0.3, 3.0, and 30 μM H_2. Data for samples of dominantly non-microbial methane from Guaymas Basin and Kidd Creek are plotted for comparison.

2.2 ACKNOWLEDGMENTS

We thank J. Hayes, R. Summons, A. Whitehill, S. Zaarur, C. Ruppel, L.T. Bryndzia, N. Blair, D. Vinson, K. Nealson, and M. Schrenk for discussions; W. Olszewski, D. Nelson, G. Lacrampe-Couloume, and B. Topçuoğlu for technical assistance; A. Whitehill, G. Luo, A. Apprill, K. Twing, W. Brazelton, A. Wray, J. Oh, A. Rowe, G. Chadwick, and A. Rietze for assistance in the field; R. Michener for the δD_{water} analyses; and R. Dias (USGS) for sharing the NGS samples. We thank R. Raiche and D. McCrory, S. Moore (Homestake Mining Co.) and the staff of the McLaughlin Natural Reserve, and Shell and other operators for access to samples. Grants from the National Science Foundation (EAR-1250394 to S.O. and EAR-1322805 to J.C.M.), N. Braunsdorf and D. Smit of Shell PTI/EG (to S.O.), the Deep Carbon Observatory (to S.O., B.S.L., M.K., and K.-U.H.), the Natural Sciences and Engineering Research Council of Canada (to B.S.L.), and the Gottfried Wilhelm Leibniz Program of the Deutsche Forschungsgemeinschaft (HI 616-14-1 to K.-U.H. and M.K.) supported this study. D.T.W. was supported by a National Defense Science and Engineering Graduate Fellowship. D.S.G. was supported by the Neil and Anna Rasmussen Foundation Fund, the Grayce B. Kerr Fellowship, and a Shell-MITEI Graduate Fellowship. Any use of trade, firm, or product names is for descriptive purposes only and does not imply endorsement by the U.S. Government.

2.3 AUTHOR CONTRIBUTIONS

D.T.W. and S.O. developed the methods, analyzed data, and performed modeling. D.T.W. and D.S.G. performed isotopic analyses. D.S.G., L.C.S., J.F.H., M.K., K.-U.H., and S.O. designed and/or conducted microbiological experiments. D.T.W., D.S.G., B.S.L., P.L.M., K.B.D., A.N.H., C.N.S., M.D.K., D.J.R., J.C.M., D.C., and S.O. designed and/or executed the field sampling campaigns. D.T.W. and S.O. wrote the manuscript with input from all authors.

Table 2.1 | Results of isotopic measurements of natural samples of methane. Uncertainties reported are 95% confidence intervals over all measurement cycles for a single analysis. Values for $\delta^{13}C$, δD, and $\Delta^{13}CH_3D$ are reported relative to PDB, SMOW, and the stochastic distribution, respectively. Samples for which $\Delta^{13}CH_3D$ is $\leq 0‰$ have no corresponding thermodynamically-allowed apparent equilibrium temperature (T_{13D}), and are noted as anti-clumped (a.c.).

Sample Set	Sample Name	$\delta^{13}C$ (‰)	δD (‰)	$\Delta^{13}CH_3D$ (‰)	T_{13D} (°C)
Bovine Rumen	Sally-1*	**−52.81** ± 0.04	**−342.56** ± 0.04	**1.46** ± 0.71	**330** +190/−101
	Sally-2-5*	**−54.15** ± 0.07	**−347.25** ± 0.07	**0.76** ± 0.49	**515** +309/−144
NCM	311-1325B-19X-4 (145-146) / Void, SB	**−68.50** ± 0.10	**−189.48** ± 0.10	**5.74** ± 0.49	**25** +16/−15
	311-1325C-6X-4 (17-18) / Void, SB	**−67.63** ± 0.07	**−188.40** ± 0.07	**5.22** ± 0.29	**42** +11/−10
	311-1328E-2X-CC (0-10) / Hyd, SB	**−63.14** ± 0.04	**−193.26** ± 0.04	**6.14** ± 0.21	**13** +6/−6
	311-1328E-2X-CC (0-10) / Hyd, Vac	**−61.63** ± 0.08	**−191.14** ± 0.08	**6.17** ± 0.34	**12** +10/−9
PRB	DR_15W-17-08-41	**−59.74** ± 0.08	**−292.75** ± 0.12	**5.42** ± 0.34	**35** +12/−11
	DR_3CA34	**−62.03** ± 0.10	**−290.80** ± 0.10	**4.95** ± 0.63	**52** +26/−22
	DR_Visborg_13W-17-08-41	**−58.58** ± 0.10	**−293.89** ± 0.10	**5.19** ± 0.43	**44** +16/−15
Swamp Y	SwampY-1	**−59.72** ± 0.06	**−322.17** ± 0.06	**0.47** ± 0.33	**660** +318/−159
	SwampY-2	**−59.25** ± 0.06	**−324.27** ± 0.06	**1.00** ± 0.55	**435** +238/−121
	SwampY-5†	**−59.70** ± 0.32	**−330.14** ± 0.21	**0.32** ± 0.10	**775** +100/−78
UML	UML 06/19/2014	**−70.96** ± 0.10	**−264.97** ± 0.10	**3.22** ± 0.43	**139** +32/−26
	UML 07/29/2014	**−70.99** ± 0.16	**−268.93** ± 0.16	**3.13** ± 0.67	**145** +54/−41
LML	LML-20m	**−65.47** ± 0.07	**−289.81** ± 0.07	**0.98** ± 0.35	**440** +133/−87
The Cedars	The Cedars NS, 2013 June	**−67.97** ± 0.12	**−333.06** ± 0.07	**−2.43** ± 0.62	**a.c.**
	The Cedars BSC, 2013 June	**−63.81** ± 0.21	**−341.98** ± 0.16	**−3.36** ± 1.42	**a.c.**
	The Cedars BSC, 2014 July	**−64.39** ± 0.05	**−341.48** ± 0.05	**−2.93** ± 0.24	**a.c.**
NAB	Marcellus Fm.	**−36.18** ± 0.09	**−157.60** ± 0.07	**3.10** ± 0.33	**147** +25/−22
	Utica Fm.	**−25.70** ± 0.08	**−153.10** ± 0.08	**2.93** ± 0.36	**160** +29/−25
Guaymas	Rebecca's Roost 4462-IGT4, VT1	**−43.96** ± 0.18	**−106.24** ± 0.16	**1.48** ± 0.67	**326** +170/−95

Continued on next page

Table 2.1 | Results of isotopic measurements of natural samples of methane (*continued*).

Sample Set	Sample Name	$\delta^{13}C$ (‰)	δD (‰)	$\Delta^{13}CH_3D$ (‰)	T_{13D} (°C)
CROMO	CROMO-CSWold	**−26.98** ± 0.07	**−169.56** ± 0.07	**4.39** ± 0.29	**76** +14/−12
	CROMO-N08-A.1	**−26.39** ± 0.07	**−157.53** ± 0.06	**5.24** ± 0.31	**42** +11/−10
	CROMO-N08-A.2	**−26.55** ± 0.12	**−157.50** ± 0.13	**4.97** ± 0.44	**52** +18/−16
Kidd Creek	14.06.2012.KC.L9500_BHY13762_Gas D	**−32.66** ± 0.07	**−420.74** ± 0.07	**4.38** ± 0.80	**76** +41/−32
	29.11.2012.KC.L9500_BH2_Gas C	**−32.28** ± 0.07	**−419.74** ± 0.06	**4.07** ± 0.29	**90** +15/−14
	KC_12.02.2008_7850L_BH12299(E)	**−39.11** ± 0.11	**−397.33** ± 0.05	**4.51** ± 0.25	**70** +11/−10
	KC_12.01.2010_7850L_BH12299(F)	**−39.73** ± 0.06	**−397.39** ± 0.06	**4.34** ± 0.52	**78** +26/−22
	KC_01.03.2012_7850L_BH12299(F)‡	**−40.19** ± 0.05	**−394.98** ± 0.03	**4.11** ± 0.37	**89** +19/−17
	02.04.2014_KC_7850L_BH12299(C)	**−39.72** ± 0.04	**−390.12** ± 0.03	**4.47** ± 0.22	**72** +10/−9
	02.04.2014_KC_7850L_BH12299(D)	**−39.72** ± 0.06	**−390.12** ± 0.06	**4.07** ± 0.26	**90** +13/−12
	KC_27.08.2007_7850L_BH12287A(C)	**−40.64** ± 0.04	**−386.48** ± 0.05	**4.36** ± 0.22	**77** +10/−10
	KC_20.06.2008_7850L_BH12287A(D)	**−40.25** ± 0.08	**−395.07** ± 0.05	**4.23** ± 0.30	**83** +15/−13
	KC_20.09.2013_7850L_BH12287A(B)	**−41.44** ± 0.06	**−388.32** ± 0.06	**4.87** ± 0.32	**56** +13/−12

Abbreviations: NCM, Northern Cascadia Margin; PRB, Powder River Basin; Swamp Y, Atlantic White Cedar Swamp; UML, Upper Mystic Lake; LML, Lower Mystic Lake; NAB, Northern Appalachian Basin; CROMO, Coast Range Ophiolite Microbial Observatory.

* Purified sample was measured twice. The uncertainties reported for these samples are 95% confidence intervals calculated from the data for each measurement (with σ taken as the larger of 1*s* or 0.3‰, which is typical analytical reproducibility) assuming the measurements follow a normal distribution.

† Sample was subsampled, purified and analyzed twice (3 weeks apart) as described in the § 2.5.3. The uncertainties reported for this sample are 2 s.e.m. (standard error of the mean) of the replicate measurements ($n = 2$).

‡ Sample was subsampled, purified and analyzed three times over a period of >3 months. The uncertainties reported for this sample are 2 s.e.m. of the replicate measurements ($n = 3$).

2.4 MATERIALS AND METHODS

2.4.1 Animal care

Sampling of methane from bovine subjects was conducted according to guidelines established by the Institutional Animal Care and Use Committee at the Pennsylvania State University.

2.4.2 Cultivation of methanogens

We established batch culture incubations of *Methanocaldococcus bathoardescens*, *Methanocaldococcus jannaschii*, *Methanothermococcus thermolithotrophicus*, and *Methanosarcina barkeri* under atmospheres containing 80% H_2 and 20% CO_2. Cultures of *M. jannaschii* (Jones *et al.*, 1983) and *M. barkeri* (strain DSM-800) (Balch *et al.*, 1979) were purchased from the German Collection of Microorganisms and Cell Cultures (DSMZ, Braunschweig, Germany). *Methanocaldococcus bathoardescens* (formerly known as strain JH146) is a recently-isolated hyperthermophilic, obligate hydrogenotrophic methanogen exhibiting optimum growth at 82 °C (Ver Eecke *et al.*, 2013; Stewart *et al.*, 2015). The growth medium for *M. jannaschii*, *M. thermolithotrophicus*, and *M. bathoardescens* was prepared according to the recipe for DSMZ medium 282, amended with 1 g/L NaS_2O_3. Aliquots of the medium (50 ml) were transferred into 160 ml glass serum vials stoppered with blue butyl rubber septa, and the headspace was filled with 2 atm H_2:CO_2 (80:20). The growth medium for *M. barkeri* was prepared according to the recipe for DSMZ medium 120, and the headspace was filled with 1.5 atm H_2:CO_2 (80:20). Cultures were incubated at ambient temperature (*M. barkeri*, in duplicate), at 40 and 60 °C (*M. thermolithotrophicus*), at 80 °C (*M. jannaschii*), or at 85 °C (*M. bathoardescens*).

2.4.3 Sample purification procedures

To extract methane quantitatively from gas samples, we applied a preparative-gas chromatography technique modified from Alei *et al.* (1987). In brief, a sample is introduced into a stream of helium. Water is removed by passing the sample through a U-trap cooled to −80 °C, and then CH_4, air (N_2, O_2, Ar), CO, CO_2, and C_{2+} are cryofocused onto a U-trap packed with activated charcoal and held at −196 °C. The condensed gases are then released by rapid heating to 120 °C, passed through a packed column (Carboxen-1000, $5' \times 1/8''$, Supelco) held at 30 °C under helium flow (~25 ml/min), and monitored using thermal conductivity detection. The methane peak is trapped on a U-trap packed with silica gel and held at −196 °C; this is analogous to a "heart-cut" technique used previously for preparative separation of SF_6 for isotopic analysis (Ono *et al.*, 2006b). After elution of methane, the column is baked at 180 °C under a reversed (backflushed) flow of helium to remove CO_2 and C_{2+}.

This sample preparation procedure induces small fractionations in $\delta^{13}C$ and δD of methane of 0.09 ± 0.06‰ and 0.20 ± 0.02‰, respectively (1*s*, $n = 4$); these effects are minor compared to the magnitude of $\delta^{13}C$ and δD variations in nature. Critically, our procedure does not discernibly alter the $\Delta^{13}CH_3D$ value; the average difference between samples treated vs. not treated with this procedure was −0.09 ± 0.16‰ (1*s*, $n = 4$), which is not significantly different from zero.

2.4.4 Reporting of $\delta^{13}C$ and δD values

The $\delta^{13}C$ and δD values we report have been calibrated relative to PDB and SMOW, respectively, by measuring samples of NGS-1 and NGS-3. These reference values for $\delta^{13}C$ and δD are, respectively, −29.0‰ and −138‰ for NGS-1, and −72.8‰ and −176‰ for NGS-3, as determined by several labs in the 1980s (Hut, 1987). Results for the calibration samples are shown in Table 2.5.

Table 2.2 | Results of isotopic measurements of methane produced experimentally by cultures of methanogens. Each line represents a separate bottle incubation of an axenic strain of methanogens. Uncertainties reported are 95% confidence intervals over all measurement cycles for a single analysis. Values for $\delta^{13}C$, δD, and $\Delta^{13}CH_3D$ are reported relative to PDB, SMOW, and the stochastic distribution, respectively. Samples for which $\Delta^{13}CH_3D \leq 0‰$ have no corresponding thermodynamically-allowed apparent equilibrium temperature, and are noted as anti-clumped (a.c.).

Culture	growth T*	$\delta^{13}C$ (‰)	δD (‰)	$\Delta^{13}CH_3D$ (‰)	T_{13D} (°C)
Methanocaldococcus bathoardescens	85 °C	**−12.58** ± 0.07	**−419.23** ± 0.07	**1.03** ± 0.45	**426** +170/−100
Methanocaldococcus jannaschii	80 °C	**−18.79** ± 0.03	**−416.90** ± 0.05	**2.29** ± 0.23	**216** +25/−22
Methanothermococcus thermolithotrophicus	60 °C	**−17.05** ± 0.05	**−409.84** ± 0.05	**0.54** ± 0.28	**620** +214/−126
Methanothermococcus thermolithotrophicus	40 °C	**−16.47** ± 0.04	**−427.76** ± 0.04	**1.38** ± 0.34	**345** +79/−58
Methanosarcina barkeri	ambient	**−59.90** ± 0.05	**−418.40** ± 0.05	**−1.34** ± 0.22	**a.c.**
Methanosarcina barkeri	ambient	**−50.30** ± 0.07	**−422.67** ± 0.07	**−1.08** ± 0.63	**a.c.**

* Uncertainty on measured growth temperatures is estimated at ±5 °C. Temperatures were not monitored throughout the *M. barkeri* incubations but are estimated at 25 ± 10 °C.

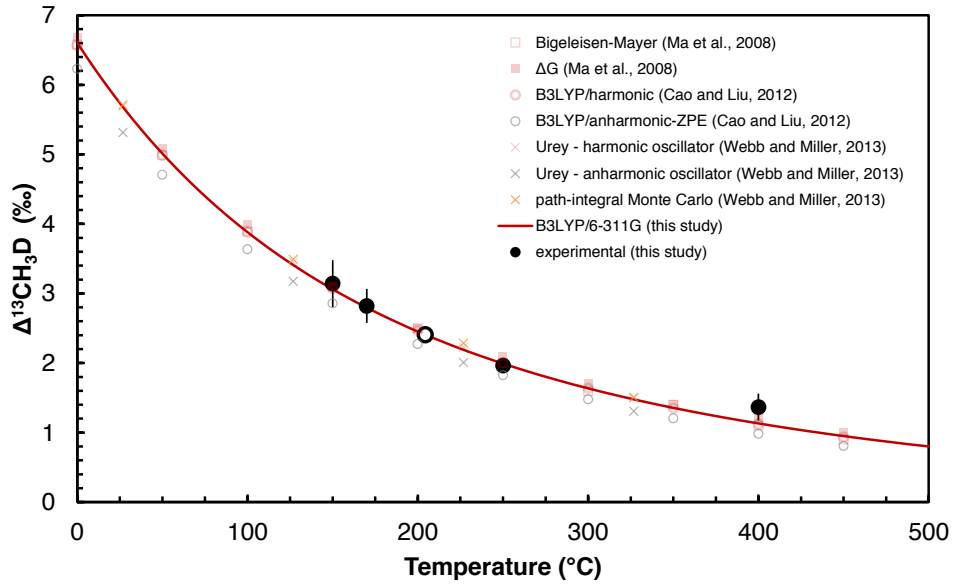

Figure 2.5 | Experimental calibration of the $\Delta^{13}CH_3D$ thermometer. Filled circles represent the mean $\Delta^{13}CH_3D$ of gases heated at that temperature, and error bars represent 95% confidence intervals calculated from a normal distribution (for the 150 °C sample, error bars represent the 95% confidence interval on the measurement cycles in a single analysis, calculated from a *t*-distribution). For the 250 °C point, the error bars are smaller than the symbol. The open circle represents our reference gas, AL1. The equilibrium curve (red line) was calculated following conventional equilibrium isotope fractionation theory under the harmonic oscillator assumption (Bigeleisen and Mayer, 1947); frequencies were calculated at the B3LYP level of theory using the 6-311G basis set as implemented in Gaussian 03 (Frisch *et al.*). For comparison, results from published computational studies (Ma *et al.*, 2008; Cao and Liu, 2012; Webb and Miller, 2014) are also plotted.

2.4.5 Heated gas calibrations

To confirm and extend a previously-published temperature calibration (Ono *et al.*, 2014), Pyrex tubes containing samples of methane with a range of $\delta^{13}C$ (−82 to −34‰ vs. PDB) and δD (−615 to +220‰ vs. SMOW) were prepared. These samples were heated over Pt catalyst at temperatures of 150, 170, 250, and 400 °C (n = 1, 3, 28, and 7, respectively). Gases were heated for 110 d, 73–76 d, 2–24 d, and 16–60 h, respectively, following a procedure described in Ono *et al.* (2014).

When the theoretical methane equilibrium line is aligned to samples heated at 150, 170, and 250 °C, measurements of the samples heated at 400 °C yielded slightly lower $\Delta^{13}CH_3D$ temperatures (347^{+42}_{-36} °C), perhaps because quenching the reaction may take longer than the time for exchange over catalyst at ~400 °C. As a result, the data from the 400 °C heated gases were not used in aligning the calibration in Fig. 2.5.

The theoretical equilibrium line we calculated agrees well with published results from both path-integral Monte Carlo simulations (Webb and Miller, 2014) and harmonic oscillator assumption-based approaches (Ma *et al.*, 2008; Cao and Liu, 2012; Webb and Miller, 2014). The results of results of calculations employing an anharmonic correction, however, differ slightly from results of models assuming harmonic-oscillator behavior (by ~0.3‰ near room temperature; Cao and Liu, 2012; Webb and Miller, 2014). Figure 2.5 shows results from recent studies comparing multiple computational approaches for estimating the temperature-dependence of the equilibrium $\Delta^{13}CH_3D$ value. We note that while the uncertainty in the theoretical curve is similar in magnitude to our analytical uncertainty, particularly at temperatures <100 °C, these calibration uncertainties do not affect the conclusions drawn in this study.

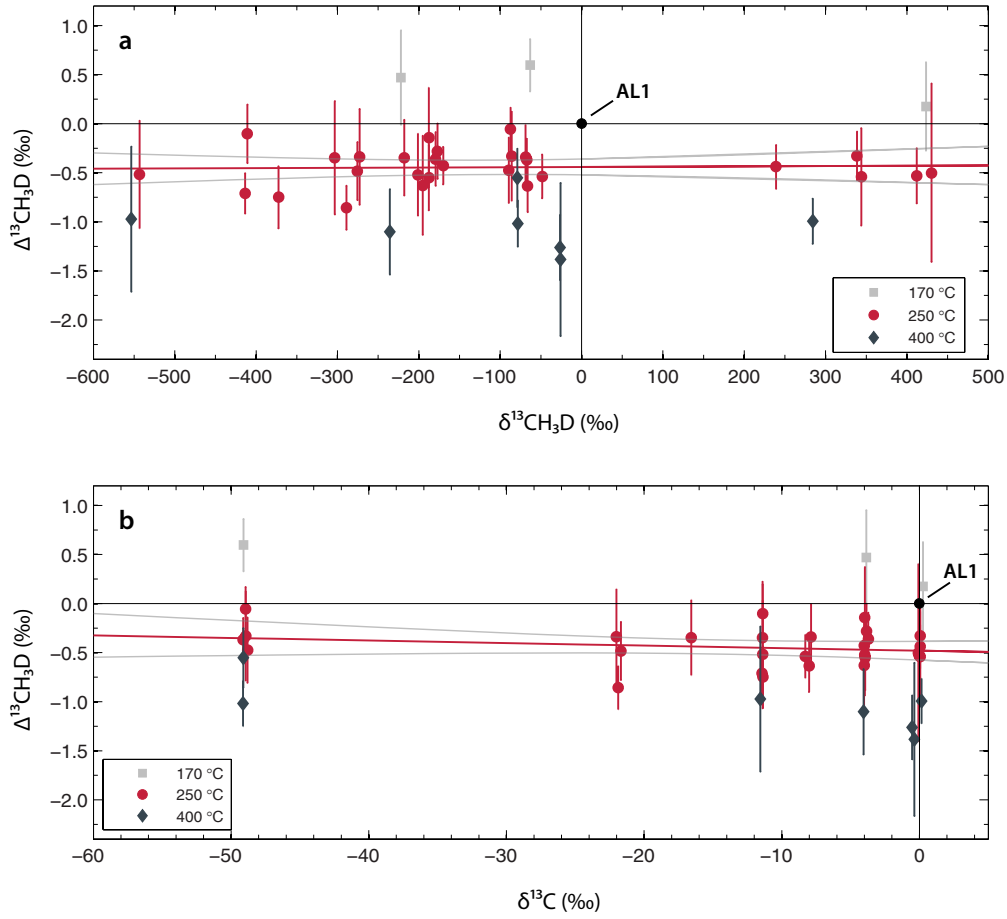

Figure 2.6 | Demonstration of linearity in $\Delta^{13}CH_3D$ over a range of bulk isotope ratios. Shown are measurements of methane heated over catalyst at three temperatures (170, 250, 400 °C). Solid red lines represent unweighted linear least squares regressions through gases equilibrated at 250 °C, and gray lines denote the 95% confidence band. Error bars represent 95% confidence intervals on multiple measurement cycles of a single analysis. Isotopic ratios are shown relative to our reference gas, AL1. Results indicate no significant correlation between $\Delta^{13}CH_3D$ and (**A**) $\delta^{13}CH_3D$ over an 800‰ range (the variation in $\delta^{13}CH_3D$ is driven mainly by differences in δD); and (**B**) $\delta^{13}C$ over a 48‰ range.

2.4.6 Spectroscopic procedures

Samples of purified methane were analyzed using a tunable-infrared laser direct absorption spectrometer (Aerodyne Research, Billerica, Massachusetts) housed at MIT as described in Ono *et al.* (2014), with improvements described here. All measurements reported in this paper were obtained at a nominal cell pressure of ca. 1.0 Torr, instead of the 0.8 Torr used in Ono *et al.* (2014). We have found that this higher cell pressure gave improved measurement stability. As suggested previously (Ono *et al.*, 2014), there is a small offset in the baseline underneath the $^{13}CH_3D$ absorption line, likely due to the insufficient accuracy of the Voigt profile for describing the contribution from tailing of adjacent $^{12}CH_4$ peak. We have used all 250 °C experiments shown in Fig. 2.6 to generate a single set of correction factors, which show no observable drift during the time period all measurements were made.

Long-term internal reproducibility was evaluated by repeated analysis of methane from a commercially-sourced gas cylinder over a period of >4 months, yielding precisions for $\delta^{13}C$ of ±0.02‰, δD of ±0.02‰,

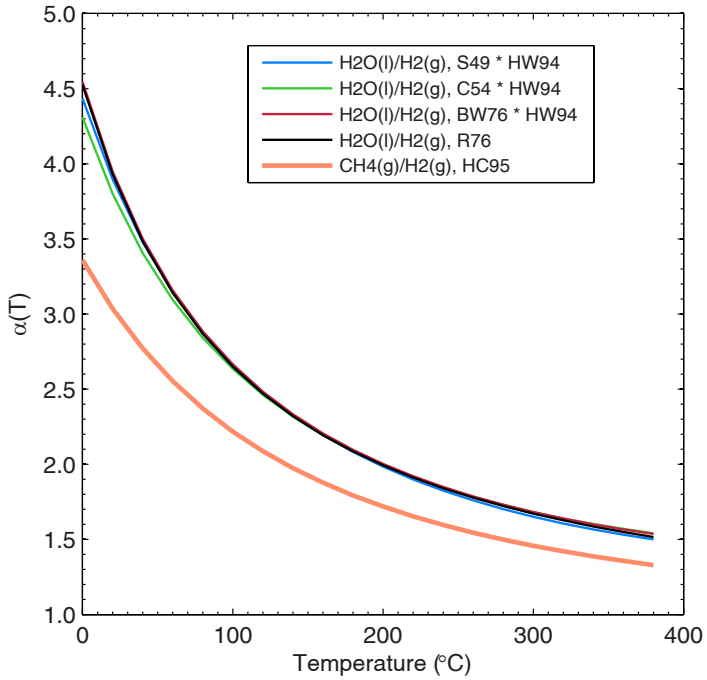

Figure 2.7 | Equilibrium hydrogen isotopic fractionation factors compiled from experimental and theoretical calibrations. When appropriate, calibrations for $H_2O(g)/H_2(g)$ have been converted using the $H_2O(l)/H_2O(g)$ calibration from Horita and Wesolowski (1994) to derive $H_2O(l)/H_2(g)$ calibrations. HW94, Horita and Wesolowski (1994); S49, Suess (1949); C54, Cerrai *et al.* (1954); BW76, Bardo and Wolfsberg (1976); R76, Rolston *et al.* (1976); HC95, Horibe and Craig (1995). For any temperature, the $CH_4(g)/H_2O(l)$ equilibrium composition is the ratio of the $CH_4(g)/H_2(g)$ line (HC95) to a $H_2O(l)/H_2(g)$ line.

and $\Delta^{13}CH_3D$ of ±0.08‰ (1*s*, $n = 13$). As described in Ono *et al.* (2014), each measurement run consists of multiple acquisition cycles (a cycle is defined as one comparison of a sample/standard pair). The number of cycles (N_{cycles}) depends on sample size, but is typically greater than 5. In this paper, $\Delta^{13}CH_3D$ measurements are reported as mean ± 95% confidence intervals (CI) on the average of all isotope ratios obtained for each acquisition cycle over a measurement run, calculated as: 95% CI = $tinv\,(\alpha, df) \cdot s/\sqrt{N_{cycles}}$, where *tinv* is the two-tailed inverse of the Student's *t*-distribution for $\alpha = 0.05$ with $N_{cycles} - 1$ degrees of freedom (*df*), and $s \geq 0.27$ ‰ [this value is the standard deviation on measurements for which 24 or more cycles were taken (0.27 ± 0.08‰, 1*s* on 1*s*, $n = 7$), and thus estimates the internal precision of the instrument]. The uncertainties on $\Delta^{13}CH_3D$ values reported for samples in Tables 2.1, 2.2, and 2.5 also contain the propagated uncertainty in the $\Delta^{13}CH_3D$ value of our methane reference gas (AL1). Based on the calibration shown in Fig. 2.5, we determined that AL1 carries a $\Delta^{13}CH_3D$ value of +2.41 ± 0.08‰ (95% CI).

To enable analysis of small (ca. 1 cm^3 STP) methane samples, we have developed a cold trap system to recover and recycle methane samples for re-analysis. In the current study, the only sample for which this recycling method was used was "Sally-1", a sample from a bovine rumen (Table 2.1).

2.4.7 Model of isotopologue systematics during microbial methanogenesis

A mathematical model was constructed to describe isotopologue compositions of methane produced from microbial methanogenesis (Fig. 2.8). To allow for the use of data from studies on experimental and natural

Table 2.3 | Isotope fractionation factors (input parameters) used in model calculations for microbial methane generated at 20 °C. A detailed description of the model setup and explanation of choices of fractionation factors is given in § 2.4.7.

	forward	backward	equilibrium
$^{13}C/^{12}C$ isotope effect ($^{13}\alpha$)	0.9600*	0.9771†	0.9824‡
D/H primary isotope effect ($^{2}\alpha_{p}$)	0.600 to 0.750§	0.751 to 0.939#	0.7989‖
D/H secondary isotope effect ($^{2}\alpha_{s}$)	0.8400¶	0.8400¶	1.0000¶
^{13}C-D clumped isotope effect (γ)	0.9987 or 0.9965**	0.9928 or 0.9907††	1.0059‡‡

* From Scheller *et al.* (2013) for the reduction of methyl-coenzyme M.

† Internally-consistent value. For comparison, Hermes *et al.* (1984) reported 0.96 for formate dehydrogenase, and Scharschmidt *et al.* (1984) reported 0.979 for alcohol dehydrogenase.

‡ From Horita (2001), who determined $^{13}\alpha_{CH_4/CO_2}$ = 0.932 at 20 °C; this reported value is equal to 0.9824 taken to the power of 4.

§ Free parameter. The range of values used here are similar to those reported for *in vitro* studies of methyl-coenzyme M reductase (0.63 to 1.0) (Scheller *et al.*, 2013) and from experimental cultures of methanogens (0.70 to 0.86) (Valentine *et al.*, 2004).

Internally-consistent value. For comparison, Scheller *et al.* (2013) determined a value of 0.41 ± 0.04 (they reported a primary isotope effect of k_H/k_D = 2.44 ± 0.22 for the activation of methane; the reciprocal of this value is $^{2}\alpha_{p}$).

‖ From the value given by Horibe and Craig (1995) for the equilibrium D/H fractionation factor between H_2O(l) and CH_4(g) at 20 °C.

¶ From Scheller *et al.* (2013) for the reduction of methyl-CoM. For comparison, Roston and Kohen (2010) reported secondary D/H isotope effects associated with the reduction of an aldehyde by alcohol dehydrogenase of 0.94 for the forward reaction and 0.81 for the reverse reaction.

** To fit the lowest $\Delta^{13}CH_3D$ values we have observed in methanogen culture experiments (0.9987, corresponding to $\Delta^{13}CH_3D$ = −1.3‰, Table 2.2) or in nature (0.9965, corresponding to $\Delta^{13}CH_3D$ = −3.5‰, Table 2.1). Calculations for the fields shown in Figs. 2.2 and 2.4 use the latter values. See § 2.4.7 for explanation of choice, and Fig. 2.9 for comparison of model results using the two different values.

†† Internally-consistent value. For comparison, Hermes *et al.* (1984) reported 0.999 for formate dehydrogenase, and Scharschmidt *et al.* (1984) reported 0.995 for alcohol dehydrogenase.

‡‡ Computed equilibrium $\Delta^{13}CH_3D$ value at 20 °C (Fig. 2.5).

systems as input parameters, our model simplifies the representation of the biochemistry involved in the microbial generation of methane, and only considers the production of methane via reduction of CO_2.

The model describes methanogenesis in six steps, and using an assumption of steady-state intermediate compositions, solves for the abundances of ^{13}C- and D-substituted isotopologues of product CH_4 and of four intermediate species (Fig. 2.8). The first step (1) is the uptake of CO_2 into the cell, and the last step (6) is export of CH_4 out of the cell; we assume that neither of these steps discriminates against isotopes or between isotopologues. Inside the cell, the reduction of CO_2 to CH_4 is treated in four steps (steps #2–5), where each step corresponds to the addition of one hydrogen (Thauer, 1998).

The main variable input in our model is metabolic reversibility, which is defined as the ratio of backwards to forwards fluxes ($\varphi_n = w_n/v_n$) through an enzymatically-mediated reaction sequence (Rees, 1973; Hayes, 2001). The reversibility is constrained by two end-members, which represent fully-irreversible ($\varphi = 0$; fully-kinetic) and fully-reversible ($\varphi \to 1$; equilibrium) conditions. We parameterize the reversibility as a simple function of H_2 concentration by assuming Michaelis-Menten kinetics for each H-addition step:

$$\varphi_n = 1 - \frac{[H_2]}{K_M + [H_2]} \tag{2.1}$$

Table 2.4 | Methane/ethane ratio, hydrogen isotopic composition of water, current environmental temperatures, and concentration of dissolved H_2 for sites studied. References are provided for previously-published descriptions of the field site; n.d., not determined.

Location	C_1/C_2 ‖	δD_{water} (‰)¶	T (°C)#	$[H_2]$**	Data Sources
Bovine rumen, Pennsylvania, USA	n.d.	**−32** ± 10	**39** ± 2	*0.1–50 μM*	this study*,‡, [1]
Northern Cascadia Margin sediments	>1000	***+5*** ± *10*	**3–17**	*2–60 nM*	[2]
Powder River Basin, Montana, USA	>1000	**−136** ± 5	**18** ± 2	n.d.	this study§
Cedar swamp, Massachusetts, USA	n.d.	**−21** ± 10	***16*** ± *5*	n.d.	this study‡
Upper Mystic Lake, Mass., USA	n.d.	**−39** ± 10	**4** ± 2	n.d.	this study‡
Lower Mystic Lake, Mass., USA	>1000	**−41** ± 10††	**6** ± 2	n.d.	this study‡
The Cedars, California, USA	>350	***−37*** ± *10*	***17*** ± *1*	*120, 310 μM*	[3]
CROMO, California, USA	>350	**−33** ± 10††	**16** ± 4	60–130 nM	this study†,‡
Kidd Creek Mine, Ontario, Canada	5.9–14	**−34** ± 6	**30** ± 2	*0.8–8 mM*	[4]
Rebecca's Roost vent, Guaymas Basin	140	***+4*** ± *2*	**299** ± 5	3.3 mM	[5]
Marcellus Fm., Penn., USA	45	***−44*** ± *10*	**51** ± 10	n.d.	[6]
Utica Fm., Penn., USA	84	***−40*** ± *15*	**93** ± 10	n.d.	[7]

* H_2 concentrations were determined using gas chromatography with thermal conductivity detection at MIT. Analytical reproducibility is typically ±5%.

† H_2 concentrations were determined using a reduced gas analyzer gas chromatograph at NASA Ames (Crespo-Medina *et al.*, 2014).

‡ The δD_{water} was measured at the Boston University Stable Isotope Laboratory using high-temperature conversion gas chromatography isotope-ratio mass spectrometry. External reproducibility on replicate analyses of samples was ± 1–3‰ (1*s*, n = 3–4), with the exception of cow rumen fluid (±8‰, 1*s*).

§ The δD_{water} values were measured at the University of Arizona Environmental Geochemistry Laboratory via isotope-ratio mass spectrometry.

‖ Unless otherwise indicated, the C_1/C_2 ratio (i.e., the ratio of the concentration of methane to that of ethane in a gas sample) was determined using gas chromatography with flame-ionization detection at MIT.

¶ The δD_{water} values are reported with respect to the VSMOW scale.

At some sites ambient temperatures were not directly measured (*in italics*) and therefore were estimated; reasonable uncertainties on those estimates are given. At all other sites temperatures were measured *in situ*.

** Dissolved H_2 concentrations estimated from the literature are *in italics*.

†† At Lower Mystic Lake and CROMO, the waters in which methane was generated may have δD_{water} values different from those in the water samples measured because of migration (see § C.3.1).

[1] Range of $[H_2]$ from Janssen (2010).

[2] For the Northern Cascadia Margin samples, an average D/H ratio of marine sediment porewater (+5‰, Friedman and Hardcastle, 1988) is assumed. The natural variability of ±10‰ is taken as the uncertainty of this estimate. Downhole temperature measurements from Expedition 311 have been reported (Riedel *et al.*, 2006). Concentrations of H_2 were assumed to be within the range of 2–60 nM, which is typical of marine sediments (Lin *et al.*, 2012). The C_1/C_2 data are from Pohlman *et al.* (2009).

[3] The $[H_2]$, δD_{water} and temperature data are from Morrill *et al.* (2013). An uncertainty of ±10‰ is applied to δD_{water} to account for potential interannual variability. Dissolved $[H_2]$ was estimated from the H_2 mole % in the gas phase, assuming equilibrium between gas bubbles and water at atmospheric pressure.

[4] Dissolved $[H_2]$ for Kidd Creek fluids was estimated using gas/water flow rate data from Holland *et al.* (2013) and gas-phase H_2 concentrations from Sherwood Lollar *et al.* (2008), and assuming that all dissolved H_2 had completely partitioned into the gas phase prior to sampling. The C_1/C_2 data are from Sherwood Lollar *et al.* (2002).

[5] Measured vent temperature and $[H_2]$ are from Reeves *et al.* (2014), and δD_{water} was assumed based on Shanks *et al.* (1995).

[6] The δD_{water} values for formation water from the Marcellus Fm. in Pennsylvania are estimated from Rowan *et al.* (2015). Uncertainty on reservoir temperature is estimated at ±10 °C.

[7] The δD_{water} values for formation water from the Utica Fm. are estimated using data for Appalachian Basin brines from pre-Middle Devonian units presented in Warner *et al.* (2012). Uncertainty on reservoir temperature is estimated at ±10 °C.

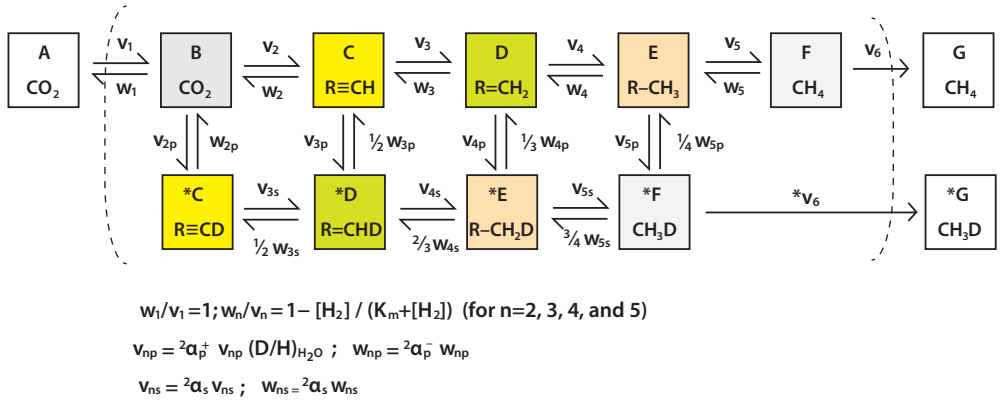

Figure 2.8 | Schematic of the model of deuterium substitution during microbial methanogenesis from CO_2. Boxes represent pools of cellular carbon involved in the methanogenic pathway, and the asterisk represents a compound containing a deuterium substitution. Forward flows are represented by *v*, and backwards flows are represented by *w*. The model setup is similar in concept to previously published models for microbial sulfate reduction (Rees, 1973; Brunner and Bernasconi, 2005; Farquhar *et al.*, 2007).

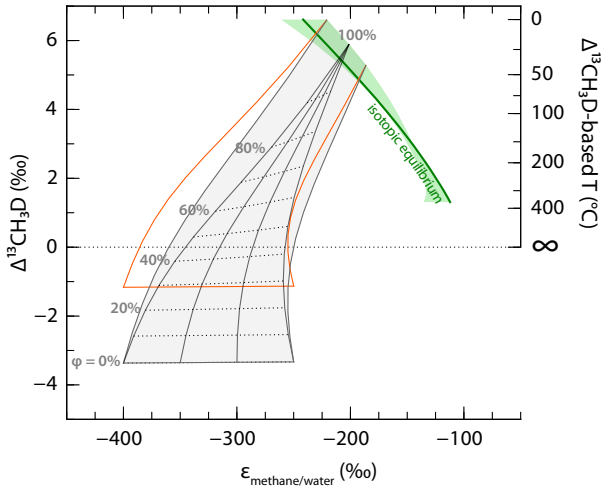

Figure 2.9 | Dependence of the modeled isotopic composition of microbial methane on the degree of reversibility and isotope fractionation factors. Orange and gray fields represent model output assuming a kinetic endmembers of −1.3‰ and −3.5‰, respectively (Table 2.3). Inner solid gray lines represent model trajectories for 20 °C assuming different values for the D/H primary intrinsic isotope effect (Table 2.3). Subhorizontal tie lines connect points of equal reversibility (φ). Outer solid lines represent bounding model trajectories calculated for 0 and 40 °C.

where *n* represents the step number and K_M is the effective half-saturation constant for H_2 (assumed identical for steps 2–5). In our model, φ_1 is set at 1 (i.e., CO_2 uptake is fully reversible).

Under an assumption of steady-state concentrations of intermediates, all fluxes for the ^{12}CH isotopologues are dependent upon the methane formation rate (v_6, in e.g., mol cell^{-1} s^{-1}) by:

$$v_n = v_6/(1-\varphi_n), \text{ and } w_n = \varphi_n v_6/(1-\varphi_n) \tag{2.2}$$

A series of continuity equations can be written for each ^{13}C-substituted isotopologue. For example:

$$\frac{d^{13}\mathbf{D}}{dt} = {}^{13}\alpha_3^+ \cdot v_3 \cdot {}^{13}r_\mathbf{C} - \left({}^{13}\alpha_4^+ \cdot v_4 + {}^{13}\alpha_3^- \cdot w_3\right) \cdot {}^{13}r_\mathbf{D} + {}^{13}\alpha_4^- \cdot w_4 \cdot {}^{13}r_\mathbf{E} \tag{2.3}$$

Here, $^{13}\mathbf{D}$ is the abundance of ^{13}C-substituted isotopologues for the pool **D** (i.e., R=CH_2; Fig. 2.8), and $^{13}r_\mathbf{X}$ is the isotopologue ratio of the pool **X** (where **X** = **A**, **B**, …, **F**), and $^{13}\alpha_n{}^+$ and $^{13}\alpha_n{}^-$ are the

$^{13}C/^{12}C$ kinetic isotope effects associated with the forward and backward reactions, respectively. There are a total of five continuity equations for pools $^{13}\mathbf{B}$, $^{13}\mathbf{C}$, $^{13}\mathbf{D}$, $^{13}\mathbf{E}$, and $^{13}\mathbf{F}$. Under an assumption of steady-state concentrations of intermediate species (i.e., $d^{13}\mathbf{X}/dt = 0$), we solve for the ratios of ^{13}C-containing to ^{12}C-containing isotopologues in the product methane (**F**; i.e., $^{13}CH_4/^{12}CH_4$) and in the intermediates (**B**, **C**, **D**, and **E**). The $^{13}C/^{12}C$ ratio of CO_2 (i.e., $r_\mathbf{A}$) is assigned.

For the deuterated isotopologues, the continuity equations account for both primary isotope effects (describing the rates at which C–D bonds are formed or broken relative to C–^{1}H bonds; fluxes shown vertically in Fig. 2.8) and secondary isotope effects (describing the change in reaction rate resulting from D substitution at a site *adjacent* to that which is site of an ^{1}H-addition or abstraction reaction; fluxes shown horizontally in Fig. 2.8). For example for reservoir **D**, the continuity equation for the D-substituted isotopologue (i.e., R=CH_2 or R=CHD) is:

$$\begin{aligned}\frac{d^2\mathbf{D}}{dt} = {}& {}^2\alpha^+_{3p}\cdot\nu_3\cdot{}^2r_\mathbf{H} + {}^2\alpha^+_{3s}\cdot\nu_3\cdot{}^2r_\mathbf{C} \\ & - \left(\tfrac{1}{2}\cdot{}^2\alpha^-_{3s}\cdot w_3 + \tfrac{1}{2}\cdot{}^2\alpha^-_{3p}\cdot w_3 + {}^2\alpha^-_{4s}\cdot\nu_4\right)\cdot{}^2r_\mathbf{D} \\ & + \tfrac{2}{3}\cdot{}^2\alpha^-_{4s}\cdot w_4\cdot{}^2r_\mathbf{E}\end{aligned} \tag{2.4}$$

Here, $^2\alpha_{np}$ and $^2\alpha_{ns}$ are primary and secondary deuterium isotope effects, $^2r_\mathbf{X}$ are D-isotopologue ratios for reservoir **X**, and $^2r_\mathbf{H}$ is the D/H ratio of the hydrogen source (i.e., cellular water). The stoichiometric factor corresponds to the probability of a primary versus secondary isotope-sensitive reaction occurring (in this case, there is a $^2/_3$ chance of removing H from R–CH_2D). Again, there are five linear equations to be solved simultaneously. Conversion between isotopologue ratios and isotope ratios requires consideration of reaction stoichiometry. For example,

$$^2r_\mathbf{D} = \frac{[\text{R=CHD}]}{[\text{R=CH}_2]} = 2\left(\frac{\text{D}}{\text{H}}\right)_{\text{R=CH}_2} \tag{2.5}$$

Clumped isotopologue ratios (e.g., [R=^{13}CHD]/[R=$^{12}CH_2$]) can be solved for in a manner similar to that used for D-substituted isotopologues above.

For simplicity, primary (α_p) and secondary (α_s) kinetic isotope fractionation factors for the four H-addition steps are assumed to be identical at a given temperature (fractionation factors calculated for a model temperature of 20 °C are shown in Table 2.3). The intrinsic (kinetic/forward) $^{13}C/^{12}C$ and D/H fractionation factors are estimated from *in vitro* and culture studies (Hermes *et al.*, 1984; Scharschmidt *et al.*, 1984; Valentine *et al.*, 2004; Roston and Kohen, 2010; Scheller *et al.*, 2013). The intrinsic ^{13}CD fractionation factor (γ, where $^{13D}\alpha = \gamma\cdot{}^{13}\alpha\cdot{}^2\alpha$) is taken to have the value required to generate a $\Delta^{13}CH_3D$ signature of either −1.3‰ or −3.5‰ under fully-kinetic conditions (Main Text and Table 2.3). The $^{13}C/^{12}C$, D/H, and $^{13}CH_3D$ equilibrium isotope fractionation factors are based on experimental and/or theoretical calibrations (Figs. 2.2, 2.5, and 2.7) (Cerrai *et al.*, 1954; Horibe and Craig, 1995; Horita, 2001; Ono *et al.*, 2014). The intrinsic fractionation factors for the reverse reactions (α^-, Table 2.3) are constrained by the requirement for consistency among equilibrium (α_{eq}), forward (α^+), and reverse reactions (i.e., $\alpha_{eq} = \alpha^-/\alpha^+$). We note that varying the secondary isotope effect (α_s, assumed to be 0.84 in either direction, for all steps) changes the curvature of the modeled microbial trajectories, but does not change the endmember $\varepsilon_{\text{methane/water}}$ values (which are set by the primary D/H isotope effect).

We initiated the model calculations at temperatures of 0, 20, and 40 °C. These temperatures bracket the range of known or inferred environmental temperatures at which the microbial methane samples we studied were generated (Table 2.4). The predicted isotopic compositions for microbial methane generated between 0 and 40 °C are shown in Figs. 2.2 and 2.4.

Table 2.5 | Results of isotopic measurements of methane in samples of natural gas standards NGS-1 and NGS-3. Uncertainties reported are 95% confidence intervals over all measurement cycles for a single analysis as described in § 2.4.6. Values for $\delta^{13}C$, δD, and $\Delta^{13}CH_3D$ are reported relative to PDB, SMOW, and the stochastic distribution, respectively.

Sample Name	$\delta^{13}C$ (‰)	δD (‰)	$\Delta^{13}CH_3D$ (‰)	T_{13D} (°C)
NGS-1	**−28.73** ± 0.05	**−137.47** ± 0.05	**2.61** ± 0.29	**186** +28/−24
	−28.79 ± 0.07	**−137.69** ± 0.07	**2.53** ± 0.29	**193** +29/−25
	−28.91 ± 0.05	**−138.07** ± 0.05	**2.62** ± 0.24	**185** +22/−19
NGS-3	**−72.82** ± 0.06	**−176.09** ± 0.06	**5.08** ± 0.26	**48** +10/−9
	−72.71 ± 0.05	**−175.82** ± 0.05	**5.18** ± 0.26	**44** +10/−9
NGS-3 + 150ml air *	**−72.99** ± 0.06	**−176.21** ± 0.06	**5.14** ± 0.49	**45** +19/−17

* This sample was a subsample of NGS-3 that was intentionally-contaminated with 150 ml of air, to check for artifacts introduced from sample preparation and analysis of samples containing large quantities of air. No significant difference was found compared to subsamples of NGS-3 that were not contaminated with air.

2.5 SUPPLEMENTARY TEXT

2.5.1 Evaluation of alternative mechanisms for isotopic disequilibria in microbial methane

There are several potential alternative mechanisms for the observed isotopic disequilibria in microbial methane shown in Fig. 2.2. It is conceivable that these signals are due to mixing of multiple methane sources with differing $\delta^{13}C$ and δD values, as $\Delta^{13}CH_3D$ changes non-linearly upon mixing. The magnitude of non-linearity in the mixing depends on the difference in both $\delta^{13}C$ and δD values of the endmembers. It can be shown, using a Taylor-series expansion (Ono *et al.*, 2006a), that two-component mixing of endmembers (A & B) produces a mixture with a $\Delta^{13}CH_3D$ value of:

$$\begin{aligned}\Delta^{13}CH_3D_{mixture} \approx f_A \cdot \Delta^{13}CH_3D_A + (1-f_A) \cdot \Delta^{13}CH_3D_B \\ + f_A \cdot (1-f_A) \cdot \left(\delta^{13}C_A - \delta^{13}C_B\right) \cdot (\delta D_A - \delta D_B)\end{aligned} \tag{2.6}$$

where f_A represents the fractional contribution from endmember A. Accordingly, the observed ~6‰ negative bias in $\Delta^{13}CH_3D$ values (from that expected for equilibrium at 0–40 °C, Fig. 2.1) requires mixing of two methane sources with $\delta^{13}C$ and δD values that differ by ±60‰ and ∓400‰, respectively; gases with these isotopic compositions are unlikely to co-occur in the environments we studied (Whiticar, 1990).

Alternatively, under a commonly-used classification based on $\delta^{13}C$ and δD values (Whiticar, 1999), methane from these sites could be interpreted as derived from methyl-type fermentation (Fig. 2.1). If so, the low $\Delta^{13}CD$ values could be inherited from those of the C–H bonds in methyl groups of the organic substrate(s). However, theoretical calculations predict consistent $\Delta^{13}CD$ clumping effects of +6.2 ± 0.3‰ at 25 °C for the C–H bond of simple organic compounds (Table 2.6), which is not significantly different from the equilibrium value for $\Delta^{13}CH_3D$ at 25 °C (+6.4‰). Thus, inheritance of equilibrium $\Delta^{13}CD$ values from organic precursors during methyl-type fermentation does not explain the observed disequilibrium $\Delta^{13}CH_3D$ signatures. While inheritance of kinetically-influenced $\Delta^{13}CD$ values from organic precursors is possible, the $\Delta^{13}CD$ values of acetate and other methyl-bearing methanogenic substrates are not currently known.

Furthermore, oxidation of methane can also be ruled out because the substantial deuterium enrichment associated with methane oxidation (Whiticar, 1999) is not observed in the samples we studied.

Table 2.6 | Partition function ratios (β-factors) for simple organic compounds calculated at 25 °C. Partition function ratios were calculated using the method of Bigeleisen and Mayer (1947). Vibrational frequencies were calculated using the Hartree-Fock method with the 6-31G* basis set. The partition function ratios listed below have been corrected with symmetry factors to account for changes in symmetry upon isotope substitution (Bigeleisen and Mayer, 1947; Urey, 1947). The average $\Delta^{13}CD$ value calculated for methanol, formaldehyde, formate, methanethiol, and acetate is +6.2 ± 0.3‰ (1*s*).

Species	Formula*	$^{13}C/^{12}C$	D/H	$^{13}CD/^{12}CH$	$\Delta^{13}CD$ (‰)
Methane	$C\mathbf{H}_4$	0.123	2.647	2.777	6.4
Methanol	$C\mathbf{H}_3OH$	0.150	2.812	2.968	6.3
Formaldehyde	$C\mathbf{H}_2O$	0.165	2.591	2.763	6.7
Formate	$\mathbf{H}COOH$	0.200	2.834	3.040	5.9
Methanethiol	$C\mathbf{H}_3SH$	0.128	2.759	2.893	6.2
Acetate	$C\mathbf{H}_3COOH$	0.147	2.775	2.927	6.0

* D/H and $^{13}CD/^{12}CH$ β-factors were calculated for D substitution at H sites shown in bold letters.

2.5.2 The equilibrium hydrogen-isotopic fractionation between water and methane

We compiled previously-published equilibrium hydrogen-isotopic fractionation factors calibrated at various temperatures, either experimentally or theoretically, for the system $CH_4(g)$-$H_2(g)$-$H_2O(g)$-$H_2O(l)$. The $H_2O(l)/H_2(g)$ fractionation factor is very large (α is ~4 at room temperature), and calibrations diverge substantially at lower temperatures (<100 °C, Fig. 2.7); this is the main source of uncertainty in estimates of $CH_4(g)/H_2O(l)$ equilibrium D/H fractionation, which is derived by combination of $H_2O(l)/H_2(g)$, $H_2(g)/H_2O(g)$, and $CH_4(g)/H_2(g)$ calibration curves. We used the Cerrai *et al.* (1954) calibration for $H_2O(l)/H_2(g)$ in the calculation of $\varepsilon_{methane/water}$ of the equilibrium endmember of our model for isotope effects accompanying microbial methanogenesis (see § 2.4.7) because amongst the published calibrations, this is likely most accurate at lower temperatures (Suess, 1949; Horibe and Craig, 1995; Roston and Kohen, 2010). The uncertainty in calibration, as well as salt and pressure effects (Horita, 2005), could explain small apparent offsets from the equilibrium line (Fig. 2.2) for some samples of thermogenic methane.

2.5.3 Field site descriptions and sampling methods

Bovine rumen, State College, Pennsylvania, USA. The bovine rumen gas samples obtained for this study were collected from cannulated, lactating Holstein dairy cows at The Pennsylvania State University using methods described previously (Tekippe *et al.*, 2011). The samples were stored at room temperature in glass serum vials stoppered with blue butyl septa. Bovine rumen fluid was also sampled for water isotope analysis (Table 2.4). The fluid was centrifuged to remove large particulate material, filtered with a 0.2 μm filter, and distilled to remove dissolved organic matter prior to isotope-ratio analysis. We note that the rumen fluid and gas samples were not taken from the same animal at the same time. However, the temporal variation of δD of tap water in the U.S. is expected to be small (generally <10‰ in any particular region over multiple seasons) (Bowen *et al.*, 2007).

Northern Cascadia Margin. Gas samples were collected from gas voids and hydrates in sediment cores drilled during IODP (Integrated Ocean Drilling Program) Expedition 311 (Riedel *et al.*, 2006). These gases were interpreted to be dominantly microbial based on isotopic and compositional analyses (e.g., C_1/C_2 > 1000) (Pohlman *et al.*, 2009). The gas samples were subsampled for previous analyses, and have remained in archive since. Samples were contained either in serum vials sealed with blue butyl stoppers, or in Vacutainers® (Becton Dickinson) sealed with orange septa and an additional silicone plug (in Table 2.1, these are denoted

"SB" or "Vac", respectively); these methods are standard IODP procedures. The sample ID's for the samples from the Northern Cascadia Margin listed in Table 2.1 are the same as those reported in Pohlman *et al.* (2009).

Powder River Basin, Montana, USA. The Powder River Basin is a major source of coal and coalbed methane. Gas samples were collected from multiple gas wells producing from the methane-rich Wall and Canyon coal seams using a wellhead gas sampler and IsoTubes (from Isotech Laboratories, Champaign, Illinois, USA). Water samples were collected concurrently from the same wells, filtered through 0.45 μm nylon filters, transported to the lab on ice in deionized water-washed glass bottles with no headspace, and kept at 4 °C prior to analysis.

Atlantic White Cedar swamp, Cape Cod, Massachusetts, USA. Atlantic White Cedar swamps are wetlands found throughout the coastal northeastern United States (Laderman *et al.*, 1989). We collected gases and water from a swamp ("Swamp Y", approximate coordinates 41°31′38.2″N, 70°39′15.5″W) on the campus of the Marine Biological Lab (MBL) in Woods Hole, MA in May 2014. Gases were collected by trapping the bubbles released when sediment on the bottom of the swamp was gently disturbed. The collected gases were transferred via syringes to serum vials (either pre-evacuated or pre-filled with NaCl brine that was displaced to make room for the gas sample) sealed with blue butyl septa, and stored at room temperature until analysis. One sample ("SwampY-5", Table 2.1) was subsampled and analyzed 3 days after sample collection, and again 3 weeks later. The measured $\Delta^{13}CH_3D$ values were indistinguishable within the precision of the measurements (0.36 ± 0.34‰ and 0.27 ± 0.52‰, respectively).

Upper Mystic Lake, Arlington, Massachusetts, USA. Upper Mystic Lake is a freshwater lake in the Boston metropolitan area. Ebullition of methane from this lake has been previously documented (Scandella *et al.*, 2011; Varadharajan and Hemond, 2012). We collected gas bubbles using inverted funnel-shaped bubble traps [modified from an inverted-funnel design described previously (Varadharajan *et al.*, 2010; Varadharajan and Hemond, 2012)] deployed ~2 m above the lake floor (~18 m water depth) using a custom rope and buoy structure.[2] The deep deployment depth was chosen to minimize dissolution and/or oxidation of bubbles during their transit from the sediment to the lake surface. The collected gases were transferred via syringes to serum vials (either pre-evacuated or pre-filled with deionized water that was displaced to make room for the gas sample) sealed with blue butyl septa, fixed with either saturated NaCl solution or 1 M NaOH, and stored at either 4 °C or room temperature until analysis. The water sample from Upper Mystic Lake listed in Table 2.4 was collected in September 2014.

Lower Mystic Lake, Arlington, Massachusetts, USA. Lower Mystic Lake (elevation 1 m above sea level, maximum depth 24 m) is a meromictic glacial kettle lake. The sample of methane reported in Table 2.1 was extracted from water we collected from 20 m water depth (mbll, meters below lake level) in August 2014. The water sample was transferred into a 2 L media bottle, taking care to minimize bubbles, immediately stoppered with a black rubber septum (Glasgerätebau Ochs, Germany), and transported to the laboratory. A headspace was created using helium, and the sample was then stored at 4 °C until extraction and analysis. The concentration of dissolved methane at 20 mbll was determined to be 4.2 mM (±5%). Field measurements indicated that the water at 20 mbll was oxygen-depleted and had elevated conductivity relative to surface water. The water sample listed in Table 2.4 was collected from 18 mbll, which is below the chemocline.

The Cedars, Cazadero, California, USA. Samples of bubbling gases were collected in June 2013 and July 2014 from sites in The Cedars as described in Morrill *et al.* (2013); the sites studied here were Barnes Spring Complex (BSC), and Nipple Spring (NS). Gas samples were collected in inverted-bucket traps positioned over seeps, and collected gases were transferred to serum bottles stoppered with blue butyl rubber septa. Samples were fixed with $HgCl_2$ or HCl to prevent microbial alteration of the methane.

[2] A description of the apparatus appears in Delwiche *et al.* (2015).

Coast Range Ophiolite Microbial Observatory, Lower Lake, California, USA. The Coast Range Ophiolite Microbial Observatory, located at the McLaughlin Natural Reserve (UC Davis), was established in 2011 with the completion of eight ultramafic-hosted groundwater monitoring wells drilled using a mud-free technique (Cardace *et al.*, 2013; Crespo-Medina *et al.*, 2014). Water was sampled from well "N-08A" in December 2013 using a bladder pump into 1–2 L bottles, stoppered immediately as described above for the Lower Mystic Lake sample, transported to the laboratory, and stored at 4 °C until extraction and analysis. We also collected water in July 2014 from an electrically-pumped non-potable groundwater well in the Core Shed area ("CSWold", approximate coordinates 38°51′42.53″N, 122°24′53.05″W). For this sample, dissolved gases were extracted on-site via equilibration with a helium headspace and stored in a stoppered serum vial fixed with 0.5 ml 1 M HCl. The water sample for which the δD_{water} value is reported in Table 2.4 was collected from CSWold in December 2013. The range of H_2 concentrations reported in Table 2.4 from CROMO are minimum and maximum values of $[H_2]$ observed over multiple sampling trips during a long-term (~3 years) sampling campaign.

Kidd Creek Mine, Timmins, Ontario, Canada. In subsurface mines in the Canadian Shield, exploration boreholes intersecting extensive fracture networks release waters rich in reduced gases (H_2, CH_4, C_{2+}) and noble gases, which exsolve upon depressurization. Sampling and characterization of fracture fluids from Kidd Creek have been described in previous studies (Sherwood *et al.*, 1988; Sherwood Lollar *et al.*, 2002; Sherwood Lollar *et al.*, 2007; Sherwood Lollar *et al.*, 2008; Holland *et al.*, 2013). We analyzed methane sampled from boreholes at the 7850′- and 9500′-levels (Table 2.1). These samples were taken between 2007 and 2014, and stored in glass serum vials stoppered with blue butyl rubber septa. The $\delta^{13}C$ values of these gases were previously measured by GC-IRMS at the University of Toronto. No evidence of any effects of long-term storage on the $\delta^{13}C$ of methane in these samples has been observed; the average difference between $\delta^{13}C$ determined via TILDAS compared to GC-IRMS was 0.09 ± 0.60‰ (1*s*, $n = 9$), and shows no correlation with the length of time the sample had been stored.

Guaymas Basin hydrothermal system (Rebecca's Roost vent), Gulf of California. Guaymas Basin in the Gulf of California hosts an active sediment-hosted mid-ocean ridge hydrothermal system (Simoneit and Lonsdale, 1982; Simoneit, 1985; Didyk and Simoneit, 1989). We analyzed methane from a sample of a 299 °C vent fluid emanating from Rebecca's Roost, a flange-like vent structure. The sample was taken in 2008 using a isobaric gas-tight sampler (Table 2.1) and poisoned with mercuric chloride (Seewald *et al.*, 2002). Fluid properties and geochemical data associated with this sample have been previously published (Reeves *et al.*, 2014). We assumed a value of +4 ± 2‰ for the δD_{water} of the vent fluid based on previous observations of Guaymas Basin hydrothermal fluids (Shanks *et al.*, 1995).

Northern Appalachian Basin, Central Pennsylvania, USA. Gases were sampled from gas wells producing from the Marcellus Formation (Middle Devonian) and Utica Formation (Upper Ordovician) in central Pennsylvania using standard wellhead sampling techniques. Gases produced from these geologic units are dry (<5% $C_{2+}/\sum C_{1-5}$) thermogenic gases of high thermal maturity (Baldassare *et al.*, 2014; Stolper *et al.*, 2014a). The C_1/C_2 ratios of the gas samples from the Marcellus and Utica Shales we analyzed were <100 (Table 2.4), which is within the range expected for thermogenic gases (Bernard *et al.*, 1976; Bernard *et al.*, 1978).

Chapter 3

Temperatures and timescales of methane synthesis and hydrogen exchange at oceanic spreading centers

ABSTRACT

Hot-spring fluids emanating from deep-sea hydrothermal systems hosted in unsedimented mafic and ultramafic rock commonly contain high concentrations of methane. Multiple hypotheses have been proposed for the origin(s) of this methane, ranging from synthesis via reduction of aqueous inorganic carbon ($\sum CO_2$) during active fluid circulation to leaching of methane-rich fluid inclusions formed in plutonic rocks at depth. To further resolve the mechanism(s) responsible for methane generation in these systems, we determined the relative abundances of several methane isotopologues (including $^{13}CH_3D$, a "clumped" isotopologue containing two rare isotope substitutions) in geochemically diverse fluids sampled at the Rainbow, Von Damm, Lost City, and Lucky Strike hydrothermal vent fields.

The methane clumped isotopologue data indicate relatively uniform apparent equilibrium temperatures (averaging 310^{+53}_{-42} °C) across the suite of endmember fluids, with no apparent relation to the wide range of fluid temperatures (96 to 370 °C), chemical compositions (pH, $[H_2]$, $[\sum CO_2]$, $[CH_4]$), and geologic settings represented. Combined with similar stable isotope ratio ($^{13}C/^{12}C$ and D/H) of methane, all available geochemical and isotopic data suggest a common mechanism of methane generation at depth, independent of actively-circulating hydrothermal fluids. Apparent isotopologue equilibrium at temperatures of ca. 270 to 360 °C indicates that hydrogen-isotope exchange is sluggish for methane at temperatures below 270 °C here. The isotopologue data are compatible with the thermodynamically-favorable reduction of $CO_2(g)$ to $CH_4(g)$ at temperatures below ca. 500 °C under redox conditions characterizing intrusive rocks derived from subridge melts. These results provide further evidence that low temperature (<200 °C) water rock reaction does not contribute significantly to the quantities of methane venting at the seafloor in mid-ocean ridge hot springs, and suggest that methane forms from respeciation of magmatic volatiles occluded in plutonic rocks of the oceanic crust, and are later leached during convective hydrothermal circulation.

A version of this chapter is being prepared as a manuscript by the following authors:

David T. Wang[a,b,*], Eoghan P. Reeves[a,b,c], Jeffrey S. Seewald[b], Jill M. McDermott[a,b,d], and Shuhei Ono[a]

[a] Department of Earth, Atmospheric and Planetary Sciences, Massachusetts Institute of Technology, Cambridge, Massachusetts 02139, USA.
[b] Marine Chemistry and Geochemistry Department, Woods Hole Oceanographic Institution, Woods Hole, Massachusetts 02543, USA.
[c] Department of Earth Science and Centre for Geobiology, University of Bergen, Bergen N-5020, Norway.
[d] Earth and Environmental Sciences Department, Lehigh University, Bethlehem, Pennsylvania 18015, USA.
[*] To whom correspondence should be addressed. *E-mail*: dtw@alum.mit.edu (D.T.W.)

3.1 INTRODUCTION

Dissolved methane (CH_4) is ubiquitous in hot spring fluids emanating from submarine hydrothermal vents, and is a potential carbon source for microbial communities living at and below the seafloor and in the water column. Constraining the sources of carbon (C) and hydrogen (H) for the production of CH_4, as well as the depths and temperatures at which CH_4 is generated in these hydrothermal systems, is critical for understanding the origin of methane (Welhan, 1988b; Charlou *et al.*, 2002; Proskurowski *et al.*, 2008; McDermott *et al.*, 2015). The abundance and isotopic composition of methane venting from submarine hydrothermal fields that are relatively free of sediment cover has been described at oceanic spreading centers characterized by a range of spreading rates (e.g., Welhan, 1988b; Charlou *et al.*, 2002; McCollom and Seewald, 2007; Proskurowski *et al.*, 2008; Cannat *et al.*, 2010; Charlou *et al.*, 2010; Proskurowski, 2010; McDermott *et al.*, 2015; McDermott, 2015). In general, fluids that have interacted with ultramafic rocks are substantially enriched in CH_4 relative to fluids that have reacted with mafic rocks (Keir, 2010), although there are exceptions in which high-CH_4 fluids are associated with apparent mafic substrates (e.g., basalt) (Charlou *et al.*, 2000).

Several distinct geochemical processes have been proposed to account for the presence of abiotic CH_4 in submarine hydrothermal fluids. Some have proposed that CH_4 is formed by reduction of aqueous inorganic carbon (i.e., $\sum CO_2$) in subsurface reaction zones during convective circulation of seawater-derived hydrothermal vent fluids in response to the highly reducing (H_2-rich) conditions that result from extensive fluid-mineral interactions during serpentinization of ultramafic rock (Charlou *et al.*, 2002; Proskurowski *et al.*, 2008). Experimental studies showed, however, that aqueous reduction of $\sum CO_2$ to CH_4 is slow under conditions thought to occur naturally in ultramafic hydrothermal systems (McCollom and Seewald, 2001; McCollom, 2016).

Earlier studies have shown that plutonic (gabbroic) rocks from the ocean floor contain copious amounts of methane (Kelley, 1996; Kelley, 1997; Kelley and Früh-Green, 1999). These authors suggested a model involving entrapment and respeciation of fluids that contained mantle-derived CO_2 into fluids rich in CH_4 (± graphite) within gabbros, and subsequent extraction of the CH_4 during hydrothermal circulation (McDermott *et al.*, 2015). Leaching of basalt-hosted gas vesicles that contain CH_4 may also be a source of CH_4 in fluids venting at fast-spreading ridges such as the East Pacific Rise (Welhan and Craig, 1983; Welhan, 1988a).

To constrain the origin of methane in unsedimented submarine hydrothermal systems, we determined the relative abundance of four stable isotopologues of methane ($^{12}CH_4$, $^{13}CH_4$, $^{12}CH_3D$, and $^{13}CH_3D$, a doubly-substituted or "clumped" isotopologue) in a diverse set of fluids collected from four hydrothermal vent fields: Rainbow (36°13′48″N, 33°54′09″W, Mid-Atlantic Ridge), Von Damm (18°22′36″N, 81°47′54″W, Mid-Cayman Rise), Lost City (30°07′24″N, 42°07′12″W, Mid-Atlantic Ridge), and Lucky Strike (37°17′30″N, 32°16′42″W, Mid-Atlantic Ridge). Fluids from these fields span a wide range of temperatures (96 to 370 °C) and represent distinct geochemical regimes and geological settings.

Data presented in this study provide constraints on the sources of C and H in methane, as well as temperature(s) associated with the formation or equilibration of the C–H bonds. Carbon- and hydrogen-isotope ratios encode signals related to the sources of C and H, respectively, as well as isotopic fractionations incurred during the synthesis of methane. Complementary to such information, measurement of methane clumped isotopologues provides an independent estimate of the temperature at which the C–H bonds in methane were formed or last equilibrated (Stolper *et al.*, 2014a; Wang *et al.*, 2015). Constraining the temperatures at which methane synthesis occurs within oceanic crust has direct implications for the distribution and availability of reduced carbon substrates and energy sources that may support a deep biosphere, as well as for the transfer of mantle-derived carbon to the Earth's surface.

Determination of temperatures from carbon or hydrogen isotope ratios of methane alone requires knowledge of or assumptions regarding the isotopic composition of other species with which methane

has exchanged C or H (e.g., CO_2 or H_2O). In contrast, temperatures determined from the abundance of $^{13}CH_3D$ do not require information regarding such coexisting species. Thus, clumped isotopologue data in conjunction with carbon- and hydrogen-isotope ratios of methane can be used to constrain the isotopic compositions of C- and H-bearing species associated with the methane source when independent constraints are unavailable. In the following discussion, we show how clumped isotopologue temperatures of methane, together with bulk $^{13}C/^{12}C$ and D/H isotope ratios, fluid chemistry, and thermodynamic considerations, collectively indicate that methane in unsedimented hydrothermal systems originates at high temperatures of (ca. 250 to 400 °C) and constrain possible environments of methane generation.

3.2 METHODS

3.2.1 Vent fluid samples

The fluid samples studied herein were collected by ROV *Jason II* using isobaric gas-tight samplers (Seewald *et al.*, 2002) during cruises to the Mid-Atlantic Ridge in 2008 and Mid-Cayman Rise in 2012. During subsampling of the vent fluids from the samplers, fluid samples were stored in pre-evacuated serum vials and sealed with blue butyl rubber stoppers that were boiled in 2 M NaOH for 2–4 hours and rinsed in deionized water prior to use. When necessary, sample aliquots in multiple serum vials were combined ("pooled") prior to purification to obtain enough CH_4 for clumped isotopologue analysis. When possible, aliquots from the same fluid sampler were used. In some cases, however, it was necessary to combine aliquots from duplicate samples collected in separate samplers deployed in the same hydrothermal fluid during a submersible dive (Table 3.1). Due to the exceedingly low concentration of dissolved CH_4 in ambient bottom seawater ($<10^{-8}$ M, Reeves *et al.*, 2014; McDermott *et al.*, 2015) relative to concentrations in endmember vent fluids (samples regressed to zero Mg content) (Table 3.2), inadvertent entrainment of seawater during fluid collection has no effect on the isotopic composition of vent-fluid derived methane measured during this study.

3.2.2 Analytical techniques

Samples of methane were purified via cryofocusing–preparative gas chromatography (Wang *et al.*, 2015). The relative abundances of the methane stable isotopologues $^{12}CH_4$, $^{13}CH_4$, $^{12}CH_3D$, and $^{13}CH_3D$ were measured using a tunable infrared laser direct absorption spectroscopy technique described previously (Ono *et al.*, 2014; Wang *et al.*, 2015). Due to the small amounts of CH_4 (ca. 1 cm^3 STP) in samples analyzed as part of this study, a cold trap system was employed to recover and recycle gas samples for re-analysis (Wang *et al.*, 2015). A set of samples with previously-determined isotopologue ratios was also re-measured using the recycling technique, to verify accuracy.

The abundance of $^{13}CH_3D$ relative to a random distribution of isotopes among the isotopologues (stochastic distribution) is tracked using the metric $\Delta^{13}CH_3D$, which is defined as: $\Delta^{13}CH_3D = \ln Q$ (or nearly equivalently, $Q - 1$), where Q is the reaction quotient of the isotope exchange reaction:

$$^{13}CH_4 + {}^{12}CH_3D \rightleftharpoons {}^{13}CH_3D + {}^{12}CH_4 \tag{3.1}$$

Values of $\Delta^{13}CH_3D > 0‰$ are used to calculate apparent equilibrium temperatures (T_{13D}) using the calibration of Wang *et al.* (2015), which is based on quantum chemical predictions for methane isotopologues in the gas phase and anchored by measurements of methane samples heated in the presence of catalyst at temperatures between 150 and 400 °C.

Isotope values are reported using standard delta-notation, i.e., $\delta^{13}C = (^{13}C/^{12}C)_{sample}/(^{13}C/^{12}C)_{VPDB} - 1$, and $\delta D = (D/H)_{sample}/(D/H)_{VSMOW} - 1$. The permil (‰) symbol represents multiplication by 10^{-3}; hence, we have omitted the factor of 1000 commonly seen in definitions of δ and other isotope values. The $\delta^{13}C$ and δD values are calibrated against community reference gases NGS-1 and NGS-3 (Wang *et al.*, 2015).

Table 3.1 | Carbon and hydrogen isotope ratios and clumped isotopologue abundances of methane in studied hydrothermal fluids.

Field	Vent	Sample(s)	$\delta^{13}C$ (‰)	δD (‰)	$\Delta^{13}CH_3D$ (‰)	T_{13D} (°C)
Rainbow	Guillaume	J2-352-IGT4	−17.6	−97.7	**0.95** ± 0.60	**450** +298/−136
	CMSP&P	J2-354-IGT3	−17.5	−97.8	**1.50** ± 0.60	**322** +142/−85
	Auberge	J2-352-IGT3	−17.4	−97.9	**1.73** ± 0.60	**285** +114/−73
Von Damm	Old Man Tree[a]	J2-612-IGT6/-IGT8	−16.2	−107.4	**1.71** ± 0.35	**288** +60/−47
	Ravelin 1	J2-617-IGT6	−16.4	−106.6	**1.56** ± 0.60	**312** +134/−82
	East Summit	J2-612-IGT2	−16.4	−106.5	**1.35** ± 0.60	**350** +167/−95
Lost City	Beehive	J2-361-IGT5/-CGTWu	−10.9	−126.6	**1.84** ± 0.60	**270** +104/−68
Lucky Strike	Medea[a]	J2-359-IGT2/-CGTY	−14.2	−99.3	**1.63** ± 0.40	**301** +75/−55
	Isabel[a]	J2-357-IGT5/-CGTY	−12.6	−100.4	**1.85** ± 0.30	**269** +45/−37

Values for $\delta^{13}C$, δD, and $\Delta^{13}CH_3D$ are reported relative to Vienna Pee Dee Belemnite (VPDB), Vienna Standard Mean Ocean Water (VSMOW), and the stochastic distribution, respectively. Analytical uncertainties for $\delta^{13}C$ and δD are both ca. ±0.1‰ (95% confidence intervals). Uncertainties listed for $\Delta^{13}CH_3D$ and T_{13D} are 95% confidence intervals; the last digit in each (hundredths and ones places, respectively) is not significant.

[a] Samples analyzed in duplicate. Uncertainties listed are 2 s.e.m. (standard error of the mean) of the replicate measurements ($n = 2$).

3.3 RESULTS

Results of stable carbon ($^{13}C/^{12}C$) and hydrogen (D/H) isotope ratio measurements are shown in Table 3.1. These results are in general agreement with previously-published methane isotopic data for these samples or systems (Proskurowski *et al.*, 2008; Charlou *et al.*, 2010; Pester *et al.*, 2012; McDermott *et al.*, 2015). Similar values were observed across the different hydrothermal fields, ranging from −18‰ to −11‰ in $\delta^{13}C$ and −127‰ to −98‰ in δD. Variation between vents in the same field (generally <1‰ in both $\delta^{13}C$ and δD) is significantly smaller than variation across different fields. The consistency of stable isotope data within each field is added evidence for the interpretations previously drawn of conservative mixing of CH_4 between bottom seawater and a single CH_4-bearing endmember fluid at Rainbow (Charlou *et al.*, 2002) and Von Damm (McDermott *et al.*, 2015). A common source fluid has also been suggested for Lucky Strike (Pester *et al.*, 2012) and Lost City (Seyfried *et al.*, 2015) based on the compositions of fluids there.

Also shown in Table 3.1 are results of methane clumped isotopologue analyses. All samples yielded values of $\Delta^{13}CH_3D > 0$‰, from which apparent equilibrium temperatures can be derived (Fig. 3.1C and Table 3.1). The unweighted mean of the $\Delta^{13}CH_3D$ values across all nine vent fluids studied was 1.57 ± 0.28‰ (standard deviation, 1*s*), corresponding to a $\Delta^{13}CH_3D$ temperature of 310^{+53}_{-42} °C. Data for individual vent fluids were analytically indistinguishable from this narrow range (Fig. 3.2B).

3.4 DISCUSSION

3.4.1 Decoupling of vent fluid chemistry and temperatures from conditions responsible for CH_4 synthesis

The four unsedimented submarine hydrothermal fields investigated in this study include on- and off-axis vent fields at slow- to ultraslow-spreading ridges, with host rock lithologies ranging from mafic to ultramafic. Compositions of fluids from these sites partially reflect this geological diversity. Supporting data for vent fluid composition are shown in Table 3.2. Concentrations of CH_4 in endmember fluids are high and lie within a range of 0.86 to 2.81 mM (Fig. 3.3B). Such high concentrations are typical of many ultramafic-hosted

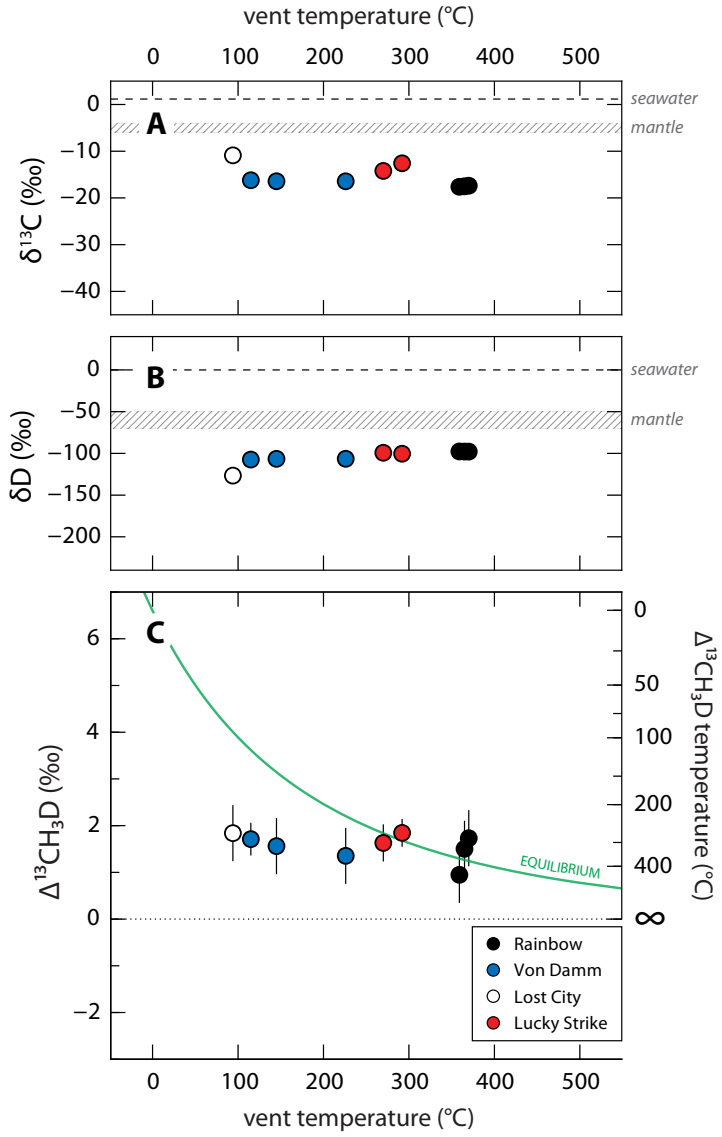

Figure 3.1 | Comparison of (**A**) $\delta^{13}C$, (**B**) δD, and (**C**) $\Delta^{13}CH_3D$ values of methane across vent sites. Data and error bars (95% confidence interval) are from Table 3.1. In all panels, points are plotted against measured vent temperature (Table 3.2). The isotopic compositions of inorganic carbon (A) and hydrogen (B) in seawater and in the mantle are shown (Javoy *et al.*, 1986; Blank *et al.*, 1993; Clog *et al.*, 2013). In (C), the green line represents the clumped isotopologue composition at equilibrium. The $\Delta^{13}CH_3D$ temperature scale corresponds to the calibration from Wang *et al.* (2015).

mid-ocean ridge hydrothermal fields, whereas basalt-hosted fields tend to have lower CH_4 contents (~0.1 mM; McCollom and Seewald, 2007; Keir, 2010). In this respect, concentrations of CH_4 in fluids at the Lucky Strike field (~0.9 mM, Table 3.2), as well as at a similar basalt-hosted field, Menez Gwen on the Mid-Atlantic Ridge (~1.7 mM, Charlou *et al.*, 2000), appear to be anomalously elevated relative to those in other basalt-hosted settings such as those on the fast-spreading East Pacific Rise, where CH_4 concentrations of ~0.1 mM are more typical (McCollom and Seewald, 2007; Keir, 2010).

Contents of low-molecular weight hydrocarbons are also similar between the studied fields, with high C_1/C_2 ratios (Fig. 3.3B) observed in fluids from Rainbow (~2300, Charlou *et al.*, 2002), Von Damm (~4500, McDermott *et al.*, 2015), Lost City (~1100, Proskurowski *et al.*, 2008), and Lucky Strike (>3000, Charlou *et al.*, 2000). Such high C_1/C_2 ratios are typical of fluids from unsedimented mid-ocean ridge hydrothermal systems (McCollom and Seewald, 2007).

Except for the Lost City fluids, total dissolved inorganic carbon ($\sum CO_2 = CO_2(aq) + HCO_3^- + CO_3^{2-}$) concentrations are comparable to or higher than CH_4 and are characterized by a wider range of values (1.9

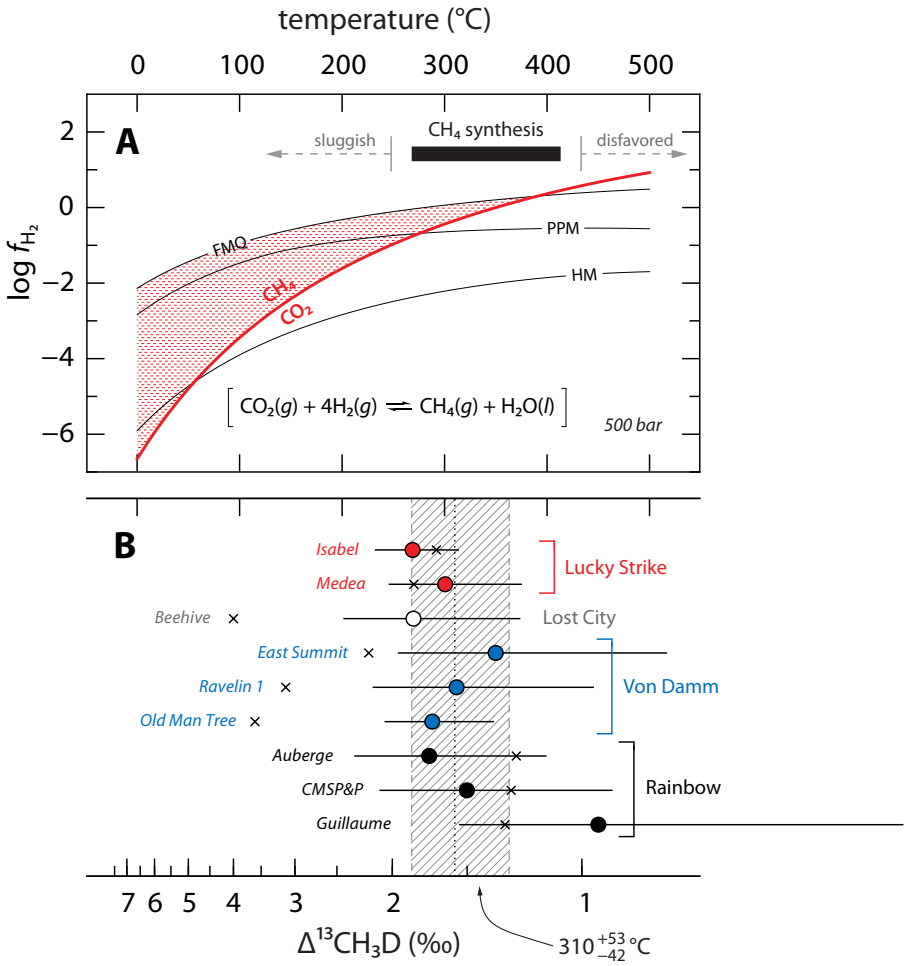

Figure 3.2 | Constraints on methane formation and stability from thermodynamics and clumped isotopologue data. (**A**) Plot of fugacity of H_2 as a function of temperature at 500 bar, after Shock (1992). Red line represents the fugacity of H_2 at equilibrium, according to the reaction $CO_2(g) + 4H_2(g) \leftrightharpoons CH_4(g) + 2H_2O(l)$, when the fugacities of CH_4 and CO_2 are equal, and assuming unit activity for $H_2O(l)$. Grey lines represent equilibrium H_2 fugacities buffered by the mineral assemblages fayalite-magnetite-quartz (FMQ), pyrite-pyrrhotite-magnetite (PPM), and hematite-magnetite (HM). Red shaded area represents the intersection of regions corresponding to geologically-relevant H_2 fugacity and where CH_4 is thermodynamically stable relative to CO_2. The black bar represents the temperature range in which the evidence explored in this study suggests that methane synthesis is both favorable and facile on timescales of relevance to hydrothermal systems. (**B**) A "Caltech plot" of the clumped isotopologue temperatures of methane from studied vents (data and error bars from Table 3.1). Equivalent $\Delta^{13}CH_3D$ values are plotted on the bottom axis, and are derived from the calibration of Wang *et al.* (2015). The dotted line and gray hatching represent the mean ± 1*s* of the $\Delta^{13}CH_3D$ values across all studied vents (+1.57 ± 0.28‰, $n = 9$). The × symbols mark measured vent temperatures (Table 3.2).

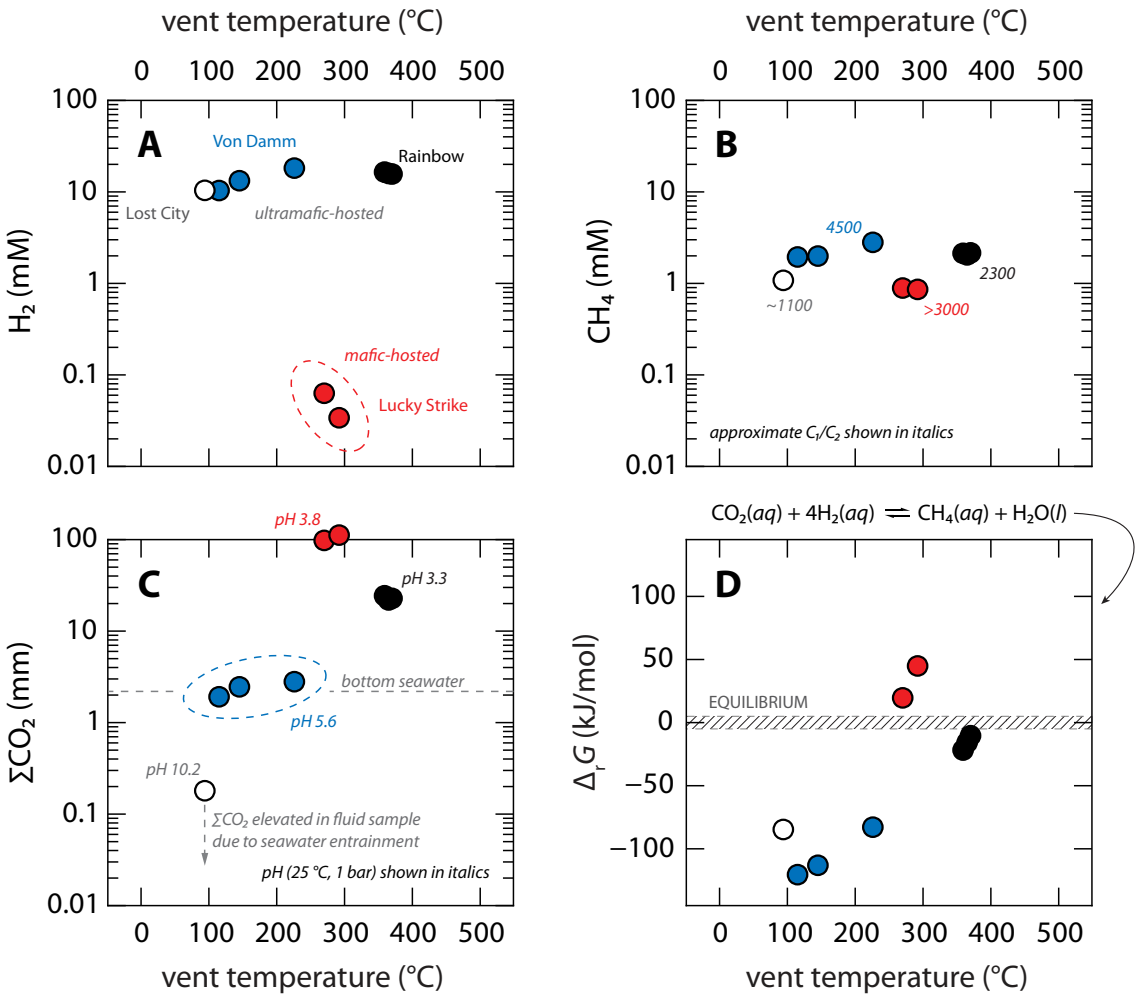

Figure 3.3 | Composition of vent fluids and energetics of methane synthesis in aqueous phase. Concentrations of (**A**) H_2, (**B**) CH_4, and (**C**) $\sum CO_2$ are plotted against measured vent temperatures (data from Table 3.2). Also shown are molar ratios of methane to ethane (C_1/C_2, see § 3.3) in (B), and pH values of endmember fluids in (C). (**D**) Gibbs energy of reaction for methane formation from CO_2 and H_2 in aqueous solution (Reaction 3.2), calculated at vent T and P conditions ($\Delta_r G$, Table 3.2). Gray hatching represents thermodynamic equilibrium (taken as $\Delta_r G = 0 \pm 5$ kJ/mol). Methane formation in aqueous solution is thermodynamically favorable for points plotting below the hatched area. Symbol colors are the same as those in Figs. 3.1 and 3.2.

Table 3.2 | Fluid compositions[a] used in thermodynamic calculations and calculated Gibbs energy of reaction ($\Delta_r G$) for abiotic methane formation via Reaction 3.2 at studied vent sites.[b]

Field	Vent	T (°C)[c]	P (bar)	pH[d]	$\sum CO_2$ (mm)	H_2 (mM)	CH_4 (mM)	$\Delta_r G$ (kJ/mol)[e]
Rainbow	Guillaume	361	230	3.33	24.3	16.5	2.13	−22
	CMSP&P	365	230	3.36	21.9	15.9	2.05	−16
	Auberge	370	230	3.35	22.8	15.7	2.16	−11
Von Damm	Old Man Tree[f]	115	235	5.81	1.80	10.5	1.97	−121
	Ravelin 1[f]	145	235	5.83	2.52	13.4	2.02	−113
	East Summit	226	235	5.56	2.80	18.2	2.81	−83
Lost City	Beehive	96	70	10.20	0.18[g]	10.4	1.08	−85
Lucky Strike	Medea	270	170	3.81	98.0	0.063	0.89	+20
	Isabel	292	170	3.81	112.0	0.034	0.86	+45

Analytical uncertainties (2s) are ±2 °C for T; ±5% for H_2, $\sum CO_2$, and CH_4; and ±0.05 units for pH. Abbreviations: mm, mmol/kg fluid; mM, mmol/L fluid.

[a] All concentrations shown are extrapolated to endmember fluid composition (regressed to zero Mg content), except where noted. Data are from Reeves *et al.* (2014) and McDermott *et al.* (2015).

[b] For each vent fluid, the energetic favorability of methane formation via this reaction was assessed by calculating the Gibbs energy of reaction ($\Delta_r G$), defined by the relationship: $\Delta_r G = RT \ln(Q/K)$, where R is the universal gas constant, T is measured fluid temperature in kelvin, Q is the reaction quotient, and K is the equilibrium constant at T and seafloor pressure P. Equilibrium constants were calculated using thermodynamic data and standard states from Shock and Helgeson (1990) and Johnson *et al.* (1992). For all calculations, the activity of $H_2O(l)$ was assumed to be unity. Activity coefficients were assumed to be unity for neutral dissolved species. For all fluids except for that from Lost City,[g] the concentration of $CO_2(aq)$ was assumed to be equal to $\sum CO_2$, a reasonable approximation given the low measured shipboard pH values and calculated equilibrium speciation of dissolved carbonate species at *in situ* temperatures and seafloor pressures.

[c] Maximum measured vent temperature.

[d] Shipboard pH measurement (25 °C and 1 atm).

[e] A negative value of $\Delta_r G$ indicates a thermodynamic drive for the reaction to proceed as written from left to right (i.e., methane formation favored). Given uncertainties associated with chemical analyses and thermodynamic data, calculated $\Delta_r G$ values within ±5 kJ/mol of zero are interpreted to indicate that the reaction has approached or attained a state of thermodynamic equilibrium (Seewald, 2001a).

[f] Concentrations for fluids from Old Man Tree and Ravelin 1 at Von Damm not extrapolated to zero Mg; Mg contents for these fluids are 14.0 and 15.0 mmol/kg fluid, respectively, indicating that endmember fluid has already mixed with seawater in the subsurface prior to discharge at the seafloor (McDermott *et al.*, 2015).

[g] An arbitrary $CO_2(aq)$ concentration of 1 nmol/kg was used in thermodynamic calculations for the Lost City fluid, similar to Reeves *et al.* (2014). The actual concentration value is subject to substantial uncertainty due to difficulties in determining the near-zero endmember $\sum CO_2$ content in vent fluids, given that some entrainment of $\sum CO_2$-replete seawater always occurs during sampling (Proskurowski *et al.*, 2008). Varying this value by as much as ten orders of magnitude would not affect the conclusion that methane formation is thermodynamically favorable in the fluid, due to the high H_2 content and the power of 4 to which the activity of $H_2(aq)$ is raised in the mass action expression.

to 112.0 mmol/kg, Fig. 3.3C). Endmember fluids from Rainbow, Von Damm, and Lucky Strike contain 2 to 50 times as much total carbon as is in bottom seawater (~2.2 mM; Reeves *et al.*, 2014; McDermott *et al.*, 2015), such that $\sum CO_2$ in recharging seawater cannot be the sole source of carbon to venting fluids. The Lost City fluid contains very low amounts of $\sum CO_2$ (~0.18 mmol/kg), the majority of which is likely derived from seawater entrainment during sample collection (Reeves *et al.*, 2014). Given the high pH (10.2), the concentration of $CO_2(aq)$ in endmember Lost City fluids must be very low (see footnote g in Table 3.2). At the relatively low pH of the other fluids (3.33 to 5.81), the majority of $\sum CO_2$ is in the form of $CO_2(aq)$.

The concentration of dissolved H_2 is high and varies from 10.4 to 18.2 mM in endmember and mixed fluids

from the Rainbow, Von Damm, and Lost City fields, whereas fluids from Lucky Strike have approximately three orders of magnitude lower concentrations (34–63 μM, Fig. 3.3A). At Rainbow, Von Damm, and Lost City, serpentinization of ultramafic rock in subsurface reaction zones with concomitant production of H_2 is thought to be a major control on fluid compositions (Kelley *et al.*, 2001; Charlou *et al.*, 2002; McDermott *et al.*, 2015). In contrast, the Lucky Strike field is hosted in basaltic rock, and vent fluids there encounter much more oxidizing conditions (Charlou *et al.*, 2000; Pester *et al.*, 2012).

The stoichiometry of the reaction

$$CO_2(aq) + 4H_2(aq) \leftrightharpoons CH_4(aq) + 2H_2O(l) \tag{3.2}$$

indicates that the abundance of $CH_4(aq)$ at thermodynamic equilibrium in vent fluids should be highly sensitive to the concentration of H_2 because of the fourth-power dependence on the activity of $H_2(aq)$ in the corresponding mass action expression. At Lucky Strike, formation of $CH_4(aq)$ in endmember fluids is thermodynamically disfavored due to the low H_2 contents (Table 3.2). In all other vent fluids studied, a thermodynamic drive for methane synthesis is present at varying magnitudes (Fig. 3.3D).

Methane $^{13}C/^{12}C$ and D/H ratios are similar across fluids from all four unsedimented hydrothermal fields studied (Fig. 3.1). The $\delta^{13}C$ values (−18‰ to −11‰) are within the range of those determined for methane at more than a dozen other basalt- and ultramafic-hosted submarine hydrothermal systems studied to date (−24‰ to −6‰), including Kairei on the Central Indian Ridge, TAG, Broken Spur, and Logatchev on the Mid-Atlantic Ridge, and 17–19°S, 9°50′N, 13°N, and 21°N on the East Pacific Rise (see McCollom and Seewald, 2007; Keir, 2010, and references therein). Published data for δD of methane are more limited; however, the δD values we measured (−127‰ to −98‰) are similar to those determined at Logatchev (−109‰ Proskurowski *et al.*, 2006) and 21°N on the East Pacific Rise (−126‰ to −102‰ Welhan and Craig, 1983).

The data described above support the general consensus that the methane in the studied hydrothermal fluids is of dominantly abiotic origin (e.g., Welhan, 1988b; Charlou *et al.*, 2002; Proskurowski *et al.*, 2008; McDermott *et al.*, 2015), and that contributions of thermogenic or microbial sources of methane are limited or insignificant. Because the four sites studied lack substantial sediment burdens, organic carbon from which thermogenic hydrocarbons or microbial methane can be generated is in scarce supply (Welhan, 1988b; Reeves *et al.*, 2014). Furthermore, high C_1/C_2 ratios (~1000 to 4000), along with high methane $\delta^{13}C$ values (−18‰ to −11‰), are distinct from thermogenic or microbial sources, which typically have lower C_1/C_2 ratios or lower $\delta^{13}C$ values, respectively (McCollom and Seewald, 2007).

The methane $\delta^{13}C$ data alone do not unambiguously exclude contributions of microbial methanogenesis, because high methane $\delta^{13}C$ values could be a result of near-quantitative conversion of $\sum CO_2$ to CH_4, particularly under $\sum CO_2$-limited and/or high-pressure conditions such as those present at Lost City (Brazelton *et al.*, 2006; Takai *et al.*, 2008; Bradley and Summons, 2010). However, radiocarbon (^{14}C) abundances for methane from Lost City and Von Damm are very low [fraction modern (F_m) averaging 0.004–0.006, near the limit of detection (F_m ~ 0.003)] (Proskurowski *et al.*, 2008; McDermott *et al.*, 2015), whereas ^{14}C contents of endmember $\sum CO_2$ at Von Damm are ~5× higher (McDermott *et al.*, 2015). Had CH_4 been derived from reduction of $\sum CO_2$, the younger ^{14}C age of the $\sum CO_2$ would have been transferred to CH_4. McDermott *et al.* (2015) further showed that $\sum CO_2$ in the vent fluids at Von Damm is likely seawater-derived, because both concentrations and $\delta^{13}C$ values of endmember $\sum CO_2$ match those of local bottom seawater. The apparent conservation of $\sum CO_2$ during convective circulation at Von Damm indicates that $\sum CO_2$ in recharging seawater at Von Damm has not been converted to CH_4 via any process—microbial or otherwise—despite high energetic favorability for CH_4 synthesis (Fig. 3.3D). Similar carbon isotopic compositions of CH_4 and contents of C_{2+} alkanes at Lost City, Lucky Strike, and Rainbow (as well as at other unsedimented fields studied to date), despite marked differences in geologic setting, fluid composition, and thermodynamic drive for CH_4 synthesis, are consistent with a common abiotic origin for methane at many, if not all, sediment-poor seafloor hydrothermal systems.

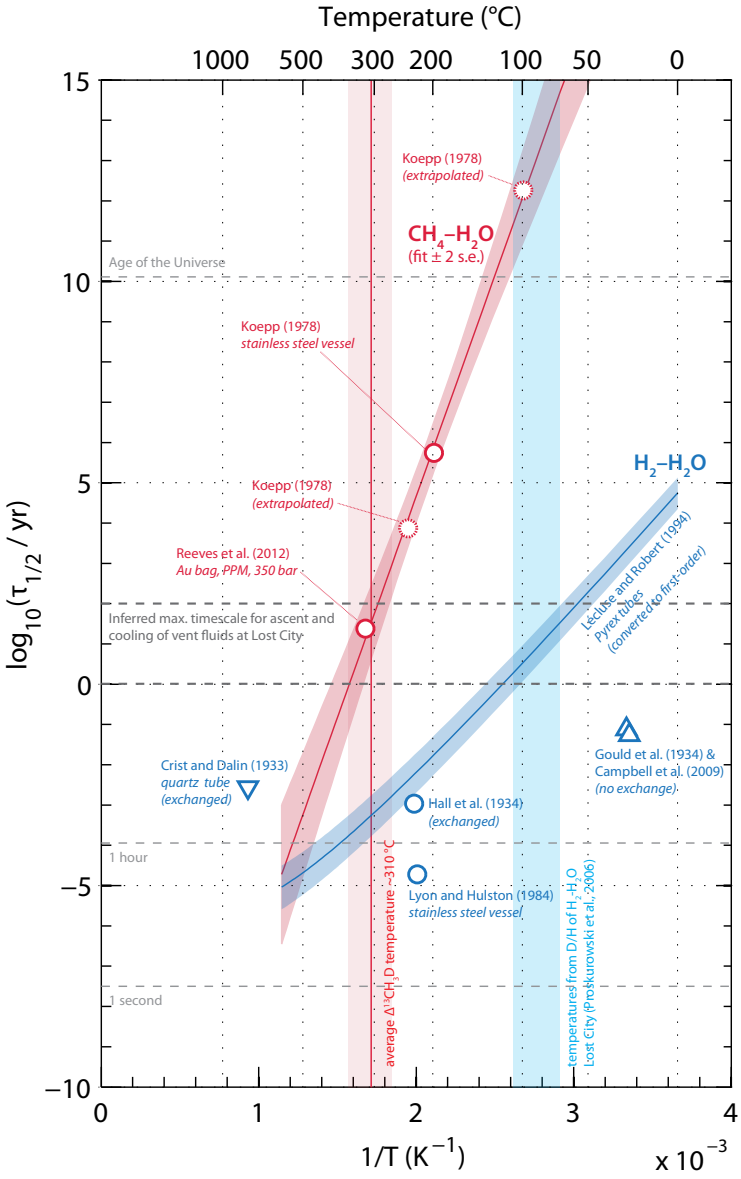

Figure 3.4 | Half-exchange timescales ($\tau_{1/2} = \ln(2)/k$) for hydrogen exchange between CH_4 & H_2O (red symbols) and H_2 & H_2O (blue) based on experiments done in the absence of added catalyst (Crist and Dalin, 1933; Gould *et al.*, 1934; Hall *et al.*, 1934; Koepp, 1978; Lyon and Hulston, 1984; Lécluse and Robert, 1994; Campbell *et al.*, 2009; Reeves *et al.*, 2012). Reactions were assumed to be first order in CH_4 or H_2. When rate constants were not provided by the authors or when exchange was not observed, the reported duration of the experiment was taken as an estimate of the timescale of exchange. Downward- and upward-pointing triangles are, respectively, maximum and minimum estimates of the exchange timescale. The $\tau_{1/2}$ for CH_4–H_2O exchange from Reeves *et al.* (2012) comes from Fig. 3.8. Second-order rate coefficients for H_2–H_2O exchange from Lécluse and Robert (1994) were converted to first-order rate coefficients by multiplying by the equilibrium vapor pressure of H_2O calculated at temperatures T and a pressure of 1 kbar. Uncertainties in exchange rates are difficult to estimate, but are probably one order of magnitude or greater. Clumped isotopologue temperatures for CH_4 from the present study (red bar) and temperatures from D/H geothermometry of H_2–H_2O in endmember fluids at the Lost City site (blue bar) (Proskurowski *et al.*, 2006) are also shown. See text for interpretation of these data with respect to timescales of fluid circulation.

Measured $\Delta^{13}CH_3D$ values (averaging 1.57 ± 0.28‰, 1*s*) and corresponding apparent equilibrium temperatures (310^{+53}_{-42} °C) are strikingly uniform in the context of the large natural variations (up to ca. 10‰) previously observed in $\Delta^{13}CH_3D$ values carried by methane sampled from different settings (Wang *et al.*, 2015). Furthermore, the studied fluids vented at a wide range of temperatures, ranging from 96 to 370 °C. Had the methane in these samples attained isotopologue equilibrium at measured vent temperatures, $\Delta^{13}CH_3D$ values from 4.0 to 1.3‰, respectively, would be expected. The observed range of clumped isotopologue data is much smaller than this predicted range (Fig. 3.1C), with $\Delta^{13}CH_3D$ temperatures generally equal to or higher than fluid temperatures (Fig. 3.2B). In lower-temperature (<250 °C) fluids, including fluids that have mixed in the subsurface (venting with non-zero Mg) such as those from Ravelin 1 (145 °C) and Old Man Tree (115 °C) vents at Von Damm (McDermott *et al.*, 2015), $\Delta^{13}CH_3D$ temperatures higher than fluid

temperatures indicate that $\Delta^{13}CH_3D$ values have not been affected by cooling below ~250 °C. In higher temperature fluids (>270 °C) however, $\Delta^{13}CH_3D$ temperatures are analytically indistinguishable from measured fluid temperatures. Experimental data suggest that hydrogen exchange between methane and water in hydrothermal fluids may be observable at temperatures of ~325 °C on relatively short timescales (years; Reeves *et al.*, 2012, and Fig. 3.8) relevant to hydrothermal systems (Fig. 3.4). Hydrogen exchange between CH_4 and H_2O may explain the uniformity of both δD and $\Delta^{13}CH_3D$ values of methane in high-temperature fluids (Fig. 3.5); the implications of this are discussed below (§ 3.4.2). The $\Delta^{13}CH_3D$ values indicate that CH_4 experienced temperatures of at least 300 °C during its residence within the oceanic crust. Our methane clumped isotopologue data indicate that temperatures and compositions of hot-spring fluids at the time of venting are decoupled from the conditions responsible for the formation of CH_4 in these fluids. The following sections discuss how the 300 °C or greater inferred temperatures are compatible with models invoking respeciation of magmatic volatiles at those temperatures to form CH_4 in plutonic layers of the oceanic crust.

3.4.2 Hydrogen exchange and the origin of hydrogen in CH_4

Hydrogen isotope ratio measurements provide constraints on the origin of the major H-bearing species within vent fluids. Apparent temperatures derived from D/H equilibria in the systems H_2–H_2O and H_2–CH_4 were first used as geothermometers in studies of geothermal or volcanic gases and waters (Árnason and Sigurgeirsson, 1968; Gunter and Musgrave, 1971; Arnason, 1977; Panichi *et al.*, 1977; Panichi and Gonfiantini, 1977; Kiyosu, 1983; Lyon and Hulston, 1984), and later examined with respect to data from seafloor hydrothermal fluids (Welhan and Craig, 1983; Horibe and Craig, 1995; Proskurowski *et al.*, 2006; Bradley and Summons, 2010; Kawagucci *et al.*, 2010; Kawagucci *et al.*, 2011; Kawagucci *et al.*, 2013), shield-hosted groundwaters (Sherwood Lollar *et al.*, 1993; Sherwood Lollar *et al.*, 2007; Sherwood Lollar *et al.*, 2008), and continental springs, seeps, and well fluids influenced by serpentinization (Neal and Stanger, 1983; Coveney *et al.*, 1987; Abrajano *et al.*, 1988; Fritz *et al.*, 1992; Etiope *et al.*, 2011a; Suda *et al.*, 2014). Temperatures returned from H_2–H_2O and H_2–CH_4 equilibria often agree with each other and with realistic geologic and hydrologic scenarios for geothermal fluids exiting at high temperatures, but these relationships do not necessarily hold for lower-temperature fluids.

Proskurowski *et al.* (2006) showed that D/H-based temperatures derived from H_2–H_2O and H_2–CH_4 in high-temperature vent fluids (>270 °C) are concordant and match measured fluid temperatures at discharge. At the low-temperature Lost City site, however, H_2–H_2O and H_2–CH_4 yielded discordant temperatures of 70–110 °C and 110–150 °C, respectively. Proskurowski *et al.* (2006) reconciled these data by suggesting that serpentinization of ultramafic basement rocks beneath the Lost City vent field occurs at low temperatures of 110–150 °C, concomitant with production of both H_2 and CH_4, and that H_2 maintained isotopic equilibrium with H_2O during slow cooling of root-zone fluids to ca. 70–110 °C prior to rapid ascent to seafloor while the higher temperature signal recorded by H_2–CH_4 was presumably not reset during cooling. In contrast, the $\Delta^{13}CH_3D$ temperature of 270^{+104}_{-68} °C we obtained for the Beehive vent fluid argues for a much higher temperature of last exchange for the C–H bonds in methane, and does not support suggestions of CH_4 production at lower temperatures. The clumped isotopologue temperature is consistent with estimates from heat balance considerations, $\delta^{18}O$ values, and alkane-alkene and mineral-fluid equilibria all suggesting that Lost City fluids experienced temperatures as high as 250 °C at depth (Allen and Seyfried, 2004; Foustoukos *et al.*, 2008; Reeves *et al.*, 2012; Seyfried *et al.*, 2015). Discrepancies between measured $\Delta^{13}CH_3D$ temperatures, temperatures from D/H geothermometry, and fluid exit temperatures at Lost City indicate that rather than directly recording the temperatures of H_2 and CH_4 synthesis, each geothermometer records a different portion of the time-temperature history of the fluids.

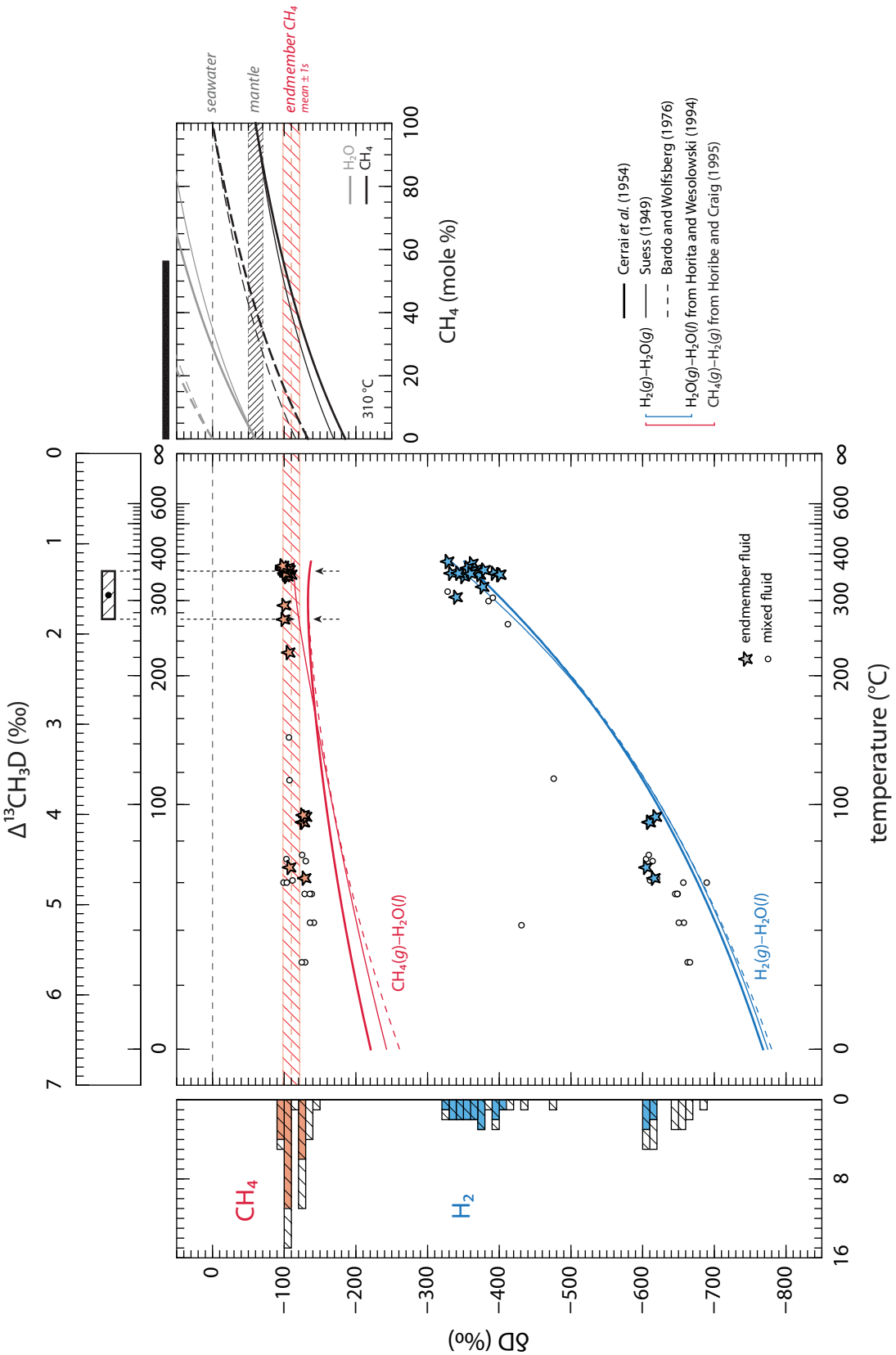
δD (‰)
temperature (°C)
Δ13CH3D (‰)
CH4
H2
CH4(g)–H2O(l)
H2(g)–H2O(l)
endmember fluid
mixed fluid
CH4 (mole %)
seawater
mantle
endmember CH4
mean ± 1s
H2O
CH4
310 °C
Cerrai et al. (1954)
Suess (1949)
Bardo and Wolfsberg (1976)
H2O(g)–H2O(l) from Horita and Wesolowski (1994)
CH4(g)–H2(g) from Horibe and Craig (1995)
H2(g)–H2O(g)

Figure 3.5 | Hydrogen isotopic composition of CH_4 (red) and H_2 (blue) in seafloor hydrothermal fluids plotted against measured vent temperatures. Data are from unsedimented fields studied in Welhan and Craig (1983), Proskurowski *et al.* (2006), Charlou *et al.* (2010), and Kawagucci *et al.* (2010), and in this study (see Tables 3.1 and 3.1), and are tabulated in Table 3.3. Endmember fluids (identified by low Mg contents) are represented by stars, and vent fluids containing a mixture of hydrothermal endmember fluid and seawater are represented by circles. Data from sites exhibiting phase separation (Charlou *et al.*, 2010) or with fluids diffusely effluxing through colonies of deep-sea snails or shrimp (Kawagucci *et al.*, 2010) are excluded from this plot (see notes under Table 3.3). Red hatching indicates the average δD of CH_4 in endmember fluids (−110 ± 12‰, 1*s*) in the compiled dataset. Red and blue curves represent the δD values of CH_4 and H_2 (respectively) in D/H equilibrium with H_2O of seawater-like isotopic composition (δD = 0‰, dashed gray line) predicted by combinations of published calibrations for $H_2(g)/H_2O(g)$ (Suess, 1949; Cerrai *et al.*, 1954; Bardo and Wolfsberg, 1976), $H_2O(g)/H_2O(l)$ (Horita and Wesolowski, 1994), and $CH_4(g)/H_2(g)$ (Horibe and Craig, 1995). [High-temperature hydrothermal fluids generally have δD values of H_2O close to 0‰ (Shanks *et al.*, 1995). Note that measured values for δD of H_2O in fluids from Lost City are +2 to +7‰ (Proskurowski *et al.*, 2006) and thus the equilibrium values for CH_4 and H_2 at Lost City are slightly (~5‰) higher than those indicated by the curves; this difference is small compared to the uncertainty in equilibrium fractionation factor calibrations at the temperatures of these fluids (~30 to 90 °C).] (***Left***) Histogram of δD values of CH_4 and H_2 in endmember (shaded) and mixed fluids (unshaded bars). (***Top***) Mean ± 1*s* of the $\Delta^{13}CH_3D$ values and corresponding clumped isotopologue temperatures (310^{+53}_{-42} °C) of methane reported in Table 3.1. Dashed black arrows point to the range of δD values of $CH_4(g)$ in equilibrium with seawater at the temperatures indicated by $\Delta^{13}CH_3D$ data. (***Right***) Modeled δD values of CH_4 (black curves) and H_2O (gray curves) as a function of mole fraction of CH_4 in a hypothetical methane-rich fluid. All H was assumed to exist as $H_2O(l)$ in isotopic equilibrium with $CH_4(g)$ at the temperature indicated by the mean $\Delta^{13}CH_3D$ value (310 °C). [At ~270 to 360 °C, D/H fractionation between $CH_4(g)$ and $H_2O(l)$ is not very sensitive to temperature (Horibe and Craig, 1995). Uncertainty in the equilibrium D/H fractionation factor is dominated by the disagreement among $H_2(g)/H_2O(g)$ calibrations. Isotopic fractionation between $CH_4(g)$ and $CH_4(aq)$ is negligible (Bacsik *et al.*, 2002), and the fractionation between $H_2O(g)$ and $H_2O(l)$ is small (~5‰) (Horita and Wesolowski, 1994). The model neglects the effects of elevated pressure and salinity (Horita, 2005; Martineau *et al.*, 2012), and ignores potential isotopic exchange with hydrous minerals (Horita *et al.*, 1999; Saccocia *et al.*, 2009; Méheut *et al.*, 2010).] The initial δD was taken to be 0‰ (dashed lines) for seawater-derived H, or −60‰ (solid lines) for mantle-derived H (Clog *et al.*, 2013). Minimum and maximum values expected for δD of CH_4 are represented by the solid and dashed lines, respectively. Mixing of seawater with mantle-derived water prior to respeciation of H_2O to CH_4 and re-equilibration of CH_4 initially formed in equilibrium with mantle-derived H_2O (both resulting in δD values of CH_4 moving upwards towards the dashed lines) affect the predictions; effects of these processes are treated in § 3.4. The black bar shows the range in CH_4 mole fraction that is compatible with the isotopic data from vent fluids.

Comparison of temperatures indicated by these H_2–H_2O and H_2–CH_4 geothermometers are only meaningful if H_2–H_2O, H_2–CH_4, and CH_4–H_2O have all attained equilibrium at a single temperature, and no further isotopic exchange has occurred during cooling. These temperatures cannot be considered in isolation because a shift in the D/H ratio of one species induces disequilibrium in two of the three reactions. Stated another way, the inferences drawn by Proskurowski *et al.* (2006) implicitly required that hydrogen exchange processes among H_2O, H_2, and CH_4 have similar kinetics and closure temperatures. This assumption may not hold at temperatures <300 °C. In particular, H_2–H_2O exchange occurs at substantially higher rates than does CH_4–H_2O (Lyon and Hulston, 1984; Lécluse and Robert, 1994; Horibe and Craig, 1995). In Fig. 3.4, we show timescales for exchange at temperatures between 0 and 600 °C, determined from published data for experimental isotopic exchange in the systems CH_4–H_2O and H_2–H_2O. This compilation indicates that although the exact rate of exchange is highly uncertain, H_2–H_2O exchange occurs much faster than CH_4–H_2O exchange. The rate coefficients of Lécluse and Robert (1994) were obtained in vapor-phase experiments where H_2 was exchanged with D_2O. They observed no discernible difference in rates of exchange when several different catalysts were added to increase available surface area for reaction. The plotted blue curve shows their data converted to rates that are first-order in $[H_2]$; whether the converted rate coefficients accurately reflect real kinetics of H_2–H_2O exchange where H_2 is dissolved in liquid H_2O remains to be evaluated. Lyon and Hulston (1984) reported D/H exchange of H_2 with liquid H_2O on timescales of ~10 minutes at 225 °C in a stainless steel reaction vessel. Their rate is faster than those we calculated from the data of Lécluse and Robert (1994), suggesting either that rates of H_2–H_2O exchange may be faster than projected by the blue curve, or that catalytic effects of stainless steel enhanced rates of exchange in Lyon and Hulston's experiment. In comparison to the H_2–H_2O data, the experimental data for CH_4–H_2O exchange (red symbols in Fig. 3.4) provide a surprisingly good fit, though alignment of the limited data could be fortuitous. However, the experiments of Reeves *et al.* (2012) were conducted in a gold-titanium reaction cell in the presence of mineral phases typical of those found in hydrothermal deposits, and may simulate natural conditions fairly well. It is not known if factors such as pH, redox state, minerals, or concentrations of sulfur, H_2, or carbon species affect hydrogen exchange rates. Regardless, CH_4–H_2O exchange is at least several orders of magnitude slower than H_2–H_2O exchange.

Across many low- and high-temperature hydrothermal systems globally, δD of H_2 varies systematically (between −700‰ and −330‰) with measured fluid temperature (40 to 370 °C, respectively), whereas δD of CH_4 falls within a much narrower range (−140‰ to −95‰) and shows no correlation with fluid temperature (Fig. 3.5). Within the Lost City site, δD of H_2 varies by up to 80‰ while δD of CH_4 shows much less variation (a 40‰ range) (Proskurowski *et al.*, 2006).[1] Hydrogen-isotope ratio data of H_2–CH_4 here indicate spurious temperatures that do not reflect recent exchange between these two species.[2] Part of the problem is that H_2–CH_4 will always give a temperature that is close to H_2–H_2O if δD of H_2O and CH_4 are within a few hundred permil because the δD of H_2 directly controls the calculated temperature for both. This means that temperatures derived from H_2–CH_4 may not be meaningful unless they can be confirmed by something else such as clumped isotopes. Decoupling of D/H data of CH_4 from H_2 at Lost City suggests that these species have not recently interacted with each other, and are more appropriately interpreted as recording separate temperatures at which these species independently equilibrated with water (H_2 at ~110 °C in endmember fluids, and CH_4 at much higher temperatures of >240 °C). An origin of CH_4 that is separated in time, space and/or temperature from that of H_2 is compatible with the fluid inclusion-leaching hypothesis (§ 3.4.3) and is corroborated by our $\Delta^{13}CH_3D$ data.

[1] At lower-temperature vents, isotopic compositions of CH_4 may reflect admixture or removal of minor amounts of CH_4 due to biological activity (Brazelton *et al.*, 2006; Proskurowski *et al.*, 2006; Bradley and Summons, 2010).

[2] While rates of D/H exchange between dissolved H_2 and CH_4 have not been experimentally studied, the discordant temperatures from D/H geothermometry in low-temperature fluids (described above) strongly suggest that direct H_2–CH_4 exchange is also much slower than H_2–H_2O exchange.

Given the rate of CH_4–H_2O isotope exchange of 10 to 100 years at 300 °C (Fig. 3.4), it is likely that the clumped methane isotopologue temperatures represent closure temperatures below which exchange becomes sluggish relative to cooling rate. The δD values of methane might constrain the source of water with which CH_4 equilibrated at that temperature. Measured δD values of CH_4 (−149 to −99‰) and H_2O (−104 to −6‰) in the gabbro-hosted inclusions from the Southwest Indian Ridge (Kelley and Früh-Green, 1999) are consistent with predictions from a model of a fluid containing mantle-derived H that partitioned into CH_4 and H_2O at ~310 °C (Fig. 3.5). The δD values of CH_4 in the inclusions overlap the observed ranges in vent fluids shown in Fig. 3.5 and Table 3.3 (−141 to −93‰). Partial or total re-equilibration of C–H bonds in CH_4 during extraction by seawater heated to >300 °C during active hydrothermal circulation would pull the δD values of CH_4 towards an equilibrium value of −130 to −110‰ (depending on the calibration), consistent with the narrow range of data from high-temperature endmember fluids (Fig. 3.5).

It is worth noting that while serpentinization of olivine and orthopyroxene in oceanic peridotites generates large quantities of H_2 (Klein *et al.*, 2009; McCollom and Bach, 2009; Klein *et al.*, 2013), methane synthesis does not necessarily require serpentinization of peridotite. At temperatures of ~400 °C, oxygen fugacities at or below FMQ are sufficiently reducing for CH_4 to be stable relative to CO_2 (Figs. 3.2 and 3.7). Rocks derived from the partial melting of the suboceanic upper mantle, including gabbros and mid-ocean ridge basalts, are typically characterized by f_{O_2} within ±1 log unit of FMQ at temperatures and pressures of the upper mantle (Bryndzia and Wood, 1990; Cottrell and Kelley, 2011). Cooling of these rocks along an f_{O_2} trajectory parallel to those of typical oxygen buffers may allow for respeciation of mantle-derived CO_2 to CH_4 to occur in the presence of mafic minerals (olivine and orthopyroxene) deep within the oceanic crust (Mathez *et al.*, 1989; Kelley and Früh-Green, 1999). Serpentinization occurring distal to the rocks from which CH_4-rich fluids are extracted may explain why CH_4 and H_2 concentrations are not tightly correlated across seafloor hydrothermal systems (Keir, 2010; Kawagucci *et al.*, 2013).

Models of convective hydrothermal circulation at Lost City indicate that the bulk of actively-venting fluids have migrated along a narrow range of flow paths that are surrounded by already fully-serpentinized rock with little additional potential for H_2 generation, suggesting that H_2 in vent fluids may have instead formed by serpentinization occurring in meandering flow paths away from the main flow channels, and later diffused or mixed into the ascending fluid (Titarenko and McCaig, 2016). Assuming that equilibration of the methane isotopologues proceeds through CH_4–H_2O exchange, $\Delta^{13}CH_3D$ temperatures for CH_4 from the present study (red bar in Fig. 3.4) suggest that the time taken by actively-circulating hydrothermal fluids (after extracting CH_4 from plutonic rocks) during ascent from the ~270 °C isotherm to temperatures below ~200 °C (at which further equilibration is no longer possible on any relevant timescale) is ~10^2 years or less. This compares favorably with estimates for fluid residence times in hydrothermal systems, which generally suggest that the bulk of vent fluids in several high-temperature systems resided in the reaction zone (>200 °C) for years to decades prior to venting (Kadko, 1996; Fisher, 2003). Projection onto the blue bar in Fig. 3.4 showing temperatures from D/H geothermometry of H_2–H_2O in endmember fluids at Lost City (Proskurowski *et al.*, 2006) shows that these timescales for fluid transit are also consistent with estimated kinetics of D/H exchange between H_2 and H_2O. Timescales inferred here may also be compared with constraints on upflow velocities from 1D reactive transport models of fluids ascending from ~750 mbsf and cooling via conduction (Seyfried *et al.*, 2015). Actual timescales of circulating fluid may vary widely due to significant contributions of both on- and off-axis recharge and circulation (Hasenclever *et al.*, 2014).

This study emphasizes that the use of bulk and position-specific D/H ratios and clumped isotopologues abundances of small organic molecules as geothermometers or geospeedometers requires an understanding of the factors controlling hydrogen exchange rates (Eiler, 2013). Rigorous exchange experiments under simulated natural conditions may yield broadly-applicable insights into interactions of CH_4 or other hydrocarbons with minerals or water. Substantial hydrogen isotopic exchange of C_2 to C_5 alkanes with D-enriched and

D-depleted water occurs during hydrothermal experiments lasting several months at 323 °C (Reeves *et al.*, 2012). In contrast, hydrogen exchange between CH_4 and H_2O proceeds much more slowly than hydrogen exchange between C_{2+} hydrocarbons and H_2O, likely because double-bond formation—which leads to metastable equilibrium between alkanes and alkenes (Seewald, 1994)—cannot occur for CH_4. Timescales determined for CH_4–H_2O exchange provide a maximum estimate of the stability of C–H bonds of organic molecules in nature, which in turn sets bounds on the integrity of interpretations that require δD values to be primary in origin (Sessions *et al.*, 2004; Schimmelmann *et al.*, 2006).

3.4.3 Magmatic volatiles in the oceanic crust and the origin of carbon in CH_4

At Von Damm, constraints from $\delta^{13}C$ and ^{14}C data of $\sum CO_2$ and CH_4 indicate that reduction of seawater-derived $\sum CO_2$ to CH_4 is not occurring to an appreciable extent in the actively convecting hydrothermal fluids (see § 3.4.1), despite the energetic favorability of reduction of $CO_2(aq)$ to $CH_4(aq)$ (Fig. 3.3D). Instead, metastable equilibrium is established between $\sum HCOOH$ (= formate + formic acid) and $\sum CO_2$ as a result of kinetic limitations on CH_4 production (McDermott *et al.*, 2015). McDermott *et al.* suggested that hydrocarbons here might instead be derived from leaching of fluids occluded in plutonic rocks of the Mount Dent oceanic core complex that originally contained magmatic CO_2 and which respeciated to form hydrocarbons at temperatures at or below 400 °C, as suggested by several studies of gabbros from the Southwest Indian Ridge (Kelley, 1996; Kelley and Früh-Green, 1999). The $\Delta^{13}CH_3D$ temperatures we obtained for fluids from three vents in the Von Damm field (averaging between 288 and 350 °C, Table 3.1) are significantly higher than the fluid temperatures measured at discharge (115 to 226 °C, Fig. 3.2B), but lower than 400 °C. The data presented here are compatible with the inclusion-leaching hypothesis of McDermott *et al.* (2015).

Proskurowski *et al.* (2008) invoked abiotic reduction of aqueous $\sum CO_2$ to explain the presence of high (~1 mmol/kg) concentrations of CH_4 and minor quantities (~1 μmol/kg or lower) of C_{2+} alkanes in vent fluids from the Lost City hydrothermal field. They postulated a scenario that involves leaching of primordial inorganic carbon from mantle host rocks, and subsequent reduction of $\sum CO_2$ to CH_4 and C_{2+} in circulating fluids at relatively low temperature (<150 °C; Proskurowski *et al.*, 2006). However, Lost City fluids contain vanishingly small amounts of $\sum CO_2$ because the highly alkaline pH and high concentrations of Ca^{2+} favor precipitation of carbonates, a process that proceeds rapidly at temperatures experienced by the circulating fluids (Kelemen *et al.*, 2011; Grozeva *et al.*, 2017). The production of methane via CO_2 reduction in an aqueous fluid depleted of $\sum CO_2$ is therefore problematic in that it requires the addition of mantle-derived CO_2 that is quickly reduced to form CH_4 (up to 56% conversion based on magmatic $C/^3He$ ratios; Proskurowski *et al.*, 2008), and the remainder of which is then subsequently scavenged (presumably by carbonate precipitation), leaving no evidence of its addition. Rates of $\sum CO_2$ reduction must be comparable to or faster than carbonate precipitation in order for CH_4 synthesis to proceed in alkaline, $\sum CO_2$-poor fluids such as those at Lost City. Carbonate precipitation occurs rapidly during alteration of peridotite (Grozeva *et al.*, 2017). In contrast, laboratory studies consistently find sluggish reaction kinetics for the reduction of $\sum CO_2$ to CH_4 in the presence and absence of powdered peridotite or mafic mineral phases (McCollom and Seewald, 2001; McCollom and Seewald, 2003; Seewald *et al.*, 2006; Reeves, 2010; McCollom, 2016; Grozeva *et al.*, 2017). Certain transition metal catalysts can enhance rates of CH_4 production (Horita and Berndt, 1999; Foustoukos and Seyfried, 2004), but H_2 concentrations several orders of magnitude higher than those found in vent fluids are required to render native Fe-Ni alloys stable (Frost, 1985; Charlou *et al.*, 2002; Sleep *et al.*, 2004; McCollom and Bach, 2009). Furthermore, rates of CH_4 synthesis in fluids deprived of $\sum CO_2$ are poorly-constrained, but generally too low to be reliably detected on timescales of laboratory experiments (Fu *et al.*, 2007; McCollom, 2012; McCollom, 2013).

Data from other vent fields are also inconsistent with synthesis of CH_4 on timescales associated with actively-circulating fluids. At the basalt-hosted Lucky Strike field, synthesis of methane within the low-H_2

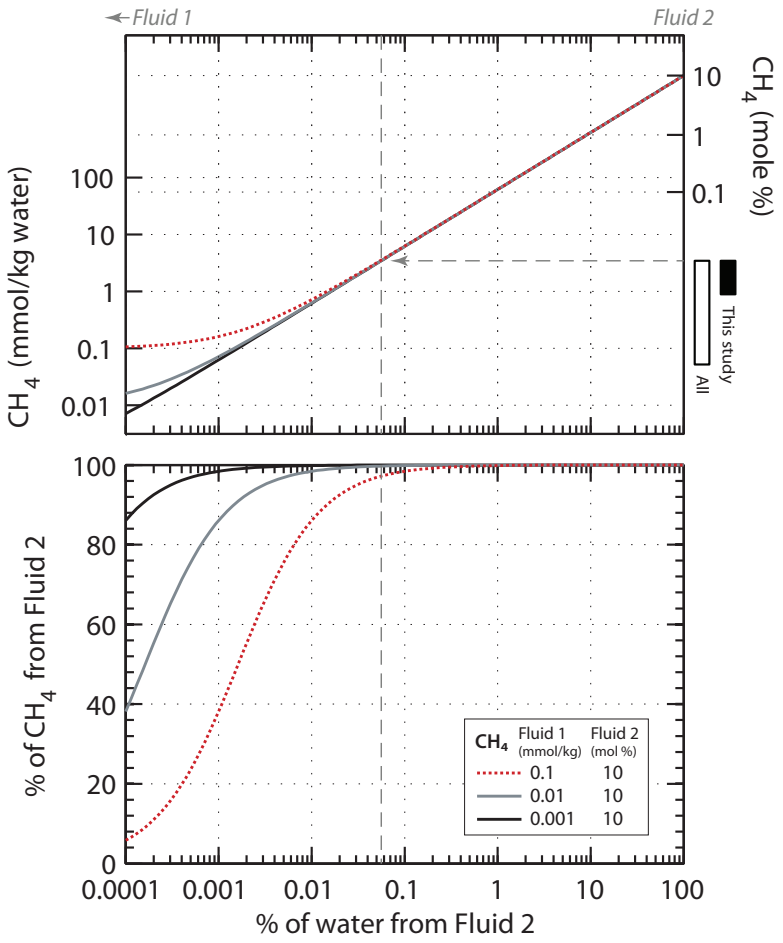

Figure 3.6 | Composition of fluids formed by mixing of a CH_4-poor actively-circulating seawater-derived hydrothermal fluid (*Fluid 1*) with a CH_4-rich fluid such as those observed in inclusions in plutonic rocks on the Southwest Indian Ridge and on the Mid-Atlantic Ridge (*Fluid 2*) (Kelley, 1996; Kelley, 1997; Kelley and Früh-Green, 1999). Mixing curves are plotted for CH_4 concentrations in the *Fluid 1* endmember ranging from 1 to 100 μmol/kg. Calculations assume that molalities of species other than CH_4 have a negligible effect on mole fractions in the high-CH_4 fluid. The black and white bars show CH_4 concentrations in vent fluids from this study (Table 3.2) and from mid-ocean ridge hydrothermal systems globally (Keir, 2010).

fluids discharging at the Medea and Isabel vents is thermodynamically disfavored at *in situ* temperatures (270–292 °C; Table 3.2 and Fig. 3.3D). With increasing temperature, methane formation becomes even more unfavorable (Fig. 3.2A), and thus aqueous CO_2 reduction at the higher temperatures (possibly as high as 475 °C) the fluids have experienced here (Pester *et al.*, 2012) is also unsupported. Concentrations of CH_4 shows no relation to either $\sum CO_2$ or H_2 in the Lucky Strike fluids here (see discussion and Fig. 2 in Pester *et al.*, 2012). These data indicate that CH_4 did not form from reduction of $\sum CO_2$ during migration of magmatic CO_2 between degassing from the magma chamber at ~3000 mbsf (meters below seafloor) and venting at the seafloor. Taken together, this evidence suggests that CH_4 originates not within an actively-convecting hydrothermal fluid, but is produced elsewhere and entrained into the circulating fluid.

The magmatic volatiles from which CH_4 forms may be sourced from gabbroic rocks formed from cooling of volatile-bearing melts beneath mid-ocean ridges. Oxidized carbon (as CO_2) is generally considered to exhibit near-perfect incompatibility, such that during decompression melting, nearly all carbon originally in the suboceanic mantle partitions into the melt fraction, leaving very little behind in residual peridotite. Estimates of the amount of carbon in the mantle suffer from large uncertainties, but are typically in the range of 20 to 300 ppm carbon (Dasgupta and Hirschmann, 2010). Serpentinitized oceanic peridotites from several mid-ocean ridges contain up to 1500 ppm carbon, and are therefore a sink for carbon (Alt *et al.*, 2013). Carbon in these rocks is thought to exist mostly as condensed phases (Früh-Green *et al.*, 2004), consistent with more recent observational and theoretical considerations (Ménez *et al.*, 2012; Pasini *et al.*, 2013; Milesi

et al., 2016). In contrast, gabbros from the same areas contain less carbon (up to 300 ppm), primarily hosted in inclusions bearing CO_2, CH_4 and/or graphite (Früh-Green *et al.*, 1996; Kelley and Früh-Green, 1999; Kelley and Früh-Green, 2001). These petrological constraints suggest that magmatic volatiles entrapped in gabbros, but probably not fresh peridotites, are a potential source for carbon in CH_4 at oceanic spreading centers. Additionally, migration of magmatic volatiles out of melts directly into layers of gabbro or peridotite may also enable carbon to come in contact with reducing conditions conducive to methane synthesis.

The occurrence and composition of methane-rich aqueous fluids within the sub-oceanic ridge lithosphere is recorded by secondary fluid inclusions hosted in plutonic rocks. Kelley (1996), Kelley (1997), and Kelley and Früh-Green (1999) documented several types of abundant volatile-rich inclusions in gabbros recovered from the slow-spreading Southwest Indian and Mid-Atlantic Ridges by several Ocean Drilling Program (ODP) expeditions. A common type of inclusion occurring along healed microcracks in plagioclase grains contained up to 47% CH_4 (with balance of H_2O). Temperatures indicated by CO_2–CH_4 carbon isotope geothermometry (300–600 °C) and homogenization temperatures of the Southwest Indian Ridge fluid inclusions (350–370 °C, corresponding to entrapment at *in situ* temperatures of ca. 400 °C) (Kelley and Früh-Green, 1999) agree with clumped isotopologue temperatures, and are compatible with formation of CH_4 during re-speciation of occluded magmatic volatiles as the host gabbros cooled to below 400 °C (Fig. 3.2A). While $\delta^{13}C$ values of CH_4 measured in fluid inclusions are somewhat lower (−34 to −20‰; Kelley and Früh-Green, 1999) than observed values in vent fluids (−18 to −9‰; Table 3.3), carbon isotopic data for inclusions may be affected by potential background sources either endogenous to the crushed mineral separates, introduced during sample handling, or formed during the stepped heating experiments. These background sources of carbon typically have relatively low $\delta^{13}C$ values of −25 to −30‰ (Des Marais, 1986; Miller and Pillinger, 1997).

Graphite is stable under conditions characterizing many hydrothermal settings (Luque *et al.*, 2009; Rumble, 2014). At isotopic equilibrium, graphite is ~10‰ enriched in ^{13}C relative to CH_4 at temperatures of 300 to 400 °C (Bottinga, 1969). It is worth noting that in all mid-ocean ridge hydrothermal fluids, $\delta^{13}C$ values of CH_4 are lower than mantle-derived CO_2 (−5‰, Fig. 3.1A). Relatively uniform $\delta^{13}C$ values (−19‰ to −9‰) are observed in vent fluids with high (millimolar) CH_4 contents (McCollom and Seewald, 2007; Keir, 2010). Furthermore, $CH_4/^3He$ ratios in vent fluids (see Keir, 2010) indicate less-than-quantitative conversion (~0.2% to 50%) of mantle carbon to CH_4 ($C/^3He \sim 1\times10^9$, Marty and Tolstikhin, 1998). Precipitation of graphite from a CH_4-rich fluid entrapped in plutonic rocks may explain both the missing carbon (McDermott *et al.*, 2015) and the observed $\delta^{13}C$ values (Luque *et al.*, 2012).

Fig. 3.7 shows predictions from a thermodynamic model of an ideal graphite-saturated C–O–H vapor with oxygen fugacity given by the fayalite-magnetite-quartz (FMQ) mineral buffer assemblage and a total pressure of 1 kbar. Calculations show that precipitation of graphite concomitant with methane formation is favored at ca. 400 °C and under water-poor conditions, consistent with many previous investigations (French, 1966; Eugster and Skippen, 1967; Ohmoto and Kerrick, 1977; Holloway, 1984; Früh-Green *et al.*, 2004). Predicted C_1/C_2 ratios are also consistent with measured values in vent fluids (McDermott, 2015, and Fig. 3.7). Propane (C_3) is in excess by two orders of magnitude compared with thermodynamic equilibrium at ~300 °C (McDermott, 2015, and Fig. 3.7). To explain the relative proportions of ethane and propane (and butanes) at this temperature requires both a high CH_4 fugacity and (paradoxically) a low H_2 fugacity of several log units below (more oxidized than) FMQ. Generation of small amounts of C_{2+} hydrocarbons (~1 μM or less) from the thermal breakdown of dissolved organic matter carried in recharging seawater (~40 μM) may account for the excess propane and butanes relative to ethane and methane. Alternatively, the C_{2+} hydrocarbons may not have equilibrated at a uniform temperature (McDermott, 2015), or may be formed via low-yield, kinetically-throttled reactions occurring in circulating fluids (Foustoukos and Seyfried, 2004). Regardless of their specific origins, similarities in the abundances and isotopic compositions of low

molecular weight hydrocarbons in vent fluids at Von Damm and other hot-spring systems at slow-spreading ridges suggest that they may share common origins.

Concentrations of CH_4 in the gabbro-hosted inclusions from the Southwest Indian Ridge and from other slow-spreading areas can be several orders of magnitude greater than those observed in corresponding vent fluids (Kelley, 1996; Kelley, 1997). Mass-balance considerations suggest that extraction of CH_4-rich fluids occluded in gabbros can explain CH_4 concentrations at all known sediment-free mid-ocean ridge hydrothermal fields. Mixing curves plotted in Fig. 3.6 show that addition of less than 0.1% of a CH_4–H_2O fluid of similar composition to those indicated by the inclusions (*Fluid 2* in the figure) to a CH_4-poor circulating hydrothermal fluid (*Fluid 1*) is sufficient to match even the highest CH_4 concentrations seen in vent fluids. Assuming carbon contents ranging from 30 to 300 ppm in the gabbro (Kelley and Früh-Green, 1999), water-to-rock ratios between 0.8 and 8 are required to explain CH_4 concentrations of up to 3 mmol/kg in vent fluids assuming all carbon in gabbro existed as leachable CH_4. Lower water-to-rock ratios are necessary if conversion efficiency is less than 100% (e.g., due to graphite precipitation) or if lower initial carbon contents are assumed. Constraints from mobile inorganic elements (e.g., Li, Rb, Sr) generally indicate that water/rock ratios are substantially lower than ~10 in many mid-ocean ridge hydrothermal systems (Von Damm *et al.*, 1985; Berndt *et al.*, 1989) with values of 0.4 to 6 calculated for the subsurface at Von Damm (McDermott, 2015) and 2 to 4 at Lost City (Foustoukos *et al.*, 2008) for example.

While only slow-spreading environments were investigated in this study, we hypothesize that the same origin of methane applies at sites on the fast-spreading East Pacific Rise, particularly given the similar $\delta^{13}C$ values of methane there (Welhan and Craig, 1983). The fact that these hydrothermal fluids contain low C_{2+} along with low CH_4 concentrations (Welhan, 1988b; Keir, 2010) suggests a genetic link between CH_4 and the C_{2+} hydrocarbons. Differences in axial structure and tectonism may account for the difference in hydrocarbon content of vent fluids at fast- and slow-spreading ridges. At magma-poor slow-spreading ridges, extension is accommodated primarily by detachment faulting, as opposed to magmatic emplacement of new crust that characterizes fast-spreading ridges (Buck *et al.*, 2005; Dunn, 2007). Low-angle, large-offset, and long-lived (>1 Myr) normal faults near vent fields at slow-spreading ridges allow for fluid penetration deep into plutonic rocks of layer 3, enabling access to fresh gabbroic material and/or inclusions to be leached (Kelley, 1996; Schroeder *et al.*, 2002; Schlindwein and Schmid, 2016). In contrast, in fast spreading environments such as the East Pacific Rise, shallow melt lenses at 1 to 2 km below seafloor may limit the depth of circulation (e.g., Hasenclever *et al.*, 2014; and references in Alt, 1995).

3.5 CONCLUSIONS

Methane clumped isotopologue data obtained for fluids venting from diverse unsedimented mid-ocean ridge hydrothermal systems uniformly indicate temperatures of last equilibration of ca. 300 °C. Taken in combination with geochemical and geologic observations and reaction rates determined in experiments, the $\Delta^{13}CH_3D$ data provide evidence that abiotic reduction of $\sum CO_2$ at low temperatures (<200 °C) is not a significant source of methane over timescales characterizing convective hydrothermal circulation at oceanic spreading centers. Furthermore, consideration of volatile contents and C–O–H speciation in melt-derived plutonic rocks and residual peridotites suggests that temperature, pressure, f_{O_2}, and f_{H_2O} conditions conducive to methane synthesis may be widespread in the oceanic crust.

Two hypotheses were considered for explaining the origin of CH_4 in hydrothermal fluids: (*i*) aqueous synthesis of CH_4 during active circulation and (*ii*) extraction of CH_4-rich fluids occluded in plutonic rocks. While both are conceivably compatible with the methane isotopologue data when taken in isolation, clumped isotopologue temperatures indicate that formation of CH_4 from $\sum CO_2$ at Lost City does not occur at temperatures <200 °C in the upflow. Furthermore, the former scenario is not compatible with thermodynamic, radioisotopic, and mass balance constraints at several sites. These lines of evidence lead

us to favor the latter hypothesis, which invokes a more straightforward scenario wherein vent fluids with millimolar quantities of CH_4 represent mixtures of a minute amount of a CH_4-rich fluid (of hypogene origin) with a large volume of an actively-circulating, CH_4-poor fluid. Proportions of mixing may be determined by the relative access that circulating fluids have to magmatic volatile-bearing rocks of the plutonic foundation. This could also explain apparent relationships of CH_4 concentration in vent fluids to tectonic setting and host rock lithology. Efforts to distinguish between the CH_4 contributed via these pathways will benefit from rigorous interrogation of factors governing fluid flow and chemical kinetics in hydrothermally-influenced settings.

The new data also provide constraints on the closure temperature of hydrogen exchange between methane and water. The observation of sluggish or indiscernible exchange of H among methane isotopologues below ca. 270 °C on timescales of ~10^2 years is relevant not only to the application of clumped isotope measurements as a novel geothermometer, but also provides information about the stability of the C–H bond in hydrocarbons in nature. Given the increasing appreciation of hydrocarbon-water-mineral interactions in economically important settings (Seewald, 2003), insights of this nature may find utility in studies of the origin and composition of aqueous and organic fluids in the Earth's subsurface.

3.6 ACKNOWLEDGMENTS

We thank Frieder Klein, Wolfgang Bach, and Grant Garven for helpful discussions regarding the petrology and plumbing of hydrothermal systems. Grants from the National Science Foundation (NSF EAR-1250394 to S.O.), NASA Astrobiology Institute (NAI #024461), N. R. Braunsdorf and D. J. H. Smit of Shell PTI/EG and the Deep Carbon Observatory (to S.O.) supported this work. S.O. thanks the Kerr-McGee Professorship at MIT. This research was conducted with Government support under and awarded by U.S. Department of Defense, Office of Naval Research, National Defense Science and Engineering Graduate (NDSEG) Fellowship (to D.T.W.), 32 CFR 168a. D.T.W. was also supported via a Shell-MITEI fellowship.

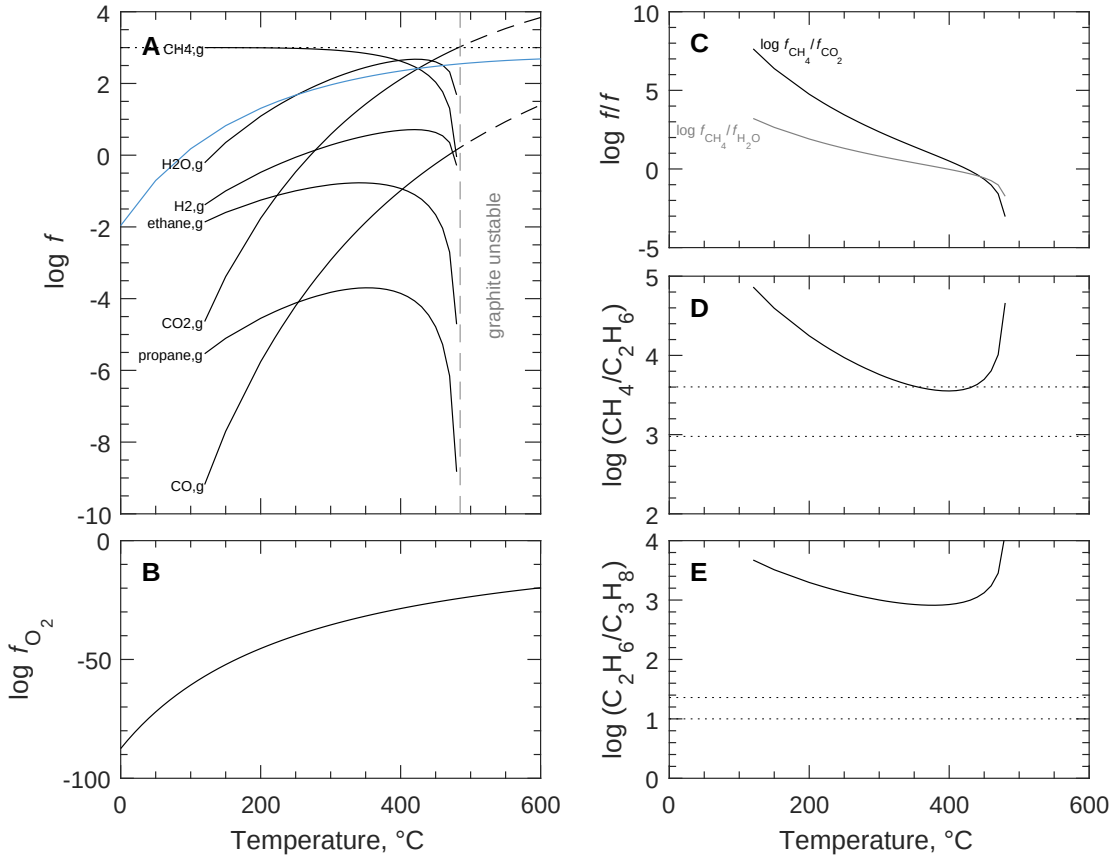

Figure 3.7 | Equilibrium composition of a graphite-saturated C–O–H fluid at 1000 bar (**A**) with oxygen fugacity (f_{O_2}) given by the fayalite-magnetite-quartz (FMQ) redox buffer (**B**). The modeled fluid is an ideal gas consisting of CO, CO_2, H_2, H_2O, O_2, ethane, and propane. The model is essentially that of French (1966), with the addition of C_{2+} compounds (as also considered by Kawagucci *et al.* (2013) and McDermott (2015), with different assumptions regarding redox, water activity, and total mass of carbon). To calculate the composition of the fluid, equilibrium constants were computed at various temperatures using CHNOSZ (Dick, 2008) from tabulated standard molal thermodynamic properties and equation of state parameters (Kelley, 1960; Helgeson *et al.*, 1978; Wagman *et al.*, 1982; Johnson *et al.*, 1992; Shock, 1993; Helgeson *et al.*, 1998), the fugacities of CO and CO_2 were calculated, and then the fugacities of all other gaseous species were solved iteratively under the constraint that $\sum f = 1000$ bar (a pressure typical of those indicated by fluid inclusion studies; Vanko, 1988). Graphite is unstable above ~500 °C, as shown by the equilibrium fugacities of $CO+CO_2$ exceeding the pressure of the system (dashed lines in A). Ratios of fugacities of selected species show that CH_4 is the dominant gas-phase species below ~400 °C (**C**), and that predicted ratios of C_1/C_2 and C_2/C_3 are ~10^3 to 10^4 between 200 and 400 °C (**D**, **E**). Dotted lines in (D) and (E) mark the range of C_1/C_2 and C_2/C_3 measured in hydrothermal fluids from the four vent fields we studied (Charlou *et al.*, 2000; Charlou *et al.*, 2002; Proskurowski *et al.*, 2008; McDermott *et al.*, 2015). The vapor pressure curve of water at 1000 bar is shown in blue in (A). Values of $\log f_{H_2O}$ that plot above this curve are inaccessible because the presence of liquid water sets the fugacity of H_2O and causes the fugacities of O_2 and all other species to adjust accordingly. Therefore, values of $\log (f_{CH_4}/f_{H_2O}) > 0$ do not necessarily indicate that total CH_4 content exceeds total water content when multiple fluid phases coexist. Liquid water has been neglected in our model, but calculations in which $H_2O(l)$ is explicitly considered show that graphite, an H_2O-dominated liquid, and a CH_4-rich gas phase can coexist at ~400 °C and f_{O_2} close to FMQ (Holloway, 1984).

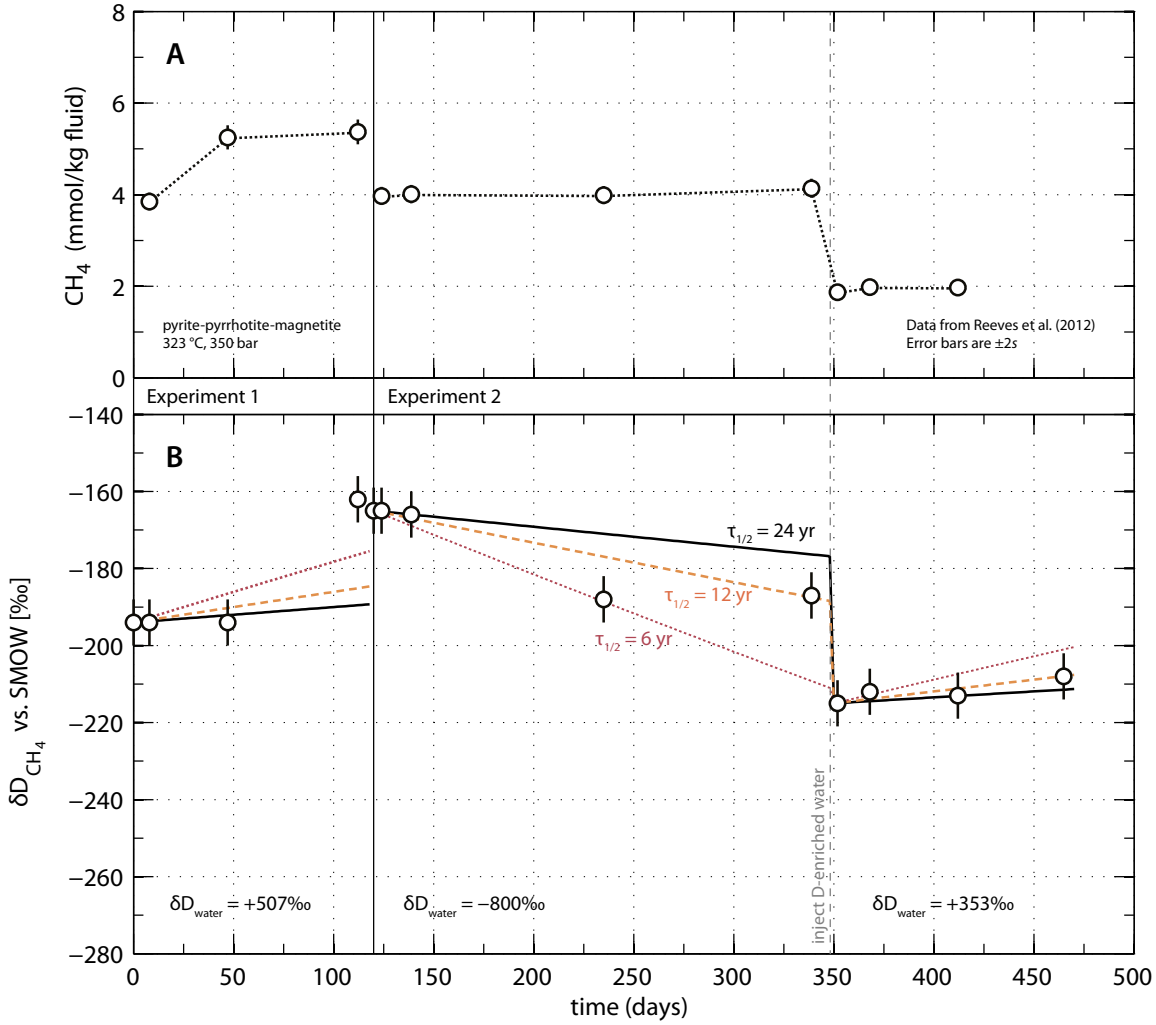

Figure 3.8 | Experimental constraints on hydrogen exchange between $CH_4(aq)$ and $H_2O(l)$ from two experiments conducted by Reeves *et al.* (2012) in a flexible cell hydrothermal apparatus at 323 °C and 350 bar. Concentrations of CH_4 (**A**) remain indistinguishable within analytical error (±5%, 2*s*) in Experiment 2, but not in Experiment 1, perhaps due to calibration or operator error as noted by those authors. Measured pH was ~4.2, and concentrations of H_2 and $\sum H_2S$ were 0.26–0.7 mmol/kg fluid and ~11 mmol/kg fluid, respectively, consistent with predictions for a Fe–S–O–H fluid buffered by PPM at experimental conditions (Reeves *et al.*, 2012). Panel (**B**) shows measurements of D/H of CH_4 compared against modeled kinetics for D/H exchange with varying half-exchange time ($\tau_{1/2} = \ln(2)/k$). The modeled kinetics assume that CH_4 concentration is constant, the rate of isotopic exchange is first order in CH_4, and the equilibrium D/H fractionation factor [$\varepsilon = (D/H)_{methane}/(D/H)_{water} - 1$] is −130‰ (see Fig. 3.5). We take $\tau_{1/2}$ = 24 yr (black curve) as a best-guess estimate of the rate of true isotopic exchange; this value is shown in Fig. 3.4.

Table 3.3 | Compilation of hydrogen isotope ratios of CH_4 and H_2 and associated data on vent fluids from sediment-poor hydrothermal systems.

Field	Vent	T_{max} (°C)[b]	Mg (mM)	$\sum CO_2$ (mm)	H_2 (mM)	CH_4 (mM)	$\delta^{13}C$ (‰)		δD (‰)			Notes
							$\sum CO_2$	CH_4	CH_4	H_2	H_2O[d]	
Mid-Atlantic Ridge												
Rainbow	Guillaume (X4)	361	0*	24.3	16.5	2.13	—	−17.6	−98	—	—	(1, 2)
	CMSP&P	365	0*	21.9	15.9	2.05	—	−17.5	−98	—	—	(1, 2)
	Auberge (X3)	370	0*	22.8	15.7	2.16	—	−17.4	−98	—	—	(1, 2)
	—	365	0*	16	16	2.5	−3.2[e]	−17.7	−105	−356	—	(3)
	—	360	0*	17	13	1.6	−2.5[e]	−17.8	−107	−379	—	(3)
Lost City	Beehive	94	0*	0.18	10.4	1.08	—	−10.9	−127	—	—	(1, 2)
		90	0*	—	—	—	—	—	−127	−609	+2 to 7	(4)
		90	0*	—	—	—	—	—	−126	−609	+2 to 7	(4)
	Marker 6	67	0*	—	—	—	—	—	−108	−605	+2 to 7	(4) †
		62	0*	—	—	—	—	—	−129	−616	+2 to 7	(4) †
	IMAX (IF)	55	—	—	—	—	—	—	−129	−649	+2 to 7	(4)
		55	—	—	—	—	—	—	−139	−646	+2 to 7	(4)
		55	—	—	—	—	—	—	−136	−648	+2 to 7	(4)
	Marker 7	28	—	—	—	—	—	—	−129	−663	+2 to 7	(4)
		28	—	—	—	—	—	—	−125	−666	+2 to 7	(4)
	Marker 8	43	—	—	—	—	—	—	−141	−658	+2 to 7	(4)
		43	—	—	—	—	—	—	−136	−651	+2 to 7	(4)
	Marker C	62	—	—	—	—	—	—	−126	−620	+2 to 7	(4)
		70	—	—	—	—	—	—	−130	−614	+2 to 7	(4)
	Marker H	60	—	—	—	—	—	—	−99	−657	+2 to 7	(4)
		60	—	—	—	—	—	—	−104	−689	+2 to 7	(4)
	Marker 3	61	—	—	—	—	—	—	−112	−610	+2 to 7	(4)
		71	—	—	—	—	—	—	−103	−605	+2 to 7	(4)
		73	—	—	—	—	—	—	−125	−609	+2 to 7	(4)
	—	93	0*	—	—	—	—	−11.9	−130	−618	—	(3)
Broken Spur	—	353	0*	—	—	—	—	—	—	−393	—	(4)

Continued on next page

Table 3.3 | Compilation of hydrogen isotope ratios of CH_4 and H_2 and associated data (*continued*).

Field	Vent	T_{max} (°C)[b]	Mg (mM)	$\sum CO_2$ (mm)	H_2 (mM)	CH_4 (mM)	$\delta^{13}C$ (‰)		δD (‰)			Notes
							$\sum CO_2$	CH_4	CH_4	H_2	H_2O[d]	
Logatchev (1?)	—	350	0*	—	—	—	—	—	−109	−372	—	(4)
Logatchev 1	—	346	0*	3.6	9	2.0	+4.1[e]	−10.2	−104	−350	—	(3)
	—	352	0*	4.4	13	2.6	+7.4[e]	−10.3	−104	−360	—	(3)
Logatchev 2	—	320	0*	6.2	11	1.2	+9.5[e]	−6.1	−93	−231	—	(3) ‡
Ashadze 1	—	353	0*	3.7	8	0.5	+2.1[e]	−12.3	−104	−333	—	(3)
	—	353	0*	—	19	1.2	+4.6[e]	−14.1	−101	−343	—	(3)
Ashadze 2	—	296	0*	—	26	0.8	+0.2[e]	−8.7	−107	−270	—	(3) ‡
Lucky Strike	Medea	270	0*	98	0.063	0.89	—	−14.2	−99	—	—	(1, 2)
	Isabel	292	0*	112	0.034	0.86	—	−12.6	−100	—	—	(1, 2)
East Pacific Rise												
9° N	—	380	0*	—	—	—	—	—	—	−328	—	(4)
21° N	Nat. Geo. Soc.	350	0*	—	30.5	1.4	−7.0	−15.0	−102	−401	+0.5	(5, 6)
Central Indian Ridge												
Kairei	Kali	362	0*	8.0	3.3	0.12	−5.3	−9.8	—	−368	—	(7, 8)
		316	8.4	12.1	3.6	—	—	—	—	−328	—	(7, 8)
	Monju	299	5.2	7.9	2.1	—	—	—	—	−385	—	(7, 8)
		42	50.9	9.3	8×10^{-4}	—	—	—	—	−431	—	(7, 8)
		87	43.7	6.0	0.69	—	—	—	—	−361	—	(7, 8) §
		22	48.3	12.6	0.13	—	—	—	—	−493	—	(7, 8) §
	Fugen	305	4.5	9.5	2.7	—	—	—	—	−391	—	(7, 8)
	Daikoku	306	0*	—	2.2	—	—	—	—	−340	—	(7)
	—	350	0*	—	—	—	—	—	—	−400	—	(4)
Edmond	Nura Nura	375	0*	12.8	0.11	0.31	−5.5	−13.5	—	−362	—	(7, 8)
	Marker 27	325	0*	12.3	0.10	—	—	—	—	−377	—	(7, 8)
	White Head	263	12.4	8.1	0.04	—	—	—	—	−412	—	(7, 8)

Continued on next page

Table 3.3 | Compilation of hydrogen isotope ratios of CH_4 and H_2 and associated data (*continued*).

Field	Vent	T_{max} (°C)[b]	Mg (mM)	$\sum CO_2$ (mm)	H_2 (mM)	CH_4 (mM)	$\delta^{13}C$ (‰)		δD (‰)			Notes
							$\sum CO_2$	CH_4	CH_4	H_2	H_2O[d]	
	Gr. Shrimp V.	281	13.4	12.1	0.48	—	—	—	—	−681	—	(7, 8) ¶
	Marker 24	116	40.6	8.7	0.07	—	—	—	—	−476	—	(7, 8)
Mid-Cayman Rise												
Von Damm	Old Man Tree	115	14.0	1.80	10.5	1.97	—	−16.2	−107	—	—	(1, 9)
	Ravelin 1	145	15.0	2.52	13.4	2.02	—	−16.4	−107	—	—	(1, 9)
	East Summit	226	0*	2.80	18.2	2.81	—	−16.4	−107	—	—	(1, 9)

Abbreviations: mm, mmol/kg fluid; mM, mmol/L fluid.

Data sources: (1) this study; (2) Reeves *et al.* (2014); (3) Charlou *et al.* (2010); (4) Proskurowski *et al.* (2006); (5) Welhan and Craig (1983); (6) Horibe and Craig (1995); (7) Kawagucci *et al.* (2010); (8) Kumagai *et al.* (2008); (9) McDermott *et al.* (2015).

Notes: † cf. T_{max} 96 °C in ref. 2; ‡ phase-separated; § snail colony; ¶ shrimp colony

[a] Dash (—) indicates that data were not reported or that samples were unable to be matched across multiple references.

[b] Maximum measured vent temperature.

[c] Asterisk (*) indicates near-endmember fluid sample (represented by stars in Fig. 3.5). For these samples, concentrations of $\sum CO_2$, H_2, and CH_4 and $\delta^{13}C$ values of $\sum CO_2$ have been extrapolated to endmember fluid composition (regressed to zero Mg content) assuming entrainment of seawater containing ~53 mM Mg.

[d] Endmember vent fluids typically have δD values of H_2O between −2 and +4‰ (Shanks *et al.*, 1995). A value of 0‰ was assumed when no data could be found (see text and Fig. 3.5).

[e] Values are as reported; it is not known whether correction for $\sum CO_2$ in seawater was applied.

Chapter 4

Fractionation of the methane isotopologues $^{13}CH_4$, $^{12}CH_3D$, and $^{13}CH_3D$ during aerobic oxidation of methane by Methylococcus capsulatus *(Bath)*

ABSTRACT

Aerobic oxidation of methane plays a major role in reducing the amount of methane emitted to the atmosphere from freshwater and marine settings. We cultured an aerobic methanotroph, *Methylococcus capsulatus* (Bath) at 30 and 37 °C, and determined the relative abundance of $^{12}CH_4$, $^{13}CH_4$, $^{12}CH_3D$, and $^{13}CH_3D$ (a doubly-substituted, or "clumped" isotopologue of methane) to characterize the clumped isotopologue effect associated with aerobic methane oxidation. In batch culture, the residual methane became enriched in ^{13}C and D relative to starting methane, with D/H fractionation a factor of 9.14 ($^{D}\varepsilon/^{13}\varepsilon$) larger than that of $^{13}C/^{12}C$. As oxidation progressed, the $\Delta^{13}CH_3D$ value (a measure of the excess in abundance of $^{13}CH_3D$ relative to a random distribution of isotopes among isotopologues) of residual methane decreased. The isotopologue fractionation factor for $^{13}CH_3D/^{12}CH_4$ was found to closely approximate the product of the measured fractionation factors for $^{13}CH_4/^{12}CH_4$ and $^{12}CH_3D/^{12}CH_4$ (i.e., $^{13}C/^{12}C$ and D/H). The results give insight into enzymatic reversibility in the aerobic methane oxidation pathway. Based on the experimental data, a mathematical model was developed to predict isotopologue signatures expected for methane in the environment that has been partially-oxidized by aerobic methanotrophy. Measurement of methane clumped isotopologue abundances can be used to distinguish between aerobic methane oxidation and alternative methane-cycling processes.

A version of this chapter has been published as:

Wang, D. T.; Welander, P. V. & Ono, S. (2016) Fractionation of the methane isotopologues $^{13}CH_4$, $^{12}CH_3D$, and $^{13}CH_3D$ during aerobic oxidation of methane by *Methylococcus capsulatus* (Bath). *Geochim. Cosmochim. Acta*, **192**, 186–202. doi:10.1016/j.gca.2016.07.031

4.1 INTRODUCTION

Methane is an important long lived (well-mixed) greenhouse gas whose atmospheric concentration has more than doubled (~720 ppb to >1800 ppb) since pre-industrial time (Wahlen, 1993; IPCC, 2013). Important sources of atmospheric methane include natural wetlands (up to one-third of emissions), agriculture (including paddy rice fields and ruminant animals), and fossil fuel usage (Bousquet *et al.*, 2006; Dlugokencky *et al.*, 2011). Methanogenic archaea are responsible for the majority of emissions, with thermogenic sources accounting for most of the remainder. The primary methane sink in the atmosphere is reaction with tropospheric hydroxyl radicals (OH). Despite rigorous bottom-up accounting and top-down estimates based on remote sensing data and high-frequency measurements, the flux of methane from sources and to sinks remains poorly constrained (e.g., Kirschke *et al.*, 2013).

Emissions from natural and human-made wetlands and other aquatic environments account for nearly two-thirds of all methane sources, though substantial uncertainty is associated with source strength estimates (Kirschke *et al.*, 2013). Methanotrophic processes consume over half of the methane produced in aquatic environments prior to emission into the atmosphere (Reeburgh, 2007). It is estimated that a large fraction of methane produced in freshwater sediments, as much as 90% at some sites (Oremland and Culbertson, 1992), is removed via the aerobic oxidation of methane. In addition, soil-dwelling aerobic methanotrophs are responsible for oxidation of a small fraction (~2%) of methane from the atmosphere (Kirschke *et al.*, 2013). Furthermore, activity of methanotrophic bacteria with high affinity for atmospheric methane in Arctic soils has been reported (Lau *et al.*, 2015). Thus, understanding the magnitude and dynamics of methanotrophic sinks is important for global methane cycle budgets and constraining inputs to climate simulations.

The bacterium *Methylococcus capsulatus* (Bath), an obligate aerobic methanotroph, is a model organism for studies of the genetics, physiology, and geomicrobiology of aerobic methane oxidation in sediments and water columns (Whittenbury *et al.*, 1970; Bowman, 2014). This organism uses the enzymes soluble methane monooxygenase (sMMO) and particulate methane monooxygenase (pMMO) to oxidize methane to methanol, which is further oxidized to CO_2 as an end product (Hanson and Hanson, 1996). Carbon derived from methane can also be assimilated into cellular biomass. The overall reaction is thus described by the stoichiometry:

$$CH_4 + 2O_2 \longrightarrow b\,C_{cell} + (1-b)\,CO_2 + 2H_2O \tag{4.1}$$

where C_{cell} represents cellular carbon and b is the fraction of carbon assimilated into biomass.

In experiments with pure and enrichment cultures, microbes utilizing this pathway have been shown to generate large and correlated carbon ($^{13}C/^{12}C$) and hydrogen (D/H) isotope fractionations during aerobic methane oxidation (Coleman *et al.*, 1981; Kinnaman *et al.*, 2007; Powelson *et al.*, 2007; Feisthauer *et al.*, 2011). Measurements of $^{13}C/^{12}C$ and D/H ratios in environmental methane samples can be used to assess whether they have experienced partial oxidation (Hornibrook *et al.*, 1997; Chanton *et al.*, 2005).

Recently, methods were developed to determine the abundance of multiply-substituted "clumped" isotopologues (e.g., $^{13}CH_3D$) in methane samples to sub-permille precision (Ono *et al.*, 2014; Stolper *et al.*, 2014b; Young *et al.*, 2016). Measurements of the abundance of multiply-substituted isotopologues are of geochemical interest because of their potential for use as an isotopic geothermometer that can be accessed via analyses of a single compound (Wang *et al.*, 2004; Eiler, 2007). Furthermore, clumped isotopologue data provide another dimension for probing kinetic and equilibrium isotope effects and for constraining isotope exchange processes in natural settings (e.g., Eiler and Schauble, 2004; Yeung *et al.*, 2012; Yeung, 2016). For example, the isotope exchange reaction

$$^{13}CH_4 + {}^{12}CH_3D \rightleftharpoons {}^{13}CH_3D + {}^{12}CH_4 \tag{4.2}$$

has an equilibrium constant K that varies between ~1.007 at 0 °C to 1.000 at temperatures approaching infinity (at which isotopes are randomly distributed amongst all possible isotopologues, i.e., the stochastic

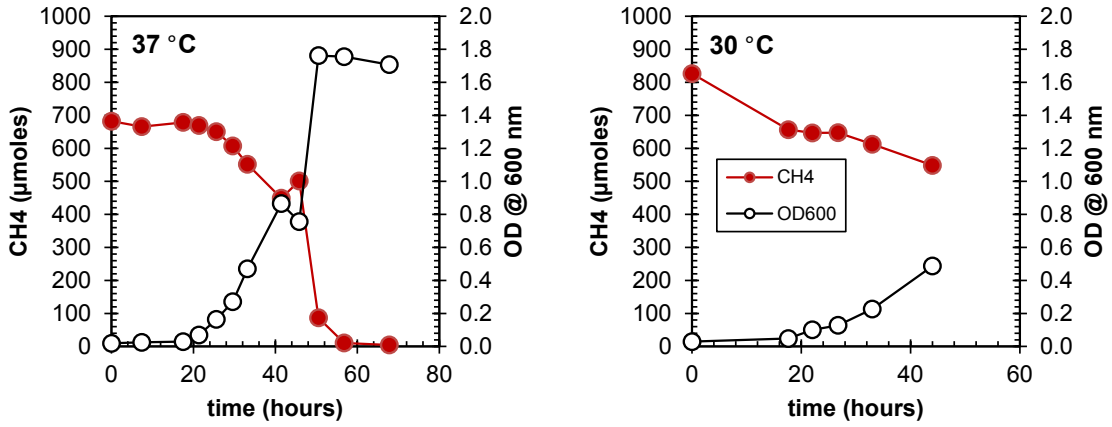

Figure 4.1 | Measured CH_4 concentrations and optical densities (OD) during preliminary experiments at 37 °C (left) and 30 °C (right) with starter cultures of *M. capsulatus* (Bath).

distribution) (see Wang *et al.*, 2015, and references therein for details regarding calculations from which K is obtained).

Subsequent surveys of methane in the environment revealed that in methane of microbial origin produced in both natural settings and pure cultures, the reaction quotient (Q, see also § 4.2.2) of Reaction 4.2 varies between 0.997 and 1.007 (Stolper *et al.*, 2014a; Inagaki *et al.*, 2015; Stolper *et al.*, 2015; Wang *et al.*, 2015; Douglas *et al.*, 2016), a range that is much larger than that expected for thermodynamic equilibrium (ca. 1.004 to 1.007) at temperatures at which microbial life is possible (~0 to 120 °C; Takai *et al.*, 2008) (Wang *et al.*, 2015). The nonequilibrium isotope signatures were attributed to intrinsic clumped isotopologue effects expressed during biological methanogenesis under conditions of low reversibility (Stolper *et al.*, 2015; Wang *et al.*, 2015). Using inferences based on $\delta^{13}C$ and δD data, methane oxidation was excluded as a significant origin of the nonequilibrium isotope signals (Wang *et al.*, 2015). However, experimental constraints on the fractionation of $^{13}CH_3D$ during biological methane oxidation are lacking in the clumped isotope literature.

In this paper, we report experimental measurements of the fractionation of $^{13}CH_3D$ during aerobic methane oxidation by cultures of the bacterium *Methylococcus capsulatus* (Bath). It is demonstrated that aerobic methanotrophy affects the abundance of $^{13}CH_3D$ in a predictable fashion relative to $\delta^{13}C$ and δD; the directionality and magnitude of these effects depend on whether oxidation occurs in a closed or open system. We present simple models to illustrate the expected shifts in $^{13}CH_3D$ abundance under different scenarios, and review available environmental clumped isotopologue data in light of the new experimental constraints.

4.2 METHODS

4.2.1 Cultures

Methylococcus capsulatus strain Bath cultures were grown in 10 ml of nitrate mineral salts medium supplemented with 5 µM $CuSO_4$ (Welander and Summons, 2012). Serum bottles (160 cm^3) were inoculated with 2%(v/v) inoculum from a starter culture that had grown for ca. 30 hours, stoppered and sealed without removing ambient air, and injected with 20 cm^3 SATP (~810 µmol) of methane from commercially-sourced cylinders using a gas-tight syringe. Tests indicated that the starting gas compositions were consistent within analytical error (±5%) between serum bottles. Multiple serum bottles were inoculated for each of the two experimental temperatures (Table 4.1). Cultures were incubated at 30 or 37 °C while shaking at 225 rpm

and sacrificed at given times by adding 1 ml of 1 M hydrochloric acid. Each row in Table 4.1 shows the composition of one serum bottle at the time at which the experiment was stopped. Experimental timepoints were selected based on monitoring of growth during preliminary incubations of starter cultures (by tracking optical density, see Fig. 4.1). However, to minimize puncturing of the serum bottles during the isotopic fractionation experiments, optical densities were not measured for the samples analyzed for isotopologues shown in Table 4.1. The combination of constant agitation, a large headspace volume relative to liquid volume, and high initial CH_4 partial pressures (>0.1 atm) ensures that diffusion into the liquid from the headspace does not limit the rate of methane consumption (Templeton *et al.*, 2006; Nihous, 2008).

4.2.2 Analytical techniques

Concentrations of headspace gases, including CH_4 and CO_2, were determined via gas chromatography (GC) using a Shimadzu GC-2014 gas chromatograph configured with a packed column (Carboxen-1000, $5' \times 1/8''$, Supelco, Bellefonte, Pennsylvania, USA) held at 140 °C and argon carrier gas, and thermal conductivity and methanizer-flame ionization detectors. Subsamples of the headspace (0.20 cm^3 at laboratory temperature, ~23 °C) from each serum bottle were taken via a gas-tight syringe and injected onto the column. Gas concentrations were determined directly as partial pressures. Accuracy of the analyses, evaluated from standards, was ±5%. The fraction of initial methane remaining, f, in each batch culture was calculated from these measurements (Table 4.1), with uncertainties propagated following Ku (1969).

Samples of methane were purified via cryofocusing–preparative gas chromatography through a packed column (Carboxen-1000, $5' \times 1/8''$, Supelco) held at 30 °C with helium carrier gas, and cryotrapping of the eluted methane on activated charcoal at liquid nitrogen temperature (Wang *et al.*, 2015). The relative abundances of the methane stable isotopologues $^{12}CH_4$, $^{13}CH_4$, $^{12}CH_3D$, and $^{13}CH_3D$ were measured using a tunable infrared laser direct absorption spectroscopy technique described previously (Ono *et al.*, 2014; Wang *et al.*, 2015).

Isotope values are reported herein using standard delta-notation.[1] In accordance with IUPAC recommendations (Coplen, 2011), we have omitted the factor of 1000‰ from the definition of δ and other isotope values (including $\Delta^{13}CH_3D$, below). Carbon and hydrogen isotope values were calibrated against community reference materials NGS-1 and NGS-3 (Wang *et al.*, 2015).

The abundance of $^{13}CH_3D$ is tracked via the $\Delta^{13}CH_3D$ value, defined according to Ono *et al.* (2014) as:

$$\Delta^{13}CH_3D = \ln Q, \text{ where } Q = \frac{\left[^{13}CH_3D\right]\left[^{12}CH_4\right]}{\left[^{13}CH_4\right]\left[^{12}CH_3D\right]} \tag{4.3}$$

Here, Q is the reaction quotient for Reaction 4.2, and $\Delta^{13}CH_3D \approx Q - 1$ because Q is close to unity in the natural and experimental systems studied herein.[2] For a methane sample that has attained a distribution of isotopes among all isotopologues consistent with equilibrium at a given temperature, $Q = K$. The temperature dependence of the equilibrium $\Delta^{13}CH_3D$ value was theoretically estimated and experimentally calibrated previously (Wang *et al.*, 2015).

Methane samples with a wide range of δD values (−480‰ to +500‰ vs. SMOW) were prepared and thermally-equilibrated over platinum catalyst at 300 °C to correct for the nonlinearity in the spectroscopic analysis described by Ono *et al.* (2014).

[1] Definitions: $\delta^{13}C = (^{13}C/^{12}C)_{sample}/(^{13}C/^{12}C)_{PDB} - 1$, and $\delta D = (D/H)_{sample}/(D/H)_{SMOW} - 1$ [for natural samples of methane, $\delta^{13}C \approx (^{13}CH_4/^{12}CH_4)_{sample}/(^{13}CH_4/^{12}CH_4)_{PDB} - 1$ and $\delta D \approx ¼ (^{12}CH_3D/^{12}CH_4)_{sample}/(D/H)_{SMOW} - 1$].

[2] From the approximation $\ln(1 + x) \approx x$ for values of x close to zero.

4.2.3 Calculation of isotope and isotopologue fractionation factors

The MMO-catalyzed reaction between methane and O_2 to produce the intermediate product methanol is the first in a sequence of enzymatic reactions involved in aerobic methanotrophy (Sirajuddin and Rosenzweig, 2015). We focus on this reaction because it is the most important isotopically-fractionating step in this sequence as it is considered to be both rate-limiting and isotope-sensitive (Nesheim and Lipscomb, 1996) under the studied experimental conditions. Limitation of the rate of methane consumption by this step requires that methane diffusion into and out of the cells be rapid relative to MMO catalysis. Following Nihous (2010), we assume that isotopic fractionation associated with transfer of methane across cell membranes is negligible.

The reaction scheme for the first step of the aerobic oxidation of the methane isotopologues $^{12}CH_4$, $^{13}CH_4$, $^{12}CH_3D$, and $^{13}CH_3D$ can be described by the following six chemical reactions:

$$^{12}CH_4 \longrightarrow {}^{12}CH_3OH \tag{4.4}$$
$$^{13}CH_4 \longrightarrow {}^{13}CH_3OH \tag{4.5}$$
$$^{12}CH_3D \longrightarrow {}^{12}CH_3OH \tag{4.6}$$
$$^{12}CH_3D \longrightarrow {}^{12}CH_2DOH \tag{4.7}$$
$$^{13}CH_3D \longrightarrow {}^{13}CH_3OH \tag{4.8}$$
$$^{13}CH_3D \longrightarrow {}^{13}CH_2DOH \tag{4.9}$$

4.2.3.1 Carbon isotope fractionation

Assuming that the reaction is irreversible, follows first-order kinetics, and occurs in a closed system, the following differential equations can be written for $^{12}CH_4$ and $^{13}CH_4$:

$$\frac{d^{12}CH_4}{dt} = -k \cdot \left[^{12}CH_4\right] \tag{4.10}$$
$$\frac{d^{13}CH_4}{dt} = -{}^{13}\alpha \cdot k \cdot \left[^{13}CH_4\right] \tag{4.11}$$

where k is the rate constant for $^{12}CH_4$ consumption (Reaction 4.4), and $^{13}\alpha$ is the fractionation factor for $^{13}C/^{12}C$ (ratio of rate constants for Reactions 4.5 and 4.4).

Combining Eqns. 4.10 and 4.11, eliminating dt, and integrating from $f = 1$ (initial) to f yields the equation:

$$\ln\left(\frac{\left[^{13}CH_4\right]_f}{\left[^{13}CH_4\right]_{\text{init}}}\right) = {}^{13}\alpha \cdot \ln\left(\frac{\left[^{12}CH_4\right]_f}{\left[^{12}CH_4\right]_{\text{init}}}\right) \tag{4.12}$$

By subtracting $\ln\left(\left[^{12}CH_4\right]_f \Big/ \left[^{12}CH_4\right]_{\text{init}}\right)$ from each side of Eqn. 4.12, and applying the approximations $f \approx \left[^{12}CH_4\right]_f \Big/ \left[^{12}CH_4\right]_{\text{init}}$ and $[^{13}CH_4]/[^{12}CH_4] \approx [^{13}C]/[^{12}C]$, we obtain a form of the classic "Rayleigh equation" (Mariotti *et al.*, 1981):

$$\ln \frac{\delta^{13}C + 1}{\delta^{13}C_{\text{init}} + 1} = \left({}^{13}\alpha - 1\right) \ln f \tag{4.13}$$

4.2.3.2 Hydrogen isotope fractionation

For the D-substituted isotopologue $^{12}CH_3D$, there are two ways to break a carbon-hydrogen bond. These two pathways are described by Reactions 4.6 and 4.7. The former involves the breakage of the C–D bond

(accompanied by a primary isotope effect, described by the fractionation factor ${}^{D}\alpha_p$), while the latter involves the breakage of any of the three C–H bonds *adjacent* to the C–D bond (incurring a secondary isotope effect, ${}^{D}\alpha_s$). Thus, the overall rate of the oxidation of ${}^{12}CH_3D$ to methanol can be described by:

$$\frac{d^{12}CH_3D}{dt} = -\tfrac{1}{4} \cdot {}^{D}\alpha_p \cdot k \cdot \left[{}^{12}CH_3D\right] - \tfrac{3}{4} \cdot {}^{D}\alpha_s \cdot k \cdot \left[{}^{12}CH_3D\right] \tag{4.14}$$

By lumping together ${}^{D}\alpha_p$ and ${}^{D}\alpha_s$, the rate equation can be simplified to:

$$\frac{d^{12}CH_3D}{dt} = -{}^{D}\alpha \cdot k \cdot \left[{}^{12}CH_3D\right] \tag{4.15}$$

where ${}^{D}\alpha = \frac{1}{4}{}^{D}\alpha_p + \frac{3}{4}{}^{D}\alpha_s$.

This parameterization of D/H fractionation is attractive in that it allows for apparent overall isotopic fractionation factors to be constrained by cell culture experiments and measurement with conventional geochemical techniques (e.g., isotope ratio mass spectrometry), without measurement of the individual reaction products. Applying the same logic used in § 4.2.3.1, the following expression is obtained:

$$\ln \frac{\delta D + 1}{\delta D_{init} + 1} = \left({}^{D}\alpha - 1\right) \ln f \tag{4.16}$$

Combining Eqns. 4.13 and 4.16 yields an equation describing the correlation between carbon and hydrogen isotope fractionation:

$$\ln \frac{\delta D + 1}{\delta D_{init} + 1} = \left(\frac{{}^{D}\alpha - 1}{{}^{13}\alpha - 1}\right) \ln \frac{\delta^{13}C + 1}{\delta^{13}C_{init} + 1} \tag{4.17}$$

4.2.3.3 $^{13}CH_3D$ fractionation

The rate of oxidation of ${}^{13}CH_3D$ can be described by:

$$\frac{d^{13}CH_3D}{dt} = -\tfrac{1}{4} \cdot \gamma_p \cdot {}^{13}\alpha \cdot {}^{D}\alpha_p \cdot k \cdot \left[{}^{13}CH_3D\right] - \tfrac{3}{4} \cdot \gamma_s \cdot {}^{13}\alpha \cdot {}^{D}\alpha_s \cdot k \cdot \left[{}^{13}CH_3D\right] \tag{4.18}$$

Here, we have introduced the terms γ_p and γ_s to characterize deviations of the clumped isotopologue fractionation factor from the product of the ${}^{13}C/{}^{12}C$ and D/H fractionation factors (α values). When there is no deviation from this product (i.e., primary and secondary isotope fractionation factors for bond breakage in ${}^{13}CH_3D$ follow what is referred to hereafter as the "product rule"), both γ_p and γ_s are unity. Deviations from the product rule represent a "clumped isotopologue effect" on bond breakage that arises from the substitution of both ${}^{13}C$ and D in the substrate methane. To simplify the treatment of clumped isotopologue effects in the absence of literature data for γ_p and γ_s, we adopt the following form of the rate equation:

$$\frac{d^{13}CH_3D}{dt} = -\gamma \cdot {}^{13}\alpha \cdot {}^{D}\alpha \cdot k \cdot \left[{}^{13}CH_3D\right] \tag{4.19}$$

Here, the "gamma-factor" (γ) is an empirically-constrained term that describes an *effective* clumped isotopologue fractionation factor. Implicit in the use of Eqn. 4.19 is that $\gamma \cdot {}^{D}\alpha = \frac{1}{4} \cdot \gamma_p \cdot {}^{D}\alpha_p + \frac{3}{4} \cdot \gamma_s \cdot {}^{D}\alpha_s$ (from the definition of ${}^{D}\alpha$ in § 4.2.3.2; also see discussion in § 4.4.1.2). This condition is satisfied, although not uniquely, when γ is equal to both γ_p and γ_s.

Equation 4.19 is convenient because it allows for γ to be constrained by measurements of the methane isotopologues in experiments conducted at natural abundance without the use of isotopically labeled substrates or measurement of individual isotopically-substituted products. Integration of Eqn. 4.19 combined

with Eqn. 4.10, subtraction of the isotopologue-ratio forms of Eqns. 4.13 and Eqn. 4.16 from the result, and substitution of the definition of $\Delta^{13}CH_3D$ (Eqn. 4.3) yields:

$$\Delta^{13}CH_3D = \Delta^{13}CH_3D_{\text{initial}} + \left(\gamma \cdot {}^{13}\alpha \cdot {}^{D}\alpha - {}^{13}\alpha - {}^{D}\alpha + 1\right) \cdot \ln f \tag{4.20}$$

Adopting this greatly simplified treatment necessarily means that differences in primary and secondary isotope effects for different forms of the enzyme in different methanotroph species are masked and lumped into an "effective" fractionation factor. A similar line of reasoning was used by Stolper *et al.* (2015) to simplify the representation of a model methanogenic system.

4.3 RESULTS

During the course of the experiments at 30 and 37 °C, the concentration of methane in the headspace decreased and the concentration of CO_2 increased (Table 4.1). The bottles incubated at 37 °C exhibited a lag phase (observed in preliminary experiments with starter cultures, Fig. 4.1), with a rapid transition into active methane consumption around 41 hours after inoculation (Table 4.1), whereas in the 30 °C experiments, methane consumption began immediately after inoculation, but at an apparently lower rate. Based on mass balance of measured CO_2 and CH_4 concentrations relative to initial CH_4 (Table 4.1), ~7% to 41% of carbon was not accounted for; this fraction of carbon was likely incorporated into cellular biomass (b in Eqn. 4.1). This range of b values is similar to ranges observed in previous studies (e.g., 0.1–0.5 in Templeton *et al.*, 2006).

The initial isotopic composition of the methane used was different between the two sets of experiments (Table 4.1). As methane was consumed, the $\delta^{13}C$ and δD values of the residual methane increased (Fig. 4.2), indicating a preferential consumption of the lighter ^{12}C and ^{1}H by the bacteria. Conversely, $\Delta^{13}CH_3D$ values of the residual methane decreased as methane was consumed, starting from initial values of ca. +2.6‰ and +2.2‰, and decreasing to "anticlumped" (<0‰) values of ca. −1.5‰ and −1.9‰, respectively, at the last time points sampled in the 30 and 37 °C experiments (Table 4.1).

Using Eqns. 4.13, 4.16, and 4.20, values of the fractionation factors ${}^{13}\alpha$, ${}^{D}\alpha$, and γ were calculated for each time point after the initial (Table 4.1). All calculations used the initial timepoint as the reference starting point; thus, the fractionation factors reported are averaged over the entire reaction occurring in the bottle, and contain correlated errors linked to the uncertainty in data from the initial timepoint. Fractionation factors were calculated for each timepoint, rather than over all bottles in an experiment, to avoid artifacts from variable growth between bottles, particularly at the lower temperature of 30 °C (see Fig. 4.1). In the earlier time points, the error in the calculated fractionation factors is large because of uncertainties in f and in $\Delta^{13}CH_3D$. For each set of experiments, the weighted-averages of the fractionation factors were determined, and are listed in Table 4.1, and the corresponding trajectories (using experimental ${}^{13}\alpha$ and ${}^{D}\alpha$ values, and variable γ) are depicted in Fig. 4.2.

Isotopic fractionation of D/H was substantially greater in magnitude than that of $^{13}C/^{12}C$ (Fig. 4.3a). In general, a greater degree of both carbon- and hydrogen-isotope fractionation was observed in the bottles incubated at 37 °C than at 30 °C (Fig. 4.3b). No systematic changes in the magnitude of isotope fractionation were observed over the course of the experiments (Table 4.1). A similar, tight correlation of D/H and $^{13}C/^{12}C$ fractionation is observed between the two sets of experiments (Fig. 4.3a).

Calculated γ values for each experimental timepoint are shown in Table 4.1. All values were close to unity, and showed no systematic changes over the course of incubation. The weighted-average γ values for the experiments were identical to unity within 2σ error (1.0005 ± 0.0006 and 1.0000 ± 0.0014 for the 30 and 37 °C experiments, respectively).

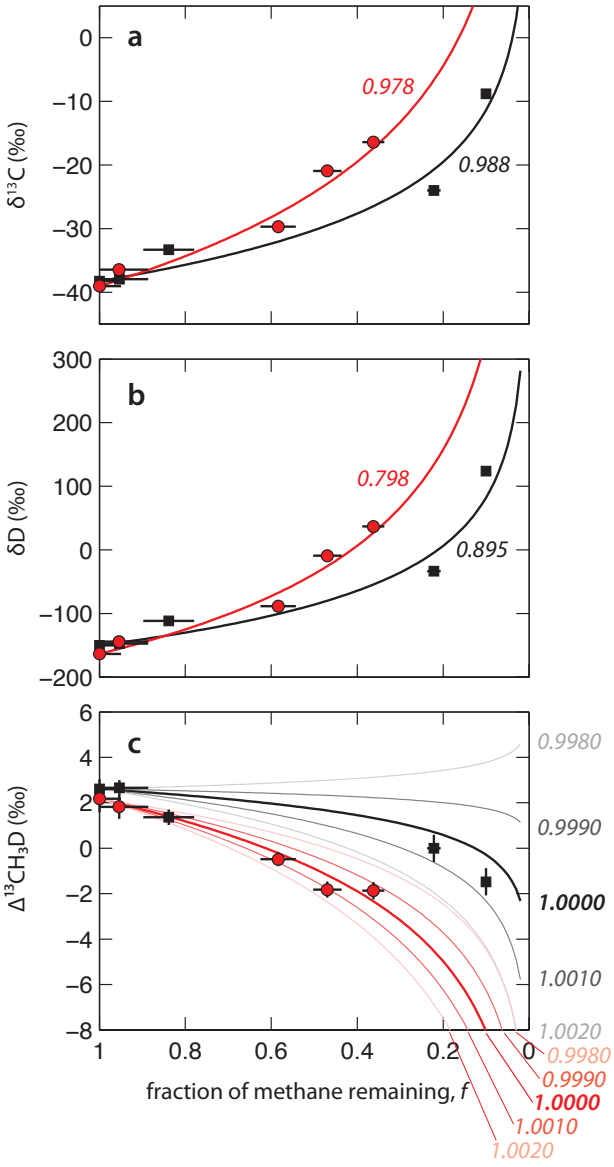

Figure 4.2 | Measured and modeled changes in **(a)** $\delta^{13}C$, **(b)** δD, and **(c)** $\Delta^{13}CH_3D$ of residual methane as a function of f, the fraction of initial methane remaining. Data points from the 30 and 37 °C experiments (Table 4.1) are shown with black and red symbols, respectively. Horizontal error bars represent propagated $\pm 1\sigma$ uncertainties from GC measurements, and vertical error bars represent 95% confidence intervals from isotopologue ratio analyses. Solid lines represent the modeled values (from Eqns. 4.13, 4.16, and 4.20) based on the calculated weighted-average carbon- and hydrogen-isotope fractionation factors for each set of experiments as listed in Table 4.1. Labels in *italics* represent ${}^{13}\alpha$, ${}^{D}\alpha$, & γ, respectively, in panels (a), (b), & (c). Panel (c) shows model results calculated assuming different values of γ varying between 0.9980 and 1.0020.

Table 4.1 | Experimental results and calculated fractionation factors for batch cultures of *Methylococcus capsulatus* Bath. Uncertainties (±1σ) listed for f, $^{13}\alpha$, $^{D}\alpha$, and γ are propagated from those associated with individual measurements according to standard formulas (Ku, 1969).

	time (h)	f	CO_2 (cm^3)[a]	$\delta^{13}C$ (‰)[c]	δD (‰)[c]	$\Delta^{13}CH_3D$ (‰)[c]	$^{13}\alpha$	$^{D}\alpha$	γ
30 °C	0	1.00 ± 0.05[b]	<0.2	−38.27	−150.12	2.61 ± 0.43			
	12	0.95 ± 0.07	0.6	−37.94	−147.20	2.66 ± 0.34	0.993 ± 0.011	0.928 ± 0.107	0.9983 ± 0.0130
	36	0.84 ± 0.06	1.9	−33.31	−111.79	1.36 ± 0.34	0.971 ± 0.012	0.749 ± 0.101	0.9997 ± 0.0060
	–[d]	0.22 ± 0.02	10.3	−24.00	−33.36	−0.01 ± 0.60	0.990 ± 0.0005	0.915 ± 0.004	1.0010 ± 0.0005
	60	0.10 ± 0.01	9.8	−8.81	123.90	−1.48 ± 0.60	0.987 ± 0.0004	0.878 ± 0.004	1.0002 ± 0.0004
						weighted average[e]	0.988 ± 0.0003	0.895 ± 0.003	1.0005 ± 0.0003
37 °C	0	1.00 ± 0.05[b]	n.d.	−39.06	−163.57	2.17 ± 0.59			
	41	0.95 ± 0.07	n.d.	−36.45	−144.23	1.82 ± 0.53	0.943 ± 0.086	0.516 ± 0.726	0.9585 ± 0.2130
	44	0.58 ± 0.04	2.5	−29.68	−88.51	−0.48 ± 0.30	0.982 ± 0.002	0.840 ± 0.021	1.0025 ± 0.0015
	48	0.47 ± 0.03	4.8	−20.95	−9.20	−1.82 ± 0.36	0.975 ± 0.002	0.776 ± 0.021	0.9997 ± 0.0014
	51	0.36 ± 0.03	6.3	−16.39	36.83	−1.87 ± 0.38	0.977 ± 0.002	0.788 ± 0.015	0.9989 ± 0.0011
						weighted average[e]	0.978 ± 0.001	0.798 ± 0.010	1.0000 ± 0.0007

n.d., not determined

[a] Total inorganic carbon in the bottle (including gaseous CO_2 and dissolved inorganic carbon), reported as cm^3-equivalent of CO_2 at standard ambient temperature and pressure (SATP; 25 °C, 1 bar), was estimated from headspace CO_2 concentration (determined via GC), the Henry's law constant for CO_2 at room temperature, and the volume of headspace and of HCl-spiked medium. Uncertainty is estimated at ±10%. Quantitative conversion of initial CH_4 (see § 4.2.1) into CO_2 (i.e., 100% oxidation with no incorporation of CH_4-derived carbon into biomass) would yield 20 cm^3 SATP of CO_2.

[b] An uncertainty of ±5% was assigned to the initial value of f to account for variability in starting amounts of methane between bottles (see § 4.2.1). This uncertainty is propagated throughout the calculations for later timepoints.

[c] Values for $\delta^{13}C$, δD, and $\Delta^{13}CH_3D$ are reported relative to PDB, SMOW, and the stochastic distribution, respectively. Uncertainties for $\delta^{13}C$, δD (both ca. 0.1‰), and $\Delta^{13}CH_3D$ (listed) are 95% confidence intervals over all cycles in a single analysis (e.g., Wang *et al.*, 2015), but are conservatively treated as 1σ for purposes of error propagation.

[d] Time not recorded.

[e] Weighted means of each set of $^{13}\alpha$, $^{D}\alpha$, and γ values, weighted by $1/\sigma^2$. Uncertainty (1σ) in weighted means was estimated following Bevington and Robinson (2002).

4.4 DISCUSSION

4.4.1 Isotope and isotopologue fractionation during aerobic methanotrophy

4.4.1.1 Fractionation of methane $^{13}C/^{12}C$ and D/H ratios

A wide range of carbon isotope fractionation factors [$^{13}\varepsilon$ (= $^{13}\alpha - 1$) ranging from −38‰ to −3‰] have been reported in culture- and field-based studies (see Templeton *et al.*, 2006, and references therein). The variable nature of the magnitude of observed carbon isotope effects complicates application of measurements of individual carbon isotope ratios in diagnosing the presence and extent of methanotrophy in the environment. As such, the use of paired $\delta^{13}C$ and δD data has been suggested as a possible method of removing some levels of ambiguity associated with the sole use of carbon isotopes (Elsner *et al.*, 2005). Although the absolute magnitudes of isotope fractionation may vary due to "masking effects" from preceding isotopically-insensitive steps such as transport across membranes or binding to an enzyme (Feisthauer *et al.*, 2011), a correlation between the fractionation of the carbon and hydrogen isotopes can be expected because both are principally influenced by the breakage of the C–H bond. Such a correlation was first noted by Coleman *et al.* (1981), with later studies by Kinnaman *et al.* (2007), Powelson *et al.* (2007), and Feisthauer *et al.* (2011) corroborating the observations in pure culture and in enrichments from other environments. The published values of $^{D}\varepsilon/^{13}\varepsilon$, corresponding to the slope of the gray lines in Fig. 4.3a, range from 5.9 to 14.9, with a mean of 8.9 ± 2.3 [standard deviation (1σ), n = 15]. The best-fit value of $^{D}\varepsilon/^{13}\varepsilon$ for the data shown in Table 4.1 is 9.14, a value which appears independent of the two growth temperatures tested, and which falls near the middle of the published range.

The consistency of the determined $^{D}\varepsilon/^{13}\varepsilon$ ratios with those in the literature provides confidence that results regarding the behavior of $\Delta^{13}CH_3D$ (discussed below) during aerobic methane oxidation by *M. capsulatus* (Bath) can be generalizable to other strains grown under other conditions. Further experiments with these strains grown under different conditions to examine clumped isotopologue fractionation will help to determine if this hypothesis is valid. In a previous study, various strains of bacteria (including *M. capsulatus*, which has two pMMOs and one sMMO; Ward *et al.*, 2004) grown in batch cultures under different copper (Cu) concentrations (with pMMO expressed under Cu-rich conditions and sMMO under low Cu) demonstrated consistently correlated fractionations of carbon and hydrogen isotopes, without apparent correlation to physiology or growth condition (Feisthauer *et al.*, 2011). Values of $^{D}\varepsilon/^{13}\varepsilon$ derived from that study range from 7.3 to 8.8, and are close to the average $^{D}\varepsilon/^{13}\varepsilon$ ratio from our dataset (9.14, Fig. 4.3a). In particular, *M. capsulatus* grown at 45 °C induced isotopic fractionations of $^{13}\alpha$ = 0.972 ± 0.002 and $^{D}\alpha$ = 0.769 ± 0.030 (published uncertainties were listed as 95% confidence interval, approximately 2σ) under Cu-rich conditions, and under Cu-poor conditions, similar values of $^{13}\alpha$ = 0.977 ± 0.003 and $^{D}\alpha$ = 0.808 ± 0.029 (Feisthauer *et al.*, 2011). The corresponding $^{D}\varepsilon/^{13}\varepsilon$ ratios (with propagated ~2σ uncertainties) indicated by their data are 8.3 ± 1.1 and 8.4 ± 1.7 under Cu-rich and Cu-poor conditions, respectively. These values are indistinguishable from the $^{D}\varepsilon/^{13}\varepsilon$ ratio derived from regression through our experimental data (9.14 ± 0.14, 2σ; see Table 4.2). This correspondence of $^{D}\varepsilon/^{13}\varepsilon$ ratios suggests that the proposed product rule for γ values (see § 4.4.1.2) could be valid for *M. capsulatus* expressing either pMMO or sMMO, and may hold for many other methanotrophic strains cultured under various conditions.

Insights into the origin of D/H fractionation during methane oxidation have been obtained from studies which separately constrain the primary and secondary hydrogen isotope effects. Using molecular dynamics simulations, Pudzianowski and Loew (1983) calculated the isotope effects associated with the abstraction of H or D from CH_4 or CH_3D by atomic oxygen, $O(^3P)$, as an analog for the methane monooxygenase reaction. Their results, expressed as fractionation factors, are $^{D}\alpha_p$ = 0.0296 and $^{D}\alpha_s$ = 0.763 (or 0.0179 and 0.759 when tunneling corrections were applied). Thus, the overall isotope fractionation, $^{D}\alpha$ (see Eqn. 4.15), would be 0.580. This fractionation factor reflects a much larger magnitude of D/H fractionation than is observed in either

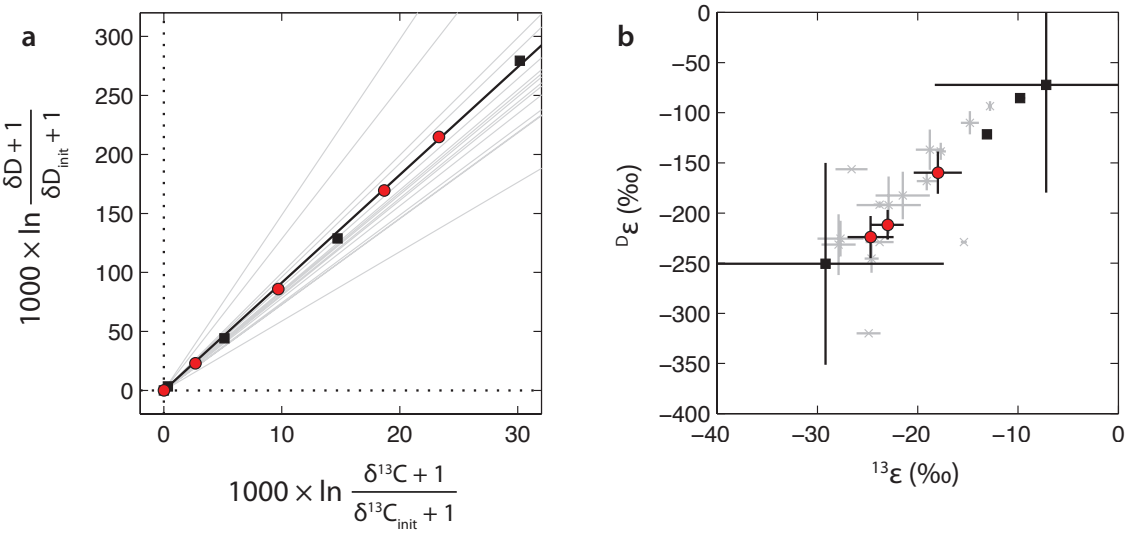

Figure 4.3 | Relationship between fractionation of carbon and hydrogen isotopes. **(a)** Data from the 30 and 37 °C experiments (Table 4.1) are shown with black and red symbols, respectively. Black line ($y = 9.14\,x$) represents the best-fit regression through the data. From Eqn. 4.17, the slope of this line is $(^{D}\alpha - 1)/(^{13}\alpha - 1)$, or $^{D}\varepsilon/^{13}\varepsilon$. Near the origin, the x- and y-axes are approximately equal to $\delta^{13}C - \delta^{13}C_{init}$ and $\delta D - \delta D_{init}$, respectively; this approximation becomes less accurate with increasing distance from the origin, particularly for hydrogen (Sessions and Hayes, 2005). Gray lines represent previously-reported correlations between fractionation of carbon and hydrogen isotopes by aerobic methanotrophs determined from experiments with pure cultures (Feisthauer *et al.*, 2011) and enrichment cultures (Coleman *et al.*, 1981; Kinnaman *et al.*, 2007; Powelson *et al.*, 2007). **(b)** Fractionation factors (ε, defined as $\alpha - 1$) calculated for individual bottle incubations from this study (Table 4.1) plotted against fractionation factors reported in the cited studies (gray). One point from the 37 °C experiment (41 h) was not plotted because of large uncertainties arising from a minimal extent of reaction.

our experiments ($^{D}\alpha$ as low as 0.718) or those reported in other studies (plotted in Fig. 4.3b). Pudzianowski and Loew (1983) note, however, that the transition state of the $CH_4/CH_3D + O(^3P)$ reaction they modeled has only qualitative similarity to the transition state of the methane hydrogen abstraction/hydroxylation reaction performed by methane monooxygenase. Such fundamental differences between the two processes may explain the difference between their calculated fractionation and the experimental observations.

Multiple experimental determinations of the kinetic isotope effects for H or D abstraction have been reported (e.g., Green and Dalton, 1989; Rataj *et al.*, 1991; Wilkins *et al.*, 1994, and references therein). Values for the primary isotope effect (corresponding to $^{D}\alpha_p = 0.73$) and secondary isotope effect ($^{D}\alpha_s = 0.93$) have been reported for methane oxidation by sMMO (Wilkins *et al.*, 1994). The overall $^{D}\alpha$ calculated from these values (0.88 via Eqn. 4.15) is not low enough to explain the observed D/H fractionations in culture (Fig. 4.3b). More recently, in experiments with a series of multiply-deuterated isotopologues of methane, Nesheim and Lipscomb (1996) determined that the isotopically-selective reaction of compound Q (the key intermediate that oxidizes CH_4) of the MMO hydroxylase ($MMOH_Q$) has very large primary and much smaller secondary kinetic isotope effects corresponding to $^{D}\alpha_p = 0.01$–0.02 and $^{D}\alpha_s = 0.9$–1.0. Via Eqn. 4.15, the corresponding overall hydrogen isotope fractionation, $^{D}\alpha$, is then between ~0.68 and ~0.76, a range which overlaps with the largest D/H fractionation observed in our experiments (0.718, Table 4.1). Note that such a direct quantitative comparison between isotope effects determined from pure cultures and those from *in vitro* experiments with labeled substrates may not be meaningful, as in culture experiments the fractionation induced by MMO is

not necessarily the only factor determining isotopic fractionation. Regardless, the very large primary kinetic isotope effect implies that nearly all of the $^{12}CH_3D$ reacts via the abstraction of H, with only a minor fraction reacting via the abstraction of D. This inference has potential implications for the interpretation of γ factors constrained by clumped isotopologue measurements (see § 4.4.1.2).

Generally larger bulk carbon and hydrogen isotopic fractionations were observed in the 37 °C cultures, compared to those grown at 30 °C (Table 4.1). This trend is an apparent reversal of the normally-expected decrease of kinetic isotope effects with increasing temperature. Such an inverse temperature effect was previously observed by Coleman *et al.* (1981) on enrichment cultures grown at 11.5 and 26 °C. They excluded species differences as the source of the apparent trend, and speculated that the partial and differential expression of a combination of kinetic and equilibrium isotope effects could explain their results.

In our experiments, only one strain of bacterium was cultured, thus also excluding species differences as a reason for the observed inverse temperature trend. If some D/H exchange with cellular water occurs during C–H bond breakage and re-forming, the overall $^{D}\varepsilon$ fractionation factor should be of smaller magnitude than would otherwise be expected given the observed $^{13}\varepsilon$ value (as the carbon does not exchange). [The δD of water used in the cultures was not measured, but is estimated to be between −95‰ and −32‰ based on tap water data from Bowen *et al.* (2007). Based on the calibration of Horibe and Craig (1995),[3] methane at D/H equilibrium with water at 30–37 °C would be expected to have δD < −200‰, which is lower than the initial δD of methane in both sets of experiments.] The observation that the ratio $^{D}\varepsilon/^{13}\varepsilon$ is nearly identical between the two temperatures (Fig. 4.3a) therefore argues against C–H bond re-equilibration as an explanation for smaller magnitudes of isotopic fractionation in the 30 °C experiments. Furthermore, our additional measurements of $\Delta^{13}CH_3D$ indicate that γ values are indistinguishable (within 2σ, Table 4.1) between the two experiments, lending additional support to the conclusion that kinetic isotope fractionation dominates the observed isotope and isotopologue signals.

Given the above analysis, an alternate explanation must be sought to explain the observed apparent inverse temperature trend. According to the theory of kinetic isotope fractionation (e.g., Bigeleisen, 1949), predictions of decreasing kinetic isotope effects with increasing temperature are generally valid only for elementary reactions. The aerobic oxidation of methane by *M. capsulatus* consists of multiple enzymatic steps, and thus expression of intrinsic kinetic isotope effects may not be complete if the isotopically-sensitive methane monooxygenase reaction is not fully rate-limiting. In particular, models proposed to explain previously published experimental data point to the depletion of soluble methane concentrations below threshold levels required to maintain rates of mass transfer into the cell as a control on the degree to which kinetic isotope effects are expressed in culture (Nihous, 2008; Nihous, 2010; Vavilin *et al.*, 2015). This behavior is analogous to that observed for $^{34}S/^{32}S$ ratios during microbial sulfate reduction, where under low sulfate conditions, sulfur isotope fractionation is suppressed due to rate limitation by the isotopically-insensitive initial transport of sulfate into the cell (Harrison and Thode, 1958; Rees, 1973). Substrate limitation has also been considered to explain trends associated with $^{13}C/^{12}C$ fractionation during methanogenesis under low intracellular CO_2 levels (e.g., Valentine *et al.*, 2004), and has been extensively studied in relation to CO_2 levels during photosynthesis (e.g., Farquhar *et al.*, 1982). Thus, the apparent inverse temperature trend in the data is possibly a result of masking of intrinsic isotope effects of MMO due to limitation from mass transport into the cell, although other explanations cannot be discounted. Experimental setups that allow rigorous accounting of carbon budgets and biomass density may allow for quantitative models of isotopologue systematics, similar to those created for $\delta^{13}C$ (Templeton *et al.*, 2006; Nihous, 2008; Nihous, 2010), to be used in evaluating the potential effects of diffusion of methane to and through cells. Our data thus also encourages consideration of

[3] Comparisons of the fractionation factor for D/H equilibrium between $CH_4(g)$ and $H_2O(l)$ derived from the calibrations of different studies reveal a substantial range in estimates (up to 30‰ at 30–37 °C, see Wang *et al.*, 2015). This is mainly due to uncertainty in extrapolations of experimental calibrations of $H_2(g)/H_2O(g)$ at >200 °C to lower temperatures. However, this level of uncertainty does not impact the interpretation developed here.

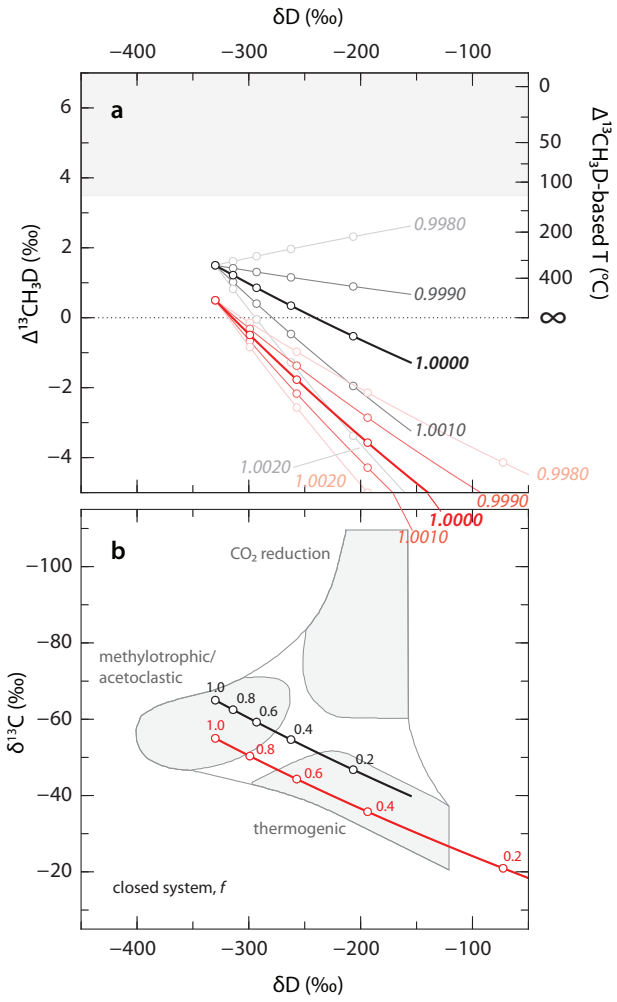

Figure 4.4 | Modeled changes in **(a)** $\Delta^{13}CH_3D$ vs. δD and **(b)** $\delta^{13}C$ vs. δD of residual methane during aerobic methane oxidation under closed system conditions. Solid lines represent model predictions (from Eqns. 4.13, 4.16, and 4.20) based on the calculated weighted-average carbon- and hydrogen-isotope fractionation factors for each set of experiments (black, 30 °C; red, 37 °C) as listed in Table 4.1 and shown in Fig. 4.2. Labels in *italics* in panel (a) represent γ values. Circles are marked at intervals of 0.2 in f, the fraction of initial methane remaining, and labeled in panel (b). For visual clarity, the models were initialized at slightly different $\delta^{13}C$ and $\Delta^{13}CH_3D$ values. The initial isotope values were chosen for illustrative purposes only and do not represent any particular natural sample; however, the chosen values are typical of modern microbial methane generated in wetland and lake sediments. Following Wang *et al.* (2015), the gray field in panel (a) represents the temperature range within which microbial life has been shown to occur (Takai *et al.*, 2008), and the gray fields in panel (b) represent empirical methane source fields suggested by Whiticar (1999).

mass transport and bioavailable methane levels when evaluating methane isotope data in field settings where oxidation may be occurring. Despite the particular mechanisms underlying apparent inverse temperature trends remaining unclear, the general observation that the fractionation of $^{13}C/^{12}C$ and D/H ratios observed in our study is consistent with previously reported experiments is key, as it suggests that the discussion below regarding patterns of fractionation of $^{13}CH_3D$ may be generally applicable to experimental cultures of aerobic methanotrophic bacteria.

4.4.1.2 Fractionation of $^{13}CH_3D$

In our batch culture experiments, the $\Delta^{13}CH_3D$ value of residual methane decreased with progressive oxidation (Table 4.1). The weighted average γ values determined for the both the 30 °C experiment (1.0005 ± 0.0006, 2σ) and the 37 °C experiment (1.0000 ± 0.0014) are indistinguishable from unity. Thus, the results of this study indicate that the overall kinetic fractionation factor for $^{13}CH_3D/^{12}CH_4$ can be closely approximated as the product of the carbon and hydrogen isotopic fractionation factors (i.e., $^{13\text{–}D}\alpha \approx {}^{13}\alpha \cdot {}^{D}\alpha$). This product rule can be used to model the $\Delta^{13}CH_3D$ value resulting from aerobic methane oxidation. If a higher level of prediction is necessary, precise constraints on primary and secondary α and γ values are required (see § 4.2.3.3 and discussion below).

Given low enough γ values (depending on $^{13}\alpha$ and $^{D}\alpha$), the $\Delta^{13}CH_3D$ value may actually *increase* over

the course of the reaction in a closed system such as a batch culture. The break-even condition, under which $\Delta^{13}CH_3D$ does not change during a closed system process, occurs when $\gamma = \left({}^{13}\alpha + {}^{D}\alpha - 1\right)/\left({}^{13}\alpha \cdot {}^{D}\alpha\right)$. For the 30 and 37 °C experiments, the break-even γ values are 0.9986 and 0.9943, respectively. These values are substantially less than those determined experimentally above (the latter by a considerable −0.0057 or −5.7‰). Therefore, it should not be assumed that $\Delta^{13}CH_3D$ values are unaffected by closed system methane oxidation. Otherwise, the apparent $\Delta^{13}CH_3D$ temperature may be substantially overestimated or become imaginary, as shown in Fig. 4.4a.

There is no *a priori* reason that γ must be close to unity.[4] The γ factor as defined in § 4.2.3.3 is empirically useful in that it is a single number that expresses the reactivity of $^{13}CH_3D$ relative to the other isotopologues. Because $^{13}CH_3D$ can react by two nonidentical hydrogen-abstraction reactions (Reactions 4.8 and 4.9), the γ value expresses the summation of the products of the hydrogen-isotope effects (${}^{D}\alpha_p$ and ${}^{D}\alpha_s$) and the "clumped isotopologue effects" (γ_p and γ_s) for D in both primary and secondary sites: $\gamma \cdot {}^{D}\alpha = \frac{1}{4} \cdot \gamma_p \cdot {}^{D}\alpha_p + \frac{3}{4} \cdot \gamma_s \cdot {}^{D}\alpha_s$. A conceptual exercise helpfully illustrates the relative weighting of D- vs. H-abstraction reactions expressed in the γ factor. Assuming ${}^{D}\alpha_p = 0.02$ and ${}^{D}\alpha_s = 0.9$ (from § 4.4.1.1), and $\gamma = 0.9990$ (i.e., −1‰ from unity, which is at the lower edge of 2σ uncertainty on the weighted average γ values for the experiments shown in Table 4.1), then ${}^{D}\alpha = 0.68$ and $0.6786 = 0.0050 \cdot \gamma_p + 0.6750 \cdot \gamma_s$. Assigning a value to either γ_p or γ_s would constrain the other; hence, two extreme cases can be considered: (*i*) if $\gamma_s = 1$, then $\gamma_p = 0.86$; or alternatively (*ii*) if $\gamma_p = 1$, then $\gamma_s = 0.9990$. The former case requires a large primary clumped isotopologue effect because proportionally very few $^{13}CH_3D$ (and $^{12}CH_3D$) molecules react through direct D-abstraction rather than H-abstraction (see § 4.4.1.1), whereas the latter requires only a much smaller secondary clumped isotopologue effect on H-abstraction from $^{13}CH_3D$ to explain a γ value that deviates slightly from unity. Although insufficient constraints on either γ_p or γ_s are currently available, this exercise indicates that a small secondary clumped isotopologue effect (i.e., $\gamma_s \neq 1$ but is very close) could exist, but may be hardly detectable. Given the uncertainties surrounding experimental determinations of ${}^{D}\alpha_p$ and ${}^{D}\alpha_s$ (discussed in § 4.4.1.1), accurate values of γ_p and γ_s cannot yet be assigned. For geochemical applications, the γ factor is at present best used as an empirically-fitted parameter, similar to the manner in which the overall D/H fractionation factor ${}^{D}\alpha$ is typically treated.

Irrespective of the exact magnitude of the γ factor, it is clear that $\Delta^{13}CH_3D$ becomes less clumped with progressive oxidation in a closed system under the growth conditions tested in this study. Because of the consistency of our ${}^{D}\varepsilon/{}^{13}\varepsilon$ results with previous experiments with organisms also using pMMO and/or sMMO (Fig. 4.3a), it is not unreasonable to expect similar results on $\Delta^{13}CH_3D$ values for methane oxidation by other strains of aerobic methanotrophic bacteria.

As mentioned above (§ 4.4.1.1), a possible explanation for the differences in the hydrogen isotopic fractionation factor for the experiments at the two temperatures relates to partial expression of equilibrium isotope effects in one or both experiments. Evidence against this explanation derives from the observation that $\Delta^{13}CH_3D$ values of residual methane in both experiments follow the predictions of the product rule (i.e., γ values are ~1); therefore it is unlikely that there is a greater degree of C–H bond re-equilibration during the course of reaction in one experiment over another. Thus, clumped isotopologue data also assist in diagnosing presence or absence of isotope exchange during enzymatic abstraction of H from methane by MMO, and are consistent with a minor (not detectable) degree of reversibility for this process. The minor degree of reversibility indicated by the data for aerobic methane oxidation here contrasts sharply with the anaerobic oxidation of methane (AOM), an oxidation process in which much greater degrees of reversibility

[4] For example, when methane effuses through a small orifice, γ (when defined as the ratio of the isotopologue fractionation factor for $^{13}CH_3D/^{12}CH_4$ to the product of those for $^{13}CH_4/^{12}CH_4$ and $^{12}CH_3D/^{12}CH_4$) will not be unity. From the kinetic theory of gases, the rate of effusion of an isotopologue is proportional to $(\text{mass})^{-1/2}$, such that $\gamma = 1.00174$. Escaping methane will have lower (lighter) $\delta^{13}C$ and δD, but *higher* $\Delta^{13}CH_3D$, than the residual methane. For a more thorough discussion, readers are referred to Eiler and Schauble (2004).

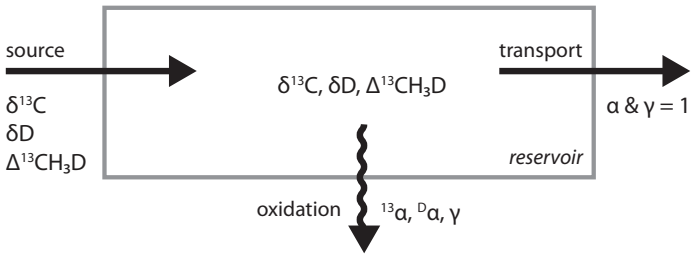

Figure 4.5 | Representation of a model open system in which methane is transported in and out via advection, and in which aerobic methane oxidation is also occurring. The fractional contribution of oxidation to the total sinks is φ_{ox}. See Fig. 4.6 and discussion in § 4.4.2.1.

have been demonstrated using carbon and hydrogen isotopes (Holler *et al.*, 2011; Yoshinaga *et al.*, 2014). The environmental implications are discussed in § 4.4.2.2.

4.4.2 Implications for biogeochemical systems

4.4.2.1 Methane isotope and isotopologue fractionation in open systems

In closed systems, e.g., batch cultures, no steady state is obtained because of the lack of mass transfer to replenish the methane consumed by methane oxidation. However, in natural systems operating close to steady state, there is replenishment of methane from lateral transport or diffusion, as well as methanogenesis, and there may be multiple sinks, including methane oxidation and mass transport (Fig. 4.5).

Experimental alternatives to batch cultures, namely flow-through bioreactors (chemostats), have been used to more directly approach the calibration of isotopic fractionation factors due to microbial metabolism in natural settings. For example, Templeton *et al.* (2006) grew pure and mixed cultures of aerobic methanotrophs in chemostats to determine the carbon isotope fractionation between methane and product methanol as a function of environmental and physiological conditions. In such an open system, there is a constant influx of reactant methane, which at steady state is balanced by the sum of methane oxidation and methane carried in the effluent out of the bioreactor (i.e., dilution).

In the simple limiting case where the fraction of methane removed by oxidation approaches 100% (i.e., no methane escapes the system intact), there is effectively one sink of methane, with fractionation factors $^{13}\alpha$, $^{D}\alpha$, and γ accompanying the removal process. At steady state, the isotopic values of methane in the bioreactor would be $\delta^{13}C = (\delta^{13}C_{in} + 1) \,/\, {}^{13}\alpha - 1$ and $\delta D = (\delta D_{in} + 1) \,/\, {}^{D}\alpha - 1$, where δ_{in} represents the isotopic composition of the influent methane. For $^{13}CH_3D$, it can be shown that

$$\Delta^{13}CH_3D = \Delta^{13}CH_3D_{in} - \ln \gamma \tag{4.21}$$

as presented in Joelsson *et al.* (2015). Since $\gamma \approx 1$, this expression can be approximated by $\Delta^{13}CH_3D = \Delta^{13}CH_3D_{in} - (\gamma - 1)$. In our batch culture experiments at 30 and 37 °C, respectively, weighted-average values for $(\gamma - 1)$ of +0.5 ± 0.3‰ and 0.0 ± 0.7‰ (1σ) were obtained (Table 4.1). Although steady-state experiments were not conducted in the current study, if it is assumed that these values are also characteristic of true open-system isotopologue fractionation factors, then the above expression can be used to place bounds on the isotopologue composition of methane in the limiting case outlined above. Examples of the calculated methane isotopic/isotopologue compositions are shown for model scenarios in Fig. 4.6a (corresponding to the endmember labeled "fully oxidative" on each curve).

Equation 4.21 also shows that in a system at steady state where methane is solely removed by one process (here, oxidation), the $\Delta^{13}CH_3D$ value is determined solely by the $\Delta^{13}CH_3D$ value of the methane source

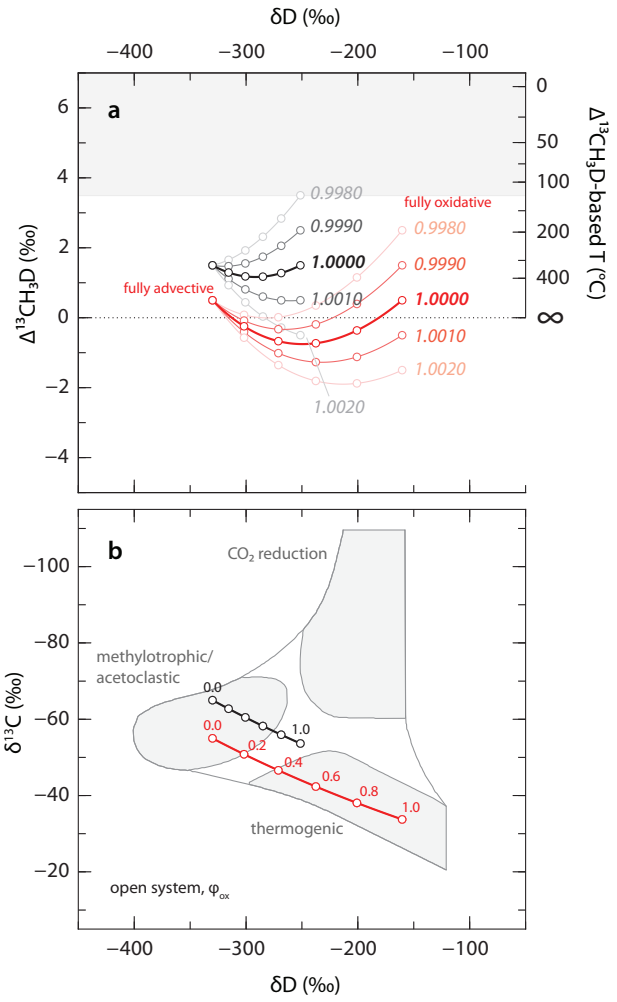

Figure 4.6 | Modeled steady-state values of **(a)** $\Delta^{13}CH_3D$ vs. δD and **(b)** $\delta^{13}C$ vs. δD of methane in an open system (Fig. 4.5) consisting of a single source and two sinks (aerobic methane oxidation and advection). Advection is assumed to be non-fractionating. Lines were modeled using Eqns. 4.22 and 4.23, and the same fractionation factors for aerobic methane oxidation as for those shown with the same line style in Fig. 4.3. Labels in *italics* in panel (a) represent γ values associated with aerobic methane oxidation. Circles are marked at intervals of 0.2 in φ_{ox}, the fraction of methane removed via oxidation, ranging from fully advective ($\varphi_{ox} = 0$) to fully oxidative ($\varphi_{ox} = 1$), and labeled in panel (b). When $\varphi_{ox} = 0$, the isotopic composition of methane in the reservoir is identical to that of the source. For visual clarity, the calculations were performed for slightly different $\delta^{13}C$ and $\Delta^{13}CH_3D$ values of input methane. For description of shaded fields, see the caption for Fig. 4.4.

and the γ factor, in contrast to closed systems where $\Delta^{13}CH_3D$ of residual methane is influenced also by the isotopic fractionations for bulk $^{13}C/^{12}C$ and D/H. However, in more complex systems with multiple removal processes and associated fractionation factors, the partitioning of flows among the removal processes must be considered (Hayes, 2001).

One example of such an open system is shown in Fig. 4.5. Here, methane is carried into the system via advection, and removed by both advection and oxidation. Oxidation of methane has associated fractionation factors $^{13}\alpha$, $^{D}\alpha$, and γ, whereas transport processes are assumed to cause no fractionation (Alperin *et al.*, 1988), i.e., values of α and γ are unity. The fraction of methane removed via oxidation, φ_{ox}, describes the partitioning of flows among the two methane sinks. It can be shown that at steady state, the hydrogen isotopic composition of the methane in the reservoir is (Hayes, 2001):

$$\delta D = \frac{\delta D_{in} + 1}{1 + \varphi_{ox}\left({}^{D}\alpha - 1\right)} - 1 \tag{4.22}$$

An analogous equation (not shown) describes the carbon isotopic composition of methane in this system at steady state. When the $\delta^{13}C$ and δD values are plotted against each other, it can be seen that the trajectory describing the continuum between the fully-advective ($\varphi_{ox} = 0$) and fully-oxidative ($\varphi_{ox} = 1$) endmembers is slightly curved (though approximately linear at most scales of interest, Fig. 4.6b).

For this system, unlike in the simple fully-oxidative case described by Eqn. 4.21, the abundance of $^{13}CH_3D$ is affected not only by the γ value, but also by the $^{13}\alpha$ and $^{D}\alpha$ values:

$$\Delta^{13}CH_3D = \Delta^{13}CH_3D_{in} - \ln \frac{1 + \varphi_{ox}\left(\gamma \cdot {}^{13}\alpha \cdot {}^{D}\alpha - 1\right)}{\left(1 + \varphi_{ox}\left({}^{13}\alpha - 1\right)\right)\left(1 + \varphi_{ox}\left({}^{D}\alpha - 1\right)\right)} \tag{4.23}$$

This results in a parabolic curve connecting the fully-advective and fully-oxidative endmembers (Fig. 4.6a). For aerobic methane oxidation, the curvature on Fig. 4.6a is always expected to be concave up, because both the $^{13}\alpha$ and $^{D}\alpha$ values are less than unity. The relative position of the endmembers in $\Delta^{13}CH_3D$ space is determined by the γ value. When $\varphi_{ox} = 1$, Eqn. 4.23 reduces to Eqn. 4.21.

4.4.2.2 $\Delta^{13}CH_3D$ as an environmental tracer of methane sink processes

Both biological and chemical processes are important sinks in the methane budget. In terrestrial ecosystems and oxygenated marine water columns, aerobic methanotrophy dominates, whereas in sulfate-rich marine sediments and gas seeps, anaerobic consumption of methane becomes important (Cicerone and Oremland, 1988; Reeburgh, 2007; Valentine, 2011; Boetius and Wenzhöfer, 2013). In the atmosphere, the primary sink (~90%) is the reaction with tropospheric OH, with small contributions from microbial oxidation in soils, loss to stratosphere, and reaction with tropospheric Cl (Kirschke *et al.*, 2013).

These methane-consuming processes impart distinct carbon- and hydrogen-isotopic fractionations. In general, biological processes (including aerobic methane oxidation, anaerobic oxidation of methane, and nitrite-dependent anaerobic methane oxidation) have $^{D}\varepsilon/^{13}\varepsilon$ ratios between 6 and 15, whereas the atmospheric sinks, CH_4 + OH and CH_4 + Cl, have $^{D}\varepsilon/^{13}\varepsilon$ ratios ~58 and ~5.5, respectively (Table 4.2). The consistent and sizable differences in isotopic behavior among the two atmospheric processes vs. biological processes is useful for constraining the balance of different sources and sinks of methane (e.g., Whiticar and Schaefer, 2007; Kai *et al.*, 2011; Rigby *et al.*, 2012).

The behavior of methane clumped isotopologues in atmospheric reactions has also been studied. Recently, Joelsson *et al.* (2014) and Joelsson *et al.* (2016) reported the fractionation factor for $^{13}CH_3D$ in relative-rate experiments on the reactions of Cl and OH, respectively. Their experiments were conducted with mixtures of $^{12}CH_4$ and $^{13}CH_3D$ (and also $^{12}CH_3D$ in the OH study). Based on their measurements, the γ value associated with methane oxidation by Cl was 0.980 ± 0.019, and by OH was 0.978 ± 0.028 (2σ, Table 4.2). The γ value for Cl oxidation is slightly less than unity, implying that less of the $^{13}CH_3D$ is oxidized than would be predicted by the product rule, whereas the γ value for OH oxidation is within error of unity. However, the uncertainty on calculated γ values is large (ca. 20 to 30‰) due to limitations associated with the experimental setup and detection technique. Because $\Delta^{13}CH_3D$ in the environment has a ca. 10‰ range (Wang *et al.*, 2015), more precise isotopologue-specific measurements of methane in experiments conducted at natural abundance will be necessary in order to constrain clumped isotopologue fractionations in atmospheric contexts. These experiments have been conducted, and the results are reported in a companion article (Whitehill *et al.*, 2017); a summary of their results are shown in Table 4.1.

In the present study, γ values for aerobic methane oxidation were determined (1.0004 ± 0.0006, 2σ, Table 4.2). These values indicate that the abstraction of H from methane by methane monooxygenase is associated with little to no reversibility (see discussion in § 4.4.1.2). This interpretation is consistent with the strong energetic favorability of methane oxidation to methanol and downstream products in the presence of abundant O_2, a strong electron acceptor (Cicerone and Oremland, 1988; Hanson and Hanson, 1996).

The new experimental constraints on clumped isotopologue fractionation during aerobic methane oxidation also afford an opportunity to briefly evaluate whether aerobic methane oxidation has influenced methane clumped isotopologue data available in the literature from various environments. In particular, because methane oxidation demonstrably produces nonequilibrium clumped isotopologue signatures in

Table 4.2 | Comparison of experimentally-determined ratios of carbon- and hydrogen-isotope fractionation factors ($^{D}\varepsilon/^{13}\varepsilon$) and $^{13}CH_3D$ fractionation factors (γ) for different methane sink processes. Uncertainties quoted are $\pm 2\sigma$ or 95% confidence interval.

	$^{D}\varepsilon/^{13}\varepsilon$	γ
Aerobic methane oxidation		
Previous work[a]	5.9 to 14.9	
This study[b]	9.14 ± 0.14	1.0004 ± 0.0006
Anaerobic oxidation of methane (AOM)		
Holler *et al.* (2009)	6.4 to 8.5	
Nitrite-dependent anaerobic methane oxidation		
Rasigraf *et al.* (2012)	7.8 ± 0.8	
CH_4 + OH		
Saueressig *et al.* (2001)	58.5 ± 6.6	
Joelsson *et al.* (2015; 2016)		0.980 ± 0.038
Whitehill *et al.* (2017)	41.3 ± 8.3	0.9997 ± 0.0012
CH_4 + Cl		
Tyler *et al.* (2000)	5.51	
Saueressig *et al.* (1995; 1996)	5.50	
Feilberg *et al.* (2005)	5.65	
Joelsson *et al.* (2014)		0.978 ± 0.051
Whitehill *et al.* (2017)	5.56	0.9965 ± 0.0007

[a] See caption of Fig. 4.3a for references. Also see Rasigraf *et al.* (2012) for a compilation of $^{13}\varepsilon$ and $^{D}\varepsilon$ values determined for biological methane oxidation in cultures and in the environment.
[b] Derived from linear regression ($^{D}\varepsilon/^{13}\varepsilon$, Fig. 4.3a) or weighted average (γ) of all timepoints in both experiments in Table 4.1.

both closed and open systems considered in this study (Figs. 4.4 and 4.6, respectively), the out-of-equilibrium clumped isotopologue signatures in samples from Upper and Lower Mystic Lakes (Massachusetts, USA), Swamp Y (Massachusetts, USA), and The Cedars (California, USA) are considered again here (Wang *et al.*, 2015), as well as a sample from a pond at Caltech for which a related parameter, the Δ_{18} value, was found to be in disequilibrium (Stolper *et al.*, 2015). At Upper Mystic Lake (a 20-m deep seasonally-stratified freshwater lake), bubble traps were deployed ~2 m above the lake floor; the deployment of traps at such deep depths, into the oxygen-depleted hypolimnion (Peterson, 2005), was designed to minimize the possibility of aerobic methane oxidation (Wang *et al.*, 2015). At Lower Mystic Lake (a 24-m deep meromictic density-stratified lake), the monimolimnion (from which the reported sample was taken) is anoxic (Wang *et al.*, 2015), rendering aerobic methane oxidation unlikely. For Swamp Y and the Caltech pond, the redox state of the sediments from which the methane bubbles were stirred and extracted is unknown. At The Cedars, the extremely high levels of H_2 in gases exsolving from the springs maintains O_2 at vanishingly low levels (near the lower bound of H_2O stability; Morrill *et al.*, 2013). Taken together, all methane samples from these four sites exhibit narrow ranges of $\delta^{13}C$ values between −59‰ and −71‰ and δD values between −265‰ and −342‰, but carry a wide range of nonequilibrium $\Delta^{13}CH_3D$ values (from −3.4‰ to +3.2‰) that are consistent within

sites but significantly different between sites (Wang *et al.*, 2015), and exhibit isotopologue patterns that do not discernably resemble those depicted in Figs. 4.4 and 4.6. Thus, although aerobic methane oxidation cannot be fully discounted at these four sites, the experimental constraints provided in the current study do not contraindicate the assumptions made by Wang *et al.* (2015) and are consistent with the hypothesis that nonequilibrium $\Delta^{13}CH_3D$ values in microbial methane in the environment and in methanogenic cultures studied to date originate primarily from intrinsic isotopologue effects during the assembly of C–H bonds during methanogenesis (Stolper *et al.*, 2015; Wang *et al.*, 2015).

Alternative biological mechanisms for methane oxidation are also important in the environment. Of particular interest is the sulfate-dependent anaerobic oxidation of methane (AOM), which is a major sink of methane in anoxic marine sediments (Reeburgh, 1976). This process operates via a very different biochemical pathway from that used by aerobic methanotrophs. While the biochemistry of AOM has not been fully characterized, it is likely that the enzymatic pathway of AOM is the reverse of methanogenesis, and involves the same or similar key enzymes (e.g., methyl-coenzyme M reductase) for addition or removal of H from single-carbon compounds (Scheller *et al.*, 2010). Previously, it was found that as the reversibility of methanogenesis decreased (controlled in part by levels of bioavailable H_2), both the δD and $\Delta^{13}CH_3D$ values of the generated methane became lower or more negative (Wang *et al.*, 2015); similar behavior was found in Δ_{18} (Stolper *et al.*, 2014a; Stolper *et al.*, 2015). From incubations of enrichment cultures of microbial consortia performing AOM, Holler *et al.* (2009) determined substantial kinetic isotope fractionations associated with this process ($^{13}\varepsilon$ = −12‰ to −36‰ and $^{D}\varepsilon$ = −100‰ to −230‰). The negative D/H fractionation factor results in the residual methane becoming enriched in D. Because of the demonstrated high levels of reversibility of AOM (Holler *et al.*, 2011) and the re-equilibration of $^{13}C/^{12}C$ ratios between methane and inorganic carbon at the sulfate-methane transition zone (Yoshinaga *et al.*, 2014), it seems reasonable to speculate that AOM may produce clumped isotope signatures distinct from those of methanogenesis (Stolper *et al.*, 2015). In particular, the expression of a combination of kinetic and equilibrium isotope effects may be observed, such that the observed $\Delta^{13}CH_3D$ value may lie between that predicted by the product rule and that predicted for thermodynamic equilibrium. If so, then measurement of $\Delta^{13}CH_3D$ may provide a way to differentiate between AOM and aerobic methanotrophy. Alternatively, if AOM also generates $\Delta^{13}CH_3D$ approximating the product rule, then the agreement of $^{D}\varepsilon/^{13}\varepsilon$ between AOM (Holler *et al.*, 2009) and aerobic methanotrophs (Table 4.2) suggests that potentially, microbially-mediated oxidation of methane produces only a small and predictable range of clumped isotopologue fractionations.

Another process, the recently-identified nitrite-dependent anaerobic methane oxidation (Ettwig *et al.*, 2010), may also be environmentally-relevant, though its global prevalence has yet to be established. The bacterium Candidatus *Methylomirabilis oxyfera* produces molecular oxygen intracellularly from the reduction of nitrite to nitric oxide (Ettwig *et al.*, 2010), in the absence of environmental O_2; the generated oxygen is then consumed along with methane by membrane-bound pMMO through the aerobic pathway. Because of the biochemical homology of the bond-breaking enzymatic step to that of aerobic methanotrophy, it is not unreasonable to expect that nitrite-dependent anaerobic methane oxidation would produce isotopic and clumped isotopologue patterns similar to those observed in this study. Indeed, carbon and hydrogen isotope fractionation factors for this process, as determined from culture experiments (Rasigraf *et al.*, 2012), correlate in a manner that overlaps with aerobic methane oxidation (Table 4.2), lending support to this hypothesis.

4.5 CONCLUSIONS

Experimental investigation of the abundance of four methane stable isotopologues ($^{12}CH_4$, $^{13}CH_4$, $^{12}CH_3D$, and a clumped isotopologue, $^{13}CH_3D$) during oxidation of methane with O_2 by *Methylococcus capsulatus* (Bath) grown at 30 and 37 °C indicates that $\Delta^{13}CH_3D$ values of residual methane decrease systematically over the course of reaction in batch culture. The isotopologue fractionation factor for $^{13}CH_3D/^{12}CH_4$ is closely

approximated by the product of those for $^{13}CH_4/^{12}CH_4$ and $^{12}CH_3D/^{12}CH_4$. Based on the isotopologue data, no significant degree of re-equilibration of C–H bonds in methane was detected.

Models were developed for simple scenarios involving variable fluxes of methane removed due to advection and oxidation. In open systems operating at steady state, $\Delta^{13}CH_3D$ values depend on the ratio of methane removed via different processes, as well as the isotoplogue fractionation factors associated with those processes, whereas in closed systems, $\Delta^{13}CH_3D$ values depend also on the fraction of methane remaining. Qualitative comparisons of model predictions with available environmental $\Delta^{13}CH_3D$ data indicate that aerobic methane oxidation has only minor, if any, influence on microbial methane samples reported to date to carry nonequilibrium $\Delta^{13}CH_3D$ values. In combination with recent experimental and theoretical work on clumped isotopologue fractionation associated with other methane sinks, the results of this study provide necessary constraints for the development of $^{13}CH_3D$ as a tracer of the biogeochemical and atmospheric cycling of methane.

4.6 ACKNOWLEDGMENTS

We thank J.H-C. Wei and W.J. Olszewski for technical assistance, and D.S. Gruen, R.E. Summons, J.W. Pohlman, J.S. Seewald, and A.R. Whitehill for discussions. D.L. Valentine and two anonymous referees are thanked for helpful and constructive reviews. Grants from the National Science Foundation (NSF EAR-1250394 to S.O. and EAR-1451767 to P.V.W.), and the Deep Carbon Observatory (to S.O.) supported this study. S.O. thanks the Kerr-McGee Professorship at MIT. This research was conducted with Government support under and awarded by U.S. Department of Defense, Office of Naval Research, National Defense Science and Engineering Graduate (NDSEG) Fellowship (to D.T.W.), 32 CFR 168a.

Chapter 5

Summary and Outlook

The preceding chapters presented a set of data (Fig. 5.1) that shows several insights into the origin and fate of the methane stable isotopologues in the environment. As of the time of writing, methane clumped isotoplogue data have appeared in at least a dozen articles (Ono *et al.*, 2014; Stolper *et al.*, 2014a; Stolper *et al.*, 2014b; Inagaki *et al.*, 2015; Stolper *et al.*, 2015; Wang *et al.*, 2015; Douglas *et al.*, 2016; Lopes *et al.*, 2016; Wang *et al.*, 2016; Young *et al.*, 2016; Whitehill *et al.*, 2017; Young *et al.*, 2017).

The $\Delta^{13}CH_3D$ data were shown to be independent of and complementary to $\delta^{13}C$ and δD. A case was built for why hydrogen (or free energy) exerts a major control on $\Delta^{13}CH_3D$ and D/H of methane; this and several other controls are shown in Fig. 5.2. And several opportunities for advancement on the technical and theoretical sides of the problem of methane origin have been highlighted (Fig. 5.3), including:

- refining the calibration at low temperatures (Larson and Hall, 1965; Robertson *et al.*, 1975; Golden *et al.*, 2001; Naito *et al.*, 2005);
- experiments to retrieve kinetics associated with the breaking and reforming of C–H bonds (Koepp, 1978; Lyon and Hulston, 1984; Reeves *et al.*, 2012);
- construction of numerical models to test hypotheses regarding biophysical controls on isotopologue abundances.

Through this work, we have also realized that there is much more information to be extracted from simple gas chemistry and conventional stable isotope data than has perhaps been widely appreciated; or that has been somewhat overlooked in the rush to develop and deploy new technologies. Measurements of clumped isotopologues provide more dimensions of data to characterize methane samples, which, as

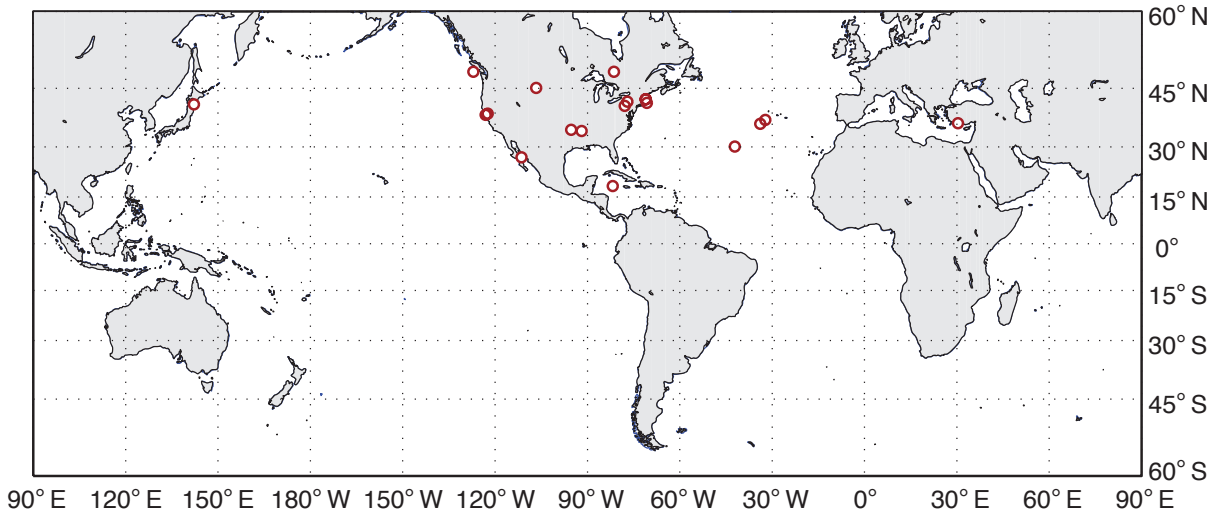

Figure 5.1 | Map showing locations of sites at which $\Delta^{13}CH_3D$ measurements on samples have been published or presented from MIT.

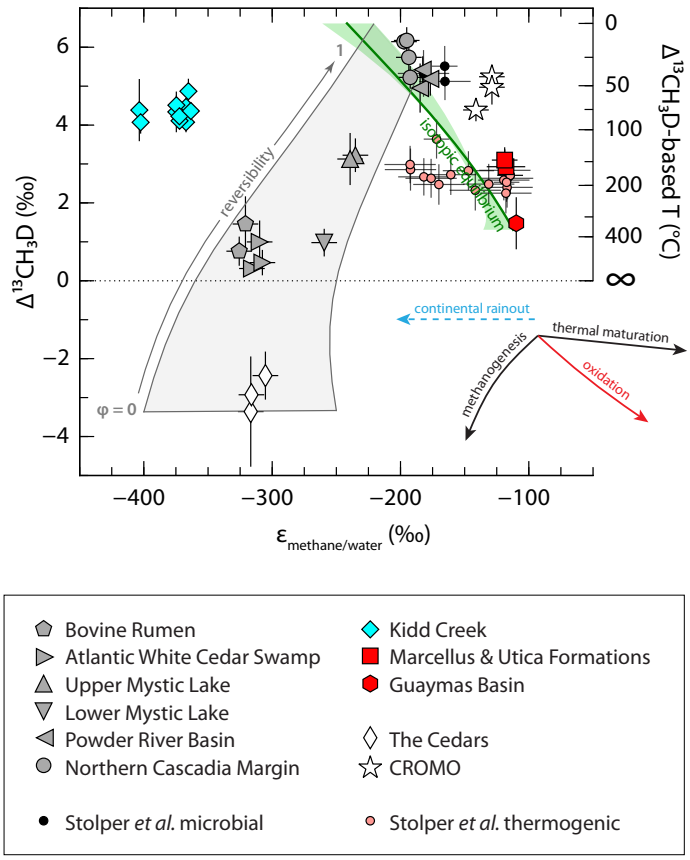

Figure 5.2 | A survey of $^{13}CH_3D$ in the environment. This figure is the same as Fig. 2.2, with the addition of schematic vectors showing basic controls on the isotopic signatures of CH_4, and data from Stolper *et al.* (2014a). The position of their data along the *x*-axis was calculated from estimated δD of formation waters, and for the *y*-axis, Δ_{18} values were converted to $\Delta^{13}CH_3D$ by assuming equilibrium and applying the conversion shown in Fig. C.1A.

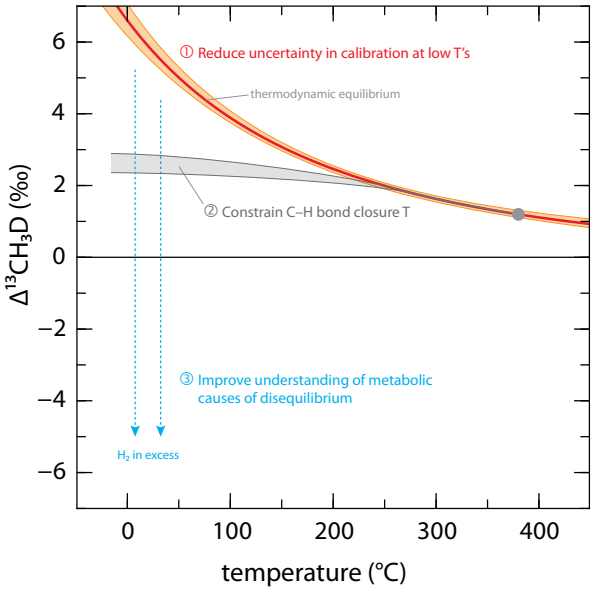

Figure 5.3 | Challenges and opportunities in understanding $\Delta^{13}CH_3D$

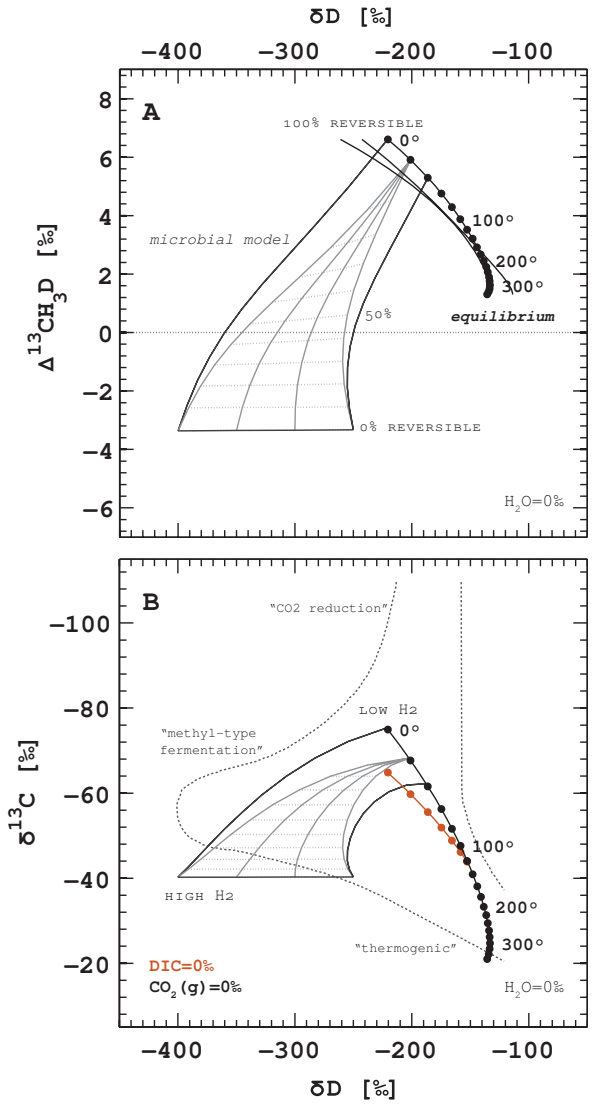

Figure 5.4 | Model of isotopologue abundances in CH_4 produced during microbial methanogenesis from CO_2+H_2 (Wang *et al.*, 2015). The model trajectories begin from a fully-reversible (equilibrium) line whose position is determined by assuming $\delta^{13}C$ of DIC or CO_2 are 0‰ vs. PDB. (This assumption is easily changed if, for example CO_2 has a higher $^{13}C/^{12}C$ ratio than PDB.) The underlay in (B) is the outline of the frequently-used plot from Whiticar (1990).

The plot indicates that modeled isotopic compositions for the fully-kinetic endmember are enriched in ^{13}C and depleted in D relative to the equilibrium endmember. The fully-kinetic endmember is related to high H_2 concentrations (which yield a very large (negative) $\Delta_r G$) (Burke, 1993). Therefore, hydrogenotrophic methanogens could produce CH_4 with isotopic signatures indistinguishable from those typically attributed to methylotrophic or acetoclastic methanogenesis (Whiticar, 1990; Vinson *et al.*, 2017). Whether this is true will require evaluation by experiments under low H_2 conditions (Valentine *et al.*, 2004; Kawagucci *et al.*, 2014; Okumura *et al.*, 2016) or *in vitro* (Scheller *et al.*, 2013). Caveats to this model include (*i*) the assumed fractionation factors may not approximate reality well, and (*ii*) the possibility that the H-addition steps involved in methanogenesis may be differentially reversible in nature.

this thesis shows, does provide additional constraints on certain Earth systems. However, instruments to measure the doubly-substituted isotopologues will likely remain a novelty for the foreseeable future.

I suspect that the most significant advances for our understanding of the origins, transport, and fate of methane are still yet to come. The biggest steps forward will come with moving away from straightforward but often restrictive phenomenological representations of legacy data and towards predictive and quantitative approaches to testing of well-defined and geologically-plausible hypotheses. Isotopologue data will certainly play a large role in helping narrow the solution space of problems of geochemical nature. Figures 5.4 and 5.5 show some attempts at making such data more easily accessible.

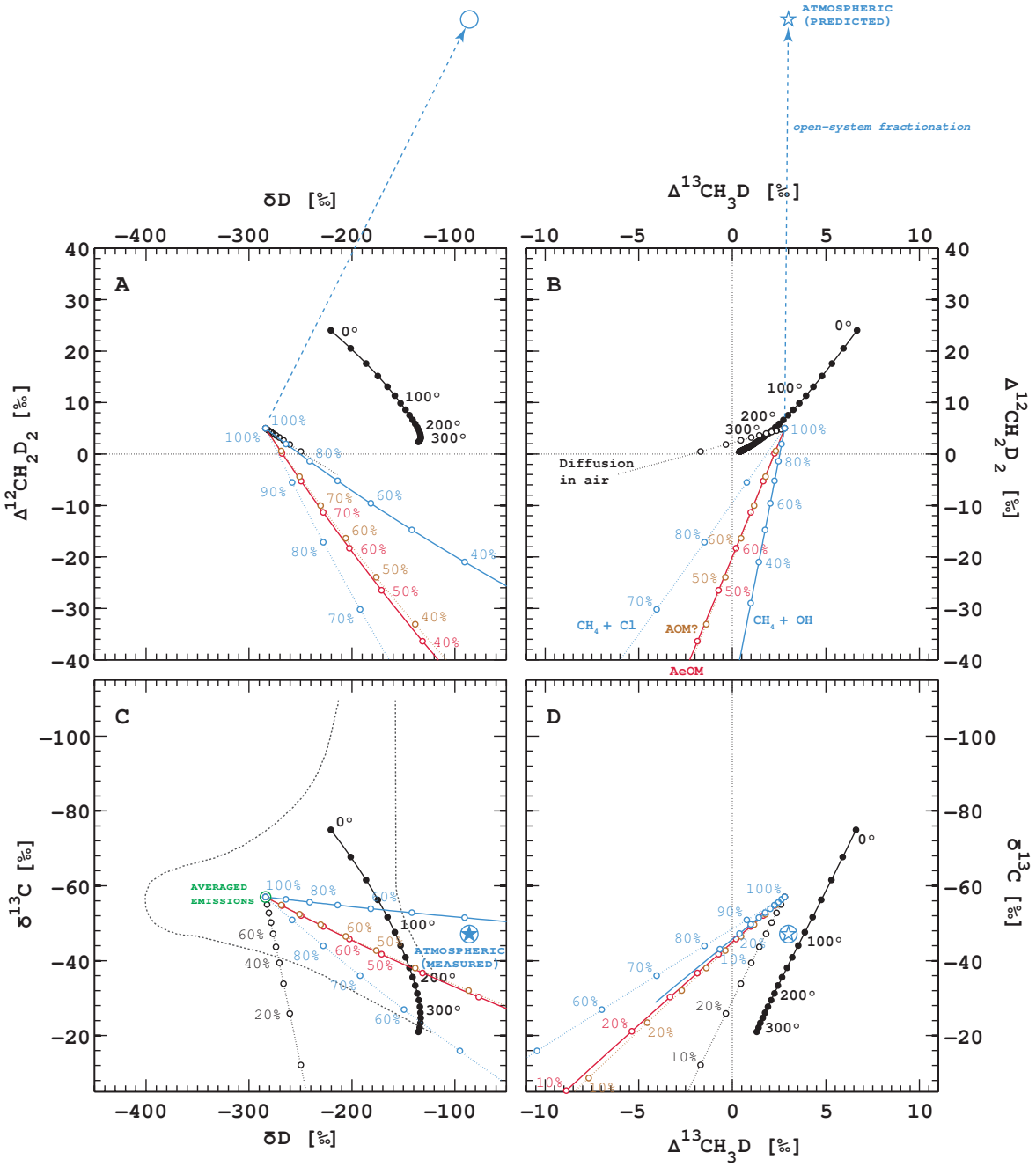

Figure 5.5 | Evolution of CH_4 isotopologue ratios in closed-system, unidirectional bond-breaking processes. Predictions are derived from models and/or data presented by the MIT and UCLA teams (Wang *et al.*, 2016; Whitehill *et al.*, 2017; Young *et al.*, 2017). Calculations used the estimated weighted average of modern sources of atmospheric methane as the starting point. Trajectory labels indicate the fraction of remaining CH_4. Predictions of atmospheric $\Delta^{13}CH_3D$ and $\Delta^{12}CH_2D_2$ assume an open system in steady-state. Note that partial reversibility of the depicted processes will tend to pull the vectors towards the equilibrium line.

Appendices

Appendix A

Abundances of methane isotopologues at the Potato Hills gas field, southeastern Oklahoma

ABSTRACT

Wells in the Potato Hills region of the Ouachita Mountains, southeastern Oklahoma, produce dry natural gas from fractured sandstone units of the Pennsylvanian-age Jackfork Group. Previous carbon- and hydrogen-isotope measurements of the C_1–C_4 hydrocarbons of these gases revealed that methane is enriched in ^{13}C and D relative to the C_{2+} components (Seewald and Whelan, 2005). This pattern of "isotopic reversal" is commonly-associated with high-maturity gases produced from unconventional deep-basin and shale reservoirs (e.g., Burruss and Laughrey, 2010; Tilley *et al.*, 2011), and suggests that gases produced in the Potato Hills may have a deep source. However, because of the structural complexity of this region, identifying potential source rocks and migration pathways has been difficult.

Here, we report additional constraints from tunable infrared laser direct-absorption spectroscopy analyses (see Ono *et al.*, 2014) of the abundance of $^{13}CH_3D$ (a methane "clumped" isotopologue) in natural gas from the Potato Hills field. The measured isotopic signatures are similar across five different wells drilled to 1.8–2.3 km depth, suggesting both a common source for the methane in these gas samples, and preservation of the C–H bond across this >50 km^2 reservoir system.

Our measurements suggest an apparent ^{13}C–D isotopic temperature of ~150 ± 30 °C for methane from the Potato Hills field. Application of a model for isotopic exchange suggests that migration of thermogenic gases generated at temperatures below 200 °C should not result in any detectable reordering of the C–H bonds in methane. We discuss uncertainties in the model calibration and implications for the preservation of clumped isotopic signatures in methane. Results are further interpreted in the context of the regional geology to highlight potential implications for natural gas occurrences in the Ouachita overthrust belt and beyond.

Preliminary data from this chapter were presented in a talk at the 24th Annual V.M. Goldschmidt Conference in Sacramento, California, USA, June 2014.

This work was done in collaboration with Jeff Seewald (and indirectly, Jean Whelan) of WHOI with oversight from Shuhei Ono.

A.1 INTRODUCTION

The subject of this study is produced gas sampled from the Potato Hills gas field in southeastern Oklahoma. The Potato Hills is located in a structurally complex region of the Ouachita Mountains within the frontal/central thrust belt (Fig. A.1).[1] Wells in the Potato Hills gas field produce from repeated (subthrusted) intervals of the fractured and porous sandstones of the Pennsylvanian-age Jackfork Group (Fig. A.2). The field was discovered in the 1960s, but produced little gas and was soon abandoned. Several decades later, The GHK Companies realized the Jackfork play concept and established several dozen wells in the area beginning in 1997. The Potato Hills is one of the most significant recent conventional gas discoveries in Oklahoma (Boyd, 2005), and has produced >300 BCF (~50 MMBOE) of gas.

Major tectonism and mountain building coincided with the collision of the South American Plate with the North American continent (Laurentia) during the late Pennsylvanian and early Permian (ca. 300 Ma, the Ouachita orogeny) (Hatcher *et al.*, 1989). During the approach and leadup to the eventual collision, large deposits of Silurian to Mississippian-age sediments derived from North American rivers filled the ocean basin between the two continents. In the Ouachitas, these sediments are known as the Arkansas Novaculite, an organic-rich (up to 4% TOC in drill cores, and possibly up to 15% originally), mixed shale-chert unit.[2] While no data from source rocks in the Potato Hills could be located, the Arkansas Novaculite elsewhere in the Ouachitas contains predominantly gas-prone Type III kerogen (Curiale, 1981).

Gases from the Potato Hills are dry (>95% $C_1/\sum C_{1-4}$) and express a partially-reversed isotopic trend in which the CH_4 is enriched in ^{13}C and D relative to C_2 and higher hydrocarbon gases (Seewald and Whelan, 2005). This partial reversal is observed in all wells studied, with the exception of the deep (6.3 km) Mary 2-34 well which produces gases with reversed $\delta^{13}C$ but normal δD (i.e., δD of $CH_4 < \delta D$ of C_2) (Seewald and Whelan, unpublished data). Notably, the δD signature of CH_4 is highly uniform amongst all studied gases (see Table A.1 for a partial listing), including the deep well.

These gases were studied for two reasons: (*i*) they were samples of opportunity that were associated with an already-existing dataset comprising analyses of the chemical and isotopic composition of produced gases, concentrations of aliphatic acids in coproduced formation waters, and cultivation-based and culture-independent microbiological data (Seewald, Whelan, and Sievert, unpublished data); and (*ii*) to test if migrated thermogenic gases that accumulated in low temperature reservoir units and were retained over timescales of millions of years would record primary clumped isotopologue signals.

A.2 METHODS

A.2.1 Samples

Samples were retrieved from a dusty Pelican case underneath a desk in Fye 142A at the Woods Hole Oceanographic Institution in October of 2013.

The studied samples were collected from the wellhead in the early 2000's by GHK in stainless steel cylinders equipped with high-pressure valves, and furnished to J. Seewald and J. Whelan for chemical and isotopic analyses. Data on carbon and hydrogen isotopes of CH_4 obtained circa 2003 at WHOI (Seewald and Whelan, 2005) are shown in Table A.1.

[1] The name is apparently due to the resemblance of the unevenly-eroded outcrops of the fractured Bigfork Chert (late Ordovician) to the knobby mounds of a potato garden: http://www.ghkco.com/contact/index.php?page=Potato_Hills

[2] The perhaps more familiar Woodford Shale (to the north of the Ouachitas, in the Arkoma Basin) is syndepositional to the Arkansas Novaculite. The Arkansas Novaculite is the basinward extension of the Woodford Fm. (Houseknecht *et al.*, 2014).

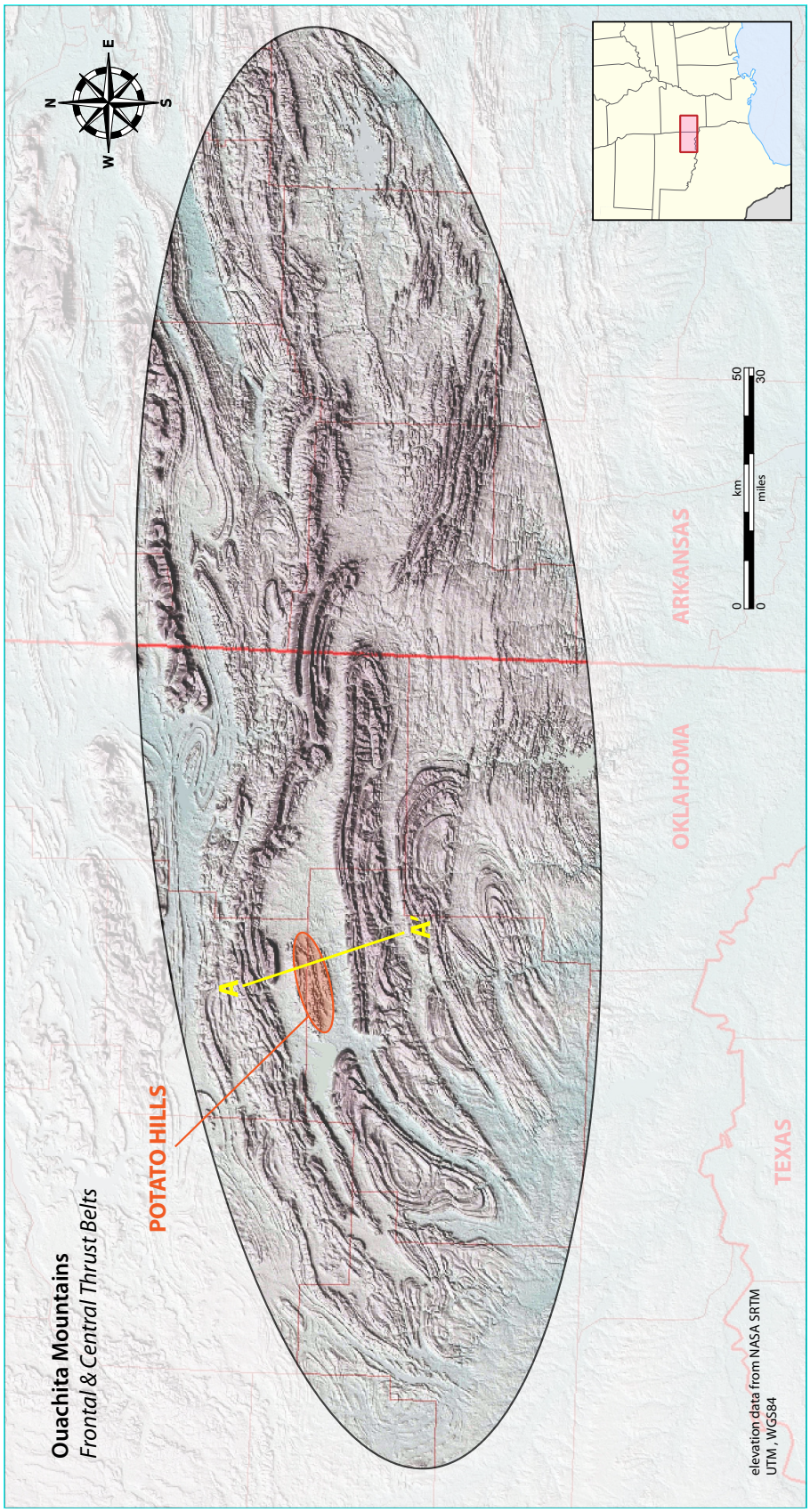

Figure A.1 | Relief map of the frontal and central Ouachita overthrust belt, southeastern Oklahoma and western Arkansas, USA.

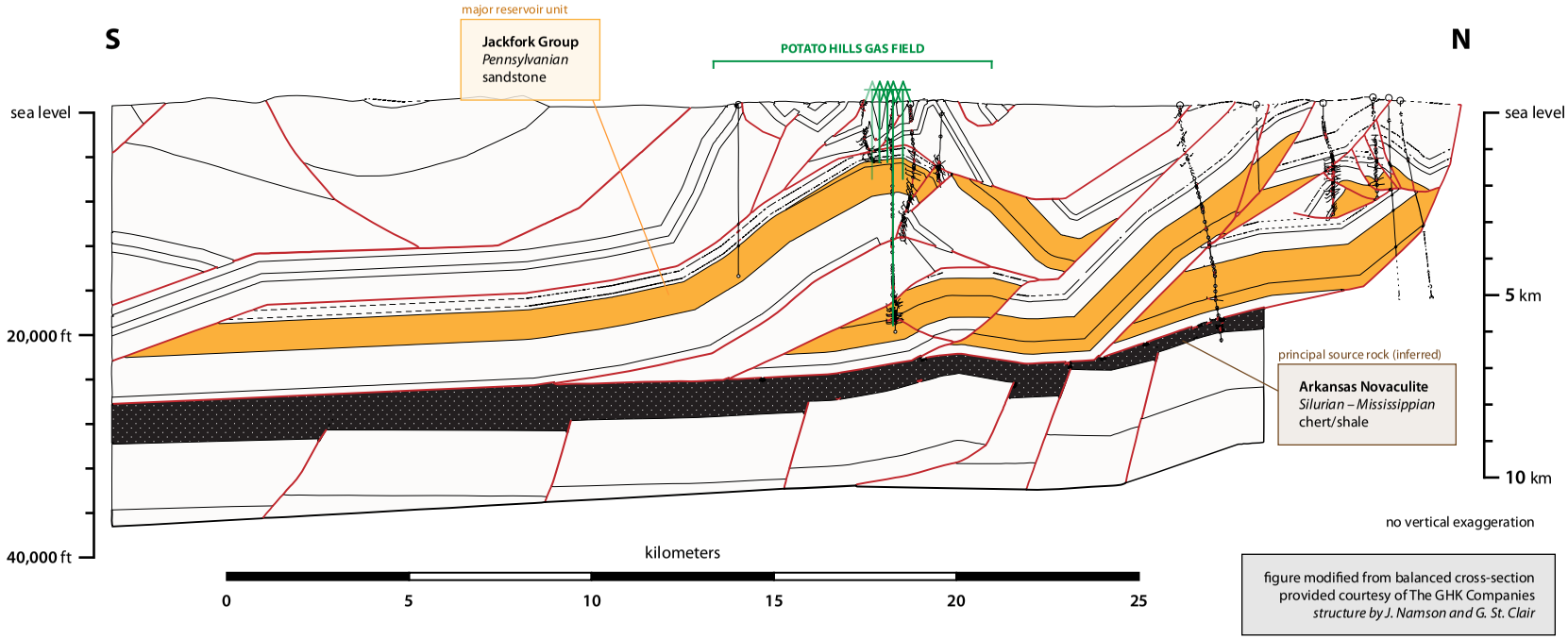

Figure A.2 | Balanced geologic cross-section through the Potato Hills for A–A′ (Fig. A.1). The original cross-section on which this figure is based was provided courtesy of The GHK Companies. Structural interpretation was by J. Namson and G. St. Clair. Reservoir sands and presumed source are highlighted in orange and black, respectively. Faults are highlighted in red. Projections of studied wells onto the cross-section are shown in green.

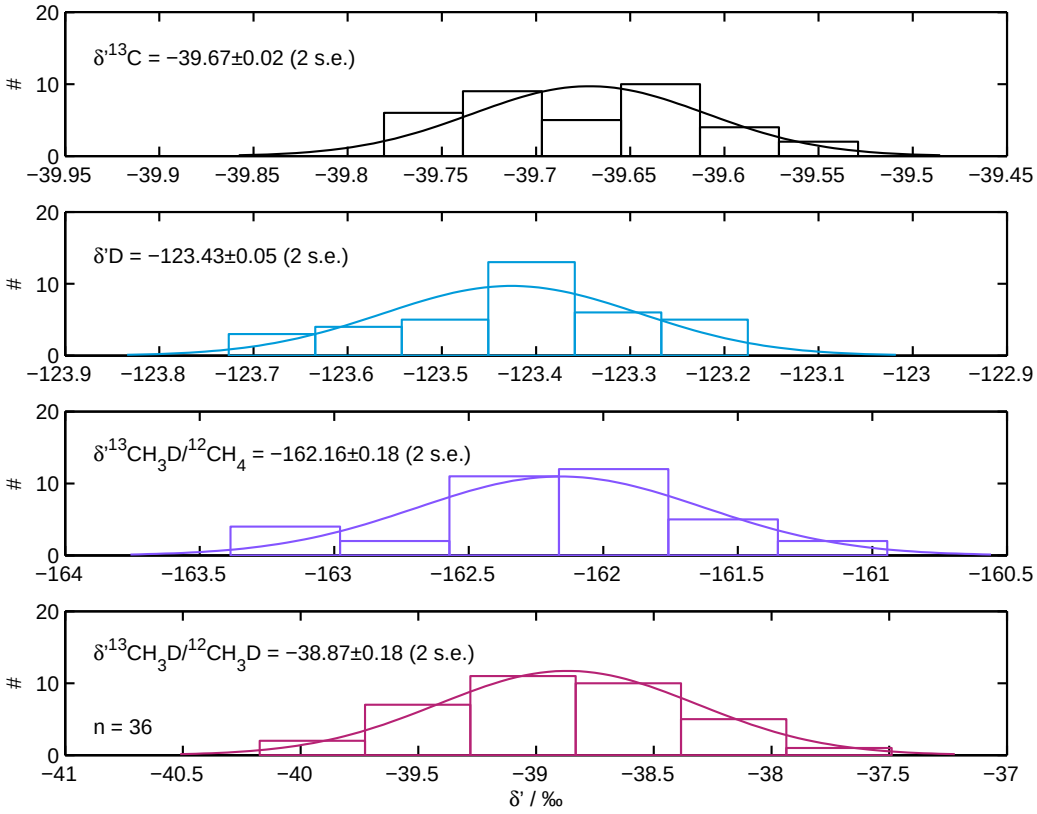

Figure A.3 | Histogram of log-delta values (referenced to an arbitrary set of isotopologue ratios) for CH_4 purified from the Hicks #1 cylinder, measured on the TILDAS during a single sample run (~10 hours). Here, *n* represents the number of measurement cycles made during this run; in each measurement cycle, samples are measured for 100 seconds, and each sample measurement is bracketed by measurements on the reference gas.

There was no evidence of compromised sample integrity when the samples were examined in 2013–2014. All gas cylinders studied contained gas at high pressure, and analyses of $\delta^{13}C$ and δD in 2014 yielded data that matched those obtained ten years earlier (Table A.1).

One sample (Mary 2-34) was later mistakenly shipped to UCLA, where it resided for a year. The missing sample was located and returned to MIT with the help of I.E. Kohl. All samples are now safely back at WHOI.

A.2.2 Analysis

These samples were the first "real" samples ever measured for clumped isotopologues of methane at MIT. At the time these data were obtained, the Methane PrepLine (Appendix C) had not yet been built, so sample purification was done manually in a cryogenic vacuum line interfaced with a gas chromatograph supplied with helium carrier and a handmade packed column held near ambient temperature.

Analyses of the methane clumped isotopologue $^{13}CH_3D$ were made with a prototype tunable infrared laser direct absorption spectrometer (TILDAS) developed by Aerodyne Research, Inc. (Billerica, MA) and housed in the Hardcore Stable Isotope Laboratory at MIT. Analytical procedures are documented in Ono *et al.* (2014). A histogram of isotopologue data obtained on multiple measurement cycles ($n = 36$) for one sample is shown in Fig. A.3.

Table A.1 | Isotopic composition of methane from the Potato Hills gas field. Data taken at WHOI soon after sampling (Seewald and Whelan, 2005) are compared with data obtained on the same cylinders measured at MIT (via TILDAS) one decade later. All isotope values are in permil (‰).

			WHOI (c. 2003)		MIT (January 2014)			
Well Name	TD (km)	T_{res} (°C)	$\delta^{13}C$	δD	$\delta^{13}C$	δD	$\Delta^{13}CH_3D$ [a]	N
Cedar Creek	1.78	45	−38.1	−134	−38.4	−136.8	3.10 ± 0.25	2
Stevens #1	1.86	50	−36.9	−139	−38.1	−136.6	3.08 ± 0.37	3
Hicks #1	2.29	51	−37.0	−135	−38.2	−136.8	3.17 ± 0.20	3
Koopmans #1	2.20	53	−39.5	−133	−40.9	−135.3	3.30 ± 0.12	5
Mary 2-34	6.29	126	−31.2	−136	−32.5	−139.7	2.94 ± 0.20	5

TD, total depth; T_{res}, reservoir temperature; and N, number of independent replicate purifications and measurements.

[a] The uncertainty on the $\Delta^{13}CH_3D$ incorporates propagated 95% confidence intervals calculated assuming a normal distribution, and also includes the error on $\Delta^{13}CH_3D$ of AL1.

A.3 RESULTS & DISCUSSION

A.3.1 Preservation potential of clumped isotopologue temperatures in migrated thermogenic gases

Drilled depths and measured reservoir temperatures shown in Table A.1 were obtained from public records on the website of the Oklahoma Corporation Commission. Comparison of bottom-hole temperatures to depth for 16 wells in this area (data from GHK, not shown) suggests a local geothermal gradient between 15 and 25 °C per kilometer, consistent with the reported reservoir temperatures and known depths of those reservoir intervals (Fig. A.2).

The $\Delta^{13}CH_3D$ values of gases from all wells were identical within error, although the deeper Mary 2-34 sample may carry a slightly lower value (by ~0.2‰). Samples yielded geologically-realistic apparent equilibrium temperatures of ~150 ± 30 °C (Fig. A.4).

To test if these signals might be primary (i.e., if $\Delta^{13}CH_3D$ values are the same as those these gases had at the time of their expulsion from the source rock), we modeled the kinetics of hydrogen isotopic exchange (Fig. A.4). This model uses the rate of CH_4–H_2O isotopic exchange reported by Koepp (1978), and assumes that rates scale with temperature according to the Arrhenius equation. These rates are subject to large uncertainty; this is discussed in more depth in Chapter 3 and in reviews by Sessions *et al.* (2004) and Schimmelmann *et al.* (2006). Furthermore, the model assumes that $\Delta^{13}CH_3D$ values will not reset unless CH_4 exchanges with H_2O—that is, homogenous isotope exchange is implicitly excluded as a mechanism for isotopologue reordering. It is unknown if mineral surfaces encountered by the hydrocarbons may serve as catalysts for homogenous isotope exchange (Shipp *et al.*, 2014); this would lower the activation energy and allow isotopic reordering at lower temperatures than indicated.

Migration from source to reservoir is generally thought to be fast relative to the process of petroleum generation in the source rock (England *et al.*, 1991). A conservative estimate of rates of cooling during fluid migration was applied (10 °C per Myr). The model results suggest that isotopic reordering of C–H bonds within CH_4 is sluggish or non-detectable on timescales relevant to petroleum migration at temperatures below 200 °C (Fig. A.4). This suggests that if methane generation occurred in the source rocks at <200 °C, the signature the methane carried at generation would have been preserved during its residence in the shallower traps. The deeper traps may have exceeded this temperature, however (see § A.3.2). The uniformity of δD but variation in $\delta^{13}C$ with depth indicates that hydrogen exchange has occurred, either by CH_4–H_2O

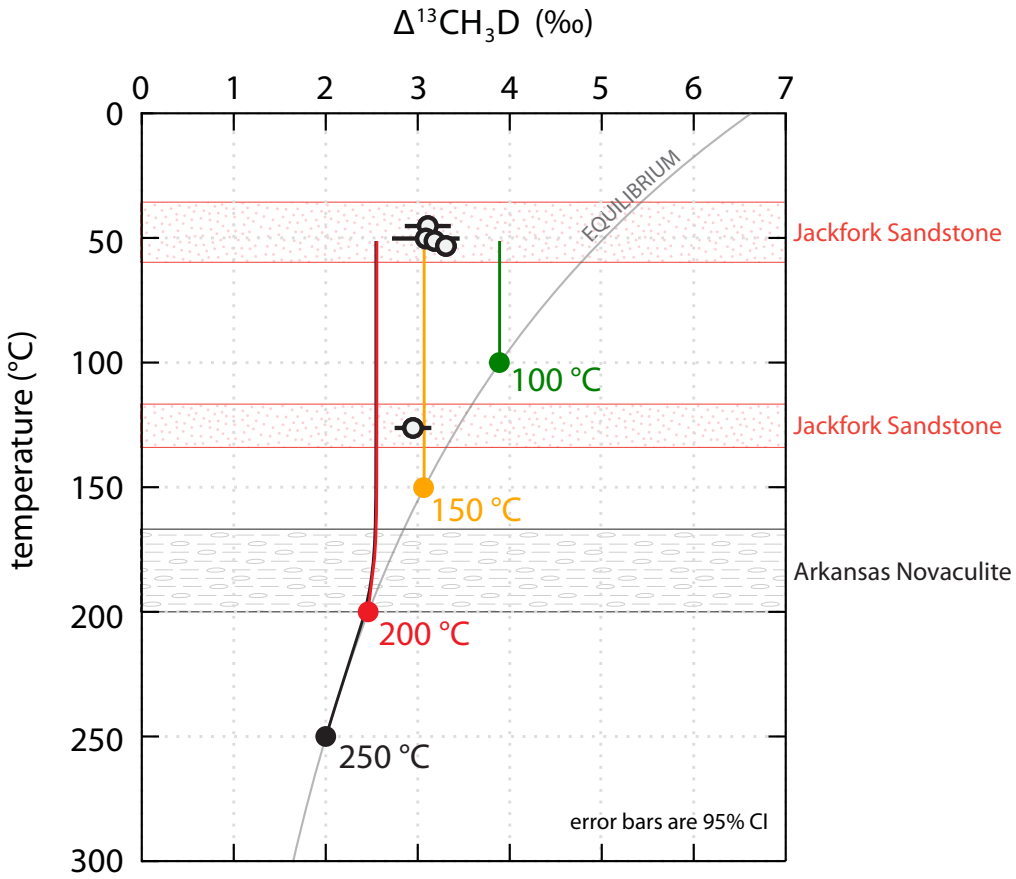

Figure A.4 | Model of migrating gases. The colored points on the model curves represent initial compositions of natural gases that were generated at 350 Ma at temperatures from 100 to 250 °C. The gases were assumed to be carrying $\Delta^{13}CH_3D$ values equal to those expected for equilibrium at these starting temperatures. These model gases then were cooled at a rate of 10 °C per Myr until 330 Ma, at which cooling ceased. Curves show the predicted clumped isotopologue compositions of gases (x-axis) with temperature (y-axis). Clumped isotopologue reordering was treated as a first-order reaction obeying the Arrhenius equation, with pre-exponential factor 6.1×10^9 s^{-1} and activation energy 209 kJ mol^{-1} (estimated from the data of Koepp, 1978). Data from Table A.1 are shown for comparison. The equilibrium curve is that of Wang *et al.* (2015), for which the equation is listed in Appendix C (Eqn. C.2).

directly, or more likely, between precursor kerogen and water (Clayton, 2003). Supporting this is evidence that the Arkansas Novaculite in wells in the vicinity of the Potato Hills may have reached very high maturities (vitrinite reflectance >4% R_o) (Guthrie *et al.*, 1986).

A.3.2 C & H isotopes and the filling or fate of fluids in the Potato Hills reservoirs

With the exception of the deep well (Mary 2-34), all $\delta^{13}C$ values for methane are quite homogeneous at around −38‰. The methane from Mary 2-34 is characterized by a distinctly ^{13}C-enriched value of −32‰, whereas δD is nearly identical to those of the wells which produce from the shallower reservoir interval.

Because $\delta^{13}C$ values of methane tend to increase with increasing thermal maturity (Hunt, 1996), the marked ^{13}C-enrichment in the Mary 2-34 sample suggests that the deeper reservoir interval was filled by gases that were, on average, generated at higher temperatures or at a later stage than the gases which accumulated and were retained in the shallower structural traps. Several scenarios are possible: (*i*) the shallower trap filled first, followed later by charging of the deeper trap by more mature gases; (*ii*) charging of the deeper trap occurred first with enough gas to fill the deeper reservoir, and spilled over such that the shallower unit received a vicarious, ^{13}C-depleted charge; or (*iii*) C_{2+} gases in the deeper reservoir have experienced thermal breakdown or stepwise oxidation such that the originally ^{13}C-depleted signature of CH_4 has been diluted by heavier carbon-isotope signals derived from C_{2+}.

Interpretations of mapped and extrapolated fault geometries suggest that thrusting in the frontal and central thrust belts of the Ouachitas occurred in a break-forward style (Miser, 1929; Cemen *et al.*, 2002). This implies that crustal shortening, accommodated by development of the imbricate thrust sheet, was characterized by the formation of new thrusts underneath older thrusts as the units in the hanging wall moved forward along the detachment (Boyer and Elliott, 1982; Shaw *et al.*, 1999). If break-forward thrusting was responsible for the development of the structural traps of the Potato Hills field, the first scenario may well be possible.

No information is available to evaluate the second scenario (fill-to-spill and tertiary migration).

The third scenario is supported by observations of high concentrations (tens of millimolar) of acetic acid in reservoirs of the Potato Hills field (Seewald and Whelan, unpublished data). Such high concentrations of short-chain carboxylic acids are not atypical of oilfield waters (Kharaka *et al.*, 1973; Willey *et al.*, 1975; Carothers and Kharaka, 1978; Seewald, 2003), and may reflect stepwise oxidation of C_{2+} alkanes to carboxylic acids during residence of the hydrocarbon fluids in the deep reservoirs (Shock, 1988; Seewald, 2001b). Considering that temperatures in the lower reservoir exceed 120 °C currently, and were likely much higher in the past given that several kilometers of overburden may have eroded since the Permian (Godo *et al.*, 2011), decomposition of C_{2+} alkanes at depth may also explain features of the isotopic reversals observed (Burruss and Laughrey, 2010; Tilley *et al.*, 2011; Zumberge *et al.*, 2012; Tilley and Muehlenbachs, 2013).

A.4 ACKNOWLEDGMENTS

I thank Jeff Seewald for sharing his samples and data. The GHK Companies provided much of the background data, the funding for visits to the producing wells by J. Seewald, J. Whelan, and S. Sievert, and support for analyses performed at WHOI in the early 2000s. My studies on the Potato Hills were conducted while under the support of the NDSEG Fellowship program.

Appendix B

Incorporation of water-derived hydrogen into methane during artificial maturation of kerogen under hydrothermal conditions

ABSTRACT

To investigate the origin of H in hydrocarbons, particularly methane, we reacted a sample of organic-rich Eagle Ford shale with D_2O under hydrothermal conditions in a flexible Au-Ti cell hydrothermal apparatus in a water:rock ratio of approximately 5:1. Temperatures were increased from 200 to 350 °C over the course of one month, maintaining pressure at 350 bar, and the concentrations of aqueous species and methane isotopologues produced were quantified. Production of H_2, CO_2, alkanes, and alkenes was observed. Methane formed during the early stages of the experiment at 200 °C was primarily CH_4 with some CH_3D, whereas at higher temperatures, increasing proportions of deuterated isotopologues were produced, such that near the end of the experiment, the concentration of CD_4 exceeded that of all other isotopologues combined. These results suggest that competition between rates of kerogen-water isotopic exchange and natural gas generation may govern the D/H ratio of thermogenic gases.

This appendix contains preliminary results from experimental work conducted in collaboration with Jeff Seewald, Eoghan Reeves, and Sean Sylva at WHOI with input from Shuhei Ono.

B.1 INTRODUCTION

Controls on δD values of thermogenic natural gases are often attributed to kinetically-controlled fractionation during pyrolysis of kerogen or oils. There are now several studies which have investigated D/H ratios of methane and other hydrocarbons as a function of maturity (Sackett, 1978; Berner *et al.*, 1995; Sackett and Conkright, 1997; Tang *et al.*, 2005; Ni *et al.*, 2011). However, kinetic isotope effects involving hydrogen addition or abstraction are often large and by themselves do not explain the geologically-reasonable apparent equilibrium temperatures of ~150 to 220 °C obtained for reservoir gases that have been studied for their clumped isotopologue compositions (Stolper *et al.*, 2014a; Stolper *et al.*, 2015; Wang *et al.*, 2015; Young *et al.*, 2017). There is also evidence that δD values of CH_4 approach values expected for isotopic equilibrium between CH_4 and H_2O in formation waters at temperatures characterizing reservoirs and/or source rocks (~150 to 250 °C) (Clayton, 2003; Wang *et al.*, 2015), although findings of insignificant hydrogen exchange occurring under these conditions also exist (Yeh and Epstein, 1981). In order for methane samples to have approached or attained equilibrium values of $\Delta^{13}CH_3D$ and $\Delta^{12}CH_2D_2$, there must be a pathway by which either (*i*) isotopes can be exchanged amongst methane isotopologues alone, (*ii*) methane isotopologues exchange hydrogen with water or organic molecules, or (*iii*) methane isotopologues are derived from methyl moieties which contain C–H bonds that have pre-exchanged with water prior to forming methane (Hoering, 1984; Smith *et al.*, 1985; Schimmelmann *et al.*, 1999; Lis *et al.*, 2006; Schimmelmann *et al.*, 2006).

Here, we study the origin of C–H bonds in thermogenic methane by heating kerogen in the presence of D_2O, and examining the degree of deuteration in the generated methane. This experiment is conceptually very similar to those conducted by Hoering (1984), Lewan (1997), and Schimmelmann *et al.* (2001). However, none of these workers quantified the extent of deuteration in the produced natural gases, though Lewan (1997) mentioned that methane formed in his experiments contained deuterium.

B.2 METHODS

B.2.1 Experimental methods

Experiments were conducted in a gold-titanium reaction cell housed within a flexible cell hydrothermal apparatus (Seyfried *et al.*, 1987) at WHOI. The reaction cell was pre-treated prior to loading by an overnight soak in acid.

A sample of Eagle Ford shale from Uvalde County, Texas, USA was used as the source material for this experiment. The sample was kindly provided to J. Seewald by Keith F. M. Thompson (PetroSurveys, Inc.), and was powdered to <250 μm and Soxhlet-extracted (by Carl Johnson, WHOI). After extraction, the rock contained about 11% total carbon, about half of which is acid-dissolvable carbonate (Table B.1). The reaction cell was loaded with 10.03 grams of the Soxhlet-extracted powder.

The starting fluid in Experiment EF-D2O-1 ("DIPPIE-1") was heavy water (D_2O, 99% purity, Cambridge Isotope Laboratories, Inc.) containing some NaCl (0.497 mol/kg). The added NaCl allows for detection of dilution of the fluid by deionized water from the pressure vessel in the case of a leak in the reaction cell. The reaction cell was loaded with 55.03 g of this starting fluid.

B.2.2 Analytical methods

To monitor the fluid composition and the extent of deuteration, samples aliquots of fluid were withdrawn through the capillary exit tube into gastight glass/PTFE syringes. Immediately prior to a sampling event, a small amount (~0.5 g) of fluid was removed and discarded in order to flush the exit tube of any residues.

The concentration of molecular hydrogen (H_2) was determined after headspace extraction using a gas chromatograph supplied with nitrogen carrier gas, and equipped with a molecular sieve 5Å column and

(wt%)	UNEX	EX*	DECA
C	12.1	11.0	6.23
H	0.38	0.25	1.24
N	0.18	0.17	0.74
S	0.37	<0.2	2.3

* Used in the experiment.

Table B.1 | Elemental analysis of Eagle Ford shale powder that was either untreated (UNEX), Soxhlet-extracted (EX), or extracted + decarbonated (DECA). Data from C. Johnson, WHOI, 1996.

thermal conductivity detector. Analytical reproducibility of H_2 data is ±10% or better (2*s*), however, accuracy of reported concentrations is currently unknown, because the relative response of H_2 and D_2 (likely to be the main form of molecular hydrogen) in the GC-TCD has not yet been determined. Residual liquid after headspace extraction was diluted with MilliQ water and saved for analysis of major cations and anions, or stored with dichloromethane in the fridge in a screw capped vial for analysis of non-volatile organic compounds.

Concentrations of total dissolved inorganic carbon ($\sum CO_2$) and C_1 to C_6 alkanes and alkenes were determined using a purge-and-trap cryofocusing device coupled to a gas chromatograph equipped with a Porapak Q column and serially-connected thermal conductivity and flame ionization detectors. Analytical procedures were as described in Reeves *et al.* (2012). Analytical reproducibility on duplicate samples was ±5% or better (2*s*). The C_5 and C_6 compounds could not be quantified accurately due to their semi-volatile nature; however, C_5 and C_6 were detected at all sampling points.

At each sampling, a separate ~1 to 2 ml aliquot was injected directly into a pre-weighed, evacuated serum vial capped with boiled blue butyl rubber stoppers, for analysis of the extent of deuteration of methane. A Hewlett-Packard (HP) 6890 gas chromatography-mass spectrometry (GC-MS) system equipped with a 5Å molecular sieve column (HP-PLOT 30 m × 0.32 mm × 12.0 µm) and HP 5973 mass selective detector was used to determine the amount of deuteration in CH_4. Ion currents were monitored at integral masses between m/z 10 and 50. Extracted ion currents were quantified at m/z 14 through 23 for methane. Expected fragmentation patterns of each of the methane-*d* isotopologues were determined by analysis of commercial synthetic standards (>98% purity, Cambridge Isotope Laboratories, Inc.).

B.3 RESULTS & DISCUSSION

B.3.1 Concentrations of aqueous species

Measured concentrations of aqueous species are shown in Fig. B.1. Concentrations of H_2 increased from undetectable (<10 µmol/kg) to up to 0.8 mmol/kg at the end of the experiment. Increasing concentrations of H_2 within temperature stages of the experiment suggests that generation of petroleum, as opposed to a mineral redox buffer, is influencing the H_2 concentration. H_2 increased much more slowly during the >300 °C stages compared to heating at 300 °C and below.

The concentration of $\sum CO_2$ increased during the early stages of the experiment, and leveled off at ~50 mmol/kg at 350 °C. This might indicate that carbonate reached saturation and began to precipitate (Seewald *et al.*, 1998); to verify this, measurements of major cations are required. Production of CO_2 as the most abundant product of hydrothermal alteration of kerogen is also consistent with prior experimental work (Seewald, 2003). Alternatively, carbonate could have been released from the rock as it had not been decalcified prior to heating.

Concentrations of methane increased at all time steps, as did concentrations of detected *n*-alkanes. Except for the beginning of the experiment, molar concentrations of C_1 and $\sum C_{2-4}$ were very similar and increased in near lock step.

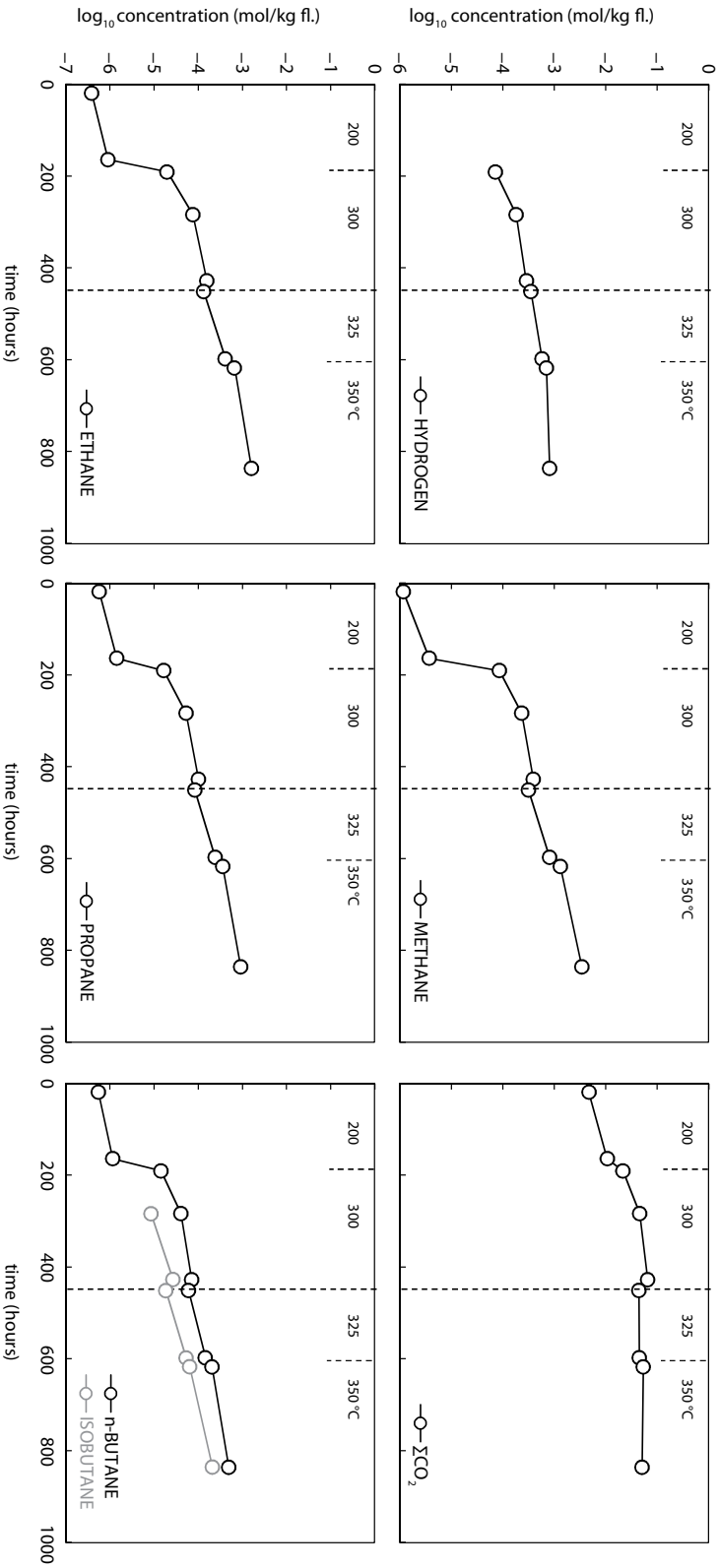

Figure B.1 | Concentrations of aqueous species during experiment EF-D2O-1. Note the log scale for concentration.

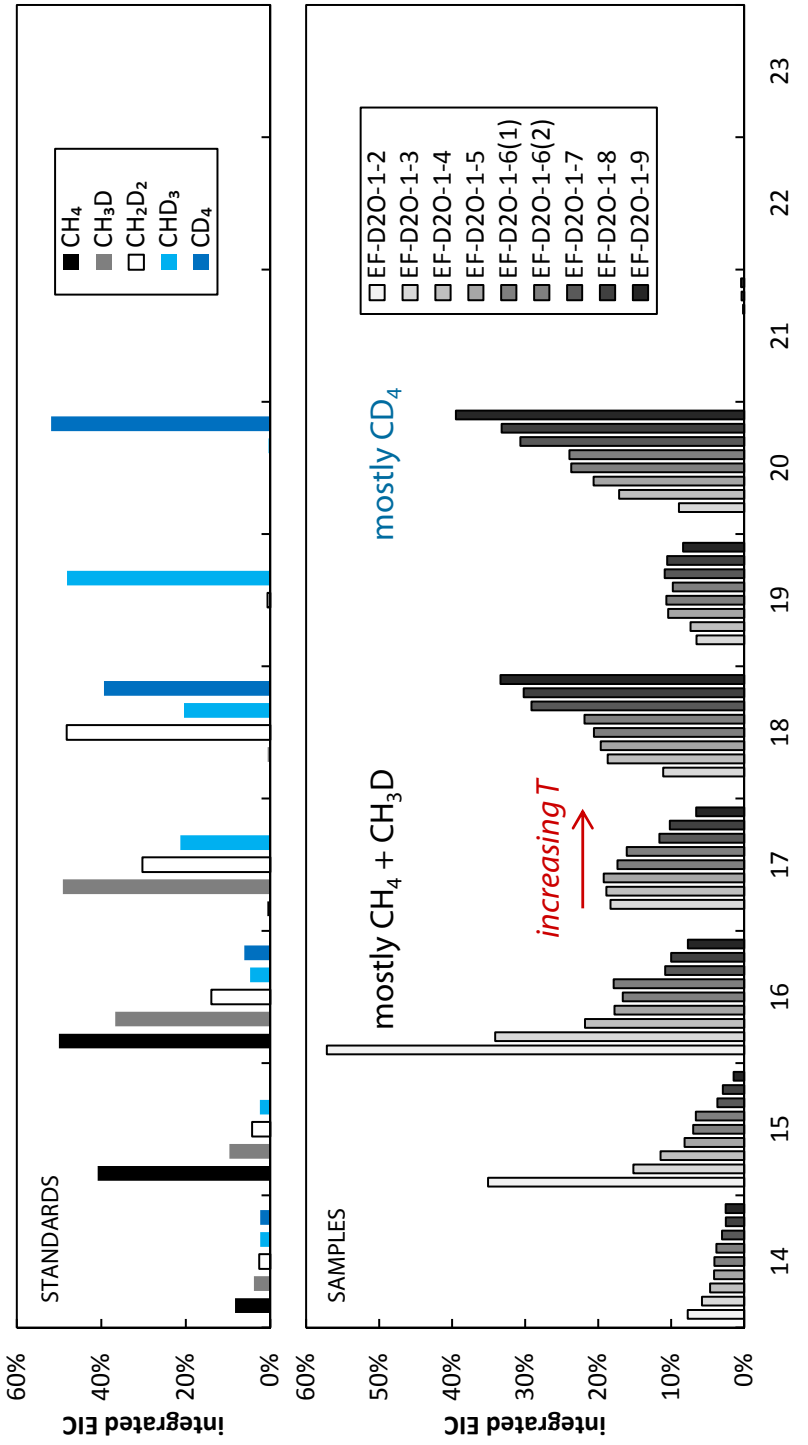

Figure B.2 | Mass spectra of methane generated from artificial maturation of Eagle Ford shale in the presence of D_2O.

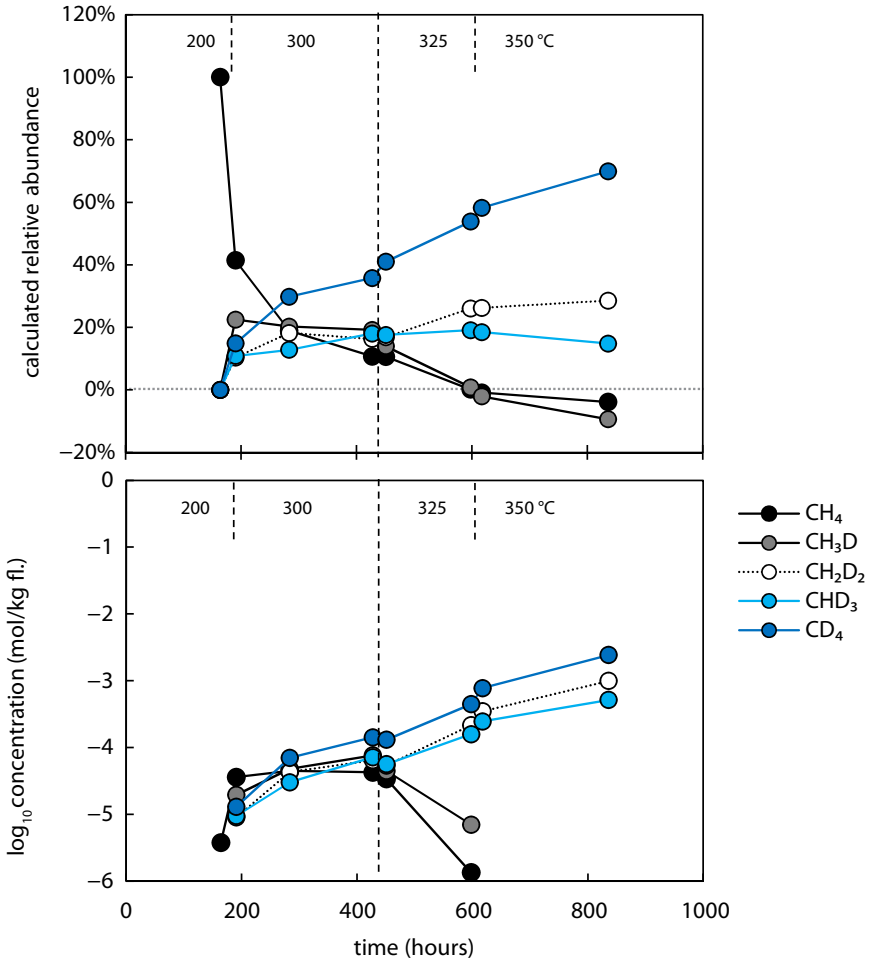

Figure B.3 | Estimated relative and absolute abundances of methane isotopologues. Concentrations less than zero are an artifact of uncertainty in standardization and may potentially be corrected by applying algorithms to account for contributions of fragment ions to peaks in the lower range of *m*/*z*. Note the log scale on the *y*-axis in the bottom panel.

B.3.2 Production of deuterated methane

The relative abundance of methane-*d* isotopologues was quantified by GC-MS for all samples except the one from timepoint #1, for which no methane peaks of usable size could be obtained (Fig. B.2).

Methane formed during the early stages of the experiment at 200 °C was primarily CH_4 with some CH_3D, whereas at higher temperatures, the isotopologues produced consist almost exclusively of CD_4, CH_3D, and CH_2D_2 (Fig. B.3). These results suggest that at relatively lower temperatures of ~200 °C, the rate of methane generation approaches or exceeds the rate of D/H exchange between water and kerogen, whereas at higher temperatures, extensive D/H exchange between kerogen (or oils, if they are also precursors of methane) and water occurs prior to methane generation. CD_4 became the dominant methane species at temperatures of 300 °C and above, suggesting that more than 50% of all labile, methane-generating sites on kerogen were fully deuterated. Alternatively, the dominance of CD_4 might be explained by direct CH_4–H_2O isotopic exchange occurring after the generation of primarily non-deuterated methane. This is unlikely given the sluggish pace at which D/H exchange occurs for methane (Reeves *et al.*, 2012). Experiments in which normal water is heated in the presence of CD_4 while the D/H of water is monitored may yield a more sensitive determination of the exchange rate constant for CH_4–H_2O.

Production of CH_4 at the beginning of the experimenst indicates that the "capping" hydrogen was derived

Table B.2 | Concentration of aqueous species during Experiment EF-D2O-1, heating of Soxhlet-extracted Eagle Ford shale at 200 to 350 °C and 350 bar in the presence of saline D_2O fluid.

Sample #	Time (h)	H_2 (µmol/kg)	CH_4 (µmol/kg)	$\sum CO_2$ (mmol/kg)	C_1/C_{2-4}	pD (25 °C)
Experiment begun with 52.6 g fluid at temperature of 200 °C						
1	19	BDL (<10)	1.2	4.8	0.11	
2	164	BDL (<10)	3.8	10.8	0.37	
Temperature raised to 300 °C						
3	191	773	87	21.9	1.00	
4	284	183	235	45.8	0.86	
5	427	290	396	65.5	0.86	
Injected ~18.3 g starting fluid and raised temperature to 325 °C						
6	451	353	319	44.7	0.89	
7	598	586	825	45.3	0.85	
Raised temperature to 350 °C						
8	617	718	1.32×10^3	54.4	0.89	
9	836	821	3.47×10^3	51.2	1.00	5.90

[a] The listed pD value was calculated from pH measured with a glass electrode: pD = $pH_{measured}$ + 0.41 (Glasoe and Long, 1960).

from kerogen or other H-containing species in the rock as opposed to water. Alternatively, the CH_4 observed at the first time point may have been sorbed to a solid phase and leached into the fluid. Production of CH_4 and CH_3D appeared to cease by midway through the 300 °C stage. Continued (though relatively minor) production of methane that was not fully-deuterated (CHD_3 and CH_2D_2, Fig. B.3, bottom panel) suggests that kerogen or oil from which methane was generated did not fully exchange before methane formed.

While examining the total ion and extracted ion chromatograms to quantify the deuteration in CH_4, an unknown and unexpected peak was found eluting immediately following the CH_4 and air peaks. This mystery peak appeared to yield methyl fragments that were also progressively more deuterated with reaction time. Re-analysis of several samples while scanning a higher mass range suggested that the mystery compound had stable fragments near m/z 45 to 50 (depending on degree of deuterium substitution). This was verified by GC-MS analysis of a commercial isobutane standard (mostly isobutane-d_0) which yielded a base peak at m/z 43. No attempt to quantify the degree of deuteration in isobutane was made.

B.4 ACKNOWLEDGMENTS

Financial support for this work was provided by a Shell-MITEI Fellowship and by NSF award EAR-1250394 to S. Ono.

Appendix C

Additional methodological details, data, and site descriptions

This section provides additional, unpublished information regarding methods or field observations that support the research presented in the preceding chapters.

C.1 EQUILIBRIUM $\Delta^{13}CH_3D$ VERSUS TEMPERATURE

Figure C.1B shows the calculated values of ln K_{eq} vs. temperature for the reaction:

$$^{13}CH_4 + {}^{12}CH_3D \rightleftharpoons {}^{13}CH_3D + {}^{12}CH_4 \tag{C.1}$$

A good fit to the curve is obtained with the expression:

$$1000 \ln K = \left(1.68169 \times 10^{14}\right)\left(\frac{1}{T^2}\right)^3 - \left(1.40754 \times 10^{10}\right)\left(\frac{1}{T^2}\right)^2 + \left(6.72697 \times 10^{5}\right)\left(\frac{1}{T^2}\right) - 0.28671 \tag{C.2}$$

where temperature T is in kelvin.

C.2 NOTES ON ANALYTICAL PROCEDURES

C.2.1 Isolation of CH_4 using cryofocusing-preparative gas chromatography

Figure C.2 shows a schematic of the methane preparation system used to isolate CH_4 for measurement of $\Delta^{13}CH_3D$ by TILDAS at MIT from mid-2014 onwards (Inagaki *et al.*, 2015; Wang *et al.*, 2015; Lopes *et al.*, 2016; Wang *et al.*, 2016; Whitehill *et al.*, 2017). The system consists of a cryotrapping-preparative gas chromatography system interfaced with a vacuum line and a helium supply. A software interface built using National Instruments LabVIEW controls all pneumatically- and electronically-actuated valves, pistons for dewars on cold traps, and heating coils. Operation is mostly automatic and hands-free. Preparation time is <45 minutes for a typical sample of 1–15 cm^3 SATP CH_4 and <200 cm^3 air. Air blanks in the purified gas are typically <0.10 cm^3 SATP.

The retention time of methane on the PrepLine column depends on the amounts of both CH_4 and "air" (O_2, Ar, N_2, CO) in the sample, as shown in Fig. C.3.

C.2.2 Correction of non-linearity in isotopologue concentration data

Data retrieved from TDLWintel (Aerodyne Research, Inc., Billerica, Mass.)[1] are in the form of number densities (ND) that the software calculates from line parameters in the HITRAN database (Brown *et al.*, 2013; Rothman *et al.*, 2013). For all clumped isotopologue data collected in this thesis except those in Appendix A,

[1] For a history of the development of TDLWintel for applications with tunable diode and quantum cascade laser instruments, see Zahniser *et al.* (1995), Horii *et al.* (1999), Nelson *et al.* (2002), and Nelson *et al.* (2004).

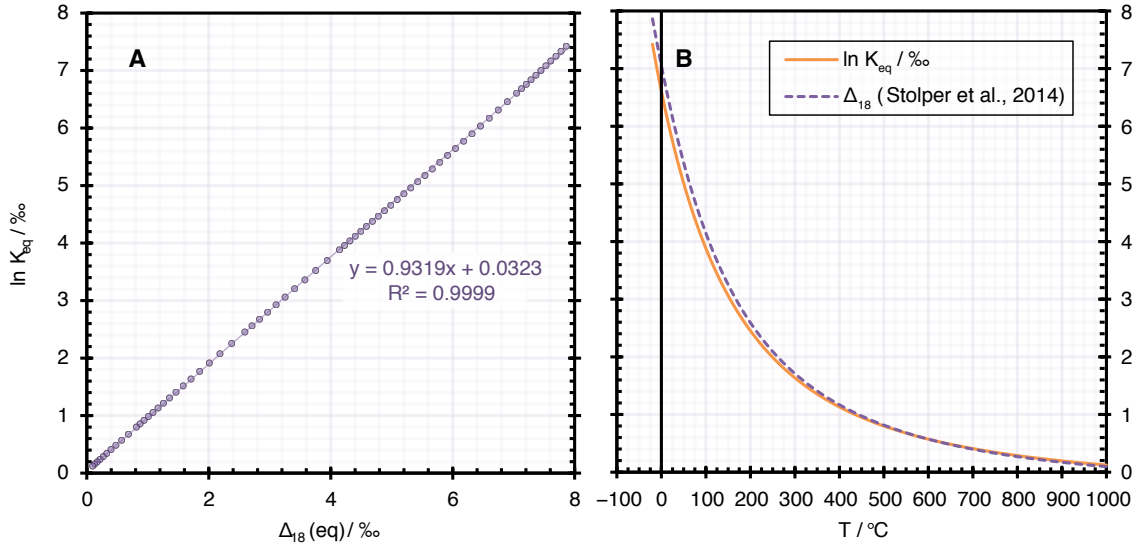

Figure C.1 | Equilibrium Δ vs. T curves. (**A**) Conversion between equilibrium Δ_{18} values and equilibrium $\Delta^{13}CH_3D$ values. Note that conversion of Δ_{18} to $\Delta^{13}CH_3D$ can only be done if it is known or can be assumed that methane isotopologues have attained their equilibrium distribution at the temperature indicated by both $\Delta^{13}CH_3D$ and $\Delta^{12}CH_2D_2$. Nonequilibrium Δ_{18} values cannot easily be converted to $\Delta^{13}CH_3D$, particularly if $\Delta < 0$ ‰ (anticlumped). (**B**) Comparison between equilibrium $\Delta^{13}CH_3D$ [= ln K_{eq} for the isotope exchange reaction (Eqn. C.1), defined following Ono *et al.* (2014) and calculated as in Wang *et al.* (2015)], and equilibrium Δ_{18} values from Stolper *et al.* (2014b).

the following correction scheme was applied. Isotopologue/isotope ratios reported were calculated from the corrected number densities (ND_{6x}^{corr}).

$$ND_{6x}^{corr} = ND_{6x}^{meas} + D_{6x} \cdot ND_{61}^{meas} + H_{6x} \cdot ND_{61}^{meas} \cdot \left(1 - \frac{ND_{61}^{meas}/P_{meas}}{ND_{61}^{pure}/P_{target}}\right) \tag{C.3}$$

Here, ND_{6x}^{meas} are the number densities returned by TDLWintel in the STR files, P_{meas} is the pressure of the sample in the cell, P_{target} = 1.0383 Torr, and ND_{61}^{pure} (= 3.88×10^6) is the number density of $^{12}CH_4$ for a sample of pure methane at the target pressure. Calibrated values for the correction factors D and H are listed in Table C.1. Note that the D and H here are just variable names, and are not related to deuterium or hydrogen. Numbering of isotopologues is from HITRAN.

I have found this correction scheme to sufficiently correct the observed non-linearity in $\delta^{13}CH_3D$ vs. $\delta^{12}CH_3D$ over a wide range of $\delta^{12}CH_3D$ values (from −600 to +400‰ vs. AL1) (the D term), as well as any air that might make its way into the system (up to 10%) (the H term; the portion enclosed in parentheses

Table C.1 | Correction factors for Eqn. C.3. Values were determined during 2014–2015. Values for D were derived from measurements of methane heated to equilibrium over a catalyst, and values for H were derived from measurements of methane admixed with different percentages of N_2 in the TILDAS cell.

#	isotopologue	D	H
61	$^{12}CH_4$	0	0
62	$^{13}CH_4$	0	−0.0033
63	$^{12}CH_3D$	0	−0.0036
64	$^{13}CH_3D$	3.00×10^{-3}	−0.0125

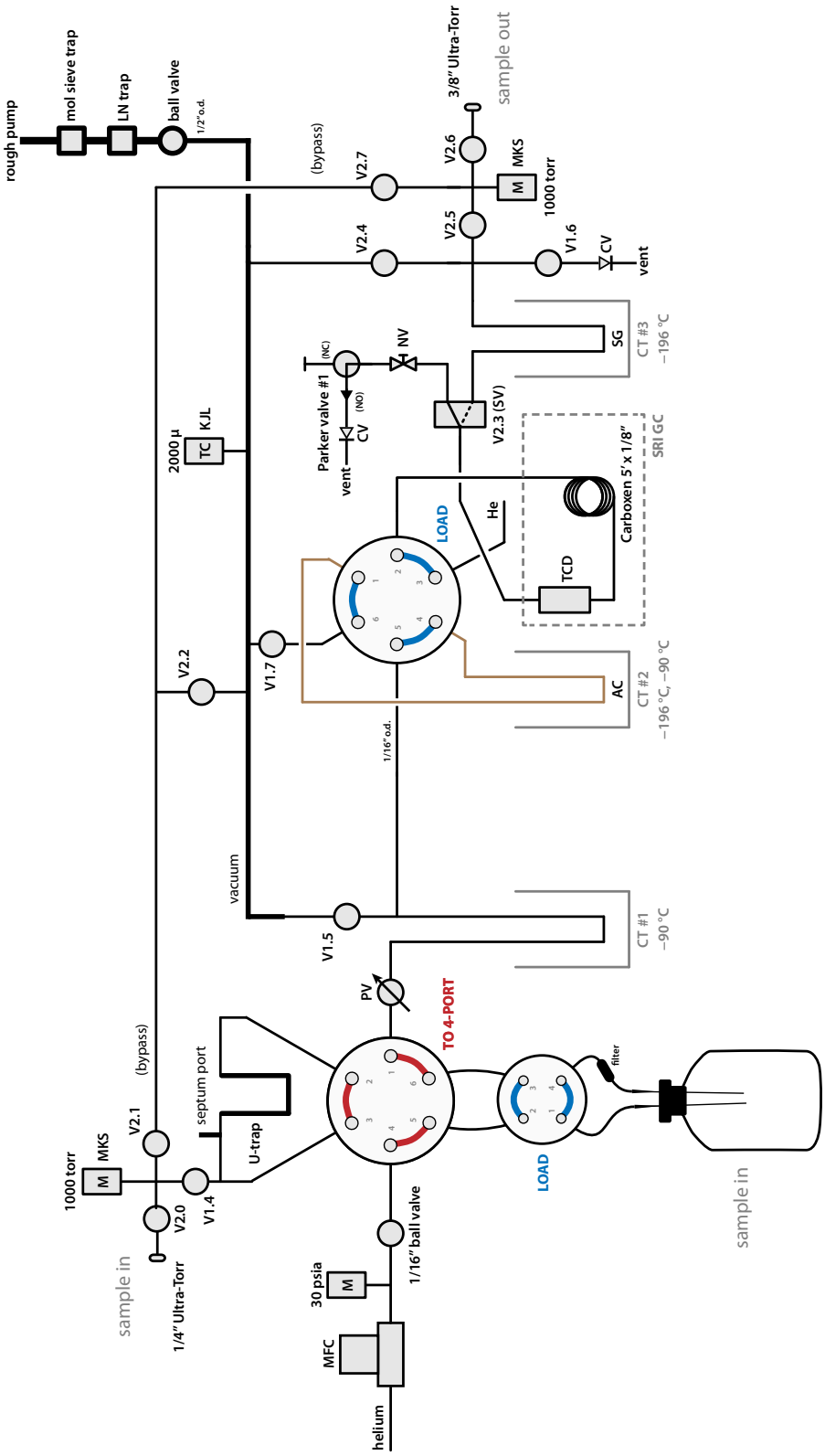

Figure C.2 | Schematic of methane preparation system at the MIT Hardcore Stable Isotope Laboratory.

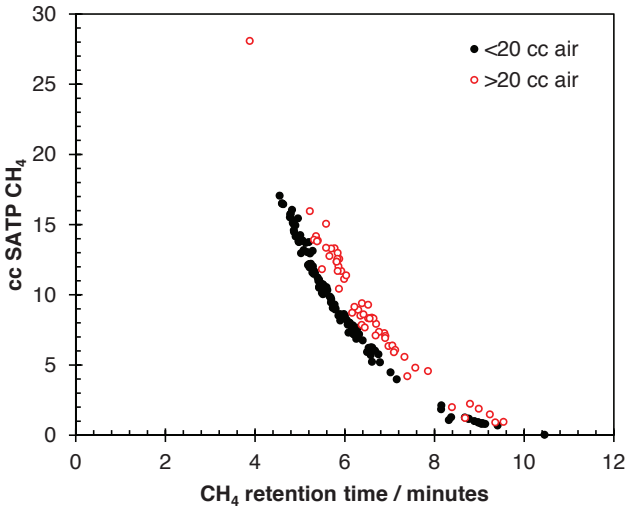

Figure C.3 | Dependence of the retention time of CH_4 (x-axis) on on-column volumes of CH_4 (y-axis) and "air" (= O_2 + Ar + N_2 + CO) on the PrepLine. The sample is heated off cold trap #2 and injected onto the column between 15 seconds and 1 minute. Compounds in order of elution are H_2, air, CH_4, and CO_2 + C_{2+}.

represents an estimate of the percentage impurity in the methane sample).[2] Part of the reason for the nonlinearity is that the Voigt profile cannot accurately account for the tailing of one or more large $^{12}CH_4$ peaks that are located immediately outside the wavelength region scanned by the laser.

C.2.3 Calibration of isotopic composition of in-house standards (AL1)

The $\delta^{13}C$ and δD values we report have been calibrated relative to PDB and SMOW, respectively, by measuring samples of NGS-1 (also known as NIST SRM 8559 and USGS-A) and NGS-3 (also known as NIST SRM 8561 and USGS-C), which are natural gas standards with published reference values for $\delta^{13}C$ and δD, as listed in § 2.4.4 (supplementary materials in Wang *et al.*, 2015). Samples of these natural gases were included in a set of calibration samples distributed by the USGS to various laboratories in the U.S. in July 2014. These samples were contained in IsoTubes (Isotech Laboratories, Illinois, USA) at pressures of ~3 bar. We subsampled aliquots of these gases through a septum adapter fitting (available from Isotech) using a 25 ml gastight syringe (SGE Analytical Science), and introduced the aliquots into our sample preparation system as described above.

Data shown in this thesis for $\delta^{13}C$, δD, and $\Delta^{13}CH_3D$ assume that reference gas AL1 has the isotopic composition −34.5‰, −147.7‰, and +2.41 ± 0.07‰ (95% CI) respectively, consistent with Wang *et al.* (2015) and with the values we provided to the UCLA group (Young *et al.*, 2016).[3]

C.3 MISCELLANEOUS UNPUBLISHED INFORMATION ON SELECTED SITES

This section contains miscellaneous data and ruminations that do not yet have a proper home in the literature.

[2] The D term corrects the observation that measured $\Delta^{13}CH_3D$ values are lower than their true values when δD of the sample is lower than that of the reference gas (and vice versa). The H terms correct an observed elevation in all three δ-values when impurities (primarily air) are present in the sample (important for the recycling technique used on small samples because air can accumulate in the sample due to small leaks in the TILDAS inlet system).

[3] The values originally reported in Ono *et al.* (2014) are quite different in δD (by ~20‰) for reasons as yet undetermined. Anecdotal experience suggests that this is probably related to a historical problem of poorly-anchored δD values for GC-IRMS analyses of methane within the isotope community, with resultant differences in calibration between the several IRMS labs from which values for δD of AL1 vs. SMOW were obtained. I favor the revised values listed above for reasons of consistency with the NGS gases and the new USGS samples.

C.3.1 Additional field notes and thoughts on selected localities studied by Wang *et al.* (2015)

C.3.1.1 Lower Mystic Lake

The water sample from Lower Mystic Lake shown in Chapter 2 was sampled from the water column at a depth of 18 mbll, which is below the chemocline. It should be noted that the isotopic composition of pore waters in Lower Mystic Lake sediments, at the time(s) and depth(s) at which the methane was generated, may be or have been significantly different than that of the water in the water column. This is because prior to the implementation of water management practices, Lower Mystic Lake was tidally-influenced, and the bottom waters were derived from seawater that flowed upriver along the bottom of the Mystic River. Dams constructed in 1908 and 1966 slowed or stopped the influx of seawater, and initiated a gradual reduction in the volume of anoxic and sulfidic bottom waters in the lake; the reduction in bottom waters was also accelerated by intentional removal of bottom waters by pumping and treatment in the 1980s and 1990s (Duval and Ludlam, 2001; Ludlam and Duval, 2001). Therefore, even though the δD of Lower Mystic Lake water at 18 mbll (−40.6 ± 1.0‰, 1*s*) was similar to that of Upper Mystic Lake (−39.2 ± 1.8‰, 1*s*), the Lower Mystic Lake sediment pore waters may have an isotopic signature that is closer to that of seawater (~0‰). This trend is observed in other coastal meromictic lakes in which seawater is trapped below the chemocline (Jeffries *et al.*, 1984). Assuming a value of 0‰ for the associated waters for methane generated in Lower Mystic Lake sediments would not affect our conclusions; on the contrary, it would suggest that the field of primary microbial methane could be constrained even more tightly than Fig. 2.2 indicates.

C.3.1.2 CROMO

The water sample from the Coast Range Ophiolite Microbial Observatory (CROMO) for which the δD_{water} value is reported in Chapter 2 was collected from the CSWold well. This well is noted in publicly-available reports on water quality monitoring in the area, but we do not presently have information on the depth(s) at which the groundwater at CSWold is derived. However, the δD value of the water is consistent with mixing between deep sedimentary-derived brines and meteoric waters (Peters, 1993).

At CROMO, the $\delta^{13}C$ and δD data alone cannot conclusively distinguish between thermogenic, abiogenic, and microbial origins of the methane. Specifically, the CROMO gases are highly similar in $\delta^{13}C$ and δD to the sample of natural gas from the Utica Shale (Table 2.1 and Fig. 2.1), where the gases are generally inferred to have been generated by thermogenic processes. The $\Delta^{13}CH_3D$ values at each field site are very dissimilar, however, with the Utica Fm. gases having an apparent temperature ~160 °C and the CROMO gases having apparent temperatures of 42 to 76 °C. Therefore, the clumped isotopic measurement provides information that is complementary to, and independent of, the bulk $\delta^{13}C$ and δD data, a conclusion that is not obvious from previous studies.

I suggest that at CROMO, the isotopic composition of the gases ($\delta^{13}C$, δD, and $\Delta^{13}CH_3D$) is inconsistent with a significant contribution from thermogenic sources of methane.[4] Furthermore, the C_1/C_2 ratio (measured using GC-FID) ranged from 360 to 1540 (Table 2.5) for samples of dissolved gases collected from 5 wells (including N-, CSW-, and QV- wells) sampled in July 2014; these C_1/C_2 ratios are within the range expected for microbial gases (>100), and outside the range of values typically observed for thermogenic gases (<100).

If the framework presented in Fig. 2.2 is correct, then a major source of uncertainty in differentiating between the possible processes of methane generation is the δD of the associated waters from which methane was produced. Specifically, meteoric water in the vicinity of CROMO generally has lower δD values (−70 to −50‰) (Peters, 1993; Kendall and Coplen, 2001) than what was measured for water from the CSWold well

[4] Note that this is somewhat different from what was written by Wang *et al.* (2015).

Table C.2 | Isotopologue data for methane samples from a rice paddy in Sherrill, Arkansas, USA, and the Chimaera seepage, Tekirova ophiolite, Turkey. Uncertainties reported are 95% confidence intervals. Values for $\delta^{13}C$, δD, and $\Delta^{13}CH_3D$ are reported relative to PDB, SMOW, and the stochastic distribution, respectively.

Site	Sample Name	$\delta^{13}C$ (‰)	δD (‰)	$\Delta^{13}CH_3D$ (‰)	T_{13D} (°C)
Sherrill	JTB-1-2	**−56.40** ± 0.05	**−336.47** ± 0.05	**−0.47** ± 0.23	**a.c.**
Chimaera*	S8_271949_4034797_12.10.2013	**−11.41** ± 0.03	**−119.50** ± 0.05	**3.19** ± 0.18	**141** +13/−12
	S4	**−11.62** ± 0.10	**−119.57** ± 0.10	**2.62** ± 0.54	**185** +55/−42
	S5	**−11.37** ± 0.10	**−119.42** ± 0.10	**2.98** ± 0.43	**156** +35/−29
	S9	**−11.38** ± 0.12	**−119.49** ± 0.14	**3.32** ± 0.34	**133** +23/−21

* Samples from Chimaera were measured more than 6 months apart (May to December 2014). The data appear to be unaffected by storage or instrumental drift over this period.

(−33‰; Table 2.5). Previous work on natural springs in the vicinity of the McLaughlin mine suggested that groundwater in this region can be best characterized as a two-component mixture consisting of formation brines derived from the Great Valley Sequence mixed with variable amounts of low-salinity meteoric water (Peters, 1993). Parenthetically, I note that the $\Delta^{13}CH_3D$-based temperatures for methane at CROMO (42 to 76 °C) would suggest isotopic equilibration with water that has a δD in the range of 0 to +20‰ (Fig. 2.2). This range is consistent with the δD value (+11‰) of the most saline waters ($[Cl^-]$ ~ 580 mmol/kg) sampled by Peters (1993) from springs in the vicinity of CROMO. The apparent temperatures of 42 to 76 °C for methane at CROMO are within the accepted temperature limits of life (generally <80 °C, but up to 122 °C for hyperthermophilic methanogens). Thus, based on the consistency of the observed isotopic signatures with other geochemical parameters (namely, $[H_2]$, Fig. 2.3), I infer a dominantly-microbial origin of the methane at CROMO originating from deep groundwater below the ophiolite body. Methanogenesis does not appear to occur to any appreciable extent in the shallow (meteoric) groundwaters. More recent microbiological work showing a total absence of archaea, including methanogens, from 16S sequences of the CROMO waters (Twing *et al.*, 2017) appears to support this conclusion.

C.3.2 Methane isotopologue data on assorted samples

C.3.2.1 Rice paddy, Sherrill, Arkansas, USA

A sample of gas was collected by J.T. Bird from a paddy rice field in Sherrill, Arkansas, USA in June of 2014. Bubbles of gas were released by gentle agitation of the submerged sediment, trapped in a funnel, and transferred to serum bottles containing several milliliters of 1 M NaOH added to inhibit microbial activity. On the day of collection, air temperature was 93 °F and skies were cloudy. Given that the daily lows had been steady at 70 °F for five days and the water on the field had been standing for "a good two weeks" (Sherrill local, via J.T. Bird, pers. comm.), estimated water temperatures are ~75 °F or about 25 °C.

Analysis of methane in the sample (Table C.2) yielded relatively low $\delta^{13}C$ and δD values (−56‰ and −336‰) typical of biologically-produced methane in wetlands. The $\Delta^{13}CH_3D$ value was anticlumped (ca. −0.5‰). This is the lowest degree of ^{13}C–D clumping we have observed in any natural methane sample aside from seep gases at The Cedars.

C.3.2.2 Chimaera seep, Tekirova ophiolite, Turkey

Four samples of gases collected by H. Hoşgörmez from the Chimaera seep (Yanartaş, meaning "flaming rock", near the Gulf of Antalya, eastern Mediterranean Sea; also the source of the first Olympic flame) were sent to us by G. Etiope. Samples arrived in glass vessels equipped with gas-tight stopcocks at both ends.

Analyses of methane in these samples yielded relatively high bulk $\delta^{13}C$ and δD values (−11‰ and −119‰, Table C.2) consistent with those previously reported for the same site (Hosgörmez, 2007; Hosgormez *et al.*, 2008; Etiope *et al.*, 2011b). The $\delta^{13}C$ values lie outside the typical range of known thermogenic methane (up to −20‰), and δD values are close to those required for D/H equilibrium with water of SMOW-like hydrogen-isotope composition at temperatures upwards of ca. 200 °C (Fig. 3.5). The $\Delta^{13}CH_3D$ data indicated apparent equilibrium temperatures averaging 153 °C. These temperatures are much higher than the <50 °C temperatures at which abiotic methane was inferred by Etiope *et al.* (2011b) to be synthesized here. Recently-published data obtained by the UCLA group on several other samples taken at Chimaera yielded $\Delta^{13}CH_3D$ values (ranging from +3.3 to +3.6‰) in general agreement with ours, as well as $\Delta^{12}CH_2D_2$ values that are at or near equilibrium at the same temperatures indicated by $\Delta^{13}CH_3D$ (Young *et al.*, 2017). These data indicate that methane carrying clumped isotopologue abundances similar to those of typical thermogenic gases probably comprises a large fraction of the Chimaera seep gas and that such gases may contribute more to the seepage flux than was previously suggested.

C.4 ERRATA AND CORRIGENDA TO PUBLISHED ARTICLES

The following mistakes have been found in the two articles published from this thesis.

Wang *et al.* (2015) (*i*) In Figure S4, the arrows denoting secondary isotope fractionation were labeled incorrectly; this is corrected in Fig. 2.8. (*ii*) Several footnotes in Table S3 were incomplete or incorrectly labeled; this is fixed in Table 2.3. (*iii*) Samples from the Powder River Basin were misstated as being from Wyoming. These samples were actually taken from wellheads located in Montana, near the border with Wyoming (API well numbers 25-003-22076, 25-003-22192, and 25-003-22074, in order of appearance in Table 2.1). Also, well "3CA34" was completed in the Cook Coal as stated in the paper, but produces from the stratigraphically-higher Canyon Coal according to information on the Montana Board of Oil & Gas Conservation website. Chapter 2 contains the corrected information. Several typographical errors have also been corrected.

Wang *et al.* (2016) In Table 2, citations to the Joelsson *et al.* papers were inadvertently switched. Joelsson *et al.* (2015) and Joelsson *et al.* (2016) should be cited for CH_4 + OH and Joelsson *et al.* (2014) for CH_4 + Cl. Table 4.2 lists the correct references.

C.5 ACKNOWLEDGMENTS

Shuhei Ono and Bill Olszewski provided key assistance with the design, construction, and troubleshooting of the Methane PrepLine. Kyle Delwiche and Genming Luo are thanked for their help in the field at Lower Mystic Lake, and for insightful conversations. Discussions with Matt Schrenk, Billy Brazelton, Katrina Twing, Mike Kubo, and Tori Hoehler helped form my views on the CROMO gases. Dan Ritter provided the information regarding locations of wells in the Powder River Basin. Jordan Bird graciously went out of his way to sample the Arkansas rice paddy (and take video footage!). Giuseppe Etiope is thanked for sending us the samples from the Chimaera seep.

References

Numbers listed in parentheses at the end of citations refer to pages on which the work was cited.

Abrajano, T., Sturchio, N., Bohlke, J., Lyon, G., Poreda, R., and Stevens, C. (1988) Methane-hydrogen gas seeps, Zambales Ophiolite, Philippines: Deep or shallow origin? *Chemical Geology*, **71** (1), 211–222. doi: 10.1016/0009-2541(88)90116-7. (57)

Alei, M., Cappis, J. H., Fowler, M. M., Frank, D. J., Goldblatt, M., Guthals, P. R., Mason, A. S., Mills, T. R., Mroz, E. J., Norris, T. L., Perrin, R. E., Poths, J., Rokop, D. J., and Shields, W. R. (1987) Determination of deuterated methanes for use as atmospheric tracers. *Atmospheric Environment*, **21** (4), 909–915. doi: 10.1016/0004-6981(87)90087-4. (34)

Allen, D. E. and Seyfried, W. (2004) Serpentinization and heat generation: constraints from Lost City and Rainbow hydrothermal systems. *Geochimica et Cosmochimica Acta*, **68** (6), 1347–1354. doi: 10.1016/j.gca.2003.09.003. (57)

Alperin, M., Reeburgh, W., and Whiticar, M. (1988) Carbon and hydrogen isotope fractionation resulting from anaerobic methane oxidation. *Global Biogeochemical Cycles*, **2**, 279–288. doi: 10.1029/gb002i003p00279. (88)

Alt, J. C. (1995) Subseafloor processes in mid-ocean ridge hydrothermal systems. In: *Seafloor Hydrothermal Systems: Physical, Chemical, Biological, and Geological Interactions*. Wiley-Blackwell, pp. 85–114. doi: 10.1029/gm091p0085. (65)

Alt, J. C., Schwarzenbach, E. M., Früh-Green, G. L., Shanks, W. C., Bernasconi, S. M., Garrido, C. J., Crispini, L., Gaggero, L., Padrón-Navarta, J. A., and Marchesi, C. (2013) The role of serpentinites in cycling of carbon and sulfur: Seafloor serpentinization and subduction metamorphism. *Lithos*, **178**, 40–54. doi: 10.1016/j.lithos.2012.12.006. (63)

Arnason, B. (1977) The hydrogen-water isotope thermometer applied to geothermal areas in Iceland. *Geothermics*, **5** (1-4), 75–80. doi: 10.1016/0375-6505(77)90011-6. (57)

Árnason, B. and Sigurgeirsson, T. (1968) Deuterium content of water vapour and hydrogen in volcanic gas at Surtsey, Iceland. *Geochimica et Cosmochimica Acta*, **32** (8), 807–813. doi: 10.1016/0016-7037(68)90096-3. (57)

Bacsik, Z., Lopes, J. N. C., Gomes, M. F. C., Jancsó, G., Mink, J., and Pádua, A. A. H. (2002) Solubility isotope effects in aqueous solutions of methane. *The Journal of Chemical Physics*, **116** (24), 10816–10824. doi: 10.1063/1.1480012. (59)

Balabane, M., Galimov, E., Hermann, M., and Letolle, R. (1987) Hydrogen and carbon isotope fractionation during experimental production of bacterial methane. *Organic Geochemistry*, **11** (2), 115–119. doi: 10.1016/0146-6380(87)90033-7. (28)

Balch, W. E., Fox, G., Magrum, L., Woese, C., and Wolfe, R. (1979) Methanogens: reevaluation of a unique biological group. *Microbiological Reviews*, **43** (2), 260. (34)

Baldassare, F. J., McCaffrey, M. A., and Harper, J. A. (2014) A geochemical context for stray gas investigations in the northern Appalachian Basin: Implications of analyses of natural gases from Neogene-through Devonian-age strata. *AAPG Bulletin*, **98** (2), 341–372. doi: 10.1306/06111312178. (26, 46)

Bardo, R. D. and Wolfsberg, M. (1976) A theoretical calculation of the equilibrium constant for the isotopic exchange reaction between water and hydrogen deuteride. *The Journal of Physical Chemistry*, **80** (10), 1068–1071. doi: 10.1021/j100551a009. (38, 59)

Bates, B. L., McIntosh, J. C., Lohse, K. A., and Brooks, P. D. (2011) Influence of groundwater flowpaths, residence times and nutrients on the extent of microbial methanogenesis in coal beds: Powder River Basin, USA. *Chemical Geology*, **284** (1), 45–61. doi: 10.1016/j.chemgeo.2011.02.004. (26, 29)

Bernard, B. B., Brooks, J. M., and Sackett, W. M. (1978) Light hydrocarbons in recent Texas continental shelf and slope sediments. *Journal of Geophysical Research: Oceans (1978–2012)*, **83** (C8), 4053–4061. doi: 10.1029/jc083ic08p04053. (46)

Bernard, B. B., Brooks, J. M., and Sackett, W. M. (1976) Natural gas seepage in the Gulf of Mexico. *Earth and Planetary Science Letters*, **31** (1), 48–54. doi: 10.1016/0012-821x(76)90095-9. (46)

Berndt, M. E., Seyfried, W. E., and Janecky, D. R. (1989) Plagioclase and epidote buffering of cation ratios in mid-ocean ridge hydrothermal fluids: Experimental results in and near the supercritical region. *Geochimica et Cosmochimica Acta*, **53** (9), 2283–2300. doi: 10.1016/0016-7037(89)90351-7. (65)

Berner, U., Faber, E., Scheeder, G., and Panten, D. (1995) Primary cracking of algal and landplant kerogens: kinetic models of isotope variations in methane, ethane and propane. *Chemical Geology*, **126** (3), 233–245. doi: 10.1016/0009-2541(95)00120-4. (108)

Bevington, P. and Robinson, D. K. (2002) Data Reduction and Error Analysis for the Physical Sciences. 3rd ed. McGraw-Hill Education. (81)

Bigeleisen, J. (1949) The relative reaction velocities of isotopic molecules. *The Journal of Chemical Physics*, **17**, 675. doi: 10.1063/1.1747368. (84)

——— (1955) Statistical mechanics of isotopic systems with small quantum corrections. I. General considerations and the rule of the geometric mean. *The Journal of Chemical Physics*, **23** (12), 2264–2267. doi: 10.1063/1.1740735. (20)

Bigeleisen, J. and Mayer, M. G. (1947) Calculation of equilibrium constants for isotopic exchange reactions. *The Journal of Chemical Physics*, **15**, 261. doi: 10.1063/1.1746492. (36, 44)

Blank, J. G., Delaney, J. R., and Des Marais, D. J. (1993) The concentration and isotopic composition of carbon in basaltic glasses from the Juan de Fuca Ridge, Pacific Ocean. *Geochimica et Cosmochimica Acta*, **57** (4), 875–887. doi: 10.1016/0016-7037(93)90175-v. (51)

Boetius, A. and Wenzhöfer, F. (2013) Seafloor oxygen consumption fuelled by methane from cold seeps. *Nature Geoscience*, **6** (9), 725–734. doi: 10.1038/ngeo1926. (89)

Bottinga, Y. (1969) Calculated fractionation factors for carbon and hydrogen isotope exchange in the system calcite-carbon dioxide-graphite-methane-hydrogen-water vapor. *Geochimica et Cosmochimica Acta*, **33** (1), 49–64. doi: 10.1016/0016-7037(69)90092-1. (64)

Bousquet, P., Ciais, P., Miller, J. B., Dlugokencky, E. J., Hauglustaine, D. A., Prigent, C., Werf, G. R. V. der, Peylin, P., Brunke, E.-G., Carouge, C., Langenfelds, R. L., Lathière, J., Papa, F., Ramonet, M., Schmidt, M., Steele, L. P., Tyler, S. C., and White, J. (2006) Contribution of anthropogenic and natural sources to atmospheric methane variability. *Nature*, **443** (7110), 439–443. doi: 10.1038/nature05132. (74)

Bowen, G. J., Ehleringer, J. R., Chesson, L. A., Stange, E., and Cerling, T. E. (2007) Stable isotope ratios of tap water in the contiguous United States. *Water Resources Research*, **43** (3). doi: 10.1029/2006wr005186. (44, 84)

Bowman, J. P. (2014) The family Methylococcaceae. In: *The Prokaryotes*. Springer, pp. 411–440. doi: 10.1007/978-3-642-38922-1_237. (74)

Boyd, D. T. (2005) Oklahoma oil and gas production: Its components and long-term outlook. *Oklahoma Geology Notes*, **65** (1), 4–23. (100)

Boyer, S. E. and Elliott, D. (1982) Thrust systems. *AAPG Bulletin*, **66** (9), 1196–1230. doi: 10.1306/03b5a77d-16d1-11d7-8645000102c1865d. (106)

Bradley, A. S. and Summons, R. E. (2010) Multiple origins of methane at the Lost City Hydrothermal Field. *Earth and Planetary Science Letters*, **297** (1), 34–41. doi: 10.1016/j.epsl.2010.05.034. (55, 57, 60)

Brazelton, W. J., Schrenk, M. O., Kelley, D. S., and Baross, J. A. (2006) Methane-and sulfur-metabolizing microbial communities dominate the Lost City hydrothermal field ecosystem. *Applied and Environmental Microbiology*, **72** (9), 6257–6270. doi: 10.1128/aem.00574-06. (55, 60)

Brown, L., Sung, K., Benner, D., Devi, V., Boudon, V., Gabard, T., Wenger, C., Campargue, A., Leshchishina, O., Kassi, S., Mondelain, D., Wang, L., Daumont, L., Régalia, L., Rey, M., Thomas, X., Tyuterev, V. G., Lyulin, O., Nikitin, A., Niederer, H., Albert, S., Bauerecker, S., Quack, M., O'Brien, J., Gordon, I., Rothman, L., Sasada, H., Coustenis, A., Smith, M., Carrington, T., Wang, X.-G., Mantz, A., and Spickler, P. (2013) Methane line parameters in the HITRAN2012 database. *Journal of Quantitative Spectroscopy and Radiative Transfer*, **130**, 201–219. doi: 10.1016/j.jqsrt.2013.06.020. (115)

Brunner, B. and Bernasconi, S. M. (2005) A revised isotope fractionation model for dissimilatory sulfate reduction in sulfate reducing bacteria. *Geochimica et Cosmochimica Acta*, **69** (20), 4759–4771. doi: 10.1016/j.gca.2005.04.015. (41)

Bryndzia, L. T. and Wood, B. J. (1990) Oxygen thermobarometry of abyssal spinel peridotites the redox state and C-O-H volatile composition of the Earth's sub-oceanic upper mantle. *American Journal of Science*, **290** (10), 1093–1116. doi: 10.2475/ajs.290.10.1093. (61)

Buck, W. R., Lavier, L. L., and Poliakov, A. N. (2005) Modes of faulting at mid-ocean ridges. *Nature*, **434** (7034), 719–723. doi: 10.1038/nature03358. (65)

Burke Jr., R. A. (1993) Possible influence of hydrogen concentration on microbial methane stable hydrogen isotopic composition. *Chemosphere*, **26** (1), 55–67. doi: 10.1016/0045-6535(93)90412-x. (28, 95)

Burke Jr., R. A., Martens, C. S., and Sackett, W. M. (1988) Seasonal variations of D/H and $^{13}C/^{12}C$ ratios of microbial methane in surface sediments. *Nature*, **332**, 829–831. doi: 10.1038/332829a0. (26)

Burruss, R. and Laughrey, C. (2010) Carbon and hydrogen isotopic reversals in deep basin gas: Evidence for limits to the stability of hydrocarbons. *Organic Geochemistry*, **41** (12), 1285–1296. doi: 10.1016/j.orggeochem.2010.09.008. (26, 99, 106)

Campbell, B. J., Li, C., Sessions, A. L., and Valentine, D. L. (2009) Hydrogen isotopic fractionation in lipid biosynthesis by H_2-consuming *Desulfobacterium autotrophicum*. *Geochimica et Cosmochimica Acta*, **73** (10), 2744–2757. doi: 10.1016/j.gca.2009.02.034. (56)

Cannat, M., Fontaine, F., and Escartin, J. (2010) Serpentinization and associated hydrogen and methane fluxes at slow spreading ridges. *Diversity of Hydrothermal Systems on Slow Spreading Ocean Ridges*, 241–264. doi: 10.1029/2008gm000760. (48)

Cao, X. and Liu, Y. (2012) Theoretical estimation of the equilibrium distribution of clumped isotopes in nature. *Geochimica et Cosmochimica Acta*, **77**, 292–303. doi: 10.1016/j.gca.2011.11.021. (36)

Cardace, D., Hoehler, T., McCollom, T., Schrenk, M., Carnevale, D., Kubo, M., and Twing, K. (2013) Establishment of the Coast Range ophiolite microbial observatory (CROMO): drilling objectives and preliminary outcomes. *Scientific Drilling*, **16**, 45–55. doi: 10.5194/sd-16-45-2013. (28–29, 46)

Carothers, W. W. and Kharaka, Y. K. (1978) Aliphatic acid anions in oil-field waters: implications for origin of natural gas. *AAPG Bulletin*, **62** (12). doi: 10.1306/c1ea5521-16c9-11d7-8645000102c1865d. (106)

Cemen, I., Sagnak, A., and Akthar, S. (2002) Geometry of the triangle zone and duplex structure in the Wilburton gas field area of the Arkoma basin, southeastern Oklahoma. *Shale Shaker*, **52** (4), 91–101. (106)

Cerrai, E., Marchetti, C., Renzoni, R., Roseo, L., Silvestri, M., and Villani, S. (1954) A thermal method for concentrating heavy water. Nuclear engineering, Part I. In: *Chem. Eng. Progr. Symposium Ser.* Vol. 50. 11. Laboratori CISE, Milan, Italy, pp. 271–280. (38, 42, 44, 59)

Chanton, J., Chasar, L., Glaser, P., and Siegel, D. (2005) Carbon and hydrogen isotopic effects in microbial methane from terrestrial environments. In: *Stable Isotopes and Biosphere-Atmosphere Interactions, Physiological Ecology Series*. Ed. by L. B. Flanagan, J. R. Ehleringer, and D. E. Pataki. Elsevier Academic Press London, pp. 85–105. doi: 10.1016/b978-012088447-6/50006-4. (74)

Charlou, J. L., Donval, J. P., Konn, C., Ondréas, H., Fouquet, Y., Jean-Baptiste, P., and Fourré, E. (2010) High production and fluxes of H_2 and CH_4 and evidence of abiotic hydrocarbon synthesis by serpentinization in ultramafic-hosted hydrothermal systems on the Mid-Atlantic Ridge. *Diversity of Hydrothermal Systems on Slow Spreading Ocean Ridges*, 265–296. doi: 10.1029/2008gm000752. (48, 50, 59, 71)

Charlou, J., Donval, J., Douville, E., Jean-Baptiste, P., Radford-Knoery, J., Fouquet, Y., Dapoigny, A., and Stievenard, M. (2000) Compared geochemical signatures and the evolution of Menez Gwen (37°50′N) and

Lucky Strike (37°17′N) hydrothermal fluids, south of the Azores Triple Junction on the Mid-Atlantic Ridge. *Chemical Geology*, **171** (1), 49–75. DOI: 10.1016/s0009-2541(00)00244-8. (48, 51, 55, 67)

Charlou, J., Donval, J., Fouquet, Y., Jean-Baptiste, P., and Holm, N. (2002) Geochemistry of high H_2 and CH_4 vent fluids issuing from ultramafic rocks at the Rainbow hydrothermal field (36°14′N, MAR). *Chemical Geology*, **191** (4), 345–359. DOI: 10.1016/s0009-2541(02)00134-1. (48, 50–51, 55, 62, 67)

Cicerone, R. J. and Oremland, R. S. (1988) Biogeochemical aspects of atmospheric methane. *Global Biogeochemical Cycles*, **2** (4), 299–327. DOI: 10.1029/gb002i004p00299. (89)

Clayton, C. (2003) Hydrogen isotope systematics of thermally generated natural gas. *International Meeting on Organic Geochemistry, 21st, Kraków, Poland, Book Abstr. Part I*, 51–52. (106, 108)

Clog, M., Aubaud, C., Cartigny, P., and Dosso, L. (2013) The hydrogen isotopic composition and water content of southern Pacific MORB: A reassessment of the D/H ratio of the depleted mantle reservoir. *Earth and Planetary Science Letters*, **381**, 156–165. DOI: 10.1016/j.epsl.2013.08.043. (51, 59)

Coleman, D. D., Risatti, J. B., and Schoell, M. (1981) Fractionation of carbon and hydrogen isotopes by methane-oxidizing bacteria. *Geochimica et Cosmochimica Acta*, **45** (7), 1033–1037. DOI: 10.1016/0016-7037(81)90129-0. (74, 82–84)

Coplen, T. B. (2011) Guidelines and recommended terms for expression of stable-isotope-ratio and gas-ratio measurement results. *Rapid Communications in Mass Spectrometry*, **25** (17), 2538–2560. DOI: 10.1002/rcm.5129. (76)

Cottrell, E. and Kelley, K. A. (2011) The oxidation state of Fe in MORB glasses and the oxygen fugacity of the upper mantle. *Earth and Planetary Science Letters*, **305** (3-4), 270–282. DOI: 10.1016/j.epsl.2011.03.014. (61)

Coveney Jr, R. M., Goebel, E. D., Zeller, E. J., Dreschhoff, G. A., and Angino, E. E. (1987) Serpentinization and the origin of hydrogen gas in Kansas. *AAPG Bulletin*, **71** (1), 39–48. DOI: 10.1306/94886d3f-1704-11d7-8645000102c1865d. (57)

Crespo-Medina, M., Twing, K. I., Kubo, M. D. Y., Hoehler, T. M., Cardace, D., McCollom, T., and Schrenk, M. O. (2014) Insights into environmental controls on microbial communities in a continental serpentinite aquifer using a microcosm-based approach. *Frontiers in Microbiology*, **5**, 604. DOI: 10.3389/fmicb.2014.00604. (40, 46)

Crist, R. H. and Dalin, G. A. (1933) Exchange reactions of protium and deuterium. *The Journal of Chemical Physics*, **1** (9), 677–677. DOI: 10.1063/1.1749349. (56)

Curiale, J. A. (1981) Source rock geochemistry and liquid and solid petroleum occurrences of the Ouachita Mountains, Oklahoma. PhD thesis. University of Oklahoma. (100)

Dasgupta, R. and Hirschmann, M. M. (2010) The deep carbon cycle and melting in Earth's interior. *Earth and Planetary Science Letters*, **298** (1-2), 1–13. DOI: 10.1016/j.epsl.2010.06.039. (63)

Delwiche, K., Senft-Grupp, S., and Hemond, H. (2015) A novel optical sensor designed to measure methane bubble sizes in situ. *Limnology and Oceanography: Methods*, **13** (12), 712–721. DOI: 10.1002/lom3.10060. (45)

Des Marais, D. J. (1986) Carbon abundance measurements in oceanic basalts: the need for a consensus. *Earth and Planetary Science Letters*, **79** (1-2), 21–26. DOI: 10.1016/0012-821x(86)90036-1. (64)

Dick, J. M. (2008) Calculation of the relative metastabilities of proteins using the CHNOSZ software package. *Geochemical Transactions*, **9** (10), 10. DOI: 10.1186/1467-4866-9-10. (67)

Didyk, B. M. and Simoneit, B. R. (1989) Hydrothermal oil of Guaymas Basin and implications for petroleum formation mechanisms. *Nature*, **342**, 65–69. DOI: 10.1038/342065a0. (46)

Dlugokencky, E. J., Nisbet, E. G., Fisher, R., and Lowry, D. (2011) Global atmospheric methane: budget, changes and dangers. *Philosophical Transactions of the Royal Society A: Mathematical, Physical and Engineering Sciences*, **369** (1943), 2058–2072. DOI: 10.1098/rsta.2010.0341. (74)

Douglas, P., Stolper, D., Smith, D., Anthony, K. W., Paull, C., Dallimore, S., Wik, M., Crill, P., Winterdahl, M., Eiler, J., and Sessions, A. (2016) Diverse origins of Arctic and Subarctic methane point source emissions identified with multiply-substituted isotopologues. *Geochimica et Cosmochimica Acta*, **188**, 163–188. DOI: 10.1016/j.gca.2016.05.031. (75, 93)

Dunn, R. (2007) Crust and lithospheric structure—seismic structure of mid-ocean ridges. In: *Deep Earth Seismology*. Ed. by G. Schubert. 2nd ed. Vol. 1. Treatise In Geophysics. Elsevier. Chap. 13, pp. 419–443. doi: 10.1016/b978-0-444-53802-4.00011-7. (65)

Duval, B. and Ludlam, S. D. (2001) The black water chemocline of meromictic Lower Mystic Lake, Massachusetts, USA. *International Review of Hydrobiology*, **86** (2), 165–181. doi: 10.1002/1522-2632(200104)86:2<165::aid-iroh165>3.3.co;2-p. (119)

Eiler, J. (2013) The isotopic anatomies of molecules and minerals. *Annual Review of Earth and Planetary Sciences*, **41** (1), 411–441. doi: 10.1146/annurev-earth-042711-105348. (61)

Eiler, J. M. (2007) "Clumped-isotope" geochemistry—The study of naturally-occurring, multiply-substituted isotopologues. *Earth and Planetary Science Letters*, **262** (3), 309–327. doi: 10.1016/j.epsl.2007.08.020. (17, 20, 74)

Eiler, J. M. and Schauble, E. (2004) $^{18}O^{13}C^{16}O$ in Earth's atmosphere. *Geochimica et Cosmochimica Acta*, **68** (23), 4767–4777. doi: 10.1016/j.gca.2004.05.035. (74, 86)

Elsner, M., Zwank, L., Hunkeler, D., and Schwarzenbach, R. P. (2005) A new concept linking observable stable isotope fractionation to transformation pathways of organic pollutants. *Environmental Science & Technology*, **39** (18), 6896–6916. doi: 10.1021/es0504587. (82)

England, W. A., Mann, A. L., and Mann, D. M. (1991) Migration from Source to Trap: Petroleum Generation and Migration. In: *Source and Migration Processes and Evaluation Techniques*. Ed. by R. K. Merrill, N. H. Foster, and E. A. Beaumont. AAPG Special Volumes. Chap. 3, pp. 23–46. (104)

Etiope, G., Baciu, C. L., and Schoell, M. (2011a) Extreme methane deuterium, nitrogen and helium enrichment in natural gas from the Homorod seep (Romania). *Chemical Geology*, **280** (1), 89–96. doi: 10.1016/j.chemgeo.2010.10.019. (57)

Etiope, G., Schoell, M., and Hosgörmez, H. (2011b) Abiotic methane flux from the Chimaera seep and Tekirova ophiolites (Turkey): Understanding gas exhalation from low temperature serpentinization and implications for Mars. *Earth and Planetary Science Letters*, **310** (1), 96–104. doi: 10.1016/j.epsl.2011.08.001. (121)

Etiope, G. and Sherwood Lollar, B. (2013) Abiotic methane on Earth. *Reviews of Geophysics*, **51**, 276–299. doi: 10.1002/rog.20011. (26)

Ettwig, K. F., Butler, M. K., Paslier, D. L., Pelletier, E., Mangenot, S., Kuypers, M. M. M., Schreiber, F., Dutilh, B. E., Zedelius, J., Beer, D. de, Gloerich, J., Wessels, H. J. C. T., Alen, T. van, Luesken, F., Wu, M. L., Pas-Schoonen, K. T. van de, Camp, H. J. M. O. den, Janssen-Megens, E. M., Francoijs, K.-J., Stunnenberg, H., Weissenbach, J., Jetten, M. S. M., and Strous, M. (2010) Nitrite-driven anaerobic methane oxidation by oxygenic bacteria. *Nature*, **464** (7288), 543–548. doi: 10.1038/nature08883. (91)

Eugster, H. and Skippen, G. (1967) Igneous and metamorphic reactions involving gas equilibria. In: *Researches in Geochemistry*. Ed. by P. Abelson. Vol. 2. Wiley New York, NY, pp. 492–520. (64)

Farquhar, G. D., O'Leary, M., and Berry, J. (1982) On the relationship between carbon isotope discrimination and the intercellular carbon dioxide concentration in leaves. *Australian Journal of Plant Physiology*, **9** (2), 121–137. doi: 10.1071/pp9820121. (84)

Farquhar, J., Johnston, D. T., and Wing, B. A. (2007) Implications of conservation of mass effects on mass-dependent isotope fractionations: influence of network structure on sulfur isotope phase space of dissimilatory sulfate reduction. *Geochimica et Cosmochimica Acta*, **71** (24), 5862–5875. doi: 10.1016/j.gca.2007.08.028. (41)

Feilberg, K. L., Griffith, D. W., Johnson, M. S., and Nielsen, C. J. (2005) The ^{13}C and D kinetic isotope effects in the reaction of CH_4 with Cl. *International Journal of Chemical Kinetics*, **37** (2), 110–118. doi: 10.1002/kin.20058. (90)

Feisthauer, S., Vogt, C., Modrzynski, J., Szlenkier, M., Krüger, M., Siegert, M., and Richnow, H.-H. (2011) Different types of methane monooxygenases produce similar carbon and hydrogen isotope fractionation patterns during methane oxidation. *Geochimica et Cosmochimica Acta*, **75** (5), 1173–1184. doi: 10.1016/j.gca.2010.12.006. (74, 82–83)

Fisher, A. T. (2003) Geophysical Constraints on Hydrothermal Circulation: Observations and Models. In: *Energy and mass transfer in marine hydrothermal systems*. Ed. by P. Halbach, V. Tunnicliffe, and J. Hein. Vol. 89. Dahlem workshop reports. Dahlem University Press. Chap. 3, pp. 29–52. (61)

Flores, R. M., Rice, C. A., Stricker, G. D., Warden, A., and Ellis, M. S. (2008) Methanogenic pathways of coal-bed gas in the Powder River Basin, United States: the geologic factor. *International Journal of Coal Geology*, **76** (1), 52–75. doi: 10.1016/j.coal.2008.02.005. (26)

Foustoukos, D. I., Savov, I. P., and Janecky, D. R. (2008) Chemical and isotopic constraints on water/rock interactions at the Lost City hydrothermal field, 30 N Mid-Atlantic Ridge. *Geochimica et Cosmochimica Acta*, **72** (22), 5457–5474. doi: 10.1016/j.gca.2008.07.035. (57, 65)

Foustoukos, D. I. and Seyfried, W. E. (2004) Hydrocarbons in hydrothermal vent fluids: the role of chromium-bearing catalysts. *Science*, **304** (5673), 1002–1005. doi: 10.1126/science.1096033. (62, 64)

French, B. M. (1966) Some geological implications of equilibrium between graphite and a C-H-O gas phase at high temperatures and pressures. *Reviews of Geophysics*, **4** (2), 223. doi: 10.1029/rg004i002p00223. (64, 67)

Friedman, I. and Hardcastle, K. (1988) Deuterium in interstitial water from deep-sea cores. *Journal of Geophysical Research: Oceans (1978–2012)*, **93** (C7), 8249–8263. (40)

Frisch, M. J., Trucks, G. W., Schlegel, H. B., Scuseria, G. E., Robb, M. A., Cheeseman, J. R., Montgomery Jr., J. A., Vreven, T., Kudin, K. N., Burant, J. C., Millam, J. M., Iyengar, S. S., Tomasi, J., Barone, V., Mennucci, B., Cossi, M., Scalmani, G., Rega, N., Petersson, G. A., Nakatsuji, H., Hada, M., Ehara, M., Toyota, K., Fukuda, R., Hasegawa, J., Ishida, M., Nakajima, T., Honda, Y., Kitao, O., Nakai, H., Klene, M., Li, X., Knox, J. E., Hratchian, H. P., Cross, J. B., Bakken, V., Adamo, C., Jaramillo, J., Gomperts, R., Stratmann, R. E., Yazyev, O., Austin, A. J., Cammi, R., Pomelli, C., Ochterski, J. W., Ayala, P. Y., Morokuma, K., Voth, G. A., Salvador, P., Dannenberg, J. J., Zakrzewski, V. G., Dapprich, S., Daniels, A. D., Strain, M. C., Farkas, O., Malick, D. K., Rabuck, A. D., Raghavachari, K., Foresman, J. B., Ortiz, J. V., Cui, Q., Baboul, A. G., Clifford, S., Cioslowski, J., Stefanov, B. B., Liu, G., Liashenko, A., Piskorz, P., Komaromi, I., Martin, R. L., Fox, D. J., Keith, T., Al-Laham, M. A., Peng, C. Y., Nanayakkara, A., Challacombe, M., Gill, P. M. W., Johnson, B., Chen, W., Wong, M. W., Gonzalez, C., and Pople, J. A. (n.d.) Gaussian 03, Revision D.01 (Gaussian Inc., Wallingford, Connecticut, 2004). Gaussian, Inc., Wallingford, CT, 2004. (36)

Fritz, P., Clark, I., Fontes, J.-C., Whiticar, M., and Faber, E. (1992) Deuterium and ^{13}C evidence for low temperature production of hydrogen and methane in a highly alkaline groundwater environment in Oman. *Water-Rock Interaction*, 793–796. (57)

Frost, B. R. (1985) On the stability of sulfides, oxides, and native metals in serpentinite. *Journal of Petrology*, **26** (1), 31–63. doi: 10.1093/petrology/26.1.31. (62)

Früh-Green, G. L., Connolly, J. A., Plas, A., Kelley, D. S., and Grobéty, B. (2004) Serpentinization of oceanic peridotites: implications for geochemical cycles and biological activity. In: *The Subseafloor Biosphere at Mid-Ocean Ridges*. Ed. by W. S. D. Wilcock, E. F. Delong, D. S. Kelley, J. A. Baross, and S. C. Cary. Geophysical Monographs 144. Wiley Online Library, pp. 119–136. doi: 10.1029/144gm08. (63–64)

Früh-Green, G. L., Plas, A., and Lécuyer, C. (1996) 14. Petrologic and stable isotope constraints on hydrothermal alteration and serpentinization of the EPR shallow mantle at Hess Deep (site 895). In: *Proceedings of the Ocean Drilling Program, Scientific Results*. Vol. 147, pp. 255–291. doi: 10.2973/odp.proc.sr.147.016.1996. (64)

Fu, Q., Sherwood Lollar, B., Horita, J., Lacrampe-Couloume, G., and Seyfried Jr, W. E. (2007) Abiotic formation of hydrocarbons under hydrothermal conditions: Constraints from chemical and isotope data. *Geochimica et Cosmochimica Acta*, **71** (8), 1982–1998. doi: 10.1016/j.gca.2007.01.022. (62)

Glasoe, P. K. and Long, F. A. (1960) Use of glass electrodes to measure acidites in deuterium oxide. *The Journal of Physical Chemistry*, **64** (1), 188–190. doi: 10.1021/j100830a521. (113)

Godo, T. J., Li, P., and Ratchford, M. E. (2011) Exploration for the Arkansas Novaculite reservoir, in the southern Ouachita Mountains, Arkansas. In: *AAPG Annual Conference and Exhibition*. AAPG Search and Discovery, Article 90124. (106)

Golden, J. T., Andersen, R. A., and Bergman, R. G. (2001) Exceptionally low-temperature carbon–hydrogen/carbon–deuterium exchange reactions of organic and organometallic compounds catalyzed by the $Cp^*(PMe_3)IrH(ClCH_2Cl)^+$ cation. *Journal of the American Chemical Society*, **123** (24), 5837–5838. doi: 10.1021/ja0155480. (93)

Gould, A. J., Bleakney, W., and Taylor, H. S. (1934) The Inter-Relations of Hydrogen and Deuterium Molecules. *The Journal of Chemical Physics*, **2** (7), 362–373. doi: 10.1063/1.1749490. (56)

Green, J. and Dalton, H. (1989) Substrate specificity of soluble methane monooxygenase. Mechanistic implications. *Journal of Biological Chemistry*, **264** (30), 17698–17703. (83)

Grozeva, N. G., Klein, F., Seewald, J. S., and Sylva, S. P. (2017) Experimental study of carbonate formation in oceanic peridotite. *Geochimica et Cosmochimica Acta*, **199**, 264–286. doi: 10.1016/j.gca.2016.10.052. (62)

Gunter, B. and Musgrave, B. (1971) New evidence on the origin of methane in hydrothermal gases. *Geochimica et Cosmochimica Acta*, **35** (1), 113–118. doi: 10.1016/0016-7037(71)90109-8. (57)

Guthrie, J. M., Houseknecht, D. W., and Johns, W. D. (1986) Relationships among vitrinite reflectance, illite crystallinity, and organic geochemistry in Carboniferous strata, Ouachita Mountains, Oklahoma and Arkansas. *AAPG Bulletin*, **70** (1). doi: 10.1306/9488561a-1704-11d7-8645000102c1865d. (106)

Hall, N. F., Bowden, E., and Jones, T. (1934) Exchange reactions of hydrogen atoms. *Journal of the American Chemical Society*, **56** (3), 750–750. doi: 10.1021/ja01318a510. (56)

Hanson, R. S. and Hanson, T. E. (1996) Methanotrophic bacteria. *Microbiological Reviews*, **60** (2), 439–471. (74, 89)

Harrison, A. and Thode, H. (1958) Mechanism of the bacterial reduction of sulphate from isotope fractionation studies. *Transactions of the Faraday Society*, **54**, 84–92. doi: 10.1039/tf9585400084. (84)

Hasenclever, J., Theissen-Krah, S., Rüpke, L. H., Morgan, J. P., Iyer, K., Petersen, S., and Devey, C. W. (2014) Hybrid shallow on-axis and deep off-axis hydrothermal circulation at fast-spreading ridges. *Nature*, **508** (7497), 508–512. doi: 10.1038/nature13174. (61, 65)

Hatcher Jr, R. D., Thomas, W. A., and Viele, G. W., eds. (1989) The Appalachian-Ouachita Orogen in the United States. Geological Society of America. doi: 10.1130/dnag-gna-f2. (100)

Hayes, J. M. (2001) Fractionation of carbon and hydrogen isotopes in biosynthetic processes. *Reviews in Mineralogy and Geochemistry*, **43** (1), 225–277. doi: 10.2138/gsrmg.43.1.225. (39, 88)

Helgeson, H. C., Delany, J. M., Nesbitt, H. W., and Bird, D. K. (1978) Summary and critique of the thermodynamic properties of rock-forming minerals. *American Journal of Science*, **278A**, 1–229. (67)

Helgeson, H. C., Owens, C. E., Knox, A. M., and Richard, L. (1998) Calculation of the Standard Molal Thermodynamic Properties of Crystalline, Liquid, and Gas Organic Molecules at High Temperatures and Pressures. *Geochimica et Cosmochimica Acta*, **62** (6), 985–1081. doi: 10.1016/s0016-7037(97)00219-6. (67)

Hermes, J. D., Morrical, S. W., O'Leary, M. H., and Cleland, W. (1984) Variation of transition-state structure as a function of the nucleotide in reactions catalyzed by dehydrogenases. 2. Formate dehydrogenase. *Biochemistry*, **23** (23), 5479–5488. doi: 10.1021/bi00318a016. (39, 42)

Hoering, T. (1984) Thermal reactions of kerogen with added water, heavy water and pure organic substances. *Organic Geochemistry*, **5** (4), 267–278. doi: 10.1016/0146-6380(84)90014-7. (108)

Holland, G., Lollar, B. S., Li, L., Lacrampe-Couloume, G., Slater, G., and Ballentine, C. (2013) Deep fracture fluids isolated in the crust since the Precambrian era. *Nature*, **497** (7449), 357–360. doi: 10.1038/nature12127. (28–29, 40, 46)

Holler, T., Wegener, G., Knittel, K., Boetius, A., Brunner, B., Kuypers, M. M., and Widdel, F. (2009) Substantial 13C/12C and D/H fractionation during anaerobic oxidation of methane by marine consortia enriched in vitro. *Environmental Microbiology Reports*, **1** (5), 370–376. doi: 10.1111/j.1758-2229.2009.00074.x. (90–91)

Holler, T., Wegener, G., Niemann, H., Deusner, C., Ferdelman, T. G., Boetius, A., Brunner, B., and Widdel, F. (2011) Carbon and sulfur back flux during anaerobic microbial oxidation of methane and coupled sulfate reduction. *Proceedings of the National Academy of Sciences of the United States of America*, **108** (52), E1484–E1490. doi: 10.1073/pnas.1106032108. (28–29, 87, 91)

Holloway, J. R. (1984) Graphite-CH_4-H_2O-CO_2 equilibria at low-grade metamorphic conditions. *Geology*, **12** (8), 455. doi: 10.1130/0091-7613(1984)12<455:gealmc>2.0.co;2. (64, 67)

Horibe, Y. and Craig, H. (1995) D/H fractionation in the system methane-hydrogen-water. *Geochimica et Cosmochimica Acta*, **59** (24), 5209–5217. doi: 10.1016/0016-7037(95)00391-6. (30, 38–39, 42, 44, 57, 59–60, 71, 84)

Horii, C. V., Zahniser, M. S., David D. Nelson, J., McManus, J. B., and Wofsy, S. C. (1999) Nitric acid and nitrogen dioxide flux measurements: a new application of tunable diode laser absorption spectroscopy. *SPIE Proceedings*, **3758**. Ed. by A. Fried, 152–161. doi: 10.1117/12.366448. (115)

Horita, J. (2001) Carbon isotope exchange in the system CO_2–CH_4 at elevated temperatures. *Geochimica et Cosmochimica Acta*, **65** (12), 1907–1919. doi: 10.1016/S0016-7037(01)00570-1. (39, 42)

——— (2005) Stable isotope thermometry: There is more to it than temperature. *Geochemical Journal*, **39** (6), 481–496. doi: 10.2343/geochemj.39.481. (44, 59)

Horita, J. and Berndt, M. E. (1999) Abiogenic methane formation and isotopic fractionation under hydrothermal conditions. *Science*, **285** (5430), 1055–1057. doi: 10.1126/science.285.5430.1055. (62)

Horita, J., Driesner, T., and Cole, D. R. (1999) Pressure effect on hydrogen isotope fractionation between brucite and water at elevated temperatures. *Science*, **286** (5444), 1545–1547. doi: 10.1126/science.286.5444.1545. (59)

Horita, J. and Wesolowski, D. J. (1994) Liquid-vapor fractionation of oxygen and hydrogen isotopes of water from the freezing to the critical temperature. *Geochimica et Cosmochimica Acta*, **58** (16), 3425–3437. doi: 10.1016/0016-7037(94)90096-5. (38, 59)

Hornibrook, E. R., Longstaffe, F. J., and Fyfe, W. S. (1997) Spatial distribution of microbial methane production pathways in temperate zone wetland soils: stable carbon and hydrogen isotope evidence. *Geochimica et Cosmochimica Acta*, **61** (4), 745–753. doi: 10.1016/s0016-7037(96)00368-7. (74)

Hosgormez, H., Etiope, G., and Yalçin, M. N. (2008) New evidence for a mixed inorganic and organic origin of the Olympic Chimaera fire (Turkey): a large onshore seepage of abiogenic gas. *Geofluids*, **8** (4), 263–273. doi: 10.1111/j.1468-8123.2008.00226.x. (121)

Hosgörmez, H. (2007) Origin of the natural gas seep of Çirali (Chimera), Turkey: Site of the first Olympic fire. *Journal of Asian Earth Sciences*, **30** (1), 131–141. doi: 10.1016/j.jseaes.2006.08.002. (121)

Houseknecht, D. W., Rouse, W. A., Paxton, S. T., Mars, J. C., and Fulk, B. (2014) Upper Devonian–Mississippian stratigraphic framework of the Arkoma Basin and distribution of potential source-rock facies in the Woodford-Chattanooga and Fayetteville-Caney shale-gas systems. *AAPG Bulletin*, **98** (9), 1739–1759. doi: 10.1306/03031413025. (100)

Hunt, J. M. (1996) Petroleum geochemistry and geology. 2nd ed. WH Freeman San Francisco. (106)

Hut, G. (1987) Consultants' group meeting on stable isotope reference samples for geochemical and hydrological investigations. Tech. rep. Vienna, Austria: *International Atomic Energy Agency*. (34)

Inagaki, F., Hinrichs, K.-U., Kubo, Y., Bowles, M. W., Heuer, V. B., Hong, W.-L., Hoshino, T., Ijiri, A., Imachi, H., Ito, M., Kaneko, M., Lever, M. A., Lin, Y.-S., Methe, B. A., Morita, S., Morono, Y., Tanikawa, W., Bihan, M., Bowden, S. A., Elvert, M., Glombitza, C., Gross, D., Harrington, G. J., Hori, T., Li, K., Limmer, D., Liu, C.-H., Murayama, M., Ohkouchi, N., Ono, S., Park, Y.-S., Phillips, S. C., Prieto-Mollar, X., Purkey, M., Riedinger, N., Sanada, Y., Sauvage, J., Snyder, G., Susilawati, R., Takano, Y., Tasumi, E., Terada, T., Tomaru, H., Trembath-Reichert, E., Wang, D. T., and Yamada, Y. (2015) Exploring deep microbial life in coal-bearing sediment down to ~2.5 km below the ocean floor. *Science*, **349** (6246), 420–424. doi: 10.1126/science.aaa6882. (75, 93, 115)

IPCC (2013) Climate Change 2013: The Physical Science Basis. Intergovernmental Panel on Climate Change, Working Group I Contribution to the IPCC Fifth Assessment Report (AR5). Ed. by T. F. Stocker, D. Qin, G. Plattner, M. Tignor, S. Allen, J. Boschung, A. Nauels, Y. Xia, V. Bex, and P. Midgley. New York: Cambridge University Press. doi: 10.1017/cbo9781107415324. (18, 74)

Janssen, P. H. (2010) Influence of hydrogen on rumen methane formation and fermentation balances through microbial growth kinetics and fermentation thermodynamics. *Animal Feed Science and Technology*, **160** (1), 1–22. doi: 10.1016/j.anifeedsci.2010.07.002. (40)

Javoy, M., Pineau, F., and Delorme, H. (1986) Carbon and nitrogen isotopes in the mantle. *Chemical Geology*, **57** (1-2), 41–62. doi: 10.1016/0009-2541(86)90093-8. (51)

Jeffries, M., Krouse, H., Shakur, M., and Harris, S. (1984) Isotope geochemistry of stratified Lake "A," Ellesmere Island, NWT, Canada. *Canadian Journal of Earth Sciences*, **21** (9), 1008–1017. doi: 10.1139/e84-105. (119)

Joelsson, L. M. T., Schmidt, J. A., Nilsson, E. J. K., Blunier, T., Griffith, D. W. T., Ono, S., and Johnson, M. S. (2015) Development of a new methane tracer: kinetic isotope effect of $^{13}CH_3D$ + OH from 278 to 313 K. *Atmospheric Chemistry and Physics Discussions*, **15** (19), 27853–27875. doi: 10.5194/acpd-15-27853-2015. (87, 90, 121)

——— (2016) Kinetic isotope effects of $^{12}CH_3D$+OH and $^{13}CH_3D$+OH from 278 to 313K. *Atmospheric Chemistry and Physics*, **16** (7), 4439–4449. doi: 10.5194/acp-16-4439-2016. (89–90, 121)

Joelsson, L., Forecast, R., Schmidt, J., Meusinger, C., Nilsson, E., Ono, S., and Johnson, M. (2014) Relative rate study of the kinetic isotope effect in the $^{13}CH_3D$ + Cl reaction. *Chemical Physics Letters*, **605**, 152–157. doi: 10.1016/j.cplett.2014.05.022. (89–90, 121)

Johnson, J. W., Oelkers, E. H., and Helgeson, H. C. (1992) SUPCRT92: A software package for calculating the standard molal thermodynamic properties of minerals, gases, aqueous species, and reactions from 1 to 5000 bar and 0 to 1000 C. *Computers & Geosciences*, **18** (7), 899–947. doi: 10.1016/0098-3004(92)90029-q. (54, 67)

Johnson, K. A. and Johnson, D. E. (1995) Methane emissions from cattle. *Journal of Animal Science*, **73** (8), 2483–2492. doi: 10.2527/1995.7382483x. (29)

Jones, N. (2012) Source code: The methane race. *EARTH Magazine*, **57**, 40–45. (17)

Jones, W., Leigh, J., Mayer, F., Woese, C., and Wolfe, R. (1983) *Methanococcus jannaschii* sp. nov., an extremely thermophilic methanogen from a submarine hydrothermal vent. *Archives of Microbiology*, **136** (4), 254–261. doi: 10.1007/bf00425213. (34)

Kadko, D. (1996) Radioisotopic studies of submarine hydrothermal vents. *Reviews of Geophysics*, **34** (3), 349–366. doi: 10.1029/96rg01762. (61)

Kai, F. M., Tyler, S. C., Randerson, J. T., and Blake, D. R. (2011) Reduced methane growth rate explained by decreased Northern Hemisphere microbial sources. *Nature*, **476** (7359), 194–197. doi: 10.1038/nature10259. (89)

Kawagucci, S., Chiba, H., Ishibashi, J.-i., Yamanaka, T., Toki, T., Muramatsu, Y., Ueno, Y., Makabe, A., Inoue, K., Yoshida, N., Nakagawa, S., Nunoura, T., Takai, K., Takahata, N., Sano, Y., Narita, T., Teranishi, G., Obata, H., and Gamo, T. (2011) Hydrothermal fluid geochemistry at the Iheya North field in the mid-Okinawa Trough: Implication for origin of methane in subseafloor fluid circulation systems. *Geochemical Journal*, **45** (2), 109–124. doi: 10.2343/geochemj.1.0105. (57)

Kawagucci, S., Kobayashi, M., Hattori, S., Yamada, K., Ueno, Y., Takai, K., and Yoshida, N. (2014) Hydrogen isotope systematics among H_2–H_2O–CH_4 during the growth of the hydrogenotrophic methanogen *Methanothermobacter thermoautotrophicus* strain ΔH. *Geochimica et Cosmochimica Acta*, doi: 10.1016/j.gca.2014.07.020. (95)

Kawagucci, S., Toki, T., Ishibashi, J., Takai, K., Ito, M., Oomori, T., and Gamo, T. (2010) Isotopic variation of molecular hydrogen in 20°–375°C hydrothermal fluids as detected by a new analytical method. *Journal of Geophysical Research: Biogeosciences*, **115** (G3). doi: 10.1029/2009jg001203. (57, 59, 71)

Kawagucci, S., Ueno, Y., Takai, K., Toki, T., Ito, M., Inoue, K., Makabe, A., Yoshida, N., Muramatsu, Y., Takahata, N., Sano, Y., Narita, T., Teranishi, G., Obata, H., Nakagawa, S., Nunoura, T., and Gamo, T. (2013) Geochemical origin of hydrothermal fluid methane in sediment-associated fields and its relevance to the geographical distribution of whole hydrothermal circulation. *Chemical Geology*, **339**, 213–225. doi: 10.1016/j.chemgeo.2012.05.003. (57, 61, 67)

Keir, R. (2010) A note on the fluxes of abiogenic methane and hydrogen from mid-ocean ridges. *Geophysical Research Letters*, **37** (24). doi: 10.1029/2010gl045362. (18, 48, 51, 55, 61, 63–65)

Kelemen, P. B., Matter, J., Streit, E. E., Rudge, J. F., Curry, W. B., and Blusztajn, J. (2011) Rates and mechanisms of mineral carbonation in peridotite: natural processes and recipes for enhanced, in situ CO2 Capture and storage. *Annual Review of Earth and Planetary Sciences*, **39** (1), 545–576. doi: 10.1146/annurev-earth-092010-152509. (62)

Kelley, D. S. (1996) Methane-rich fluids in the oceanic crust. *Journal of Geophysical Research: Solid Earth*, **101** (B2), 2943–2962. doi: 10.1029/95jb02252. (48, 62–65)

——— (1997) Fluid evolution in slow-spreading environments. In: *Proceedings of the Ocean Drilling Program. Scientific Results*. Vol. 153. Ocean Drilling Program, pp. 399–415. doi: 10.2973/odp.proc.sr.153.038.1997. (48, 63–65)

Kelley, D. S. and Früh-Green, G. L. (1999) Abiogenic methane in deep-seated mid-ocean ridge environments: Insights from stable isotope analyses. *Journal of Geophysical Research: Solid Earth*, **104** (B5), 10439–10460. doi: 10.1029/1999jb900058. (48, 61–65)

——— (2001) Volatile lines of descent in submarine plutonic environments: Insights from stable isotope and fluid inclusion analyses. *Geochimica et Cosmochimica Acta*, **65** (19), 3325–3346. doi: 10.1016/s0016-7037(01)00667-6. (64)

Kelley, D. S., Karson, J. A., Blackman, D. K., Früh-Green, G. L., Butterfield, D. A., Lilley, M. D., Olson, E. J., Schrenk, M. O., Roe, K. K., Lebon, G. T., Rivizzigno, P., and the AT3-60 Shipboard Party (2001) An off-axis hydrothermal vent field near the Mid-Atlantic Ridge at 30° N. *Nature*, **412** (6843), 145–149. doi: 10.1038/35084000. (55)

Kelley, K. K. (1960) Contributions to the data on theoretical metallurgy XIII, High-temperature heat-content, heat-capacity, and entropy data for the elements and inorganic compounds. Bulletin 584. *U.S. Dept. of the Interior, Bureau of Mines*. (67)

Kendall, C. and Coplen, T. B. (2001) Distribution of oxygen-18 and deuterium in river waters across the United States. *Hydrological Processes*, **15** (7), 1363–1393. doi: 10.1002/hyp.217. (119)

Kharaka, Y. K., Berry, F. A., and Friedman, I. (1973) Isotopic composition of oil-field brines from Kettleman North Dome, California, and their geologic implications. *Geochimica et Cosmochimica Acta*, **37** (8), 1899–1908. doi: 10.1016/0016-7037(73)90148-8. (106)

Kinnaman, F. S., Valentine, D. L., and Tyler, S. C. (2007) Carbon and hydrogen isotope fractionation associated with the aerobic microbial oxidation of methane, ethane, propane and butane. *Geochimica et Cosmochimica Acta*, **71** (2), 271–283. doi: 10.1016/j.gca.2006.09.007. (74, 82–83)

Kirschke, S., Bousquet, P., Ciais, P., Saunois, M., Canadell, J. G., Dlugokencky, E. J., Bergamaschi, P., Bergmann, D., Blake, D. R., Bruhwiler, L., Cameron-Smith, P., Castaldi, S., Chevallier, F., Feng, L., Fraser, A., Heimann, M., Hodson, E. L., Houweling, S., Josse, B., Fraser, P. J., Krummel, P. B., Lamarque, J.-F., Langenfelds, R. L., Quéré, C. L., Naik, V., O'Doherty, S., Palmer, P. I., Pison, I., Plummer, D., Poulter, B., Prinn, R. G., Rigby, M., Ringeval, B., Santini, M., Schmidt, M., Shindell, D. T., Simpson, I. J., Spahni, R., Steele, L. P., Strode, S. A., Sudo, K., Szopa, S., Werf, G. R. van der, Voulgarakis, A., Weele, M. van, Weiss, R. F., Williams, J. E., and Zeng, G. (2013) Three decades of global methane sources and sinks. *Nature Geoscience*, **6** (10), 813–823. doi: 10.1038/ngeo1955. (18, 74, 89)

Kiyosu, Y. (1983) Hydrogen isotopic compositions of hydrogen and methane from some volcanic areas in northeastern Japan. *Earth and Planetary Science Letters*, **62** (1), 41–52. doi: 10.1016/0012-821x(83)90069-9. (57)

Klein, F., Bach, W., Jöns, N., McCollom, T., Moskowitz, B., and Berquó, T. (2009) Iron partitioning and hydrogen generation during serpentinization of abyssal peridotites from 15°N on the Mid-Atlantic Ridge. *Geochimica et Cosmochimica Acta*, **73** (22), 6868–6893. doi: 10.1016/j.gca.2009.08.021. (61)

Klein, F., Bach, W., and McCollom, T. M. (2013) Compositional controls on hydrogen generation during serpentinization of ultramafic rocks. *Lithos*, **178**, 55–69. doi: 10.1016/j.lithos.2013.03.008. (61)

Koepp, M. (1978) D/H isotope exchange reaction between petroleum and water: a contributory determinant for D/H-isotope ratios in crude oils. In: *The Fourth International Conference, Geochronology, Cosmochronology, Isotope Geology USGS Open-File Report 78-701*. Vol. 701. http://pubs.er.usgs.gov/publication/ofr78701, pp. 221–222. (56, 93, 104–105)

Ku, H. (1969) Notes on the use of propagation of error formulas. *Journal of Research of the National Bureau of Standards—Section C: Engineering and Instrumentation*, **70C** (4), 263–273. doi: 10.6028/jres.070c.025. (76, 81)

Kumagai, H., Nakamura, K., Toki, T., Morishita, T., Okino, K., Ishibashi, J., Tsunogai, U., Kawagucci, S., Gamo, T., Shibuya, T., Sawaguchi, T., Neo, N., Joshima, M., Sato, T., and Takai, K. (2008) Geological background of the Kairei and Edmond hydrothermal fields along the Central Indian Ridge: Implications of their vent fluids' distinct chemistry. *Geofluids*, **8** (4), 239–251. doi: 10.1111/j.1468-8123.2008.00223.x. (71)

Kvenvolden, K. A. (1988) Methane hydrate—a major reservoir of carbon in the shallow geosphere? *Chemical Geology*, **71** (1), 41–51. doi: 10.1016/0009-2541(88)90104-0. (18)

Laderman, A. D., Brody, M., and Pendleton, E. (1989) The ecology of Atlantic white cedar wetlands: a community profile. (45)

Larson, J. G. and Hall, W. K. (1965) Studies of the hydrogen held by solids. VII. The exchange of the hydroxyl groups of alumina and silica-alumina catalysts with deuterated methane. *The Journal of Physical Chemistry*, **69** (9), 3080–3089. doi: 10.1021/j100893a044. (93)

Lau, M. C., Stackhouse, B., Layton, A., Chauhan, A., Vishnivetskaya, T., Chourey, K., Ronholm, J., Mykytczuk, N., Bennett, P., Lamarche-Gagnon, G., Burton, N., Pollard, W., Omelon, C., Medvigy, D., Hettich, R., Pfiffner, S., Whyte, L., and Onstott, T. (2015) An active atmospheric methane sink in high Arctic mineral cryosols. *The ISME Journal*, **9** (8), 1880–1891. doi: 10.1038/ismej.2015.112. (74)

Lécluse, C. and Robert, F. (1994) Hydrogen isotope exchange reaction rates: Origin of water in the inner solar system. *Geochimica et Cosmochimica Acta*, **58** (13), 2927–2939. doi: 10.1016/0016-7037(94)90126-0. (56, 60)

Lewan, M. (1997) Experiments on the role of water in petroleum formation. *Geochimica et Cosmochimica Acta*, **61** (17), 3691–3723. doi: 10.1016/s0016-7037(97)00176-2. (108)

Lin, Y.-S., Heuer, V. B., Goldhammer, T., Kellermann, M. Y., Zabel, M., and Hinrichs, K.-U. (2012) Towards constraining H_2 concentration in subseafloor sediment: A proposal for combined analysis by two distinct approaches. *Geochimica et Cosmochimica Acta*, **77**, 186–201. doi: 10.1016/j.gca.2011.11.008. (40)

Lis, G. P., Schimmelmann, A., and Mastalerz, M. (2006) D/H ratios and hydrogen exchangeability of type-II kerogens with increasing thermal maturity. *Organic Geochemistry*, **37** (3), 342–353. doi: 10.1016/j.orggeochem.2005.10.006. (108)

Lopes, J., Matos, L. de, Harper, M., Giallongo, F., Oh, J., Gruen, D., Ono, S., Kindermann, M., Duval, S., and Hristov, A. (2016) Effect of 3-nitrooxipropanol on methane and hydrogen emissions, methane isotopic signature, and ruminal fermentation in dairy cows. *Journal of Dairy Science*, **99** (7), 5335–5344. doi: 10.3168/jds.2015-10832. (93, 115)

Ludlam, S. D. and Duval, B. (2001) Natural and management-induced reduction in monimolimnetic volume and stability in a coastal, meromictic lake. *Lake and Reservoir Management*, **17** (2), 71–81. doi: 10.1080/07438140109353975. (119)

Luque, F., Crespo-Feo, E., Barrenechea, J., and Ortega, L. (2012) Carbon isotopes of graphite: Implications on fluid history. *Geoscience Frontiers*, **3** (2), 197–207. doi: 10.1016/j.gsf.2011.11.006. (64)

Luque, F., Ortega, L., Barrenechea, J., Millward, D., Beyssac, O., and Huizenga, J.-M. (2009) Deposition of highly crystalline graphite from moderate-temperature fluids. *Geology*, **37** (3), 275–278. doi: 10.1130/g25284a.1. (64)

Lyon, G. and Hulston, J. (1984) Carbon and hydrogen isotopic compositions of New Zealand geothermal gases. *Geochimica et Cosmochimica Acta*, **48** (6), 1161–1171. doi: 10.1016/0016-7037(84)90052-8. (56–57, 60, 93)

Ma, Q., Wu, S., and Tang, Y. (2008) Formation and abundance of doubly-substituted methane isotopologues ($^{13}CH_3D$) in natural gas systems. *Geochimica et Cosmochimica Acta*, **72** (22), 5446–5456. doi: 10.1016/j.gca.2008.08.014. (36)

Mariotti, A., Germon, J., Hubert, P., Kaiser, P., Letolle, R., Tardieux, A., and Tardieux, P. (1981) Experimental determination of nitrogen kinetic isotope fractionation: some principles; illustration for the denitrification and nitrification processes. *Plant and Soil*, **62** (3), 413–430. doi: 10.1007/bf02374138. (77)

Martineau, F., Fourel, F., Bodergat, A.-M., and Lécuyer, C. (2012) D/H equilibrium fractionation between H_2O and H_2 as a function of the salinity of aqueous solutions. *Chemical Geology*, **291**, 236–240. doi: 10.1016/j.chemgeo.2011.10.017. (59)

Marty, B. and Tolstikhin, I. N. (1998) CO_2 fluxes from mid-ocean ridges, arcs and plumes. *Chemical Geology*, **145** (3-4), 233–248. doi: 10.1016/s0009-2541(97)00145-9. (64)

Mathez, E. A., Dietrich, V. J., Holloway, J. R., and Boudreau, A. E. (1989) Carbon distribution in the Stillwater Complex and evolution of vapor during crystallization of Stillwater and Bushveld magmas. *Journal of Petrology*, **30** (1), 153–173. doi: 10.1093/petrology/30.1.153. (61)

McCalley, C. K., Woodcroft, B. J., Hodgkins, S. B., Wehr, R. A., Kim, E.-H., Mondav, R., Crill, P. M., Chanton, J. P., Rich, V. I., Tyson, G. W., and Saleska, S. W. (2014) Methane dynamics regulated by microbial community response to permafrost thaw. *Nature*, **514** (7523), 478–481. doi: 10.1038/nature13798. (26)

McCollom, T. (2012) Methane generation during experimental serpentinization of olivine. *Proceedings of the National Academy of Sciences of the United States of America*, **109** (49), E3334–E3334. doi: 10.1073/pnas.1214629109. (62)

McCollom, T. M. (2013) Laboratory simulations of abiotic hydrocarbon formation in Earth's deep subsurface. *Reviews in Mineralogy and Geochemistry*, **75**, 467–494. doi: 10.2138/rmg.2013.75.15. (62)

McCollom, T. M. (2016) Abiotic methane formation during experimental serpentinization of olivine. *Proceedings of the National Academy of Sciences of the United States of America*, **113** (49), 13965–13970. doi: 10.1073/pnas.1611843113. (48, 62)

McCollom, T. M. and Bach, W. (2009) Thermodynamic constraints on hydrogen generation during serpentinization of ultramafic rocks. *Geochimica et Cosmochimica Acta*, **73** (3), 856–875. doi: 10.1016/j.gca.2008.10.032. (61–62)

McCollom, T. M. and Seewald, J. S. (2001) A reassessment of the potential for reduction of dissolved CO_2 to hydrocarbons during serpentinization of olivine. *Geochimica et Cosmochimica Acta*, **65** (21), 3769–3778. doi: 10.1016/s0016-7037(01)00655-x. (48, 62)

——— (2003) Experimental constraints on the hydrothermal reactivity of organic acids and acid anions: I. Formic acid and formate. *Geochimica et Cosmochimica Acta*, **67** (19), 3625–3644. doi: 10.1016/s0016-7037(03)00136-4. (62)

——— (2007) Abiotic synthesis of organic compounds in deep-sea hydrothermal environments. *Chemical Reviews*, **107** (2), 382–401. doi: 10.1002/chin.200720264. (48, 51, 55, 64)

McDermott, J. M., Seewald, J. S., German, C. R., and Sylva, S. P. (2015) Pathways for abiotic organic synthesis at submarine hydrothermal fields. *Proceedings of the National Academy of Sciences of the United States of America*, **112** (25), 7668–7672. doi: 10.1073/pnas.1506295112. (48–51, 54–56, 62, 64, 67, 71)

McDermott, J. M. (2015) Geochemistry of deep-sea hydrothermal vent fluids from the Mid-Cayman Rise, Caribbean Sea. PhD thesis. Massachusetts Institute of Technology and Woods Hole Oceanographic Institution. doi: 10.1575/1912/7128. (48, 64–65, 67)

Méheut, M., Lazzeri, M., Balan, E., and Mauri, F. (2010) First-principles calculation of H/D isotopic fractionation between hydrous minerals and water. *Geochimica et Cosmochimica Acta*, **74** (14), 3874–3882. doi: 10.1016/j.gca.2010.04.020. (59)

Ménez, B., Pasini, V., and Brunelli, D. (2012) Life in the hydrated suboceanic mantle. *Nature Geoscience*, **5** (2), 133–137. doi: 10.1038/ngeo1359. (63)

Milesi, V., McCollom, T. M., and Guyot, F. (2016) Thermodynamic constraints on the formation of condensed carbon from serpentinization fluids. *Geochimica et Cosmochimica Acta*, **189**, 391–403. doi: 10.1016/j.gca.2016.06.006. (63)

Miller, M. F. and Pillinger, C. (1997) An appraisal of stepped heating release of fluid inclusion CO_2 for isotopic analysis: A preliminary to $\delta^{13}C$ characterisation of carbonaceous vesicles at the nanomole level. *Geochimica et Cosmochimica Acta*, **61** (1), 193–205. doi: 10.1016/s0016-7037(96)00328-6. (64)

Miser, H. D. (1929) Structure of the Ouachita Mountains of Oklahoma and Arkansas. Bulletin 50. *Oklahoma Geological Survey*. (106)

Morrill, P. L., Kuenen, J. G., Johnson, O. J., Suzuki, S., Rietze, A., Sessions, A. L., Fogel, M. L., and Nealson, K. H. (2013) Geochemistry and geobiology of a present-day serpentinization site in California: The Cedars. *Geochimica et Cosmochimica Acta*, **109**, 222–240. doi: 10.1016/j.gca.2013.01.043. (28, 40, 45, 90)

Naito, S., Takada, A., Tokizawa, S., and Miyao, T. (2005) Mechanistic study on the methane activation over various supported molybdenum carbide catalysts with isotopic tracer methods. *Applied Catalysis A: General*, **289** (1), 22–27. doi: 10.1016/j.apcata.2005.04.011. (93)

Neal, C. and Stanger, G. (1983) Hydrogen generation from mantle source rocks in Oman. *Earth and Planetary Science Letters*, **66**, 315–320. doi: 10.1016/0012-821x(83)90144-9. (57)

Nelson, D. D., Shorter, J. H., McManus, J. B., and Zahniser, M. S. (2002) Sub-part-per-billion detection of nitric oxide in air using a thermoelectrically cooled mid-infrared quantum cascade laser spectrometer. *Applied Physics B: Lasers and Optics*, **75** (2-3), 343–350. doi: 10.1007/s00340-002-0979-4. (115)

Nelson, D. D., McManus, B., Urbanski, S., Herndon, S., and Zahniser, M. S. (2004) High precision measurements of atmospheric nitrous oxide and methane using thermoelectrically cooled mid-infrared quantum cascade lasers and detectors. *Spectrochimica Acta Part A: Molecular and Biomolecular Spectroscopy*, **60** (14), 3325–3335. doi: 10.1016/j.saa.2004.01.033. (115)

Nesheim, J. C. and Lipscomb, J. D. (1996) Large kinetic isotope effects in methane oxidation catalyzed by methane monooxygenase: evidence for C–H bond cleavage in a reaction cycle intermediate. *Biochemistry*, **35** (31), 10240–10247. doi: 10.1021/bi960596w. (23, 77, 83)

Ni, Y., Ma, Q., Ellis, G. S., Dai, J., Katz, B., Zhang, S., and Tang, Y. (2011) Fundamental studies on kinetic isotope effect (KIE) of hydrogen isotope fractionation in natural gas systems. *Geochimica et Cosmochimica Acta*, **75** (10), 2696–2707. doi: 10.1016/j.gca.2011.02.016. (108)

Nihous, G. C. (2008) A quantitative interpretation of recent experimental results on stable carbon isotope fractionation by aerobic CH_4-oxidizing bacteria. *Geochimica et Cosmochimica Acta*, **72** (18), 4469–4475. doi: 10.1016/j.gca.2008.06.016. (76, 84)

——— (2010) Notes on the temperature dependence of carbon isotope fractionation by aerobic CH_4-oxidising bacteria. *Isotopes in Environmental and Health Studies*, **46** (2), 133–140. doi: 10.1080/10256016.2010.488724. (77, 84)

Ohmoto, H. and Kerrick, D. M. (1977) Devolatilization equilibria in graphitic systems. *American Journal of Science*, **277** (8), 1013–1044. doi: 10.2475/ajs.277.8.1013. (64)

Okumura, T., Kawagucci, S., Saito, Y., Matsui, Y., Takai, K., and Imachi, H. (2016) Hydrogen and carbon isotope systematics in hydrogenotrophic methanogenesis under H_2-limited and H_2-enriched conditions: implications for the origin of methane and its isotopic diagnosis. *Progress in Earth and Planetary Science*, **3** (1), 1–19. doi: 10.1186/s40645-016-0088-3. (95)

Ono, S., Wang, D. T., Gruen, D. S., Sherwood Lollar, B., Zahniser, M., McManus, B. J., and Nelson, D. D. (2014) Measurement of a doubly-substituted methane isotopologue, $^{13}CH_3D$, by tunable infrared laser direct absorption spectroscopy. *Analytical Chemistry*, **86**, 6487–6494. doi: 10.1021/ac5010579. (17, 26, 36–38, 42, 49, 74, 76, 93, 99, 103, 116, 118)

Ono, S., Wing, B., Johnston, D., Farquhar, J., and Rumble, D. (2006a) Mass-dependent fractionation of quadruple stable sulfur isotope system as a new tracer of sulfur biogeochemical cycles. *Geochimica et Cosmochimica Acta*, **70** (9), 2238–2252. doi: 10.1016/j.gca.2006.01.022. (43)

Ono, S., Wing, B., Rumble, D., and Farquhar, J. (2006b) High precision analysis of all four stable isotopes of sulfur (^{32}S, ^{33}S, ^{34}S and ^{36}S) at nanomole levels using a laser fluorination isotope-ratio-monitoring gas chromatography–mass spectrometry. *Chemical Geology*, **225** (1-2), 30–39. doi: 10.1016/j.chemgeo.2005.08.005. (34)

Oremland, R. S. and Culbertson, C. W. (1992) Importance of methane-oxidizing bacteria in the methane budget as revealed by the use of a specific inhibitor. *Nature*, **356** (6368), 421–423. doi: 10.1038/356421a0. (74)

Panichi, C., Ferrara, G., and Gonfiantini, R. (1977) Isotope geothermometry in the Larderello geothermal field. *Geothermics*, **5** (1-4), 81–88. doi: 10.1016/0375-6505(77)90012-8. (57)

Panichi, C. and Gonfiantini, R. (1977) Environmental isotopes in geothermal studies. *Geothermics*, **6** (3-4), 143–161. doi: 10.1016/0375-6505(77)90024-4. (57)

Pasini, V., Brunelli, D., Dumas, P., Sandt, C., Frederick, J., Benzerara, K., Bernard, S., and Ménez, B. (2013) Low temperature hydrothermal oil and associated biological precursors in serpentinites from Mid-Ocean Ridge. *Lithos*, **178**, 84–95. doi: 10.1016/j.lithos.2013.06.014. (63)

Pester, N. J., Reeves, E. P., Rough, M. E., Ding, K., Seewald, J. S., and Seyfried, W. E. (2012) Subseafloor phase equilibria in high-temperature hydrothermal fluids of the Lucky Strike Seamount (Mid-Atlantic Ridge, 37°17′N). *Geochimica et Cosmochimica Acta*, **90**, 303–322. doi: 10.1016/j.gca.2012.05.018. (50, 55, 63)

Peters, E. K. (1993) D-^{18}O enriched waters of the Coast Range Mountains, northern California: connate and ore-forming fluids. *Geochimica et Cosmochimica Acta*, **57**, 1093–1104. doi: 10.1016/0016-7037(93)90043-v. (119–120)

Peterson, E. J. R. (2005) Carbon and electron flow via methanogenesis, SO_4^{2-} , NO_3^- and Fe^{3+} reduction in the anoxic hypolimnia of Upper Mystic Lake. PhD thesis. Massachusetts Institute of Technology. (90)

Pohlman, J., Kaneko, M., Heuer, V., Coffin, R., and Whiticar, M. (2009) Methane sources and production in the northern Cascadia margin gas hydrate system. *Earth and Planetary Science Letters*, **287** (3), 504–512. doi: 10.1016/j.epsl.2009.08.037. (26, 29, 40, 44–45)

Powelson, D., Chanton, J., and Abichou, T. (2007) Methane oxidation in biofilters measured by mass-balance and stable isotope methods. *Environmental Science & Technology*, **41** (2), 620–625. doi: 10.1021/es061656g. (74, 82–83)

Proskurowski, G. (2010) Abiogenic hydrocarbon production at the geosphere-biosphere interface via serpentinization reactions. In: *Handbook of Hydrocarbon and Lipid Microbiology*. Ed. by K. N. Timmis. Springer. Chap. 14, pp. 215–231. doi: 10.1007/978-3-540-77587-4_14. (48)

Proskurowski, G., Lilley, M. D., Kelley, D. S., and Olson, E. J. (2006) Low temperature volatile production at the Lost City Hydrothermal Field, evidence from a hydrogen stable isotope geothermometer. *Chemical Geology*, **229** (4), 331–343. doi: 10.1016/j.chemgeo.2005.11.005. (55–57, 59–62, 71)

Proskurowski, G., Lilley, M. D., Seewald, J. S., Früh-Green, G. L., Olson, E. J., Lupton, J. E., Sylva, S. P., and Kelley, D. S. (2008) Abiogenic hydrocarbon production at Lost City hydrothermal field. *Science*, **319** (5863), 604–607. doi: 10.1126/science.1151194. (48, 50–51, 54–55, 62, 67)

Pudzianowski, A. T. and Loew, G. H. (1983) Hydrogen abstractions from methyl groups by atomic oxygen. Kinetic isotope effects calculated from MNDO/UHF results and an assessment of their applicability to monooxygenase-dependent hydroxylations. *The Journal of Physical Chemistry*, **87** (6), 1081–1085. doi: 10.1021/j100229a029. (82–83)

Rasigraf, O., Vogt, C., Richnow, H.-H., Jetten, M. S., and Ettwig, K. F. (2012) Carbon and hydrogen isotope fractionation during nitrite-dependent anaerobic methane oxidation by *Methylomirabilis oxyfera*. *Geochimica et Cosmochimica Acta*, **89**, 256–264. doi: 10.1016/j.gca.2012.04.054. (90–91)

Rataj, M., Kauth, J., and Donnelly, M. (1991) Oxidation of deuterated compounds by high specific activity methane monooxygenase from *Methylosinus trichosporium*. Mechanistic implications. *Journal of Biological Chemistry*, **266** (28), 18684–18690. (83)

Reeburgh, W. S. (1976) Methane consumption in Cariaco Trench waters and sediments. *Earth and Planetary Science Letters*, **28** (3), 337–344. doi: 10.1016/0012-821x(76)90195-3. (91)

——— (2007) Oceanic methane biogeochemistry. *Chemical Reviews*, **107** (2), 486–513. doi: 10.1002/chin.200720267. (74, 89)

Rees, C. E. (1973) A steady-state model for sulphur isotope fractionation in bacterial reduction processes. *Geochimica et Cosmochimica Acta*, **37** (5), 1141–1162. doi: 10.1016/0016-7037(73)90052-5. (28, 39, 41, 84)

Reeves, E. (2010) Laboratory and field-based investigations of subsurface geochemical processes in seafloor hydrothermal systems. PhD thesis. Massachusetts Institute of Technology and Woods Hole Oceanographic Institution. doi: 10.1575/1912/3730. (62)

Reeves, E. P., McDermott, J. M., and Seewald, J. S. (2014) The origin of methanethiol in midocean ridge hydrothermal fluids. *Proceedings of the National Academy of Sciences of the United States of America*, **111** (15), 5474–5479. doi: 10.1073/pnas.1400643111. (26, 40, 46, 49, 54–55, 71)

Reeves, E. P., Seewald, J. S., and Sylva, S. P. (2012) Hydrogen isotope exchange between *n*-alkanes and water under hydrothermal conditions. *Geochimica et Cosmochimica Acta*, **77**, 582–599. doi: 10.1016/j.gca.2011.10.008. (26, 56–57, 60, 62, 68, 93, 109, 112)

Riedel, M., Collett, T., Malone, M., and the Expedition 311 Scientists (2006) Proceedings of the Integrated Ocean Drilling Program. Vol. 311. Integrated Ocean Drilling Program Management International, Inc. doi: 10.2204/iodp.proc.311.101.2006. (40, 44)

Rigby, M., Manning, A., and Prinn, R. (2012) The value of high-frequency, high-precision methane isotopologue measurements for source and sink estimation. *Journal of Geophysical Research: Atmospheres (1984–2012)*, **117** (D12). doi: 10.1029/2011jd017384. (89)

Robertson, P. J., Scurrell, M. S., and Kemball, C. (1975) Exchange of alkanes with deuterium over γ-alumina. A Brønsted linear free energy relationship. *Journal of the Chemical Society, Faraday Transactions 1: Physical Chemistry in Condensed Phases*, **71** (0), 903–912. doi: 10.1039/F19757100903. (93)

Rolston, J., Den Hartog, J., and Butler, J. (1976) The deuterium isotope separation factor between hydrogen and liquid water. *The Journal of Physical Chemistry*, **80** (10), 1064–1067. doi: 10.1021/j100551a008. (38)

Roston, D. and Kohen, A. (2010) Elusive transition state of alcohol dehydrogenase unveiled. *Proceedings of the National Academy of Sciences of the United States of America*, **107** (21), 9572–9577. doi: 10.1073/pnas.1000931107. (39, 42, 44)

Rothman, L. S., Gordon, I. E., Babikov, Y., Barbe, A., Benner, D. C., Bernath, P. F., Birk, M., Bizzocchi, L., Boudon, V., Brown, L. R., Campargue, A., Chance, K., Cohen, E. A., Coudert, L. H., Devi, V. M., Drouin, B. J., Fayt, A., Flaud, J.-M., Gamache, R. R., Harrison, J. J., Hartmann, J.-M., Hill, C., Hodges, J. T., Jacquemart, D., Jolly, A., Lamouroux, J., Roy, R. J. L., Li, G., Long, D. A., Lyulin, O. M., Mackie, C. J., Massie, S. T., Mikhailenko, S., Müller, H. S. P., Naumenko, O. V., Nikitin, A. V., Orphal, J., Perevalov, V., Perrin, A., Polovtseva, E. R., Richard, C., Smith, M. A. H., Starikova, E., Sung, K., Tashkun, S., Tennyson, J., Toon, G. C., Tyuterev, V. G., and Wagner, G. (2013) The HITRAN2012 molecular spectroscopic database. *Journal of Quantitative Spectroscopy and Radiative Transfer*, **130**, 4–50. doi: 10.1016/j.jqsrt.2013.07.002. (115)

Rowan, E. L., Engle, M. A., Kraemer, T. F., Schroeder, K. T., Hammack, R. W., and Doughten, M. W. (2015) Geochemical and isotopic evolution of water produced from Middle Devonian Marcellus shale gas wells, Appalachian basin, Pennsylvania. *AAPG Bulletin*, **99** (02), 181–206. doi: 10.1306/07071413146. (40)

Rumble, D. (2014) Hydrothermal Graphitic Carbon. *Elements*, **10** (6), 427–433. doi: 10.2113/gselements.10.6.427. (64)

Saccocia, P. J., Seewald, J. S., and Shanks, W. C. (2009) Oxygen and hydrogen isotope fractionation in serpentine–water and talc–water systems from 250 to 450 °C, 50 MPa. *Geochimica et Cosmochimica Acta*, **73** (22), 6789–6804. doi: 10.1016/j.gca.2009.07.036. (59)

Sackett, W. M. (1978) Carbon and hydrogen isotope effects during the thermocatalytic production of hydrocarbons in laboratory simulation experiments. *Geochimica et Cosmochimica Acta*, **42** (6), 571–580. doi: 10.1016/0016-7037(78)90002-9. (108)

Sackett, W. M. and Conkright, M. (1997) Summary and re-evaluation of the high-temperature isotope geochemistry of methane. *Geochimica et Cosmochimica Acta*, **61** (9), 1941–1952. doi: 10.1016/s0016-7037(97)00039-2. (108)

Saueressig, G., Bergamaschi, P., Crowley, J., Fischer, H., and Harris, G. (1995) Carbon kinetic isotope effect in the reaction of CH_4 with Cl atoms. *Geophysical Research Letters*, **22** (10), 1225–1228. doi: 10.1029/95gl00881. (90)

——— (1996) D/H kinetic isotope effect in the reaction CH_4+ Cl. *Geophysical Research Letters*, **23** (24), 3619–3622. doi: 10.1029/96gl03292. (90)

Saueressig, G., Crowley, J. N., Bergamaschi, P., Brühl, C., Brenninkmeijer, C. A., and Fischer, H. (2001) Carbon 13 and D kinetic isotope effects in the reactions of CH_4 with $O(^1D)$ and OH: New laboratory measurements and their implications for the isotopic composition of stratospheric methane. *Journal of Geophysical Research: Atmospheres (1984–2012)*, **106** (D19), 23127–23138. doi: 10.1029/2000jd000120. (90)

Scandella, B. P., Varadharajan, C., Hemond, H. F., Ruppel, C., and Juanes, R. (2011) A conduit dilation model of methane venting from lake sediments. *Geophysical Research Letters*, **38** (6). doi: 10.1029/2011gl046768. (45)

Scharschmidt, M., Fisher, M. A., and Cleland, W. (1984) Variation of transition-state structure as a function of the nucleotide in reactions catalyzed by dehydrogenases. 1. Liver alcohol dehydrogenase with benzyl alcohol and yeast aldehyde dehydrogenase with benzaldehyde. *Biochemistry*, **23** (23), 5471–5478. doi: 10.1021/bi00318a015. (39, 42)

Scheller, S., Goenrich, M., Boecher, R., Thauer, R. K., and Jaun, B. (2010) The key nickel enzyme of methanogenesis catalyses the anaerobic oxidation of methane. *Nature*, **465** (7298), 606–608. doi: 10.1038/nature09015. (91)

Scheller, S., Goenrich, M., Thauer, R. K., and Jaun, B. M. (2013) Methyl-coenzyme M reductase from methanogenic archaea: isotope effects on the formation and anaerobic oxidation of methane. *Journal of the American Chemical Society*, doi: 10.1021/ja406485z. (39, 42, 95)

Schimmelmann, A., Boudou, J.-P., Lewan, M. D., and Wintsch, R. P. (2001) Experimental controls on D/H and $^{13}C/^{12}C$ ratios of kerogen, bitumen and oil during hydrous pyrolysis. *Organic Geochemistry*, **32** (8), 1009–1018. doi: 10.1016/s0146-6380(01)00059-6. (108)

Schimmelmann, A., Lewan, M. D., and Wintsch, R. P. (1999) D/H isotope ratios of kerogen, bitumen, oil, and water in hydrous pyrolysis of source rocks containing kerogen types I, II, IIS, and III. *Geochimica et Cosmochimica Acta*, **63** (22), 3751–3766. doi: 10.1016/s0016-7037(99)00221-5. (108)

Schimmelmann, A., Sessions, A. L., and Mastalerz, M. (2006) Hydrogen isotopic (D/H) composition of organic matter during diagenesis and thermal maturation. *Annual Review of Earth and Planetary Sciences*, **34**, 501–533. doi: 10.1146/annurev.earth.34.031405.125011. (62, 104, 108)

Schlindwein, V. and Schmid, F. (2016) Mid-ocean-ridge seismicity reveals extreme types of ocean lithosphere. *Nature*, doi: 10.1038/nature18277. (65)

Schoell, M. (1988) Multiple origins of methane in the earth. *Chemical Geology*, **71** (1), 1–10. doi: 10.1016/0009-2541(88)90101-5. (26)

Schroeder, T., John, B., and Frost, B. R. (2002) Geologic implications of seawater circulation through peridotite exposed at slow-spreading mid-ocean ridges. *Geology*, **30** (4), 367–370. doi: 10.1130/0091-7613(2002)030<0367:giosct>2.0.co;2. (65)

Seewald, J. S. (1994) Evidence for metastable equilibrium between hydrocarbons under hydrothermal conditions. *Nature*, **370**, 285–287. doi: 10.1038/370285a0. (62)

——— (2001a) Aqueous geochemistry of low molecular weight hydrocarbons at elevated temperatures and pressures: constraints from mineral buffered laboratory experiments. *Geochimica et Cosmochimica Acta*, **65** (10), 1641–1664. doi: 10.1016/s0016-7037(01)00544-0. (54)

——— (2001b) Model for the origin of carboxylic acids in basinal brines. *Geochimica et Cosmochimica Acta*, **65** (21), 3779–3789. doi: 10.1016/s0016-7037(01)00702-5. (106)

——— (2003) Organic–inorganic interactions in petroleum-producing sedimentary basins. *Nature*, **426** (6964), 327–333. doi: 10.1038/nature02132. (66, 106, 109)

Seewald, J. S., Benitez-Nelson, B. C., and Whelan, J. K. (1998) Laboratory and theoretical constraints on the generation and composition of natural gas. *Geochimica et Cosmochimica Acta*, **62** (9), 1599–1617. doi: 10.1016/s0016-7037(98)00000-3. (109)

Seewald, J. S., Doherty, K. W., Hammar, T. R., and Liberatore, S. P. (2002) A new gas-tight isobaric sampler for hydrothermal fluids. *Deep Sea Research Part I: Oceanographic Research Papers*, **49** (1), 189–196. doi: 10.1016/s0967-0637(01)00046-2. (46, 49)

Seewald, J. S., Zolotov, M. Y., and McCollom, T. (2006) Experimental investigation of single carbon compounds under hydrothermal conditions. *Geochimica et Cosmochimica Acta*, **70** (2), 446–460. doi: 10.1016/j.gca.2005.09.002. (62)

Seewald, J. and Whelan, J. (2005) Isotopic and chemical composition of natural gas from the Potato Hills field, southeastern Oklahoma: Evidence for an abiogenic origin? In: *AAPG Research Conference, Origin of Petroleum*. (99–100, 104)

Sessions, A. L. and Hayes, J. M. (2005) Calculation of hydrogen isotopic fractionations in biogeochemical systems. *Geochimica et Cosmochimica Acta*, **69** (3), 593–597. doi: 10.1016/j.gca.2004.08.005. (83)

Sessions, A. L., Sylva, S. P., Summons, R. E., and Hayes, J. M. (2004) Isotopic exchange of carbon-bound hydrogen over geologic timescales. *Geochimica et Cosmochimica Acta*, **68** (7), 1545–1559. doi: 10.1016/j.gca.2003.06.004. (62, 104)

Seyfried Jr., W. E., Janecky, D. R., and Berndt, M. E. (1987) Rocking autoclaves for hydrothermal experiments, II. The flexible reaction-cell system. *Hydrothermal Experimental Techniques*, **9**, 216–239. (108)

Seyfried, W., Pester, N. J., Tutolo, B. M., and Ding, K. (2015) The Lost City hydrothermal system: Constraints imposed by vent fluid chemistry and reaction path models on subseafloor heat and mass transfer processes. *Geochimica et Cosmochimica Acta*, **163**, 59–79. doi: 10.1016/j.gca.2015.04.040. (50, 57, 61)

Shanks, W. C., Böhlke, J. K., and Seal, R. R. (1995) Stable isotopes in mid-ocean ridge hydrothermal systems: interactions between fluids, minerals, and organisms. In: *Seafloor Hydrothermal Systems: Physical, Chemical,*

Biological, and Geological Interactions. Ed. by S. E. Humphris, R. A. Zierenberg, L. S. Mullineaux, and R. E. Thomson. American Geophysical Union, pp. 194–221. doi: 10.1029/gm091p0194. (40, 46, 59, 71)

Shaw, J. H., Bilotti, F., and Brennan, P. A. (1999) Patterns of imbricate thrusting. *Geological Society of America Bulletin*, **111** (8), 1140–1154. doi: 10.1130/0016-7606(1999)111<1140:poit>2.3.co;2. (106)

Sherwood Lollar, B., Frape, S., Weise, S., Fritz, P., Macko, S., and Welhan, J. (1993) Abiogenic methanogenesis in crystalline rocks. *Geochimica et Cosmochimica Acta*, **57** (23), 5087–5097. doi: 10.1016/0016-7037(93)90610-9. (57)

Sherwood Lollar, B., Lacrampe-Couloume, G., Voglesonger, K., Onstott, T., Pratt, L., and Slater, G. (2008) Isotopic signatures of CH_4 and higher hydrocarbon gases from Precambrian Shield sites: A model for abiogenic polymerization of hydrocarbons. *Geochimica et Cosmochimica Acta*, **72** (19), 4778–4795. doi: 10.1016/j.gca.2008.07.004. (26, 29, 40, 46, 57)

Sherwood Lollar, B., Voglesonger, K., Lin, L.-H., Lacrampe-Couloume, G., Telling, J., Abrajano, T., Onstott, T., and Pratt, L. (2007) Hydrogeologic controls on episodic H_2 release from Precambrian fractured rocks—Energy for deep subsurface life on Earth and Mars. *Astrobiology*, **7** (6), 971–986. doi: 10.1089/ast.2006.0096. (46, 57)

Sherwood Lollar, B., Westgate, T., Ward, J., Slater, G., and Lacrampe-Couloume, G. (2002) Abiogenic formation of alkanes in the Earth's crust as a minor source for global hydrocarbon reservoirs. *Nature*, **416** (6880), 522–524. doi: 10.1038/416522a. (26, 28–29, 40, 46)

Sherwood Lollar, B., Onstott, T. C., Lacrampe-Couloume, G., and Ballentine, C. J. (2014) The contribution of the Precambrian continental lithosphere to global H_2 production. *Nature*, **516** (7531), 379–382. doi: 10.1038/nature14017. (29)

Sherwood, B., Fritz, P., Frape, S., Macko, S., Weise, S., and Welhan, J. (1988) Methane occurrences in the Canadian Shield. *Chemical Geology*, **71** (1), 223–236. doi: 10.1016/0009-2541(88)90117-9. (46)

Shipp, J. A., Gould, I. R., Shock, E. L., Williams, L. B., and Hartnett, H. E. (2014) Sphalerite is a geochemical catalyst for carbon- hydrogen bond activation. *Proceedings of the National Academy of Sciences of the United States of America*, **111** (32), 11642–11645. doi: 10.1073/pnas.1324222111. (104)

Shock, E. L. (1988) Organic acid metastability in sedimentary basins. *Geology*, **16** (10), 886–890. doi: 10.1130/0091-7613(1988)016<0886:oamisb>2.3.co;2. (106)

Shock, E. L. (1992) Chapter 5. Chemical environments of submarine hydrothermal systems. *Origins of Life and Evolution of the Biosphere*, **22** (1), 67–107. doi: 10.1007/BF01808019. (52)

——— (1993) Hydrothermal dehydration of aqueous organic compounds. *Geochimica et Cosmochimica Acta*, **57** (14), 3341–3349. doi: 10.1016/0016-7037(93)90542-5. (67)

Shock, E. L. and Helgeson, H. C. (1990) Calculation of the thermodynamic and transport properties of aqueous species at high pressures and temperatures: Standard partial molal properties of organic species. *Geochimica et Cosmochimica Acta*, **54** (4), 915–945. doi: 10.1016/0016-7037(90)90429-o. (54)

Simoneit, B. R. (1985) Hydrothermal petroleum: genesis, migration, and deposition in Guaymas Basin, Gulf of California. *Canadian Journal of Earth Sciences*, **22** (12), 1919–1929. doi: 10.1139/e85-208. (46)

Simoneit, B. R. and Lonsdale, P. F. (1982) Hydrothermal petroleum in mineralized mounds at the seabed of Guaymas Basin. *Nature*, **295**, 198–202. doi: 10.1038/295198a0. (46)

Sirajuddin, S. and Rosenzweig, A. C. (2015) Enzymatic oxidation of methane. *Biochemistry*, **54** (14), 2283–2294. doi: 10.1021/acs.biochem.5b00198. (77)

Sleep, N., Meibom, A., Fridriksson, T., Coleman, R., and Bird, D. (2004) H_2-rich fluids from serpentinization: geochemical and biotic implications. *Proceedings of the National Academy of Sciences of the United States of America*, **101** (35), 12818–12823. doi: 10.1073/pnas.0405289101. (62)

Smith, J., Rigby, D., Gould, K., Hart, G., and Hargraves, A. (1985) An isotopic study of hydrocarbon generation processes. *Organic Geochemistry*, **8** (5), 341–347. doi: 10.1016/0146-6380(85)90013-0. (108)

Stewart, L. C., Kwon, S.-W., Kim, Y.-T., Jung, J.-H., Holden, J. F., and Park, C.-S. (2015) *Methanocaldococcus bathoardescens* sp. nov., a hyperthermophilic methanogen isolated from a volcanically active deep-sea hydrothermal vent.

International Journal of Systematic and Evolutionary Microbiology, **65** (4), 1280–1283. DOI: 10.1099/ijs.0.000097. (34)

Stolper, D. A., Lawson, M., Davis, C. L., Ferreira, A. A., Santos Neto, E. V., Ellis, G. S., Lewan, M. D., Martini, A. M., Tang, Y., Schoell, M., Sessions, A. L., and Eiler, J. M. (2014a) Formation temperatures of thermogenic and biogenic methane. *Science*, **344** (6191), 1500–1503. DOI: 10.1126/science.1254509. (26–27, 46, 48, 75, 91, 93–94, 108)

Stolper, D., Martini, A., Clog, M., Douglas, P., Shusta, S., Valentine, D., Sessions, A., and Eiler, J. (2015) Distinguishing and understanding thermogenic and biogenic sources of methane using multiply substituted isotopologues. *Geochimica et Cosmochimica Acta*, **161**, 219–247. DOI: 10.1016/j.gca.2015.04.015. (75, 79, 90–91, 93, 108)

Stolper, D., Sessions, A., Ferreira, A., Neto, E. S., Schimmelmann, A., Shusta, S., Valentine, D., and Eiler, J. (2014b) Combined ^{13}C–D and D–D clumping in methane: methods and preliminary results. *Geochimica et Cosmochimica Acta*, **126**, 169–191. DOI: 10.1016/j.gca.2013.10.045. (17, 26–27, 74, 93, 116)

Suda, K., Ueno, Y., Yoshizaki, M., Nakamura, H., Kurokawa, K., Nishiyama, E., Yoshino, K., Hongoh, Y., Kawachi, K., Omori, S., Yamada, K., Yoshida, N., and Maruyama, S. (2014) Origin of methane in serpentinite-hosted hydrothermal systems: The CH_4–H_2–H_2 O hydrogen isotope systematics of the Hakuba Happo hot spring. *Earth and Planetary Science Letters*, **386**, 112–125. DOI: 10.1016/j.epsl.2013.11.001. (57)

Suess, H. (1949) Das Gleichgewicht H_2+ HDO = HD + H_2O und die weiteren Austauschgleichgewichte im System H_2, D_2 und H_2O. *Zeitschrift Naturforschung Teil A*, **4**, 328. (38, 44, 59)

Takai, K., Nakamura, K., Toki, T., Tsunogai, U., Miyazaki, M., Miyazaki, J., Hirayama, H., Nakagawa, S., Nunoura, T., and Horikoshi, K. (2008) Cell proliferation at 122°C and isotopically heavy CH_4 production by a hyperthermophilic methanogen under high-pressure cultivation. *Proceedings of the National Academy of Sciences of the United States of America*, **105** (31), 10949–10954. DOI: 10.1073/pnas.0712334105. (27, 55, 75, 85)

Tang, Y., Huang, Y., Ellis, G. S., Wang, Y., Kralert, P. G., Gillaizeau, B., Ma, Q., and Hwang, R. (2005) A kinetic model for thermally induced hydrogen and carbon isotope fractionation of individual *n*-alkanes in crude oil. *Geochimica et Cosmochimica Acta*, **69** (18), 4505–4520. DOI: 10.1016/j.gca.2004.12.026. (108)

Tekippe, J., Hristov, A., Heyler, K., Cassidy, T., Zheljazkov, V., Ferreira, J., Karnati, S., and Varga, G. (2011) Rumen fermentation and production effects of *Origanum vulgare* L. leaves in lactating dairy cows. *Journal of Dairy Science*, **94** (10), 5065–5079. DOI: 10.3168/jds.2010-4095. (44)

Templeton, A. S., Chu, K.-H., Alvarez-Cohen, L., and Conrad, M. E. (2006) Variable carbon isotope fractionation expressed by aerobic CH_4-oxidizing bacteria. *Geochimica et Cosmochimica Acta*, **70** (7), 1739–1752. DOI: 10.1016/j.gca.2005.12.002. (76, 79, 82, 84, 87)

Thauer, R. K. (1998) Biochemistry of methanogenesis: a tribute to Marjory Stephenson: 1998 Marjory Stephenson Prize Lecture. *Microbiology*, **144** (9), 2377–2406. DOI: 10.1099/00221287-144-9-2377. (39)

Tilley, B., McLellan, S., Hiebert, S., Quartero, B., Veilleux, B., and Muehlenbachs, K. (2011) Gas isotope reversals in fractured gas reservoirs of the western Canadian Foothills: Mature shale gases in disguise. *AAPG Bulletin*, **95** (8), 1399–1422. DOI: 10.1306/01031110103. (99, 106)

Tilley, B. and Muehlenbachs, K. (2013) Isotope reversals and universal stages and trends of gas maturation in sealed, self-contained petroleum systems. *Chemical Geology*, **339**, 194–204. DOI: 10.1016/j.chemgeo.2012.08.002. (106)

Titarenko, S. S. and McCaig, A. M. (2016) Modelling the Lost City hydrothermal field: influence of topography and permeability structure. *Geofluids*, **16** (2), 314–328. DOI: 10.1111/gfl.12151. (61)

Twing, K. I., Brazelton, W. J., Kubo, M. D. Y., Hyer, A. J., Cardace, D., Hoehler, T. M., McCollom, T. M., and Schrenk, M. O. (2017) Serpentinization-influenced groundwater harbors extremely low diversity microbial communities adapted to high pH. *Frontiers in Microbiology*, **8**, 308. DOI: 10.3389/fmicb.2017.00308. (120)

Tyler, S. C., Ajie, H. O., Rice, A. L., Cicerone, R. J., and Tuazon, E. C. (2000) Experimentally determined kinetic isotope effects in the reaction of CH_4 with Cl: Implications for atmospheric CH_4. *Geophysical Research Letters*, **27** (12), 1715–1718. DOI: 10.1029/1999gl011168. (90)

Urey, H. C. (1947) The thermodynamic properties of isotopic substances. *Journal of the Chemical Society*, 562–581. DOI: 10.1039/jr9470000562. (44)

Valentine, D. L. (2011) Emerging topics in marine methane biogeochemistry. *Annual Review of Marine Science*, **3**, 147–171. doi: 10.1146/annurev-marine-120709-142734. (89)

Valentine, D. L., Chidthaisong, A., Rice, A., Reeburgh, W. S., and Tyler, S. C. (2004) Carbon and hydrogen isotope fractionation by moderately thermophilic methanogens. *Geochimica et Cosmochimica Acta*, **68** (7), 1571–1590. doi: 10.1016/j.gca.2003.10.012. (26, 28, 39, 42, 84, 95)

Vanko, D. A. (1988) Temperature, pressure, and composition of hydrothermal fluids, with their bearing on the magnitude of tectonic uplift at mid-ocean ridges, inferred from fluid inclusions in oceanic layer 3 rocks. *Journal of Geophysical Research*, **93** (B5), 4595. doi: 10.1029/jb093ib05p04595. (67)

Varadharajan, C. and Hemond, H. F. (2012) Time-series analysis of high-resolution ebullition fluxes from a stratified, freshwater lake. *Journal of Geophysical Research*, **117** (G2), G02004. doi: 10.1029/2011jg001866. (29, 45)

Varadharajan, C., Hermosillo, R., and Hemond, H. F. (2010) A low-cost automated trap to measure bubbling gas fluxes. *Limnology and Oceanography: Methods*, **8**, 363–375. doi: 10.4319/lom.2010.8.363. (45)

Vavilin, V. A., Rytov, S. V., Shim, N., and Vogt, C. (2015) Non-linear dynamics of stable carbon and hydrogen isotope signatures based on a biological kinetic model of aerobic enzymatic methane oxidation. *Isotopes in Environmental and Health Studies*, **52** (3), 185–202. doi: 10.1080/10256016.2016.1092965. (84)

Ver Eecke, H. C., Akerman, N. H., Huber, J. A., Butterfield, D. A., and Holden, J. F. (2013) Growth kinetics and energetics of a deep-sea hyperthermophilic methanogen under varying environmental conditions. *Environmental Microbiology Reports*, **5** (5), 665–671. doi: 10.1111/1758-2229.12065. (34)

Vinson, D. S., Blair, N. E., Martini, A. M., Larter, S., Orem, W. H., and McIntosh, J. C. (2017) Microbial methane from in situ biodegradation of coal and shale: A review and reevaluation of hydrogen and carbon isotope signatures. *Chemical Geology*, **453**, 128–145. doi: 10.1016/j.chemgeo.2017.01.027. (95)

Von Damm, K. L., Edmond, J. M., Grant, B., Measures, C. I., Walden, B., and Weiss, R. F. (1985) Chemistry of submarine hydrothermal solutions at 21° N, East Pacific Rise. *Geochimica et Cosmochimica Acta*, **49** (11), 2197–2220. doi: 10.1016/0016-7037(85)90222-4. (65)

Wagman, D. D., Evans, W. H., Parker, V. B., Schumm, R. H., and Halow, I. (1982) The NBS tables of chemical thermodynamic properties. Selected values for inorganic and C_1 and C_2 organic substances in SI units. *Journal of Physical and Chemical Reference Data*, **11** (Supplement 2), 1–151. (67)

Wahlen, M. (1993) The global methane cycle. *Annual Review of Earth and Planetary Sciences*, **21**, 407–426. doi: 10.1146/annurev.earth.21.1.407. (74)

Wang, D. T., Gruen, D. S., Lollar, B. S., Hinrichs, K.-U., Stewart, L. C., Holden, J. F., Hristov, A. N., Pohlman, J. W., Morrill, P. L., Könneke, M., Delwiche, K. B., Reeves, E. P., Sutcliffe, C. N., Ritter, D. J., Seewald, J. S., McIntosh, J. C., Hemond, H. F., Kubo, M. D., Cardace, D., Hoehler, T. M., and Ono, S. (2015) Nonequilibrium clumped isotope signals in microbial methane. *Science*, **348** (6233), 428–431. doi: 10.1126/science.aaa4326. (48–49, 51–52, 56, 75–76, 81, 84–85, 89–91, 93, 95, 105, 108, 115–116, 118–119, 121)

Wang, D. T., Welander, P. V., and Ono, S. (2016) Fractionation of the methane isotopologues $^{13}CH_4$, $^{12}CH_3D$, and $^{13}CH_3D$ during aerobic oxidation of methane by *Methylococcus capsulatus* (Bath). *Geochimica et Cosmochimica Acta*, **192**, 186–202. doi: 10.1016/j.gca.2016.07.031. (93, 96, 115, 121)

Wang, Z., Schauble, E. A., and Eiler, J. M. (2004) Equilibrium thermodynamics of multiply substituted isotopologues of molecular gases. *Geochimica et Cosmochimica Acta*, **68** (23), 4779–4797. doi: 10.1016/j.gca.2004.05.039. (74)

Ward, N., Larsen, Ø., Sakwa, J., Bruseth, L., Khouri, H., Durkin, A. S., Dimitrov, G., Jiang, L., Scanlan, D., Kang, K. H., Lewis, M., Nelson, K. E., Methé, B., Wu, M., Heidelberg, J. F., Paulsen, I. T., Fouts, D., Ravel, J., Tettelin, H., Ren, Q., Read, T., DeBoy, R. T., Seshadri, R., Salzberg, S. L., Jensen, H. B., Birkeland, N. K., Nelson, W. C., Dodson, R. J., Grindhaug, S. H., Holt, I., Eidhammer, I., Jonasen, I., Vanaken, S., Utterback, T., Feldblyum, T. V., Fraser, C. M., Lillehaug, J. R., and Eisen, J. A. (2004) Genomic insights into methanotrophy: the complete genome sequence of *Methylococcus capsulatus* (bath). *PLoS Biology*, **2** (10), e303. doi: 10.1371/journal.pbio.0020303. (82)

Warner, N. R., Jackson, R. B., Darrah, T. H., Osborn, S. G., Down, A., Zhao, K., White, A., and Vengosh, A. (2012) Geochemical evidence for possible natural migration of Marcellus Formation brine to shallow aquifers in

Pennsylvania. *Proceedings of the National Academy of Sciences of the United States of America*, **109** (30), 11961–11966. DOI: 10.1073/pnas.1121181109. (40)

Webb, M. A. and Miller, T. F. (2014) Position-specific and clumped stable isotope studies: comparison of the Urey and path-integral approaches for carbon dioxide, nitrous oxide, methane, and propane. *The Journal of Physical Chemistry A*, **118**, 467–474. DOI: 10.1021/jp411134v. (36)

Welander, P. V. and Summons, R. E. (2012) Discovery, taxonomic distribution, and phenotypic characterization of a gene required for 3-methylhopanoid production. *Proceedings of the National Academy of Sciences of the United States of America*, **109** (32), 12905–12910. DOI: 10.1073/pnas.1208255109. (75)

Welhan, J. A. (1988a) Methane and hydrogen in mid-ocean-ridge basalt glasses: analysis by vacuum crushing. *Canadian Journal of Earth Sciences*, **25** (1), 38–48. DOI: 10.1139/e88-004. (48)

Welhan, J. A. and Craig, H. (1983) Methane, hydrogen and helium in hydrothermal fluids at 21°N on the East Pacific Rise. In: *Hydrothermal Processes at Seafloor Spreading Centers*. Springer, pp. 391–409. DOI: 10.1007/978-1-4899-0402-7_17. (48, 55, 57, 59, 65, 71)

Welhan, J. and Lupton, J. (1987) Light hydrocarbon gases in Guaymas Basin hydrothermal fluids: thermogenic versus abiogenic origin. *AAPG Bulletin*, **71** (2), 215–223. DOI: 10.1306/94886d76-1704-11d7-8645000102c1865d. (26)

Welhan, J. A. (1988b) Origins of methane in hydrothermal systems. *Chemical Geology*, **71** (1), 183–198. DOI: 10.1016/0009-2541(88)90114-3. (48, 55, 65)

Whitehill, A. R., Joelsson, L. M. T., Schmidt, J. A., Wang, D. T., Johnson, M. S., and Ono, S. (2017) Clumped isotope effects during OH and Cl oxidation of methane. *Geochimica et Cosmochimica Acta*, **196**, 307–325. DOI: 10.1016/j.gca.2016.09.012. (21, 23, 89–90, 93, 96, 115)

Whiticar, M. J. (1990) A geochemial perspective of natural gas and atmospheric methane. *Organic Geochemistry*, **16** (1), 531–547. DOI: 10.1016/0146-6380(90)90068-b. (26, 43, 95)

——— (1999) Carbon and hydrogen isotope systematics of bacterial formation and oxidation of methane. *Chemical Geology*, **161** (1), 291–314. DOI: 10.1016/s0009-2541(99)00092-3. (26–27, 43, 85)

Whiticar, M. J., Faber, E., and Schoell, M. (1986) Biogenic methane formation in marine and freshwater environments: CO_2 reduction vs. acetate fermentation—Isotope evidence. *Geochimica et Cosmochimica Acta*, **50** (5), 693–709. DOI: 10.1016/0016-7037(86)90346-7. (26)

Whiticar, M. and Schaefer, H. (2007) Constraining past global tropospheric methane budgets with carbon and hydrogen isotope ratios in ice. *Philosophical Transactions of the Royal Society A: Mathematical, Physical and Engineering Sciences*, **365** (1856), 1793–1828. DOI: 10.1098/rsta.2007.2048. (89)

Whittenbury, R., Phillips, K., and Wilkinson, J. (1970) Enrichment, isolation and some properties of methane-utilizing bacteria. *Journal of General Microbiology*, **61** (2), 205–218. DOI: 10.1099/00221287-61-2-205. (74)

Wilkins, P. C., Dalton, H., Samuel, C. J., and Green, J. (1994) Further evidence for multiple pathways in soluble methane-monooxygenase-catalysed oxidations from the measurement of deuterium kinetic isotope effects. *European Journal of Biochemistry*, **226** (2), 555–560. DOI: 10.1111/j.1432-1033.1994.tb20080.x. (83)

Willey, L., Kharaka, Y., Presser, T., Rapp, J., and Barnes, I. (1975) Short chain aliphatic acid anions in oil field waters and their contribution to the measured alkalinity. *Geochimica et Cosmochimica Acta*, **39** (12), 1707–1711. DOI: 10.1016/0016-7037(75)90092-7. (106)

Wing, B. A. and Halevy, I. (2014) Intracellular metabolite levels shape sulfur isotope fractionation during microbial sulfate respiration. *Proceedings of the National Academy of Sciences of the United States of America*, **111** (51), 18116–18125. DOI: 10.1073/pnas.1407502111. (28)

Yeh, H.-W. and Epstein, S. (1981) Hydrogen and carbon isotopes of petroleum and related organic matter. *Geochimica et Cosmochimica Acta*, **45** (5), 753–762. DOI: 10.1016/0016-7037(81)90046-6. (108)

Yeung, L. Y. (2016) Combinatorial effects on clumped isotopes and their significance in biogeochemistry. *Geochimica et Cosmochimica Acta*, **172**, 22–38. DOI: 10.1016/j.gca.2015.09.020. (74)

Yeung, L. Y., Young, E. D., and Schauble, E. A. (2012) Measurements of $^{18}O^{18}O$ and $^{17}O^{18}O$ in the atmosphere and the role of isotope-exchange reactions. *Journal of Geophysical Research: Atmospheres (1984–2012)*, **117** (D18). DOI: 10.1029/2012jd017992. (74)

Yoshinaga, M. Y., Holler, T., Goldhammer, T., Wegener, G., Pohlman, J. W., Brunner, B., Kuypers, M. M., Hinrichs, K.-U., and Elvert, M. (2014) Carbon isotope equilibration during sulphate-limited anaerobic oxidation of methane. *Nature Geoscience*, **7** (3), 190–194. doi: 10.1038/ngeo2069. (87, 91)

Young, E. D., Kohl, I. E., Lollar, B. S., Etiope, G., Rumble, D., Li, S., Haghnegahdar, M. A., Schauble, E. A., McCain, K. A., Foustoukos, D. I., Sutclife, C., Warr, O., Ballentine, C. J., Onstott, T. C., Hosgormez, H., Neubeck, A., Marques, J. M., Pérez-Rodriguez, I., Rowe, A. R., LaRowe, D. E., Magnabosco, C., Yeung, L. Y., Ash, J. L., and Bryndzia, L. T. (2017) The relative abundances of resolved $^{12}CH_2D_2$ and $^{13}CH_3D$ and mechanisms controlling isotopic bond ordering in abiotic and biotic methane gases. *Geochimica et Cosmochimica Acta*, **203**, 235–264. doi: 10.1016/j.gca.2016.12.041. (93, 96, 108, 121)

Young, E. D., Rumble, D., Freedman, P., and Mills, M. (2016) A large-radius high-mass-resolution multiple-collector isotope ratio mass spectrometer for analysis of rare isotopologues of O_2, N_2, CH_4 and other gases. *International Journal of Mass Spectrometry*, **401**, 1–10. doi: 10.1016/j.ijms.2016.01.006. (17, 74, 93, 118)

Zahniser, M. S., Nelson, D. D., McManus, J. B., Kebabian, P. L., and Lloyd, D. (1995) Measurement of trace gas fluxes using tunable diode laser spectroscopy. *Philosophical Transactions of the Royal Society A: Mathematical, Physical and Engineering Sciences*, **351** (1696), 371–382. doi: 10.1098/rsta.1995.0040. (115)

Zumberge, J., Ferworn, K., and Brown, S. (2012) Isotopic reversal ('rollover') in shale gases produced from the Mississippian Barnett and Fayetteville formations. *Marine and Petroleum Geology*, **31** (1), 43–52. doi: 10.1016/j.marpetgeo.2011.06.009. (106)

The Geochemistry of Methane Isotopologues

David T. Wang (王戴维)

E-mail: dtw@alum.mit.edu
ORCID: 0000-0002-2656-8951

Submitted 5th May 2017
Cambridge, Massachusetts

Prepared using LaTeX.